

PHASE TRANSFORMATIONS IN NANOCRYSTALLINE
ALLOYS: EFFECT OF GRAIN SIZE AND GRAIN
BOUNDARIES

THESIS SUBMITTED FOR THE DEGREE OF
DOCTOR OF PHILOSOPHY

BY
SUBHAJIT SARKAR



SCHOOL OF PHYSICS
UNIVERSITY OF HYDERABAD
HYDERABAD-500 046
INDIA
DECEMBER 2003

DECLARATION

I hereby declare that the matter embodied in this thesis is the result of investigations carried out by me in the School of Physics, University of Hyderabad, India, under the supervision of Prof. C. Bansal.

Place: Hyderabad

Date: 27.12.2003

Subhajit Sarkar


(Subhajit Sarkar)


CERIFICATE

This is to certify that the research work described in this thesis entitled **"PHASE TRANSFORMATIONS IN NANOCRYSTALLINE ALLOYS: EFFECT OF GRAIN SIZE AND GRAIN BOUNDARIES"**, has been carried out by Mr. Subhajit Sarkar under my direct supervision and the same has not been submitted for the award of research degree of any university.

Place: Hyderabad

Date: 27.12.2003


(Thesis Supervisor)



Dean

DEAN
School of Physics
University of Hyderabad
Hyderabad-500 046, INDIA

to my parents

ACKNOWLEDGEMENTS

It is my great pleasure to express my sincere gratitude to Prof. C. Bansal for his excellent guidance and constant encouragement throughout this Ph.D work. He always appreciated my independent thinking and I was greatly benefited from the fruitful discussions. I was also touched by his very friendly attitude.

I would like to express my sincere gratitude to our Ex-Dean Prof. S. N. Kaul and present Dean Prof. V. S. S. Sastry for providing with me a very good working atmosphere in the department. I greatly acknowledge the time-to-time help I received from them.

I would like to take this opportunity to thank all the respected faculty members in the school of Physics for their co-operation.

I must acknowledge my seniors Dr. J. T. T. Kumaran, Dr. Gautam Dev Mukherjee, Dr. Ashoka and Dr. P. D. Babu for their healthy interactions.

I thank Mr. Ravi Sankar for his timely help and friendly co-operation whenever I needed them most. I also thank Suresh Babu, Abraham, Gaddam Srinivas and other non-teaching staff of the school for their co-operation.

I am grateful to Dr. K. V. Readdy, Principal Scientific Officer of Central Instrumentation Laboratory towards utilizing the facilities. I thank Mr. Murthy, Mr. Prasad Rao, Dr. Manjunath, Mr. Hemanth, Mr. Krishna Readdy and other staff of CIL for their kind co-operation.

The help and co-operation from Mr. Yusufuddin, Central Workshop, and Mr. Vincent, Mr. Ratnam, workshop and Mr. Prasad, glass blowing section is also acknowledged.

I would like to thank all my friends in the department as well as in the university and juniors, M. Phil and Ph.D students making my stay in the university very charming.

It is pleasure to acknowledge the Bengali Community in the campus for making my life here very homely.

Financial assistance in the form of Junior and Senior research fellowship from UGC is highly acknowledged. I also like to thank CSIR for providing me the passage money to attend NANO-2000 conference in Japan.

It is my great pleasure to acknowledge everybody in the home front-my parents, relatives, in-laws, friends and my wife for their constant encouragement, support and best wishes.

Contents

List of Publications

Papers Presented in National and International Conferences

Chapter 1 Introduction

1.1	Nanocrystalline materials	1
1.1.1	Mechanical alloying	3
	a. Mechanism of structure refinement in mechanical milling	7
	b. Mechanism of alloying	9
	c. Extension of solid solubility	11
1.2	Metallurgical phase transformations in alloys	16
1.2.1	Spinodal decomposition	19
1.3	Mossbauer effect	22
1.3.1	Hyperfine interactions	28
	a. Electric monopole interaction	28
	b. Electric quadrupole interactions	32
	c. Magnetic hyperfine interaction	35
	d. Origin of nuclear magnetic field	36
	e. Intensities of the ^{57}Fe absorption lines	37
1.4	Phase transformations in nanocrystalline alloys	38
	References	41

Chapter 2 Experimental Techniques

2.1	Sample preparation by mechanical alloying	50
2.2	Heat treatments	56
2.3	Energy Dispersive X-Ray (EDAX) composition analysis	57
2.4	Powder X-ray Diffraction	58
2.5	Mossbauer Spectrometer	60
	a, Mossbauer Source	61

	b. Velocity drive and feedback system	62
	c. γ -Radiation detection system and associated electronics	62
	d. PC based Mossbauer data acquisition system	66
	e. Mossbauer absorber preparation	68
	f. Various methods of Mossbauer data analysis	68
	g. Mossbauer data analysis procedure adopted by us	73
	References	80
Chapter 3	Chemical Order-Disorder Transformations	
	Introduction	82
3.1	Binary Systems	85
3.1.1	Fe-Al system	
	a. Introduction	92
	b. Experimental	94
	c. Results and discussion	95
3.1.2	Fe-Ge	
	a. Introduction	117
	b. Experimental	119
	c. Results and discussion	119
3.2	Pseudo Binary System (Fe-Mn-Ge)	
	a. Introduction	130
	b. Experimental	132
	c Results and Discussion	132
3.3	Quasi Binary Systems	
	a. Introduction	150
3.3.1	Fe-Co-Mo	
	a. Experimental	152
	b.. Results and discussion	153

3.3.2	Fe-Co-Ge	161
3.3.3	Fe-Co-W	164
	References	179
Chapter 4	Spinodal Decomposition in Nanocrystalline Fe-Cr alloys	
4.1	Introduction	183
4.2	Experimental	183
4.3	Results and discussion	183
	References	215
Chapter 5	Precipitation Phase Transformation in Nanocrystalline Fe-Mo Alloys	
5.1	Introduction	216
5.2	Experimental	216
5.3	Results and discussion	218
	References	234
Chapter 6	Structural Phase Transformations in Fe-Ge and Fe-Mn-Ge alloys: Manifestation of Gibbs-Thompson Effect	
6.1	Fe-Ge	
	a. Experimental	236
	b. Results and discussion	236
6.2	Fe-Mn-Ge	
	a. Experimental Results and Discussions	248
	References	259
	Summary of work and future perspectives	260

List of Publications

- [1] Atomic disorder-order phase transformation in nanocrystalline Fe-Al
S. Sarkar and C. Bansal
J. Alloys and Compounds 334, 135 (2002).
- [2] Gibbs-Thomson effect in nanocrystalline Fe-Ge
S. Sarkar, C. Bansal, and Ashok Chatterjee,
Phys. Rev. B 62, 3218 (2000).
- [3] Disorder-order and structural phase transformations in nanocrystalline
Fe_{3-x}Mn_xGe alloys synthesized by mechanical alloying
S. Sarkar and C. Bansal
Accepted for publication in J. Alloys and Compounds (July 2003).
- [4] Kinetic paths for B2 order in nanocrystalline FeCo-Mo: A Mossbauer
Spectroscopic study
S. Sarkar and C. Bansal
Acta Materialia 49,1789 (2001).
- [5] Kinetic paths for B2 order in nanocrystalline FeCo-Ge: A Mossbauer
Spectroscopic study
S. Sarkar, N. Chakraborty, and C. Bansal
Solid State Physics (India) 41,203(1998).
- [6] Evolution of B2 Order and grain growth in nanocrystalline FeCo-W
S. Sarkar and C. Bansal
Manuscript under preparation.
- [7] Spinodal decomposition in nanocrystalline Fe-Cr alloys
S. Sarkar and C. Bansal
Abstract Book of Recent Developments and Challenges in Physics
(Hyderabad, India, December 2002), p. PP 23.
Manuscript under preparation.
- [8] Precipitation phase transformation in nanocrystalline Fe-Mo alloys
Subhajit Sarkar and Chandrashekar Bansal
J. Nanosci. Nanotech. 4, (in press) 2004.

Publication list outside the scope of this thesis work:

- [1] Magnetic enhancement of $\text{Co}_{0.2}\text{Zn}_{0.8}\text{Fe}_2\text{O}_4$ spinal oxide by mechanical milling
R. N. Bhowmik, R. Ranganathan, S. Sarkar, C. Bansal and R. Nagarajan
Physical Review B 68, 134433 (2003)
- [2] Magnetic properties of amorphous $\text{Co}_{2-x}\text{Fe}_x\text{Ge}$ alloys synthesized by mechanical attrition
R.N. Bhowmik, R. Ranganathan, S. Sarkar and C. Bansal
J. Mat. Sc. and Engg. A304-306, 1014, 2001.
- [3] Hydrogen insertion studies in the NASICON type material
K. Koteswara Rao, A. K. Bhatnagar, S. Sarkar, M. Vithal
Materials Letters 57 (2003) 4478-4481.

Papers presented in international/national conferences/symposiums

- i) BCC-DO₃-L1₂ Phase Transformation in Nanocrystalline Fe₃Ge alloys Synthesized by Mechanical Milling
S. Sarkar and C. Bansal
Proc. Symposium on New Materials and Processing Technologies, p. 15 (1998)
- ii) Mossbauer Effect Study of nanophase and amorphous Fe and Fe₂O₃ synthesized by ultrasonification
S. Sarkar, C. Bansal and A. Gedanken
National Seminar on Nanostructured materials p. 11 (1998)
- iii) Study of phase transformations in nanocrystalline Fe-Al alloys synthesized by mechanical milling.
S. Sarkar and C. Bansal
Abstract Book, pp. 167, IUMRS-ICA '98, Bangalore, India.
- [iv] Kinetic paths for B2 Order in Nanocrystalline FeCo-Ge: A Mossbauer Spectroscopic Study
S. Sarkar, N. Chakraborty and C. Bansal
Presented in the DAE Solid State Physics Symposium, (1998).
- [v] Magnetic properties of amorphous Co_{2-x}Fe_xGe alloys synthesized by mechanical attrition
R.N. Bhowmik, R. Ranganathan, S. Sarkar and C. Bansal
Presented at RQ10, Bangalore, India, 1999
- [vi] Microstructure Evolution in Nanocrystalline Fe_{3-x}Mn_xGe Alloys Synthesized by Mechanical Alloying
S. Sarkar and C. Bansal
Presented in 5th International Conference on Nanostructured Materials (NANO '2000) held in Sendai, Japan during August 20-25 2000
- [vii] Micro structure Evolution and Phase Decomposition Behavior of nanocrystalline Fe-Mo Alloys
S. Sarkar and C. Bansal
Presented in the DAE-SSP 2000 Symposium
- [viii] Influence of Grain Boundaries on Phase Transformations in Nanocrystalline Alloys
Presented in EUROMAT-2001 Conference Proceedings Held in Rimini, ITALY, 10-14 July 2001.
- [ix] Phase transformations in nanocrystalline alloys synthesized by mechanical alloying
International Conference on Mechanochemistry and Mechanical Alloying, (INCOME 2003) Held in Braunschweig, Germany, September 7-11, 2003.

Chapter 1

Introduction

In the quest for new and advanced materials having better physical, chemical, mechanical, thermal, magnetic and other properties, it was understood that the microstructure and the constitution of the materials have a vital role to play. It was also realized that the microstructure and the constitution can be better controlled by processing them under non-equilibrium (or far from equilibrium) conditions [1]. Rapid **quenching/solidification** from the melt (RSP) [2, 3], vapour deposition (VD) [1,4], plasma processing (PP) [1, 5], ion implantation (II) [6], and since last 2-3 decades the process of mechanical alloying (MA) [7-11] are some of the commonly used non equilibrium processing techniques. The central underlying theme in all these processes is to bring the material in a highly non-equilibrium state by energizing through some external dynamic forcing, e.g., through melting, evaporation, irradiation, application of pressure, or storing of mechanical energy by plastic deformation [12, 13, 14], and such materials are referred to as 'driven materials' by Martin and Bellon [15]. Among these techniques the departure from equilibrium is substantially high in case of MA as well as VD and II (of the order of 30 kJ/mole or more) [12, 16-18].

1.1 Nanocrystalline materials

Nanocrystalline materials (alloys, ceramics, intermetallics, pure metals, polymers, composites etc.) are characterized by the small size of the randomly oriented grains separated by high angle grain boundaries. Various novel properties (thermal, chemical, magnetic, mechanical, optical, electrical etc.) of nanocrystalline materials are largely influenced by the presence of large amounts of grain boundaries (**typically** 10^{19} / cc) or inter-crystalline or inter-phase interfaces present in the structure [19]. The properties of these materials are often controlled by the grain size distribution and the atomic structure of the grain boundaries and their excess volume along with the cohesive energy. The nanostructured phase is a nonequilibrium phase because of the presence of

these grain boundaries and therefore grain growth is inevitable to approach equilibrium by reducing the boundary regions. The stability of nanostructured materials against their grain growth under compaction and annealing to obtain the desired size and shape is a field of immense interest to preserve the novel properties showed by them for industrial production and applications [20-23, 6, 24-26]. The grain growth behavior was studied under hot isostatic pressing (HIP) [27, 28] with a pressure of 138 M Pa and at temperature of 800°C in Cu-15 at.% Nb, and electro discharge compaction (EDC) in Al_3Nb alloy systems and it was concluded that not much grain growth took place [29, 30]. It was also found that grain growth could be controlled by mixing nano intermetallics in appropriate composition, e.g. by mixing Ni_3Al and NiAl in nearly equal proportions grain growth was slowed down up to 500°C [31]. Among the various ways of preparing nanostructured materials (NsM) inert gas condensation/ vacuum compaction [32], electro-deposition [33], sputtering [34], mechanical milling (MM), and thermo-chemical routes [35] are some of the important methods. They can be classified in two broad categories i) down-top method, e.g. cluster assembly and ii) top-down method, e.g. MM. In the first process atom-by-atom is assembled to get the nano structure and in the second process bulk material is refined to produce the nanostructured materials [36]. Nanocomposites prepared by MA [37, 38, 39] or when the amorphous phases obtained by MA/MM are crystallized at relatively low temperatures show in some cases improved strength and ductility. Another important attribute of these nanocomposites is in preventing or minimizing grain growth till very high temperatures. Reinforcement of Cu and Mg with Al_2O_3 was reported to prevent grain growth up to the melting point of the metals [40]. Formations of metallic glass/ceramic composites [41, 42] by MA are an example of dispersion strengthened amorphous alloys with better strength and wear resistance. Alloys in the nanocrystalline form have also been shown to have much higher hydrogen absorption properties at low temperature. Drastic changes occur in

the mechanical properties of materials due to reduction in grain size [43, 44] and the behavior in many instances become similar to that of amorphous materials [45]. Hardness also increases as grain size decreases. It was observed for pure Fe that the hardness increased nearly seven fold (~ 9 GPa for n-Fe in comparison to 1.3 GPa for μ -Fe) and Young's modulus decreased by 10% [46]. In fact the hardness of pure nano Fe became comparable with that of the hard intermetallics Nb_3Sn [47]. Similar observation was reported for Nb also [48]. It was argued that this increase was not due to plasticity of the crystal by dislocation movement but due to cohesion of grain boundaries. This increase in hardness is very promising for their future applications.

1.1.1 Mechanical alloying

Among the various processes of preparation of NsM, mechanical milling (MM) and mechanical alloying (MA) in a high-energy ball mill are two of the very common and widely used methods. In my work also the alloy samples were prepared by MA and therefore to start with I would like to give a brief introduction of mechanical alloying: how structural refinement occurs and the key attributes. Ordinary ball milling was routinely used in minerals, ceramic processing, and powder metallurgy industries with an objective of particle size reduction, mixing, blending, and particle shape change [49]. But since its inception around 1966 by Benjamin [50-53] high energy ball milling is used to produce: 1) oxygen dispersion strengthened (ODS) Fe and Ni based alloys used for gas turbine and aerospace engineering. 2) Alloys with metal of quite different melting points with the goal of improved strength and corrosion resistance. 3) Alloys in a non-equilibrium state with extended solid solubility than the equilibrium solubility, which in turn produces amorphous alloys in a number of alloy systems by destabilizing the crystalline lattice by the incorporation of large amount of defects. Mechanical alloying (attrition, also

commonly known as high energy ball milling) has proved to be a very versatile tool to produce nano structured materials with a wide variety of chemical composition and atomic structure [54, 7, 55, 6, 47, 46 and references therein]. The mechanism of microstructure formation is very different in MA but the resultant microstructure formed is very similar to that obtained by other synthesis routes to produce nanostructured materials. Numerous binary and multinary alloys, intermetallics, ceramics, polymers, quasicrystals [table 9 of 6], nanostructured pure metals, composites, dispersion strengthened alloys and amorphous materials are produced by this versatile method [56-85]. This is recognized as a relatively inexpensive non-equilibrium solid-state powder processing technique involving repeated welding, fracture, and rewelding of powder particles to produce nano materials. The starting raw material for MA/MM is commercially available pure elemental powder and pre-alloyed materials and intermetallics (either in powder form or in some other compacted form), generally in micron size grains. The initial size of the material/particle does not matter much as long as its size is small in comparison to the balls size because with high energy impact of the balls the material gets grinded within a very short span of time and becomes powder. In general this is a dry and room temperature (RT) process but occasionally wet milling, in which solid particles are milled with liquid medium [86-90], milling at an elevated temperature [91] or cryomilling (milling in LN₂ atmosphere or low temperature) [92, 93] are also carried out depending on specific need and applications.

Different nomenclatures have been adopted depending on the nature of the starting materials to be milled. Mechanical alloying (MA) is used where blended elemental powder mixtures in the required composition or elemental powders with intermetallics are milled until the final alloy phase with desired composition is formed. Material transfer takes place in this process for homogeneous alloying. Mechanical milling (MM) is the term used when pre-alloyed powders, pure metallic or single phase intermetallics are milled to

obtain structural refinement ultimately leading to fine grained or nano structure. No material transfer takes place in MM. Frequently Mechanical Attrition is loosely used to mean either MA or MM. If only disordering of ordered intermetallics or alloys is done, then the process is known as mechanical disordering (MD). In all cases the resultant microstructure is either nano-crystalline (i.e. having randomly orientated coherently diffracting crystallites with long range translational symmetry and average crystallites sizes ranges from 5 to few tens of nanometer) or amorphous (i.e. having no long range translational symmetry but short range order in the range of less than 2 nm) structure. It will be discussed in the next chapter in the context of Fe-Mn-Si and Fe-Ge alloys that MM takes place much faster than MA. This is in accordance to the earlier observation [94]. Some other terms are also used in the literature on Mechanical Alloying depending on the process involved with MA. These include mechanochemical synthesis by reaction (or reactive ball) milling (RM), mechanically activated annealing (M2A), double mechanical alloying (dMA), and mechanically activated self-propagating high-temperature synthesis (MASHS) [95-103]. In RM chemical reaction is induced at either RT or at much lower temperature than that required during the conventional methods by mechanically activating the powder mixtures [104, 105]. M2A refers to the process where low temperature isothermal annealing follows the short duration MA to produce the material (e.g. refractory materials such as silicides). In dMA the powder mixture is initially milled for refinement of the powder particles and to obtain an intimate mixture, which is subjected to high temperature heat treatment to produce the macrocrystalline intermetallics-the production of which would not have been possible directly by milling. The intermetallics formed in this way is once again milled to reduce the grain size and to produce the nano-sized grains. MASHS is the process where MA precedes the SHS to reduce the operating high temperature by as much as 100 C - several Fe and Nb- aluminides, prepared by this method. It is clear

from the above discussion that the underlying common phenomenon in all the above cases is the initial excitation of the powder mixture by mechanical deformation.

Commonly used milling equipments include shaker mills, planetary mills, vibratory mills, attritor mills, tumbler mills, and commercial mills [106, 107]. Among these different types of milling apparatus, shaker mills, such as SPEX 8000 mixer mill from Certiprep, NY, USA is the most high energetic and the alloying and /or grinding process takes place much faster than the other milling apparatus [6, 46, 47]. The amount of powder that could be milled differs largely in different mills and it ranges from few grams in a SPEX mill to few thousand of grains in attritor and commercial mills. A variety of vial and grinding medium materials is available for the SPEX and other mills and these include hardened steel, alumina, tungsten carbide, zirconia, stainless steel, silicon nitride, agate, plastic, sintered corundum and methacrylate. As the energy of milling depends on the balls kinetic energy hence dense materials such as hardened steel, stainless steel (SS), tungsten carbide (WC) are most commonly used for the balls and vial in the milling process.

The final phase, micro-structural constitution (e.g. minimum grain size), and alloying of the material depends on factors such as intensity of milling (i.e. milling equipment), time of milling, ball to powder weight ratio (BPR), temperature of milling, type, size, size distribution and speed of the grinding balls, extent of filling the vial, mechanical properties (ductility, brittleness etc) of the constituents elements and the material of the vial and the balls [6, 72]. It was found that the minimum grain size attained was inversely proportional to BPR. The rate at which nano structure evolution takes place depends on the temperature of milling. It was found in case of Fe-Cu system that the minimum grain size attained was depending on concentration of Fe in the Cu matrix and vice versa [108, 109].

a. Mechanism of structure refinement in MM

In high energy milling the powder particles are repeatedly flattened, cold welded, fractured and rewelded during collisions between the balls and the balls and the milling container. Several attempts have been made to model the mechanical milling/alloying process [110-114]. As shown in figure 2.1b when some amount of powder particles are impacted between the balls or between the balls and the container walls during their collisions while moving with high velocity, the particles get plastically deformed leading to work hardening and fracture. Typically 1000 particles with an aggregate weight of 0.2 mg get impacted during the collisions with collisions time of 1-2 μsec . This fracture opens up new surfaces of the particles, which helps in cold welding of the particles among each other. Particle size increases because of this cold welding and some time it can go as high as 3 times than the starting size. Mechanical attrition is characterized by cyclic shear deformation of powder particles with high strain rate ($\sim 10^1$ - $10^4/\text{sec}$) within the particles resulting in the reduction of grain size. TEM observations, by Hellstern [115] showed that at the early stages of MM, shear bands (heavily deformed regions) were formed due to the production of inhomogeneous deformation at a high rate during MM. These shear bands, which contain a high dislocation density, have a typical width of approximately 0.5-1.0 μm and are separated by lateral regions of low defect density. With continued milling, the average atomic level strain increases due to the increasing dislocation density, and at a certain dislocation density within these heavily strained region, the crystal disintegrates into subgrains that are separated by low-angle grain boundaries. HREM images of the shear bands revealed the presence of grains of approximately 20 nm size separated by low angles ($\sim 20^\circ$). This results in a decrease of the lattice strain. On further processing, deformation occurs in shear bands located in previously unstrained parts of the material. The grain size decreases steadily and the shear bands

coalesce. The small angle boundaries are replaced by higher angle grain boundaries, implying grain rotation due to grain boundary sliding because of the enhanced diffusivity of the atoms through grain boundaries even at low temperatures [116]. This was reflected by the absence of texture in the electron diffraction patterns and random orientation of the grains observed from the lattice fringes in the high-resolution electron micrographs. Consequently, dislocation-free nanocrystalline grains are formed. Li et al. [117] have also proposed a model for the refinement of grain size during ball milling and noted that the grain size in the early stages of milling follows the relation:

$$d = Kt^{-2/3}$$

where d is the grain size, t is the time and K is a constant.

The minimum grain size achievable by milling is determined by the competition between the plastic deformation via dislocation motion and the recovery and recrystallization behavior of the material [118, 119]. This balance gives a lower bound for the grain size of pure metals and alloys. It is also governed by the Hall-Petch relation (dislocation pile-up model) [120-122], i.e. $\sigma = \sigma_0 + K(d_{\min})^{-1/2}$, where σ 's are the yield stresses and d_{\min} is the minimum average grain size. The minimum grain size obtained therefore depends on the maximum stress that could be generated by mechanical deformation.

. The d_{\min} obtained by MM was found to vary inversely with the melting point of Al, Ag, Cu, and Ni (all having an fcc structure) [118], and directly with the stacking fault energy. However, when data from the bcc and hcp metals as well as several intermetallics are included, only fcc metals (with a relatively low melting point) showed this clear inverse dependence of minimum grain size on the melting point [47, 124]. The minimum grain size was virtually independent of the melting point for the hcp, bcc, and other fcc metals with high melting points [71, 125]. For these elements it appears that

d_{\min} is in the order: fcc < bcc < hcp. The range of d_{\min} obtained was 10-20 nm for pure metallic and some of the intermetallics with CsCl structure [47].

b. Mechanism of alloying

The phenomenon of MA between two or more elemental components is one step forward to MM. In this case the composite particles result at the early stages of milling due to cold welding have a characteristic layered structure consisting of various combinations of the starting constituents. Due to the steady refinement of the structure of the composite particles by mechanical deformation the inter layer or lamellar spacing decreases and the nanometer sized crystallites (grains) results. The number of grains or layers in a particle increases. Large amount of defects in the form of dislocations, vacancies, grain boundaries, stacking faults etc. are produced by mechanical deformation which in turn along with a decrease in the diffusion length increase the atomic diffusion of the species largely. In most of the cases the temperature rise during milling is slightly above the operating temperature (e.g. RT) but in some cases temperature rise was observed but maximum within 200 C, most commonly between 100-120° C [6]. The nominal temperature rise during milling also helps in atomic diffusion. Hence true alloying takes place between the constituent atoms through mechanically enhanced interdiffusion and a homogeneous alloy results. Occasionally it is required to anneal the milled sample to obtain the homogeneous alloy. This is specially required in case of some intermetallics [6].

Generally alloying is conducted with three different combinations of elements: 1) ductile-ductile, 2) ductile-brittle, 3) brittle-brittle.

Ductile-ductile System: According to Benjamin [50, 126] this is the best combination for mechanical alloying. He suggested that to achieve better alloying at least 15% of the alloying ingredients should be ductile to enhance

the cold welding process. Our Fe-Al, FeCo-W, FeCo-Mo, Fe-Cr, and Fe-Mo systems belong to this category. The alloying and particle structure refinement process is as described above. This is the best combination also from the point of view of contamination from milling, as will be discussed later.

Ductile-Brittle System: In this combination, e.g. our Fe-Ge, FeCo-Ge, FeMn-Ge, and FeMn-Si, the ductile component get work hardened and fractured while the brittle component gets fragmented by the impact of the balls during collisions. These fragments get occluded and closely spaced along the **interlamellar** spacing in the composite lamellar structure of the ductile particles after cold welding. These brittle particles get finely dispersed or alloyed **depending** on their solubility in the ductile matrix [52, 63, 127-129].

Brittle-Brittle System: MA is difficult in this combination and this is not of interest in our work. However some reports regarding alloying in this combination exists [82, 113, 130-132]. Structural refinement even in brittle ceramics (e.g. ZrO_2 , Nb_3Sn) similar to that obtained if a large hydrostatic pressure component (e.g. hydrostatic extrusion) is present is also observed by MM [133-135]. In this process both the components get fragmented /comminuted at the early stages of milling until the 'limit of comminution' is reached and they start behaving like ductile components. At this stage between the two components harder component gets embedded into the softer component, like in the Ge-Si system Si got embedded in the Ge matrix [130].

The important fact about MA/MM is that the **efficiency** of particle size reduction in milling is too low and a maximum of only 1 % particle size reduction could be attained even in high energy ball milling. This is because with continued deformation upon milling the composite particles once again get work hardened and fractured by a fatigue failure mechanism and/or by the fragmentation of fragile flakes. This process of cold welding and fracture repeats over many cycles still a steady stage is reached when rate of cold welding and fracture become equal with the steady state particle size of few

microns. At this stage each particle contains substantially all of the starting ingredients, in the proportion they were mixed together and the particles reach saturation hardness due to the accumulation of strain energy. Therefore the resultant particle size remains in the micron range but the grains within the particles reach nano-size with a narrow size distribution, verified by TEM measurements [46, 136].

The nanostructure formation through the process of cyclic shear deformation with high strain rate in MA/MM is very similar to that observed in other solid state techniques like cold rolling, wire drawing of materials, friction induced wearing of surfaces, production of chips during machining, filing of materials [137-144]. Plastic deformation was not only observed in metals and alloys [145] but also in ceramics and diamond surfaces [146, 147]. The micro structure formed in Fe-Cu system through MA was very similar to that obtained by cold rolling [148].

c. Extension of solid solubility

The extension of equilibrium solid solubility is achieved by MA similar to that obtained in case of Rapid Solidification Process (RSP) [149], in vapour deposition [1], or by gas condensation method [150]. In addition to stable (equilibrium) solid solution MA also produces metastable (non-equilibrium) supersaturated solid solution or amorphous phase of blended elemental powders-forming binary or higher order alloy systems, intermetallics [151-155, table 10 of 6]. In his review article Suryanarayana [table 7 of 6] has given an extensive list of solid solutions (both equilibrium and non-equilibrium) of different solute and solvent elemental combinations. In many cases this extended solid solubility results in amorphous phase by destabilizing the crystal against amorphization [46]. It was understood that soft milling conditions (such as high BPR, low temperature, moderate milling intensity,

less time of milling etc.) are preferable to produce metastable phases [156-159]. In some cases high temperature and high pressure (HP) phases are retained by MA at RT and atmospheric pressure-which is also an example of metastable phase formation [6]. It was estimated from the formation of the HP phase that the pressure generated during milling is of the order of 6 GPa [160, 113].

The formation of nano-phase in mostly all case of MA wherein diffusion of atoms increases through large amount of grain boundaries [161-163], production of defects and local stresses [164, 165], high enthalpy stored in the grain boundaries due to heavy deformations [SY 71, 166-167], capillary pressure developed at the tip of the elemental fragments formed upon deformation [168-170], local melting of the alloying elements [171], Hume-Rothery (H-R) rule for equilibrium solid solutions formations (i.e. the difference between the metallic radii of the solute and solvent atoms should not be more than 15%, they should have the same crystal structure, same valency, and very close electro negativity values to achieve complete or in some cases very good solid solubility) [172-174], modified Darken-Gurry plot [175] of electro negativity vs. metallic radius are various explanations of solid solubility extension by MA. It was observed by Bansal et al. [173] that in case of elemental Fe milled with 25 at. % Al, As, Ge, In, Sb, Si, Sn, and Zn, an extended solubility of as large as 25 at.% could be attained if the elements metallic radii satisfy H-R criterion but otherwise also a notable solubility of 5 at.% was observed even with metallic radii differing by 30 at. % by MA. In some cases amorphous phase formation occurs under metallic radii differing by more than 15 % [176]. Similarly extended solubility was observed with component elements differing in electro negativity by as high as 0.3 units. In some systems like Cu-Ag, H-R criterion predicts 100% solubility and which was obtained by MA under non equilibrium conditions whereas under

equilibrium processing conditions only few, 7-8 at. % of Ag was soluble in Cu [Figure 19 of 6].

The vital example of MA as a non-equilibrium processing technique is its ability to produce alloying in otherwise immiscible systems, which have positive heat of mixing, and in this regard MA has an edge over RSP, in which alloying requires large negative heat of mixing in most cases. The alloying with extended solubility in otherwise immiscible systems through deformation was predicted by Monte Carlo simulations resulting in high temperature and high entropy state [177, 178]. In the Fe-Ag system intimate fine dispersion of particles in the nano-dimension took place [62].

Various Cu-based alloys were produced by MA [181, 182, 168, 166] and among them most important was Fe-Cu system [183, 184]. Solid solutions of up to 45 at. % Cr in Fe and that of Mo up to 5 at. % in Fe were obtained through MA by us and will be discussed in chapter 4 and 5. These systems show phase decomposition behavior under normal equilibrium conditions. The enhanced solid solubility is attributed to the competition between the excess pressure (due to small size) and the negative surface energy contributions to the total Gibbs' free energy of the nano-system.

The synthesis of intermetallics in the quasicrystalline, metastable-crystalline or in equilibrium disordered or ordered crystalline phases is one of the important attributes of MA [6]. Disorder of ordered intermetallics by means of anti-site disorder, triple defects, and redistribution of interstitials to obtain better strength by MM is one of the important aspect of it [6]. The milling energy supplied can be stored as energy due to disorder and grain boundary energy, i.e.

$$\Delta G_{\text{milling}} = \Delta G_{\text{disorder}} + \Delta G_{\text{GB}}$$

Amorphization also occurs due to incorporation of various kinds of defects by milling and depending on whether the intermetallics is permanently

ordered or reversibly ordered. If the alloy is reversibly ordered than solid solution formation is preferred but if it is permanently ordered than amorphous phase formation is preferred. In some cases no transformation occurs instead the system transform from low temperature phase to high temperature phase [6].

MA of the elemental powder mixtures also forms amorphous alloys by the incorporation of large amount of defects. In some cases amorphous phase are directly formed and in some other cases disordered or ordered intermediate crystalline phases are formed before amorphization [75, table 17 of 6]. Milling temperature plays a critical role in the process of amorphization by MA/MM against recrystallization. It was observed that milling at a lower temperature favored the amorphous phase formation whereas at an elevated temperature recrystallization was taking place. It was also observed that prolonged milling was required at higher temperature than at lower temperature to achieve amorphization [6]. Bulk metallic glass formation was also observed [185, 186].

The energy stored in the Nano structured materials (NsM) produced by MA/MM is order of magnitude more than the materials produced by ordinary deformation mechanism. Typically the enthalpy released in the differential scanning calorimetry (DSC) measurements of the pure metals or single phase intermetallics is of the order of 7-10 kJ/mole in contrary to enthalpy released by ordinarily deformed same materials of the order of 1-2 kJ/mole [187]. The enthalpy released by these nano materials is a substantial fraction of the heat of fusion (H_f) and it is as high as 40 % of H_f for elemental Ru. This enthalpy is much larger than that obtained for ordinary deformation process governed by steady state dislocations (both screw and edge) density and dislocation movements. Hence it is argued that the source of this excess energy arising due to mechanical deformation is mostly the grain boundaries. Therefore the deformation process takes place in two steps; initially it takes place through

production of dislocations and in a later stage through grain boundaries. It was observed in favour of this argument that the grain boundary shear modulus decreases by nearly 40 % when grain boundary volume is comparable to the crystalline fraction [46].

The release of this excess energy by thermally activated grain growth gives rise to the broad peak in the DSC curve over the entire temperature range up to around 800 °C. Severe plastic deformation during MA as well as grain boundary stress due to pinning of GB's give rise to atomic level lattice strain of the order of 0.3-1.0% [47, 173]. This strain decreases rapidly below 200°C giving rise to the low temperature low intensity peak in DSC. The specific heat (C_p) also increases at small sizes of the grains and a linear relationship was found for pure metals between ΔC_p and stored enthalpy AH (expressed as a fraction of H_f as AH / AH_f), which is also expected considering excess free volume model for grain boundaries [188].

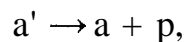
Often the vexing problem in MA/MM is the contamination from the milling medium, milling atmosphere and occasionally from other sources like process control agent or LN_2 in case of cryomilling. The contamination also depends on the milling apparatus and hence milling intensity, milling time and to some extent temperature of milling [189-192]. The source of contamination is the wear and tear of the grinding medium and the container and at the same time availability of fresh surfaces of the particles by fracture with the small (nano) size developed due to milling and therefore the large surface area. The extent of contamination ranges from few to several atomic percents. However the amount of contamination can greatly be reduced and restricted to within 1-2 at. % by sealing the vial under high purity inert atmosphere and by using ultra high purity elemental powder. Another way of reducing the contamination is rod milling [193], where instead of balls grinding medium is of rod shape, which introduces shearing stress and hence the scratching of materials from the grinding mediums is less. In this way the

contamination during milling in some cases is less than that results in other methods such as chemical routes or inert gas evaporation and condensation process of preparing NsM [46]. In some cases contamination plays a important role for deciding the final phase formed due to milling, especially amorphous phase formations [6] but in some other cases contamination is introduced intentionally to produce ceramics or nanocomposites [46].

1.2 Metallurgical phase transformations in alloys

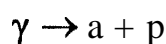
The different types of diffusional phase transformations possible in binary alloys can be divided into the following groups: a) Precipitation reactions, b) Eutectoid transformations, c) ordering reactions, d) massive transformations, and e) Polymorphic changes [194]. Figure 1.1 shows the different types of binary phase diagrams that are representative of these transformations. We will not consider diffusionless transformations like martensite.

Precipitation transformations can be expressed in reaction terms as follows



where a' is a metastable supersaturated solid solution, β is a stable or metastable precipitate, and a is a more stable solid solution with the same crystal structure as a' , but with a composition closer to equilibrium (figure 1.1a).

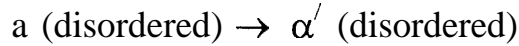
Eutectoid transformations involve the replacement of a metastable phase (γ) by a more stable mixture of two other phases ($a + p$) and can be expressed as



This reaction is characteristic of phase diagrams, such as those shown in figure 1.1b.

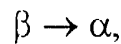
Both precipitation and eutectoid transformations involve the formation of phases with different compositions to the matrix and therefore long range

diffusion is required. The remaining reaction types can, however, proceed without any composition change or long-range diffusion. Figure 1.1 c shows phase diagrams where ordering reaction can occur. In this case the reaction can be simply written as



Here disorder means that all the lattice positions are occupied by alloy atoms randomly and ordered means that the lattice sites are grouped into sublattices, each of which is occupied predominantly by one species of atoms.

In a massive transformation the original phase decomposes into one or more new phases, which have the same composition as the parent phase, but different crystal structure. Figure 1.1d illustrates two simple examples of the type



Where only one new phase results, which can either be stable (figure 1.1 d(i) or metastable (figure 1.1 d(ii)).

Polymorphic transformations are the simplest transformations and not of much interest. These kinds of transformations occur in systems where different crystal structures are stable over different temperature ranges, Figure 1.1 e.

The change in Gibbs free energy caused by homogeneous alloying of two elements (A and B) is given by $\Delta G_{\text{mix}} = \Delta H_{\text{mix}} - T\Delta S_{\text{mix}}$, where ΔH_{mix} (also known as heat of solution) is the heat absorbed or evolved by mixing, and ignoring volume changes during the process at atmospheric pressure, it represents only the difference in internal energy (U) before and after mixing. ΔS_{mix} is the difference in entropy before and after alloying. In the above expression ΔS_{mix} is always '+ve' and ΔH_{mix} can be either '+ve' or '-ve', depending on the bond energies of the constituent atoms, assuming the so called quasi chemical approach, wherein the volume change during mixing is neglected. ΔH_{mix} (or ΔU_{mix}) is '+ve' for the alloys, which have thermodynamic tendencies to precipitate or decompose to A-rich and B-rich regions. This

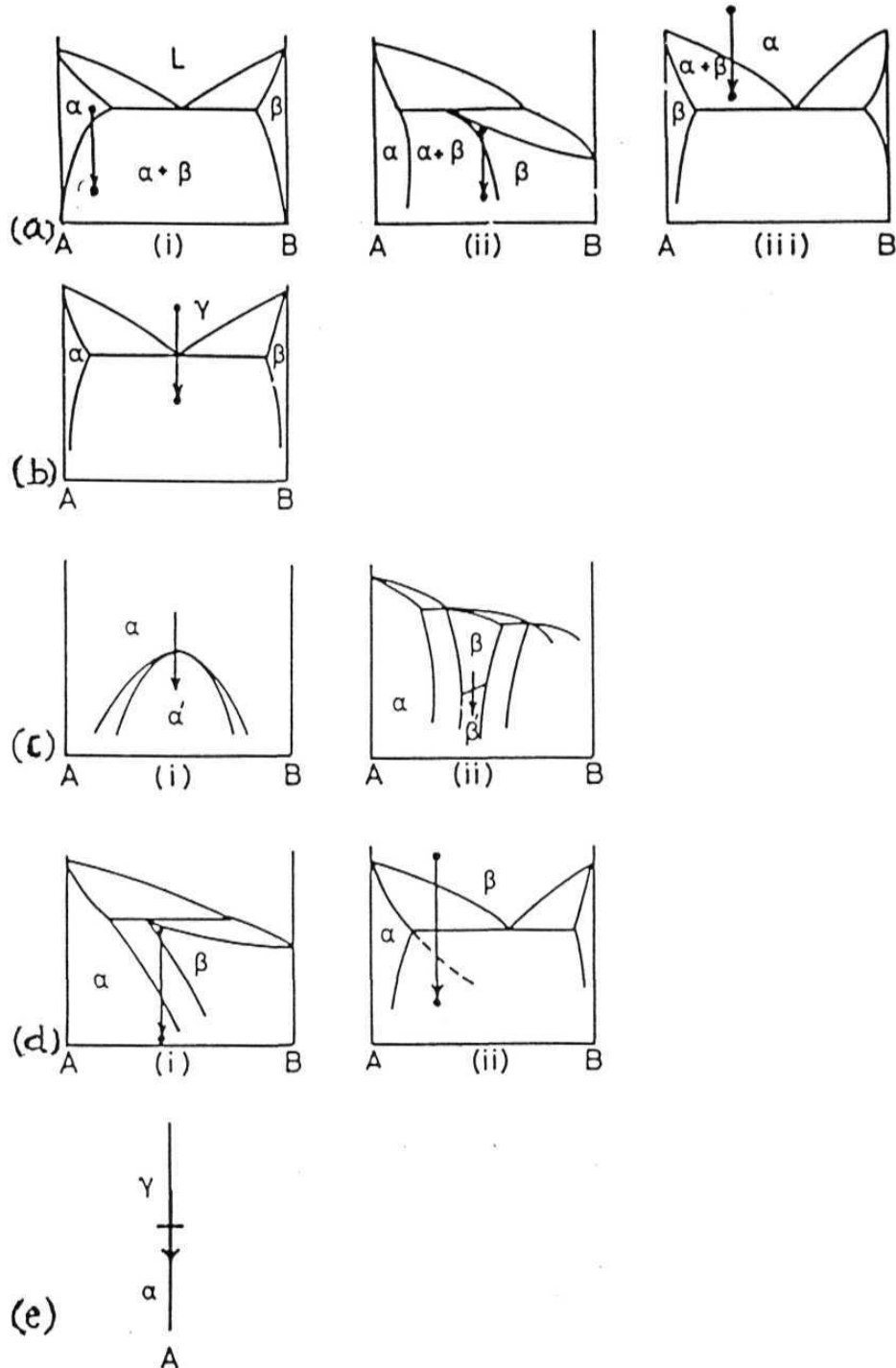


Figure 1.1: Examples of different categories of diffusional phase transformations: (a) precipitation, (b) eutectoid, (c) ordering, (d) massive, and (e) polymorphous (single component) [194],

means that A-A and B-B bonds are preferable than A-B bonds. On the other hand for alloys having thermodynamic tendencies towards ordering, ΔH_{mix} is 've' indicating that A-B bonds are preferable than A-A or B-B bonds.

Long range and short-range atomic diffusion is the underlying mechanism in all these transformations. Many of these transformations occurs through nucleation and growth but in some cases of order-disorder transformations there can be a continuous increase in short-range-order by local rearrangements occurring homogeneously throughout the crystal which finally leads to long range order.

In the following section we discuss about a the special class of precipitation transformation (known as Spinodal decomposition), where there is no barrier of nucleation.

1.2.1 Spinodal decomposition

The phase diagram (temperature vs composition) responsible for Spinodal decomposition of an alloy is shown in figure 1.2a. The homogenous alloy with initial composition X_0 could be formed by some nonequilibrium methods (such as MA) with free energy G_0 on the G curve, shown in figure 1.2b. However the alloy will be immediately unstable because small fluctuations in composition that produce A-rich and B-rich regions will cause the total free energy to decrease. Therefore 'up-hill' diffusion (diffusion from lower concentration side to higher) takes place as shown in figure 1.3a until the equilibrium compositions X_1 and X_2 are reached. The change in Gibbs free energy by small fluctuation of compositions on either side of X_0 is given by $\Delta G_c = (dG / dX) (\Delta X)$. Therefore the Spinodal process can occur for any arbitrary composition where the free energy curve has a '-ve' curvature, (i.e. $d^2G/dX^2 < 0$). This means that the alloy must lie between the two points of

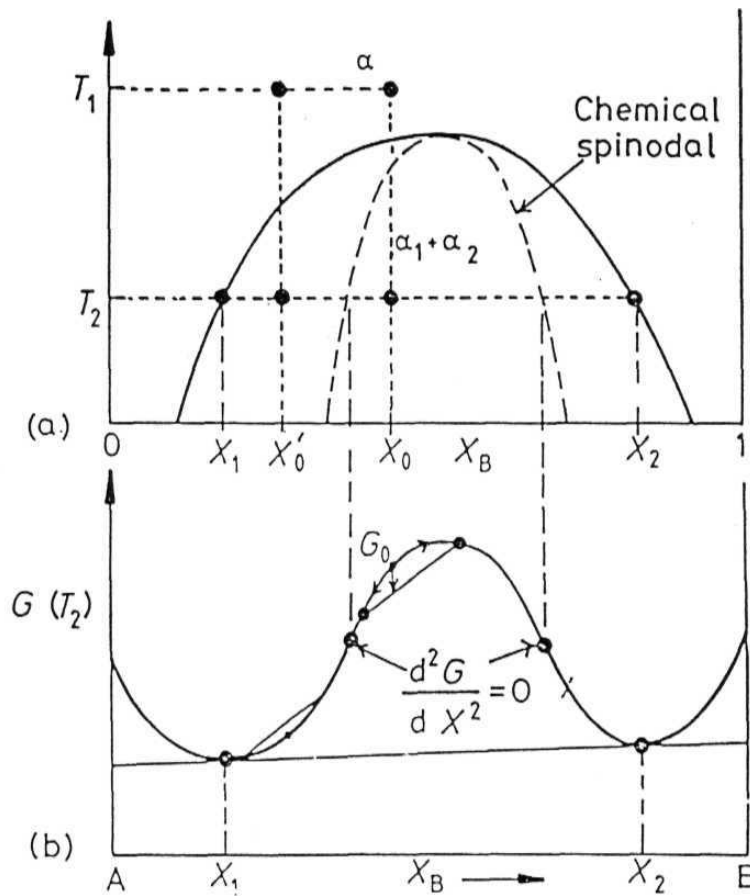


Figure 1.2: Alloys between Spinodal points are unstable and can decompose into two coherent phases α_1 and α_2 without overcoming an activation energy **barrier**. Alloys between the coherent miscibility gaps and the Spinodal (X'_0) are metastable and can decompose only after nucleation of the other phase,[194].

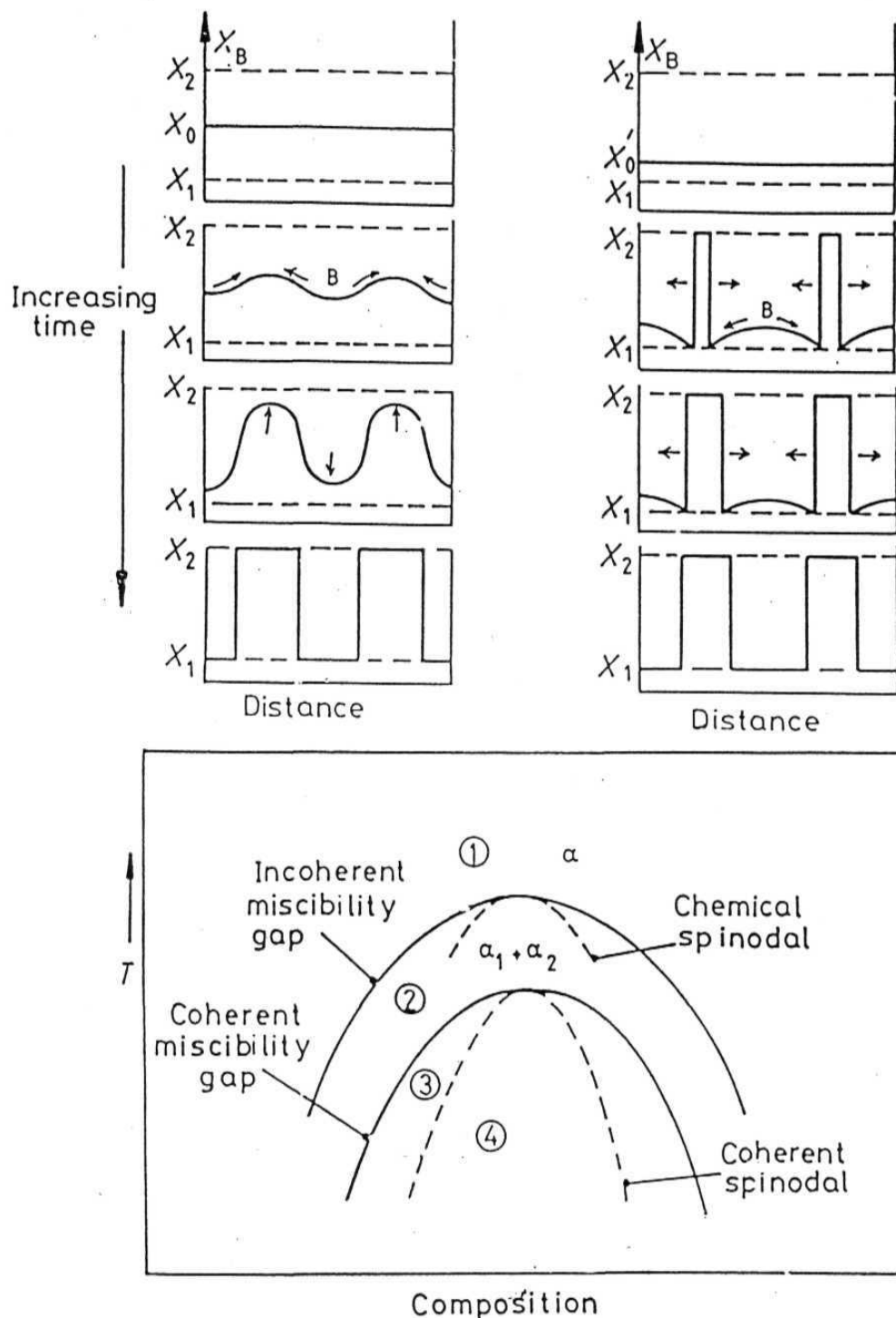


Figure 1.3: (a) Schematic composition profiles at increasing times in an alloy synthesized in the Spinodal region (X_0 in figure 1.2). (b) Schematic composition profiles at increasing times in an alloy synthesized outside the Spinodal region (X_0' in figure 1.2). (c) Schematic phase diagram for a clustering system. Region 1: homogeneous α stable. Region 2: homogeneous α metastable, only incoherent phases can nucleate. Region 3: homogeneous α metastable, coherent phases can nucleate. **Region 4: homogeneous α unstable, no nucleation barrier, Spinodal decomposition occurs.** [194].

inflections on the free energy curve (figure 1.2b). The locus of the points on the phase **diagram**, figure 1.2a, is known as the chemical Spinodal.

If the alloy lies outside the Spinodal (X_0' in figure 1.2a), small variations in composition lead to an increase in free energy and the alloy is therefore metastable. The free energy of the system can only be decreased in this case if nuclei are formed with a composition very different from the matrix. Therefore, outside the Spinodal the transformation must proceed by a process of **nucleation** and growth. Normal down-hill diffusion (diffusion from higher concentration side to lower) occurs in this case as shown in figure 1.3b.

The rate of Spinodal transformation is controlled by the interdiffusion coefficient, D . Within the Spinodal $D < 0$ and the composition fluctuations shown in figure 1.3 a will therefore increase exponentially with time, with a characteristic time constant $\tau = -X^2 / 4\pi^2 D$, where X is the wavelength of the composition fluctuations (assumed one-dimension). The rate of transformation can therefore become very high by making X as small as possible. However by considering the gradient energy (arising due to interfacial energy, the magnitude of which depends on the composition gradient across the interface) and the coherency strain energy (arising due to misfit strain between A and B-rich regions) contributions to the total Gibbs free energy change, there is a minimum value of λ below which Spinodal decomposition cannot occur [194]. The typical value of X is ~ 5 nm. Figure 1.3c shows the coherent miscibility gap and the coherent Spinodal region, which is the region defining the equilibrium compositions of the coherent phases that result from Spinodal decomposition.

1.3 Mossbauer effect

Since its discovery in 1957 by Rudolph Mossbauer [195], Mossbauer spectroscopy emerged out to be a versatile tool to study various physical (in particular condensed matter physics), chemical, biological and space materials. The application of Mossbauer spectroscopy is widespread in spite of the fact

that only a few dozen isotopes (most commonly Fe, Sn, and Eu) are recognized as potential Mossbauer isotopes that satisfy the criteria specified for the correct and useful implementation of the technique [196-200]. The recoilless emission of γ -rays and resonance absorption by an identical nucleus is known as Mossbauer effect. The recoil energy (E_R) experienced by a isolated nucleus undergoing transition from excited to ground state resulting in the emission of γ -rays is given by

$$E_R = \frac{E_\gamma^2}{2 mc^2} \quad (1.1)$$

Where E_γ is the energy of the emitted γ -ray photon, m is the mass of the nucleus and c is the velocity of light. Typical values of E_γ and E_R are in the range of 10^4 eV and 10^{-2} eV. In case of ^{57}Fe transition $E_\gamma = 14.4$ keV and $E_R = 1.95 \times 10^{-7}$ eV. The same amount of recoil energy is experienced by the absorbing nucleus also. The net result of these recoils is to shift the emitted and absorption line profiles each by an amount E_R and overall by an amount $2E_R$, as shown in figure 1.4a. The natural line width of the γ -radiation is determined by Heisenberg uncertainty relation $\Delta E \Delta t > \hbar/2\pi$. More conveniently, this can be written as Γ (eV) = $(4.562 \times 10^{-16}) / (t_{1/2} \text{ (s)})$, where $\Gamma = \Delta E$, the spread (FWHM) in energy and $t_{1/2}$ is the half life of the excited state which is related to the mean life time (Δt) of the excited state by $\Delta t = \ln 2 \times t_{1/2}$. The values of Γ typically range from 10^{-6} to 10^{-9} eV and the value for ^{57}Fe is 4.67×10^{-9} eV. This is nearly 10^6 times less than the value of E_R and hence there will not be any chance for resonance absorption because the basic criterion for resonance absorption is overlap up to a certain extent between the emission and absorption profiles. As shown in figure 1.4b, in a gas at finite temperature there is very small overlap between the emission and absorption profiles due to Doppler broadening ($E_D \sim 10^{-2}$ eV) arising from the motion of the emitting and absorbing nucleus. This much overlap is not useful for any practical purpose. The situation can be compared with the ultraviolet absorption by an atom,

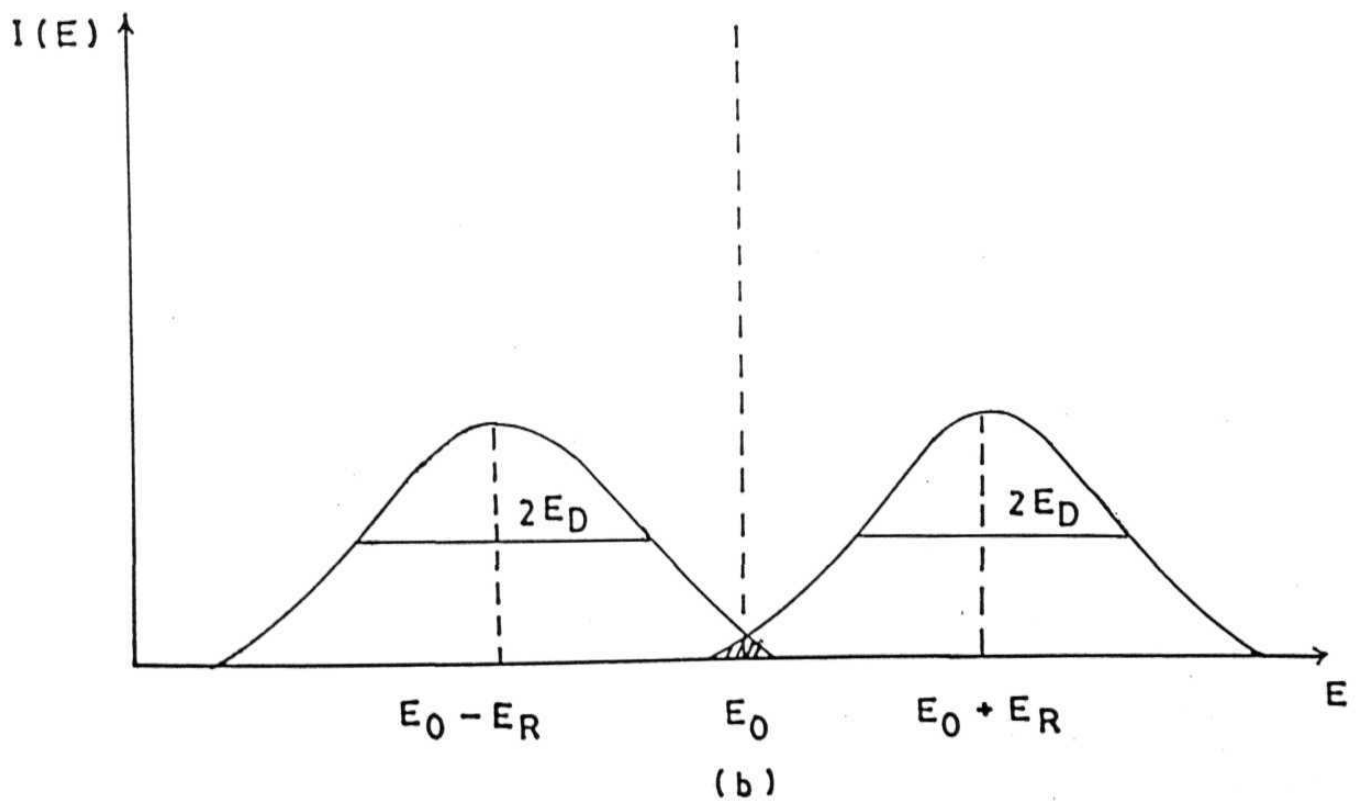
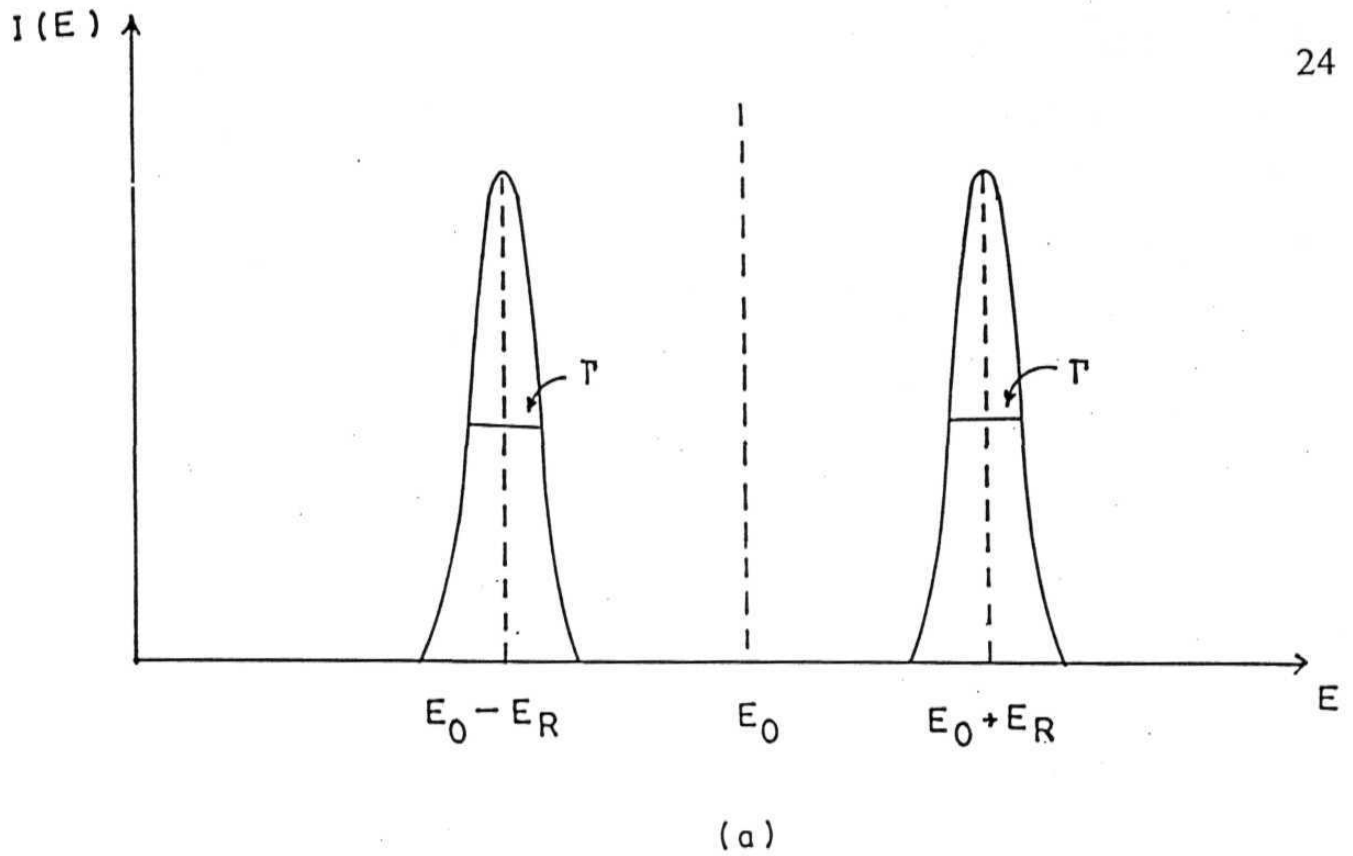


Figure 1.4: (a) Shift in γ -radiation energy (E_γ) of a free nucleus due to recoil energy (E_R); Γ is the Heisenberg width. (b) Emission and absorption profiles in presence of Doppler broadening (E_D).

where E_R is of the order of 10^{10} eV and $E_{\text{ultraviolet}}$ is of the order of 6.2 eV and E_D is of the order of 10^6 eV. Hence strong **absorption** takes place due to large overlap between the emission and absorption profiles. Problem arises for energetic nuclear transitions. The effect of recoil was tried to be compensated by imparting Doppler velocity and hence increasing E_D . The magnitude of Doppler velocity required for Hg source and absorber was very high, $\sim 7 \times 10^5$ mm/s, and the recoil was not eliminated but compensated [201]. Mossbauer effect eliminates the recoil leading to a technique where resolution of the order of 1 part in 10^{12} is obtained.

Mossbauer effect is realized by embedding the nucleus in a crystal lattice. The recoil energy is transferred to the crystal vibrational energy i.e. phonon energy spectra (having energy of the same order of magnitude as E_R). However because the phonon energies are quantized (e.g. $\hbar\omega$, $2\hbar\omega$, $3\hbar\omega$, ..., for a phonon mode of vibrational frequency of ω), there exists a finite probability of having a fraction 'f' of y-ray photons, which will not excite the phonon energy spectra. This fraction is called recoil free fraction and this process is called zero phonon process. If 'f' represents the recoil free fraction then $(1-f)$ represents the fraction of y-photon undergoing recoil by exciting phonon spectra. Lipkin [202] has shown assuming only lowest energy (i.e. $\hbar\omega$) phonon excitation through many y-transitions that average energy transferred per event is exactly free atom recoil energy

$$\begin{aligned} (1-f) \hbar\omega &= E_R \\ \text{or, } f &= 1 - E_R / \hbar\omega \end{aligned} \quad (1.2)$$

The recoil free fraction is given by

$$f = (\text{const}) (| \langle L_i | e^{i \mathbf{k} \cdot \mathbf{x}} | L_i \rangle |^2) \quad (1.3)$$

where L_j 's are the vibrational states assuming nuclear decay is independent of the vibrational state of the lattice and vice versa [203], $\mathbf{k} = (\mathbf{p}/\hbar)$ is the wave vector of the y-ray photon. If we employ Einstein's model of lattice vibration, f can be written as

$$f = \exp(-E_R / \hbar \omega_E) = \exp(-E_R / k \theta_E) \quad (1.4)$$

Where ω_E is the frequency of vibration and θ_E is the characteristic temperature of the lattice given by $k \theta_E = \hbar \omega_E$. If $E_R \ll k \theta_E$ then $f \approx 1 - (E_R / k \theta_E)$, which is of the form of equation (1.2).

Considering Debye model of lattice vibration, with vibrational frequencies ranging continuously from zero up to a maximum ω_D and following a distribution formula $N(\omega) = (\text{const}) \times \omega^2$, we get

$$f = \exp \left[- (6E_R / k \theta_D) \left\{ (1/4) + (T/\theta_D)^2 \int_0^{\theta_D/T} x dx / (\exp(x)-1) \right\} \right] \quad (1.5)$$

where Debye temperature θ_D is defined as $\hbar \omega_D = k \theta_D$.

The above equation (1.5) is often expressed as $f = \exp(-2W)$; W is called as Lamb-Mössbauer factor. Theoretically this factor is linearly proportional to T at high temperature ($T > \theta_D/2$) using harmonic approximation, but in practice deviation from linearity, which could be explained by incorporating anharmonicity of lattice vibration in the model. We have seen that there exists a finite probability of recoil less emission and similar arguments could be given for the finite probability for the recoil less absorption process also.

The resonance absorption cross-section at an energy E , is given by the Lorentzian distribution of the form [204]

$$\sigma(E) = \sigma_0 \frac{(\Gamma_a / 2)^2}{(E - E_\gamma)^2 + (\Gamma_a / 2)^2} \quad (1.6)$$

Where Γ_a is the Heisenberg width at half height of the absorption profile and σ_0 is the effective cross-section given by

$$\sigma_0 = 2\pi\lambda^2 \frac{2I_e + 1}{2I_g + 1} \frac{1}{1 + \alpha}$$

Where I_e and I_g are the nuclear spin quantum numbers of the excited and ground states and α is the internal conversion coefficient (defined as the ratio

of the number of conversion electrons to the number of γ -ray photon emitted) of the γ -ray of wavelength X . Using the usual relation between X and E_γ we obtain the expression

$$\sigma_0(\text{Cm}^2) = \frac{2.446 \times 10^{-15}}{(E_\gamma \text{ keV})^2} \frac{2I_e + 1}{2I_g + 1} \frac{1}{1 + \alpha} \quad (1.7)$$

σ_0 values are expressed in units of bams ($=10^{-24} \text{ cm}^2$). It is important that the cross-section for nuclear resonance absorption should be higher than that for any other method of γ -ray attenuation, such as photoelectric absorption. Equation (1.7) shows that the desirability of a high absorption cross-section requires that both E_γ and α should have low values: this criterion puts restriction to many naturally occurring isotopes to exhibit Mossbauer effect, only those which have low lying nuclear excited states are useful for Mossbauer spectroscopic technique.

The preceding equation already indicates the numerous parameters which will influence the intensity of an emission-absorption resonance:

- (1) Nuclear properties: the cross-section of γ -ray absorption and hence E_γ , I_e , I_g , and α .
- (2) Source properties: the recoil free fraction f_s , and the Heisenberg width Γ_s
- (3) Absorber properties: the recoil free fraction for absorption f_a and the Heisenberg width Γ_a .

Though complete general evaluation of the problem is impossible, but Margulies and Ehrman [205, 196] have given an expression of γ -ray transmission through a uniform resonant absorber based on the assumption that both source and absorber have the same natural line width ($\Gamma = \Gamma_s = \Gamma_a$). According to them, ideal Lorentzian line shape is obtained for an absorber thickness tending to zero but for an absorber with finite effective thickness also the line shape is basically Lorentzian with extra broadening due to thickness.

They have shown that the optimum absorber thickness for ^{57}Fe Mossbauer experiment is 10 mg of natural Fe / cm^2 .

1.3.1 Hyperfine interactions

The key feature of Mossbauer spectroscopy is its ability to detect small energy changes of the nucleus due to its interaction with the surrounding electrons. These interactions are termed as hyperfine interactions. The interaction Hamiltonian can be written as

$$H = E_0 + E_2 + M_1 + \dots \quad (1.8)$$

Where E_0 refers to electric monopole (i.e. Coulombic) interaction between the nucleus and the electrons; E_2 refers to electric quadrupole interactions; and M_1 refers to magnetic dipole interactions.

a. Electric monopole interaction (Chemical isomer shift (IS))

It arises from the Coulombic interaction. Electrons of charge ($-e$) in the field of a point nucleus of charge ($+Ze$) experiences a normal Coulombic potential and the integrated electro static energy will be

$$E_0 = - (Ze^2 / \kappa) \int \rho_e \frac{d\tau}{r} \quad (1.9)$$

Where K is the dielectric constant of vacuum, r is the radial distance from the nucleus, and $-\rho_e$ is the charge density of the orbital electrons in the volume element $d\tau$. However, the nucleus has a finite volume and this must be taken in to account when considering nucleus-electron interaction because an **s-electron wave function** implies a non-zero electron charge density within the nuclear volume.

If we assume a spherical nucleus of finite radius R , then equation (1.9) is still correct for $r > R$, but for $r < R$, the electrostatic energy is given by

$$E = -e \int \rho_n \phi_e d\tau \quad (1.10)$$

Where ρ_n is the uniform charge density of the nucleus over the sphere and ϕ_e is the electrostatic potential of the electrons. The change W is the electrostatic energy caused by the finite radius of the nucleus can therefore be expressed as

$$W = e \int_0^R \rho_n \phi_e d\tau - (Ze^2 / \kappa) \int_0^R \rho_e \frac{d\tau}{r} \quad (1.11)$$

Because of the lack of knowledge of the precise charge distribution and potential inside the nucleus if we further assume a continuous potential which has the same gradient at $r=R$ to that of the point nucleus Coulombic potential, then equation (1.11) becomes

$$W = \frac{24\pi(\rho+1) |\psi_s(0)|^2 Ze^2}{\kappa 2\rho (2\rho+1)(2\rho+3)\Gamma^2(2\rho+1)} (2Z / a_H)^{2\rho-2} R^{2\rho} \quad (1.12)$$

Where $\rho = \sqrt{1 - \alpha^2 Z^2}$, $\alpha = e^2/\hbar c$, a_H is the first Bohr radius, $\psi_s(0)$ is the non-relativistic Schrodinger wave-function of the s-electron at $r=0$, and Γ is the gamma function.

During the course of nuclear γ -transition, it is usual for the effective nuclear size to alter, or in other words the nuclear radii (R_e and R_g) in the excited and ground states are different by ($\delta R = R_e - R_g$). The difference in energy by the nuclear radius change δR will then be

$$\Delta W = \frac{24\pi(\rho+1) |\psi_s(0)|^2 Ze^2}{\kappa(2\rho+1)(2\rho+3)\Gamma^2(2\rho+1)} (2Z / a_H)^{2\rho-2} R^{2\rho} \frac{\delta R}{R} \quad (1.13)$$

The chemical isomer shift (IS), δ , as measured in a Mossbauer experiment is a difference in energy between two chemical environments A and B and from equation (1.13) is seen to be

$$I = \frac{24\pi (\rho+1) \{ |\psi_s(0)_A|^2 - |\psi_s(0)_B|^2 \} Z e^2}{\kappa(2\rho+1) (2\rho+3) \Gamma^2 (2\rho+1)} (2Z / a_H)^{2\rho-2} R^{2\rho} \frac{\delta R}{R} \quad (1.14)$$

This can be simplified by assuming $\rho=1$, which is not strictly valid for the heavier elements (for $Z=26$ (Fe) $\rho=0.98$ and for $Z=80$ (Hg) $\rho=0.80$), with $\kappa=1$ and $p=1$,

$$I = (4/5) \pi Z e^2 \{ |\psi_s(0)_A|^2 - |\psi_s(0)_B|^2 \} R^2 (\delta R/R) \quad (1.15)$$

The nucleus will usually be slightly non-spherical and the chemical isomer shift is therefore frequently designated in terms of the differences in the rms radii of the excited and ground states,

$$I = (2/3) \pi Z e^2 \{ |\psi_s(0)_A|^2 - |\psi_s(0)_B|^2 \} \{ \langle R_e^2 \rangle - \langle R_g^2 \rangle \} \quad (1.16)$$

Where $\{ \langle R_e^2 \rangle - \langle R_g^2 \rangle \} \equiv (6/5) R^2 (\delta R/R)$ and $\delta \langle R^2 \rangle / \langle R^2 \rangle = 2(5R/R)$

$R = 1.2 \times A^{1/3}$ fm to a close approximation. Equation (1.15) and (1.16) can be seen to be the product of a chemical term and a nuclear term. If the electron densities are known, the latter can be calculated or vice versa. In practice the nuclear term is a constant for a given transition, and for chemical applications the important equation is

$$I = \text{Const} \times \{ |\psi_s(0)_A|^2 - |\psi_s(0)_B|^2 \} \quad (1.17)$$

Figure 1.5c shows the effect of IS in case of Fe.

A and B are normally the absorber and source respectively. $|\psi_s(0)|$ should not be confused with the number of s-electrons in the atomic environment. It is the s-electron density at the nucleus, and as such will be effected not only s- electron population but also by the screening effects of p-, d-, and f-electrons and by covalency and bond formation, that is by the chemical bonding of the atom. If $(\delta R/R)$ is positive, a positive chemical isomer shift implies an increase in s-electron density at the nucleus in going from source to absorber. If $(\delta R/R)$ is negative the same shift signifies a decrease in s-

Formulation	^{57}Fe energy level diagram with allowed transitions Source (S) Absorber (A)	Schematic representation of observation (resonance absorption vs. velocity)
$r = \exp -k^2 \langle x^2 \rangle$	(a)	
$\Gamma_{\text{eff}} = \frac{\hbar}{\tau_{\text{eff}}}$	(b)	
$\delta = C \frac{\delta R}{R} [\psi_A(0) ^2 - \psi_S(0) ^2]$	(c)	
$E_m = -g_N \beta_N H m_I$	(d)	
$E_Q = \pm \frac{1}{2} e Q V_{zz}$ $(1 + \frac{1}{3} \eta^2)^{1/2}$	(e)	
$\delta_R = \frac{v^2}{2c^2} E_\gamma$	(f)	

Figure 1.5: Effect of Hyperfine interactions on nuclear energy levels of ^{57}Fe

electron density. Electrons in 1s, 2s, 3s, shells all contribute to $|\psi_s(0)|$ but in decreasing amounts as the principal quantum number rises. However the inner shells are not markedly affected by chemical bonding so that the principal influence on the chemical isomer shift will be by outermost occupied s-orbital. Shielding by other electrons effectively increases the s-radial functions and decreases the s-density at the nucleus. For example, a $3d^6 4s^1$ outer configuration will have a higher s-density than $3d^7 4s^1$; likewise for $3s^2 3p^6 3d^6$ because of the penetration of the 3d-orbitals into the 3 s.

The IS values gets affected slightly by temperature variation as shown in figure 1.5f, this arises due to second order (relativistic) Doppler shifts of the energy levels. The application of external pressure also slightly affect the observed IS values [196].

b Electric **quadrupole** interactions

The existence of an electric quadrupole interaction is one of the most useful features of Mossbauer spectroscopy. The theory is closely related to that used in nuclear quadrupole resonance spectroscopy [206]. Any nucleus with a spin quantum number of greater than $1/2$ has a non-spherical charge distribution, which if expanded as a series of multipoles contains a quadrupole term. The magnitude of the charge deformation is described as the nuclear quadrupole moment Q , given by

$$eQ = \int p r^2 (3(\cos\theta)^2 - 1) d\tau \quad (118)$$

Where e is the charge of the proton, p is the charge density in a volume element $d\tau$, which is at a distance r from the center of the nucleus and making an included angle θ to the nuclear spin quantization axis. The sign of Q depends on the shape of the deformation. A negative quadrupole moment indicates that the nucleus is oblate or flattened along the spin axis, whereas for a positive moment it is prolate or elongated.

In a chemically bonded atom, the electronic charge distribution is usually not spherically symmetric. The electric field gradient at the nucleus is defined as the tensor $E_{ij} = -V_{ij} = -(\partial^2 V / \partial x_i \partial x_j)$ ($x_i, x_j = x, y, z$) where V is the electrostatic potential. It is customary to define the axis system of the resonant atom so that $V_{zz} = eq$ is the maximum value of the field gradient. The orientation of the nuclear axis with respect to the principal axis, z , is quantized. There is an interaction energy between Q and eq which is different for each possible orientation of the nucleus.

The Laplace equation requires that the electric field gradient be a traceless tensor, i.e. the sum of the second derivatives of the electrostatic potential vanish:

$$V_{zz} + V_{xx} + V_{yy} = 0 \quad (1.19)$$

Consequently, only two independent parameters are needed to specify the electric field gradient completely, and the two which are usually chosen are V_{zz} and an asymmetry parameter η defined as

$$\eta = (V_{xx} - V_{yy}) / V_{zz} \quad (1.20)$$

Using the convention that $|V_{zz}| \geq |V_{yy}| \geq |V_{xx}|$ ensures that $0 \leq \eta \leq 1$.

The Hamiltonian describing the interaction can be written as

$$H = \frac{eQ}{2I(2I-1)} (V_{zz} \hat{I}_z^2 + V_{xx} \hat{I}_x^2 + V_{yy} \hat{I}_y^2) \quad (1.21)$$

Where I is the nuclear spin and I_z, I_x, I_y are the conventional spin operators.

Using equation (1.22) the Hamiltonian therefore becomes

$$H = \frac{e^2 q Q}{4I(2I-1)} [3\hat{I}_z^2 - I(I+1) + \eta(\hat{I}_x^2 - \hat{I}_y^2)] \quad (1.22)$$

or

$$H = \frac{e^2 q Q}{4I(2I-1)} [3\hat{I}_z^2 - I(I+1) + \eta(\hat{I}_+^2 - \hat{I}_-^2)] \quad (1.23)$$

Where I_+ and I_- are shift operators.

The simplest case to consider is when the electric field gradient has axial symmetry, i.e. $V_{xx}=V_{yy}$ and $\eta=0$. The matrix elements for the nucleus of spin I are given by

$$\langle I_z' | H | I_z \rangle = \frac{e^2 q Q}{4I(2I-1)} [3I_z'^2 - I(I+1)] \delta_{I_z' I_z} \quad (1.24)$$

$|I_z\rangle$ and $|I_z'\rangle$ are two different quantum states of the orientation and $\delta_{I_z' I_z}$ is a Kronecker delta such that $\delta_{I_z' I_z}=0$ unless $I_z'=I_z$. In other words the matrix is diagonal in form and the energy levels are given directly by

$$E_Q = \frac{e^2 q Q}{4I(2I-1)} [3I_z^2 - I(I+1)] \quad (1.25)$$

Because of the quadrupolar interaction the $I = 3/2$ nuclear energy level will be split into two distinct energy eigenvalues of $+e^2 q Q/4$ (for $I_z = \pm 3/2$) and $-e^2 q Q/4$ (for $I_z = \pm 1/2$). Using change in z-quantum number, $\Delta Z ((I_z)_e - (I_z)_g)$, to be equal to 0 or ± 1 we get two lines for γ -ray transition between the levels. The ^{57}Fe energy level diagram with allowed transitions is shown in figure 1.5e. Energy separation between the lines is $|e^2 q Q/2|$, which is also known as the quadrupole coupling constant. The magnitude of the quadrupole interaction is product of two factors: eQ is the nuclear constant and eq arising from electronic chemical environments. The observed sign of $e^2 q Q$ is an important factor in deciding the origin of EFG. For non-zero value of η the above expression of equation 1.25 is multiplied by a factor of $(1+\eta^2/3)^{1/2}$ for $I = 3/2$ state. The transitions with ΔZ values equals to ± 2 are also allowed with non-zero values of η [207]. It should be noted that in pure Fe with cubic symmetry, no EFG is possible at the nucleus. For Fe atoms in ferromagnetic alloys, such as Fe_3Al , the presence of the solute atoms in the nearest neighbour shells of Fe

breaks the cubic symmetry but the resultant EFG in most of the cases is negligible in comparison to the magnetic hyperfine interaction (discussed in the next section).

c. Magnetic hyperfine interaction

Third important hyperfine interaction is nuclear **Zeeman** effect. This will occur if there is a magnetic field at the nucleus. The magnetic field can originate either within the atom itself, within the crystal via exchange interactions, or as a result of placing the compound in an externally applied magnetic field; for the moment, however, it is only necessary to consider that there is a magnetic field with a flux density of H and that its direction defines the principal z -axis.

The Hamiltonian describing the magnetic dipole hyperfine interaction is

$$H = -\boldsymbol{\mu} \cdot \mathbf{H} = -g\mu_N \mathbf{I} \cdot \mathbf{H} \quad (1.26)$$

Where μ_N is the nuclear Bohr magneton ($eh/2Mc$), μ is the nuclear magnetic moment, I is the nuclear spin, and g is the nuclear g -factor, which has the value of 5.04929×10^{-24} ergs per gauss or 5.04929×10^{-27} J T⁻¹]. The energy eigenvalues are

$$E_m = \frac{-\mu H m_I}{I} = -g\mu_N H m_I$$

Where m_I is the magnetic quantum number. The magnetic field splits the nuclear level of spin I into $(2I+1)$ equi-spaced non-degenerate sub-states. As already seen for quadmpole spectra, the Mossbauer transition can take place between different nuclear levels if the change in m_I value is 0, ± 1 , or additionally in some cases ± 2 . The allowed γ -ray transitions for $3/2 \rightarrow 1/2$ nuclear levels of ^{57}Fe are illustrated in figure 1.5d. The level splitting are according to g -factors of excited (negative g) and ground states.

In a similar way to the chemical isomer shift and quadrupole splitting, the magnetic hyperfine effect is the product of a nuclear term, which is a constant for a given Mossbauer transition, and a magnetic field, which as will now be discussed, can be produced by the electronic structure.

d. Origin of nuclear magnetic field

The magnetic field at the nucleus can originate in several ways [208, 209]. A general expression would be

$$H = H_0 - DM + \frac{4}{3} \pi M + H_S + H_L + H_D \quad (1.28)$$

H_0 is the value of the magnetic field at the nucleus generated by an external magnet. The next term $-DM$, is the demagnetising field and $\frac{4}{3} \pi M$ is the classical Lorentz field (the coefficient is strictly applicable for cubic symmetry only), but both are small. H_S arises due to the interaction of the nucleus with an imbalance of s-electron spin density at the nucleus-also referred to as the Fermi contact field. Its origin may be from intrinsic unpairing of the actual s-electron, or indirectly as a result of core or conduction electron polarization effects on filled s-orbital, which can occur if the atom has unpaired electrons in d- or f-orbitals, or if it is chemically bonded to such an atom.

H_L arises due to non zero orbital magnetic moment of the parent atom. The final term in equation 1.28 arises from the dipolar interaction of the nucleus with the spin moment of the atom. This term is zero in cubic symmetry for transition elements, but can be large in rare earths because L is not quenched. The term H_S , H_L , and H_D can all be of the order of $10^4 - 10^5$ Gauss and their sum is usually referred to as the internal magnetic field or hyperfine magnetic field (HMF). The sign of an HMF can be determined by applying an external field (typically of strength of 30-50 kG produced generally by superconducting magnets), which will cause the apparent HMF to increase or decrease according to whether the applied field is parallel or anti-parallel to HMF. The temperature dependence of HMF follows Brillouin function,

becoming zero at the Curie or Neel temperature. It is clear now that the origin of HMF is basically electronic.

The presence of solute atoms in the nearest neighbour environment of a Mossbauer isotope (say Fe) in alloy systems affect the HMF at the Fe atom which is proportional to the change in local magnetic moment at the ^{57}Fe atom, because of the local and non local core and conduction electron polarization induced by the solute atoms. Magnetic polarization model [210, 211] has been used to obtain the total perturbation of the ^{57}Fe HMF due to the presence of solute atoms in the nearest neighbour shells.

e. Intensities of the ^{57}Fe absorption lines

It is possible to calculate the relative intensities of the absorption lines from the theory of the coupling of two angular momentum states, using appropriate Clebsch-Gordan coefficients under dipolar transitions. The angular dependence of the allowed transitions in the nuclear Zeeman pattern are given in table 1.1, where θ_m is the angle between the direction of the magnetic field at the nucleus and the propagation of the γ -radiation. For a polycrystalline sample free of texture and without any external magnetic field, the total radiation pattern is isotropic. By integrating over all directions we can get the relative line intensities for the six Zeeman-split lines arising from randomly oriented magnetic domains, which are 3:2:1:1:2:3. The observed intensities will be different for θ_m values of 0 and 90° respectively. For the quadrupole split spectrum the line intensities are equal for random orientation of EFG tensor and the γ -radiation direction.

Table 1.1: Angular dependence of the allowed transitions in a pure Zeeman pattern of ^{57}Fe

Transition	Δm_l	Angular dependence	line positions	Intensity
$\pm 3/2 \rightarrow \pm 1/2$	± 1	$\frac{3}{4} (1 + \cos^2 \theta_m)$	outermost lines	3
$\pm 1/2 \rightarrow \pm 1/2$	0	$\sin^2 \theta_m$	middle lines	2
$\mp 1/2 \rightarrow \pm 1/2$	∓ 1	$\frac{1}{4} (1 + \cos^2 \theta_m)$	innermost lines	1

The above-mentioned interactions are the major interactions seen in Mossbauer spectroscopy. Apart from these it may be possible that both EFG and HMF are present at the nucleus in which case the separation between the Zeeman-split lines does not remain the same; separation between first and second lines will be different from that between fifth and sixth lines. Another deviation known as relaxation phenomenon is seen in cases where electron spin (generating the HMF) relaxation time becomes comparable to the Mossbauer excited state life time or in other words γ -transition time. A motional narrowing of the HMF is observed in such cases. Superparamagnetic behavior is another effect seen for small sizes of the resonating particles.

1.4 Phase transformations in nanocrystalline alloys

This work describes the phase transformation behaviour of alloys prepared in the nanocrystalline state. Phase transformations were observed to be different from that of the coarse grained microcrystalline alloys due to the presence of a large volume fraction of grain boundary regions as well as due to the nano size of the grains. For grain sizes in the nanometer range, the surface energy contribution to Gibbs free energy modifies the Gibbs free energy of a phase relative to the bulk system and affects the stability of a phase. The enhanced rate of atomic diffusion through grain boundaries also influenced the phase transformation behaviors in the nanocrystalline alloys studied.

Sample preparation, sealing apparatus and furnace set-up for heat treatments, measurement techniques used, and data analysis procedures adopted are described in chapter 2. The atomic disorder to order transformation is discussed in chapter 3. It is shown that in case of nanocrystalline Fe-Al alloys near Fe_3Al stoichiometry the kinetics of equilibrium DO_3 ordered phase evolution from an initial disordered state was of first order due to faster diffusion through grain boundaries as compared to a 3rd order process obtained in microcrystalline alloys. The growth of DO_3 order was limited by the grain size and a substantial amount of B32 ordered phase was stabilized in the anti phase domain boundaries between equilibrium DO_3 ordered domains. The evolution of DO_3 order in Fe-Ge systems ($\sim\text{Fe}_3\text{Ge}$ and $\text{Fe}_{0.83}\text{Ge}_{0.17}$ compositions) was also studied. Equilibrium B2 order in FeCo-X (X=Mo, Ge, W) alloys evolved along the same kinetic path at different temperatures due to the grain boundary regions providing rapid short-circuited diffusion paths for atom movements. On the evolution of DO_3 order in $\text{Fe}_{3-x}\text{Mn}_x\text{Ge}$ ($x = 0.3, 0.45, 0.6, 0.75$) alloys, Mn atoms were segregated to GB regions from an initial disordered state instead of going preferentially to the 4(b) Wyckoff site of the DO_3 lattice, which was the case for microcrystalline alloys. The same grain growth kinetics was observed at the ordering temperature for both Fe-Ge as well as Fe-Mn-Ge systems.

The formation of homogeneous alloys and subsequent phase decomposition behavior in Fe-Cr system is discussed in chapter 4. It is found that near the equiatomic composition region the decomposition proceeds through Spinodal Decomposition (SD) process. The temperature independent linear relationship between grain growth and SD is the key feature of this study.

Precipitation phase transformation in Fe rich Fe-Mo alloys was found to be taking place through a coherent Mo clustering to GBs from the initial disordered matrix. A concept of negative surface energy was introduced to

explain the Mo clustering beyond a critical grain size of the homogeneous alloy. The formation of the equilibrium Fe_2Mo phase took place in the GB regions without any reentrant dissolution of Mo atoms in the Fe matrix, this was in contrast to what observed in polycrystalline alloys. This behavior is dealt with in chapter 5.

In the last chapter Fe-Ge nanocrystalline alloy system is discussed undergoing massive structural phase transformation. We observed that the DO3 ordered α_1 phase did not transform to the equilibrium L1_2 ordered ϵ phase until a critical grain size was reached. This was shown to be due to the higher surface energy contributions to Gibbs free energy in the fcc phase as compared to the bcc phase, which rendered the bcc phase stable relative to the fcc phase for small grain sizes.

References

- [1] Non-equilibrium Processing of Materials, edited by C. Suryanarayana (Pergamon Press, Oxford, 1999).
- [2] Rapidly Solidified Alloys: Processes, structures, properties, applications, edited by H. H. Liebermann (Marcel Dekker, NY 1993).
- [3] T. R. Anantharaman and C. Suryanarayana, Rapidly Solidified Metals- a technological overview (Trans Tech Publications, Aedermannsdorf, Switzerland, 1987).
- [4] R. L. Bickerdike, D. Clark, J. N. Easterbrook, G. Hughes, W. N. Mair, P. G. Partridge, and H. C. Ranson, Internat J Rapid Solidification 1, 305 (1984).
- [5] Plasma Synthesis and Processing of Materials, edited by K. Upadhyaya (TMS, Warrendale, PA, 1993).
- [6] C. Suryanarayana, Progress in Materials Science 46, 1 (2001).
- [7] C. C. Koch, In: Processing of Metals and Alloys, edited by R. W. Cahn Vol. 15 of Materials Science and Technology-A Comprehensive Treatment, (VCH Verlagsgesellschaft, Weinheim, Germany, GmbH, 1991), p. 193.
- [8] C. Suryanarayana, Bibliography on Mechanical Alloying and Milling, (International Science Publishing, Cambridge, UK, 1995).
- [9] C. Suryanarayana, Metals and Materials 2, 195 (1996).
- [10] M. O. Lai and L. Lu, Mechanical Alloying, (Kluwer Academic Publishers, Boston, MA, 1998).
- [11] B. S. Murty and S. Ranganathan, Internat Mater Rev. 43, 101 (1998).
- [12] D. Turnbull, Metall Trans. **12A**, 695 (1981).
- [13] M. B. Bever, D. L. Holt, and A. L. Titchener, Prog. Mat. Sci. 17, 5 (1973).
- [14] F. Miani and H. J. Fecht, Int. J. of Refract. Met. and Hard Mater. 17, 133 (1999).
- [15] G. Martin and P. Bellon, Solid State Phys. 50, 189 (1997).
- [16] P. H. Shingu, In: Processing Materials for Properties, edited by H. Henein and T. Oki (TMS, Warrendale, PA, 1993), p. 1275.
- [17] F. H. Froes, C. Suryanarayana, K. Russell, C. M. Ward-Close, In: Novel Techniques in Synthesis and Processing of Advanced Materials, edited by J. Singh and S. M. Copley (TMS, Warrendale, PA, 1994), p. 1.
- [18] F. H. Froes, C. Suryanarayana, K. Russell, and C-G. Li, Mater Sci and Eng. **A192/193**, 612 (1995).
- [19] G. W. Nieman, J. R. Weertman and R. W. Siegel, J. Mater. Res. 6, 1012(1991).
- [20] Y. R. Abe and W. L. Johnson, Mater Sci Forum **88-90**, 513 (1992).

- [21] M. L. Trudeau, R. Schulz, L. Zaluski, S. Hosatte, D. H. Ryan, C. B. Doner, P. Tessier, J. O. Strom-Olsen, and A. Van Neste, *Mater Sci Forum* 88-90, 537 (1992).
- [22] C. C. Koch, *Internat. Mater. Rev.* 33, 201 (1988).
- [23] C. Moelle and H. J. Fecht, *Nanostructured Materials* 6, 421 (1995).
- [24] Z. Q. Gao, Ph. D. Thesis, California Institute of Technology (1994).
- [25] H. Gleiter, *Acta. Mater.* 48, 1 (2000).
- [26] H. Kuwano, H. Ouyang, and B. Fultz, *Nanostructured Materials* 1, 143 (1992).
- [27] R. Porat, S. Berger, and A. Rosen, *Mat. Sci. Forum* 225-227, 629 (1996).
- [28] T. Pfullmann, M. Oehring, R. Bohn, and R. Bormann, *Mat. Sci. Forum* 225-227, 757 (1996).
- [29] R. R. Vance and T. H. Courtney, *Scripta Metall. et Mater.* 26, 1435 (1992).
- [30] D. K. Kim and K. Okazaki, in "Mechanical Alloying", *Materials Science Forum* (Trans. Tech. Publications, Switzerland, 1992), Vols. 88-90, p. 553.
- [31] G. B. Schaer, *Scripta Metall. Mater.* 27, 1 (1992).
- [32] H. Gleiter, "Nanocrystalline Materials", *Prog. Mater. Sci.* 33, 223 (1990).
- [33] R. O. Hughes, S. D. Smith, C. S. Pande, H. R. Johnson, and R. W. Armstrong, *Scripta Metall.* 20, 93 (1986).
- [34] Z. G. Li and D. J. Smith, *Appl. Phys. Lett.* 55, 919 (1989).
- [35] L. E. McCandlish, B. H. Kear, and B. K. Kim, *Nanostructured Materials* 1, 119 (1992).
- [36] *Handbook of Nanoscience, Engineering, and Technology*, edited by W. Goddard, III, D. W. Brenner, S.E. Lyshevski, and G. J. Lafrate (CRC Press, USA, 2003).
- [37] Z. Fu, H. J. Fecht, and W. L. Johnson, *Mat. Res. Soc. Symp. Proc.* **186**, 169(1991).
- [38] R. S. Schwarz, P. B. Desch, S. Srinivasan, and P. Nash, *Nanostructured Materials* 1, 37 (1992).
- [39] E. M. Schulson and D. R. Barker, *Scripta Met.* 17, 519 (1983).
- [40] J. Naser, W. Reinhemann, and H. Ferkel, *Mater. Sci. and Eng.* A234, 467(1997).
- [41] I. R. Lu, C. Moelle, A. Sagel, R. K. Wunderlich, J. H. Perepezko and H. J. Fecht, *Materials Letters* 35, 297 (1998).
- [42] C. Moelle, I. R. Lu, A. Sagel, R. K. Wunderlich, J. H. Perepezko and H. J. Fecht, *Mater. Sci. Forum* 269-272, 47 (1998).
- [43] D. G. Morris, *Mechanical Behaviour of Nanostructured Materials*, (Trans Tech Publications, Zuerich: Switzerland, 1998).
- [44] C. C. Koch, *J. of Metastable and Nanocrystalline Materials* 2-6, 565 (1999).

- [45] H. J. Fecht, *Phil. Magazine* **B76**, 495 (1997).
- [46] H. J. Fecht, in *Nanostructured Materials: Processing, Properties, and Applications*, edited by C. C. Koch (Noyes Publications, William Andrew Publishing, Norwich, NY, 2002), p. 73.
- [47] C. C. Koch, *Nanostructured Materials* 2, 109 (1993).
- [48] *Nanophase Materials*, edited by G. C. Hadjipanayis and R. W. Siegel (Kluwer Acad. Publ, 1994).
- [49] J. S. Benjamin, *Mat. Sci. Forum* 88, 1 (1992).
- [50] J. S. Benjamin, *Sci. Amer.* 234, 40 (1976).
- [51] J. S. Benjamin, In: *New Materials by Mechanical Alloying Techniques*, edited by E. Arzt, and L. Schultz (DGM Informationsgesellschaft, Oberursel: Germany, 1989), p. 3.
- [52] J. S. Benjamin, *Metal Powder Rep.* 45, 122 (1990).
- [53] J. S. Benjamin, *Metall. Trans.* 1, 2943 (1970).
- [54] H. Gleiter, *Prog. Mater. Sci.* 33, 223 (1989).
- [55] R. W. Siegel, in *Mat. Sci. and Tech.*, edited by R. W. Cahn, P. Haasen, and E. S. Kramer (VCH, Weinheim, 1991), Vol. 15, p. 583.
- [56] A. E. Yermakov, E. E. Yurchikov, and V. A. Rarinov, *Phys. Met. Metallogr.* 52(6), 50 (1981).
- [57] C. C. Koch, O. B. Cavin, C. G. McKamey, and J. O. Scarbrough, *Appl. Phys. Lett.* 43, 1017 (1983).
- [58] J. Eckert, L. Schultz, and K. Urban, *Appl. Phys. Lett.* 55, 117 (1989).
- [59] R. B. Schwarz and C. C. Koch, *Appl. Phys. Lett.* 49, 146 (1986).
- [60] Y. S. Cho and C. C. Koch, *J. Alloys and Compounds* 194, 287 (1993).
- [61] C. C. Koch, J. S. C. Jang, and P. Y. Lee, In: *New Materials by Mechanical Alloying Techniques*, edited by E. Arzt and L. Schultz (DGM Informationsgesellschaft, Oberursel, Germany, 1989), p. 101.
- [62] P. H. Shingu, B. Huang, S. R. Nishitani, and S. Nasu, *Suppl. Trans. Japan Inst. Metals* 29, 3 (1988).
- [63] W. Schlump and H. Grewe, In: *New Materials by Mechanical Alloying Techniques*, edited by E. Arzt and L. Schultz (Deutsche Gesellschaft für Metallkunde, Oberursel, Germany, 1989), p. 307.
- [64] E. Hellstern, H. J. Fecht, Z. Fu, and W. L. Johnson, *J. Appl. Phys.* 65, 305 (1989).
- [65] J. S. C. Jang and C. C. Koch, *J. Mater. Res.* 5, 498 (1990).
- [66] M. A. Morris and D. G. Morris, *Mater. Sci. Forum* 88-90, 529 (1992).
- [67] M. A. Morris and D. G. Morris, *J. Mater. Sci.* 26, 4687 (1991).
- [68] R. B. Schwarz, R. R. Petrich, and C. K. Saw, *J Non-Cryst. Solids* 76, 281 (1985).
- [69] E. Hellstern and L. Schultz, *Appl. Phys. Lett.* 48, 124 (1986).

- [70] P. H. Shingu, (editor), Mechanical Alloying, In: Mater. Sci. Forum 88-90, (Trans Tech Publications, Aedermannsdorf, Switzerland, 1992).
- [71] H. J. Fecht, E. Hellstern, Z. Fu, and W. L. Johnson, Metall. Trans. **A21**, 2333 (1990).
- [72] K. Yamada and C. C. Koch, J. Mater. Res. 8, 1317 (1993).
- [73] M. Oehring and R. Bormann, J. de Physique 51, 169 (1990).
- [74] L. M. Di and H. Bakker, J. Appl. Phys. 71, 5650 (1992).
- [75] H. J. Fecht, G. Han, Z. Fu, and W. L. Johnson, J. Appl. Phys. 67, 1744(1990).
- [76] A. M. Tonejc and A. Tonejc, Mater. Sci. Forum 225-227, 497 (1996).
- [77] M. S. El-Eskandarany, K. Sumiyama, K. Aoki, and K. Suzuki, Mater. Sci. Forum 88-90, 801 (1992).
- [78] A. Calka, Appl. Phys. Lett. 59, 1568 (1991).
- [79] A. Calka and J. S. Williams, Mater. Sci. Forum 88-90, 787 (1992).
- [80] C. Suryanarayana and F. H. Froes, Nanostructured Mater. 3, 147 (1993).
- [81] C. Suryanarayana, G. H. Chen, A. Frefer, and F. H. Froes, Mater. Sci. and Eng. A158, 93 (1992).
- [82] D. Michel, L. Mazerolles and E. Chichery, Materials Science Forum 269-272, 99(1998).
- [83] W. J. D. Shaw, Materials Science Forum 269-272, 19 (1998).
- [84] J. Pan and W. J. D. Shaw, J. Appl. Poly. Sci. 56, 57 (1995).
- [85] M. Karttunen and P. Ruuskanen, Materials Science Forum 269-272, 849(1998).
- [86] E. Ivanov, Mater. Sci. Forum 88-90, 475 (1992).
- [87] T. Yamazaki, K. Terayama, T. Shimazaki, and K. Sugimoto, J Mater. Sci. Lett. 16, 1357 (1997).
- [88] K. Okada, S. Kikuchi, T. Ban, and N. Otsuka, J. Mater. Sci. Lett. 11, 862(1992).
- [89] G. Nicoara, D. Fratiloiu, M. Nogues, J. L. Dormann, and F. Vasiliu, Mater. Sci. Forum 235-238, 145 (1997).
- [90] A. Bellosi, F. Montverde, S. Botti, and S. Martelli, Mater. Sci. Forum 235-238, 255(1997).
- [91] L. B. Hong, C. Bansal, and B. Fultz, Nanostructured materials 4, 949(1994).
- [92] M. J. Luton, C. S. Jayanth, M. M. Disko, M. M. Matras, and J. Vallone, In: Multicomponent Ultrafine Microstructures, edited by L. E. McCandlish, D. E. Polk, R. W. Siegel, and B. H. Kear (Mater Res. Soc, Pittsburgh, PA, 1989), vol. 132, p. 79.

- [93] B. J. M. Aikin and J. J. Juhas, In: Advanced Particulate Materials and Processes, edited by F. H. Froes and J. C. Hebeisen (Metal Powder Industries Federation, Princeton, NJ, 1997), p. 287.
- [94] A. W. Weeber, H. Bakker, and F. R. deBoer, *Europhys. Lett.* 2, 445 (1986).
- [95] P. G. McConnick, *Mater. Trans. Japan Inst. Metals* 36, 161 (1995).
- [96] G. Jangg, F. Kuttner, and G. Korb, *Aluminium* 51, 641 (1975).
- [97] A. Calka, J. J. Nikolov, and J. S. Williams, *Mater. Sci. Forum* 225-227, 527 (1996).
- [98] K. Tokumitsu, T. Nasu, K. Suzuki, and A. L. Greer, *Materials Science Forum* 269-272, 181 (1998).
- [99] G. B. Schaffer and P. G. McConnick, *Appl. Phys. Lett.* 55, 45 (1989).
- [100] E. Galet E, Malhouroux-Galet N. J. *Alloys and Compounds* 205, 27 (1994).
- [101] L. Froyen, L. Delaey, Niu X-P, P. LeBrun and C. Peytourt, *JOM* **47(3)**, 16 (1995).
- [102] F. Chariot, Galet E, B. Zeghmami, F. Bernanrd, and J. C. Niepce, *Mater. Sci. and Eng. A262*, 279 (1999).
- [103] V. Gauthier, C. Josse, F. Bernard, E. Galet, and J. P. Larpin, *Mater. Sci. and Eng. A265*, 117 (1999).
- [104] G. B. Schaffer and P. G. McCormick, *Appl. Phys. Lett.* 55, 45 (1989).
- [105] P. G. McConnick, V. N. Whartan, and G. B. Schaffer, In: *Physical Chemistry of Powder Metals Production and Processing*, edited by W. M. Small (TMS, Warrendale, PA, 1989), p. 19.
- [106] W. E. Kuhn, I. L. Friedman, W. Summers, and A. Szegvari, *Powder Metallurgy (ASM Metals Handbook, Metals Park, OH 1985)*, Vol. 7, p. 56.
- [107] C. Suryanarayana, In: *Powder Metal Technologies and Applications, ASM Handbook, vol. 7*, (ASM International, Materials Park, OH, 1998), p. 80.
- [108] J. Eckert, J. C. Holzer, and W. L. Johnson, *Scripta Met. et Mater.* 27, 1105 (1992).
- [109] J. Eckert, J. C. Holzer, C. E. Krill III, and W. L. Johnson, *J. Mater. Res.* 7, 1980 (1992).
- [110] B.T McDennott, M.S. Thesis, North Carolina State University, 1988.
- [111] D. Maurice and T. H. Courtney, *J. of Metals* 44, 10 (1992).
- [112] G. Martin and E. Gaffet, *J. Phys., France* 51, C4-71 (1990).
- [113] R. M. Davis, B. McDennott, and C. C. Koch, *Metall. Trans. A* **19**, 2867 (1988).
- [114] N. Burgio, A. Iasonna, M. Magini, S. Martelli, and F. Padella, *Nuovo Cimento* **13D**, 459 (1991).

- [115] E. Hellstern, H. J. Fecht, C. Garland, and W. L. Johnson, In: Multicomponent Ultrafine Microstructures, edited by L. E. McCandlish, D. E. Polk, R. W. Siegel, and B. H. Kear (Mater. Res. Soc, Pittsburgh, PA, 1989), vol. 132, p. 137.
- [116] J. Karch, R. Birringer, and H. Gleiter, *Nature* 330, 556 (1987).
- [117] S. Li, K. Wang, L. Sun, and Z. Wang, *Scripta Metall. Mater.* 27, 437(1992).
- [118] J. Eckert, J. C. Holzer, C. E. Krill III, and W. L. Johnson, *J. Mater. Res.* 7, 1751 (1992).
- [119] I. BoE rner and J. Eckert, *Mater. Sci. Forum* 225-227, 377 (1996).
- [120] M. A. Myers and K. K. Chawla, *Mechanical Metallurgy-Principles and Applications* (Prentice-Hall, 1984).
- [121] E. O. Hall, *Proc. Phys. Soc, London*, 643, 747 (1951).
- [122] N. J. Petch, *J. Iron Steel Inst, London*, 173, 25 (1953).
- [123] R. O. Scattergood and C. C. Koch, *Scripta Met. et Mater.* 27, 1195 (1992).
- [124] C. C. Koch, *Nanostructured Mater.* 9, 13 (1997).
- [125] H. J. Fecht, E. Hellstern, Z. Fu, and W. L. Johnson, *Adv. Powder Metallurgy* 1, 111 (1989).
- [126] J. S. Benjamin and T. E. Volin, *Metall. Trans.* 5, 1929 (1974).
- [127] P. S. Gilman and J. S. Benjamin, *Annu. Rev. Mater. Sci.* 13, 279 (1983).
- [128] P. Y. Lee and C. C. Koch, *J. Mater. Sci.* 23, 2837 (1988).
- [129] J. S. C. Yang and C. C. Koch, *J. Mat. Res.* 5, 325 (1990).
- [130] R. M. Davis and C. C. Koch, *Scripta Metall.* 21, 305 (1987).
- [131] P. Y. Lee and C. C. Koch, *Appl. Phys. Lett.* 50, 1578 (1987).
- [132] C. C. Harris, *Trans. Soc. Min. Engrs.* 238, 17 (1967).
- [133] V. Qi and H. J. Fecht, *Mat. Sci. Forum* 269-272, 187 (1998).
- [134] R. N. Wright, *Metall. Trans. A* 8, 2024 (1977).
- [135] Y. S. Cho and C. C. Koch, *Mater. Sci. and Engr. A* 141, 139 (1991).
- [136] P. Y. Lee, J. L. Yang, and H. M. Lin, *J. Mater. Sci.* 33, 235 (1998).
- [137] D. A. Rigney, L. H. Chen, M. G. S. Naylor, and A. R. Rosenfield, *Wear* 100, 195(1984).
- [138] D. A. Rigney, *Ann. Rev. Mater. Sci.* 18, 41 (1988).
- [139] D. Turley, *J. Inst. Metals* 99, 271 (1971).
- [140] C. N. J. Wagner, *Acta Met.* 5, 477 1957).
- [141] B. E. Warren, *X-ray Studies of Deformed Metals in Prog. Metals Phys.* 3, 147(1956).
- [142] V. A. Pavlov, O. V. Antonova, A. P. Adakhovskiy, A. A. Kuranov, V. M. Alya'ev, and A. I. Deryagin, *Phys. Met. Metall.* 58, 158(1984).
- [143] V. A. Pavlov, *Phys. Met. Metall.* 59, 1 (1985).

- [144] M. Hatherly and A. S. Malin, *Scripta Met.* 18, 449 (1984).
- [145] F. D. Doyle and R. L. Aghan, *Metal 1. Trans. B6*, 143 (1975).
- [146] P. K. Mehrotra, *Proc. Int. Conf. on Wear of Materials* (Reston, VA, ASME, New York, 1983), p. 194.
- [147] P. Humble and R. H. J. Hannink, *Nature* 273, 37 (1978).
- [148] F. Bordeaux and A. R. Yavari, *Z. Metallkd.* 81, 130 (1990).
- [149] T. R. Anantharaman and C. Suryanarayana, *J. Mater. Sci.* 6, 1111 (1971).
- [150] R. Birringer, H. Hahn, H. Höfler, J. Karch, and H. Gleiter, *Defect and Diffusion Forum* 59, 17 (1988).
- [151] R. B. Schwarz, *Mat. Sci. Forum* 269-272, 269 (1998).
- [152] P. H. Shingu, B. Huang, J. Kuyama, K. N. Ishihara, S. Nasu, in *New Materials by Mechanical Alloying Techniques*, edited by E. Arzt and L. Schultz (Informationsgesellschaft, Oberursel: DGM, 1989), p.319.
- [153] B. Huang, N. Tokizane, K. N. Ishihara, P. Shingu, and S. Nasu, *J. Non -Cryst. Solids* 117/118, 688 (1990).
- [154] I. S. Polkin, Eya. Kaputkin, and A. B. Borzov, In: *Structural Applications of Mechanical Alloying*, edited by F. H. Froes and J. J. DeBarbadillo (ASM International, Materials Park, OH, 1990), p. 251.
- [155] R. Sundaresan and F. H. Froes, In: *New Materials by Mechanical Alloying Techniques*, edited by E. Arzt and L. Schultz (Deutsche Gesellschaft für Metallkunde, Oberursel, Germany, 1989), p. 243.
- [156] J. Eckert, L. Schultz, and K. Urban, *Z. Metallkde.* 81, 862 (1990).
- [157] C. Suryanarayana, E. Ivanov, R. Nou®, M. A. Contreras, and J. J. Moore, *J. Mater. Res.* 14, 377 (1999).
- [158] K. B. Gerasimov, A. A. Gusev, E. Y. Ivanov, and V. V. Boldyrev, *J. Mater. Sci.* 26, 2495(1991).
- [159] L. Liu, S. Casadio, M. Magini, C. A. Nannetti, Y. Qin, and K. Zheng, *Mater. Sci. Forum* 235-238, 163 (1997).
- [160] D. R. Maurice and T. H. Courtney, *Metall. Trans. A21*, 289 (1990).
- [161] C. Suryanarayana and F. H. Froes, *J. Mater. Res.* 5, 1880 (1990).
- [162] J. Y. Huang, Y. K. Wu, A. Q. He, and H. Q. Ye, *Nanostructured Mater.* 4, 293(1994).
- [163] H. X. Sui, M. Zhu, M. Qi, G. B. Li, and D. Z. Yang, *J. Appl. Phys.* 71,2945(1992).
- [164] J. Eckert, J. C. Holzer, and W. L. Johnson, *J. Appl. Phys.* 73, 131 (1993).
- [165] P. J. DesreA, *Nanostructured Mater.* 4, 957 (1994).

- [166] G. Veltl, B. Scholz, and H-D. Kunze, Mater. Sci. and Eng. A134, 1410(1991).
- [167] C. Gente, M. Oehring, and R. Bormann, Phys. Rev. B48, 13244 (1993).
- [168] A. R. Yavari, P. J. DesreA, and T. Benamuer, Phys. Rev. Lett. **68**, 2235(1992).
- [169] A. R. Yavari, Mater. Sci. and Eng. A179/180, 20 (1994).
- [170] O. Drbohlav and A. R. Yavari, Acta Mater. 43, 1799 (1995).
- [171] Y-S. Kwon, K. B. Gerasimov, O. I. Lomevsky, and S. V. Pavlov, J. Alloys and Compounds 353, 194 (2003).
- [172] J. Eckert, L. Schultz, and K. Urban, J. Less-Common Metals **166**, 293(1990).
- [173] C. Bansal, Z. Q. Gao, L. B. Hong, and B. Fultz, J. Appl. Phys. 76, 5961 (1994).
- [174] W. Hume-Rothery and G. V. Raynor, The Structure of Metals and Alloys, (Institute of Metals, London, 1962).
- [175] L. S. Darken and R. W. Gurry, Physical Chemistry of Metals, (McGraw-Hill, New York, NY, 1962).
- [176] Solid-State Amorphization Transformation, Less Comm. Metals, edited by R. B. Schwarz and W. L. Johnson, (1988), p.140.
- [177] P. Pochet, P. Bellon, L. Boulanger, L. Chaffron, and G. Martin, Materials Science Forum 269-272, 655 (1998).
- [178] E. Ma, J-H. He, and P. J. Schilling, Phys. Rev. B55, 5542 (1997).
- [179] J. S. C. Jang and C. C. Koch, J. Mater. Res. 5, 325 (1990).
- [180] P. Boolchand and C. C. Koch, J. Mater. Res. 7, 2876 (1992).
- [181] T. Fukunaga, M. Mori, K. Inou, and U. Mizutani, J. Mat. Sci. Eng. A134, 863(1991).
- [182] Y. R. Abe, J. C. Holzer, and W. L. Johnson, (MRS Fall Meeting, Boston, MA, December 2-6, 1991).
- [183] A. R. Yavari and P. J. Desre, in Ordering and Disordering in Alloy, edited by A. R. Yavari (Elsevier, 1992), p. 414.
- [184] J. Eckert, R. Birringer, J. C. Holzer, C. E. Ill. Krill, and W. L. Johnson, J. Mat. Res. (1993).
- [185] A. Sagel, N. Wanderka, R. K. Wunderlich, N. Schubert-Bischoff, and H. J. Fecht, Scripta Mater.**38**, 163 (1998).
- [186] H. J. Fecht, Mat. Sci. and Eng. A 179/180, 491 (1994).
- [187] M. B. Bever, D. L. Holt, and A. L. Titchener, Prog. Mater. Sci. 15, 5(1973).
- [188] H. J. Fecht, Phys. Rev. Lett. 65, 610 (1990).
- [189] G. M. Wang, S. J. Campbell, A. Calka, and W. A. Kaczmarek, J. Mater. Sci. 32, 1461 (1997).
- [190] W. Guo, S. Martelli, F. Padella, M. Magini, N. Burgio, E. Paradiso, and U. Franzoni, Mater. Sci. Forum 88-90, 139 (1992).

- [191] S. Saji, S. Abe, and K. Matsumoto, Mater. Sci. Forum 88-90, 367 (1992).
- [192] T. H. Courtney and Z. Wang, Scripta. Metal 1. Mater. 27, 777 (1992).
- [193] M. S. El-Eskandarany, K. Aoki, and K. Suzuki, J. Less-Common Metals 167, 113 (1990).
- [194] D. A. Porter and K. E. Easterling, Phase Transformations in Metals and Alloys (2nd Ed., Chapman and Hall, 1992).
- [195] R.L. Mossbauer, Z. Physik, 151, 124 (1958).
- [196] N. N. Greenwood and T. C. Gibb, Mossbauer Spectroscopy (Chapman and Hall, London, 1971).
- [197] Mossbauer Effect Methodology, edited by R. J. Gruverman (Plenum Press, New York, 1965-1976), vol. 1-11.
- [198] Mossbauer effect data index, edited by J. G. Stevens and V. E. Stevens, (Plenum Press, New York, 1966-1975).
- [199] Mossbauer Effect, edited by L. S. Kothari, J. S. Baijal and S. P. Tewari, (Academic Publications, India, 1984).
- [200] Mossbauer Spectroscopy, Topics in Applied Physics, edited by G. Gonser (Springer Verlag, 1975), vol. 5.
- [201] P.B. Moon, Proc. Phys. Soc. 63, 1189 (1950).
- [202] H. J. Lipkin, Quantum Mechanics: new approaches to selected topics, (Chapman and Hall, North Holland, Amsterdam, 1973). Also in Ann. Phys. 9, 332 (1960).
- [203] W. E. Lamb, Jr, Phys. Rev. 49, 519 (1936).
- [204] G. Breit and E. Wigner, Phys. Rev. 49, 519 (1936).
- [205] S. Margulies and J. R. Ehrman, Nuclear Instr. Methods 12, 131 (1961).
- [206] T. P. Das and E. L. Haln, Nuclear Quadrupole Resonance Spectroscopy, Solid State Physics (Academic Press, 1958), Supp. No.1.
- [207] G. K. Shenoy and B. D. Dunlap, Nuclear Instr. Methods 71, 285 (1969).
- [208] C. E. Johnson, M. S. Ridout, and T. E. Cranshaw, Proc. Phys. Soc, 81, 1079(1963).
- [209] R. E. Watson and A. J. Freeman, Phys. Rev. 123, 2027 (1961).
- [210] V. A. Niculescu, T. J. Burch, and J. I. Budnick, J. Mag. and Mag. Mat. 39, 223(1983).
- [211] B. Fultz and J. W. Morris. Jr, Phys. Rev. B34, 4480 (1986).

Chapter 2

Experimental Techniques

In this chapter I discuss the various experimental techniques used in this work, such as sample preparation methods, heat treatments, Mossbauer data acquisition system and analysis procedures.

2.1 Sample preparation by mechanical alloying

The alloy samples were prepared by mechanical alloying of high purity elemental powders in a SPEX 8000 mixer mill from CERTIPREP, USA. Hardened steel vial and a set of six balls (two of diameter $\frac{1}{2}$ " and four of diameter $\frac{1}{4}$ ") were used to prepare the alloys. A schematic drawing of the stainless steel vial and balls and the process of milling are shown in figures 2.1a and 2.1b. The ball to powder weight ratio chosen was 5:1. The elemental powders were weighed according to the desired composition and transferred to the vial. The net powder weight was around 4.2 grams and the balls weight was around 21 grams. The vial with the powders and the balls was sealed in high purity (IOLAR II grade from British Oxygen Company) Argon atmosphere in a glove bag before the milling was started. The vial, containing the sample and grinding balls, was secured in the clamp of the milling apparatus. The back-and-forth shaking motion of the mill is combined with lateral movements of the ends of the vial, so that the vial appears to be describing a figure 8 or infinity sign as it moves. With each swing of the vial the balls impact against the sample and the end of the vial, both milling and mixing the sample. Because of the small amplitude (about 5 cm) and high speed/frequency (about 1200 rpm) of the clamp motion, the ball velocities are high (of the order of 4 - 5 m/s) and consequently the force of the ball's impact is unusually great giving rise to high-energy alloying/milling.

Figure 2.2 shows the alloying behavior observed from the Mossbauer HMF distributions in case of Fe-Ge alloy chosen as a representative system. It was observed that a milling time of about 20 hours was necessary for the formation of a homogeneous alloy. This was confirmed for the alloy

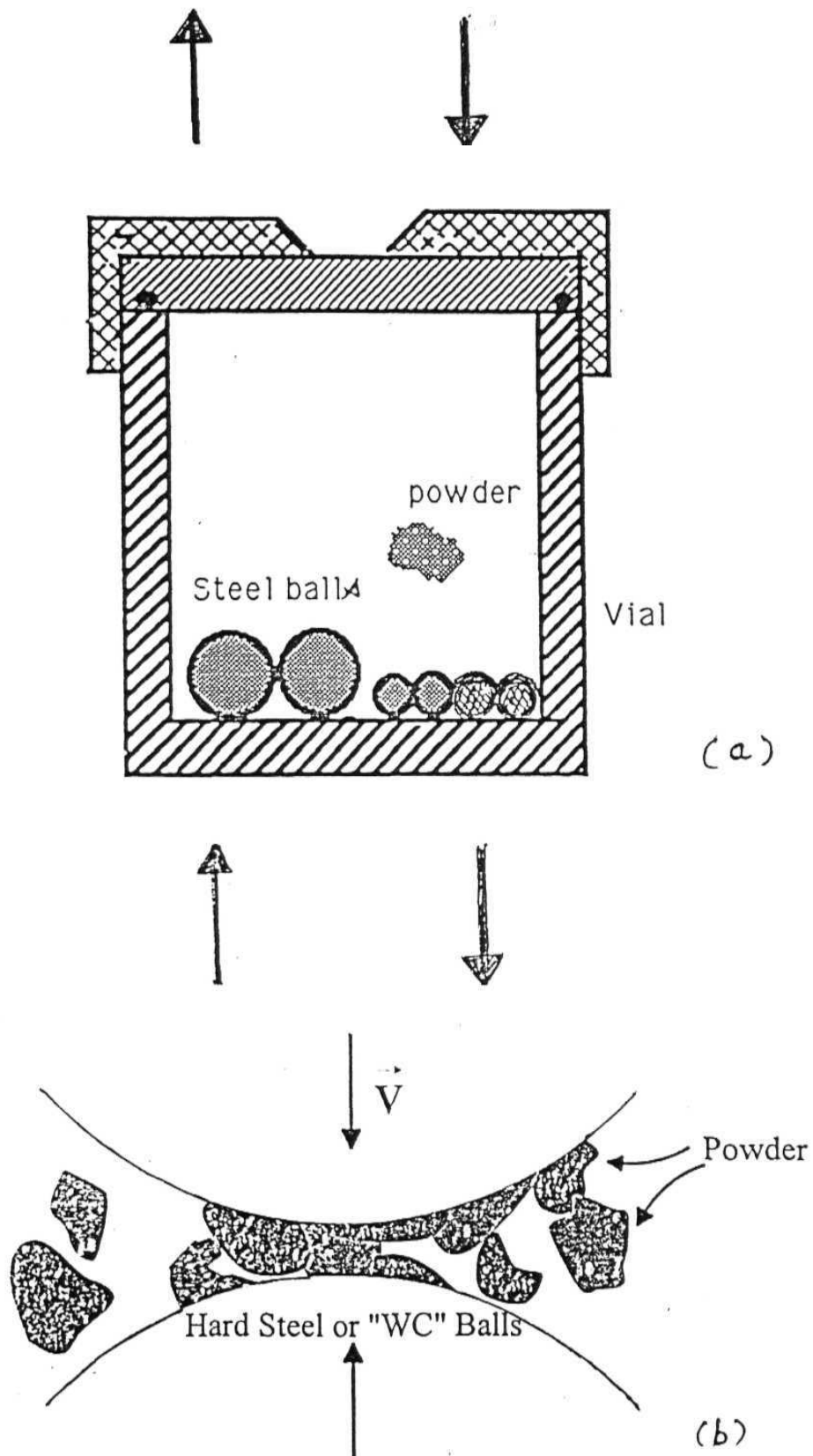


Figure 2.1: Schematic sketches of a) vial and balls arrangement of the ball-mill apparatus and b) the process of structure refinement by MA/MM.

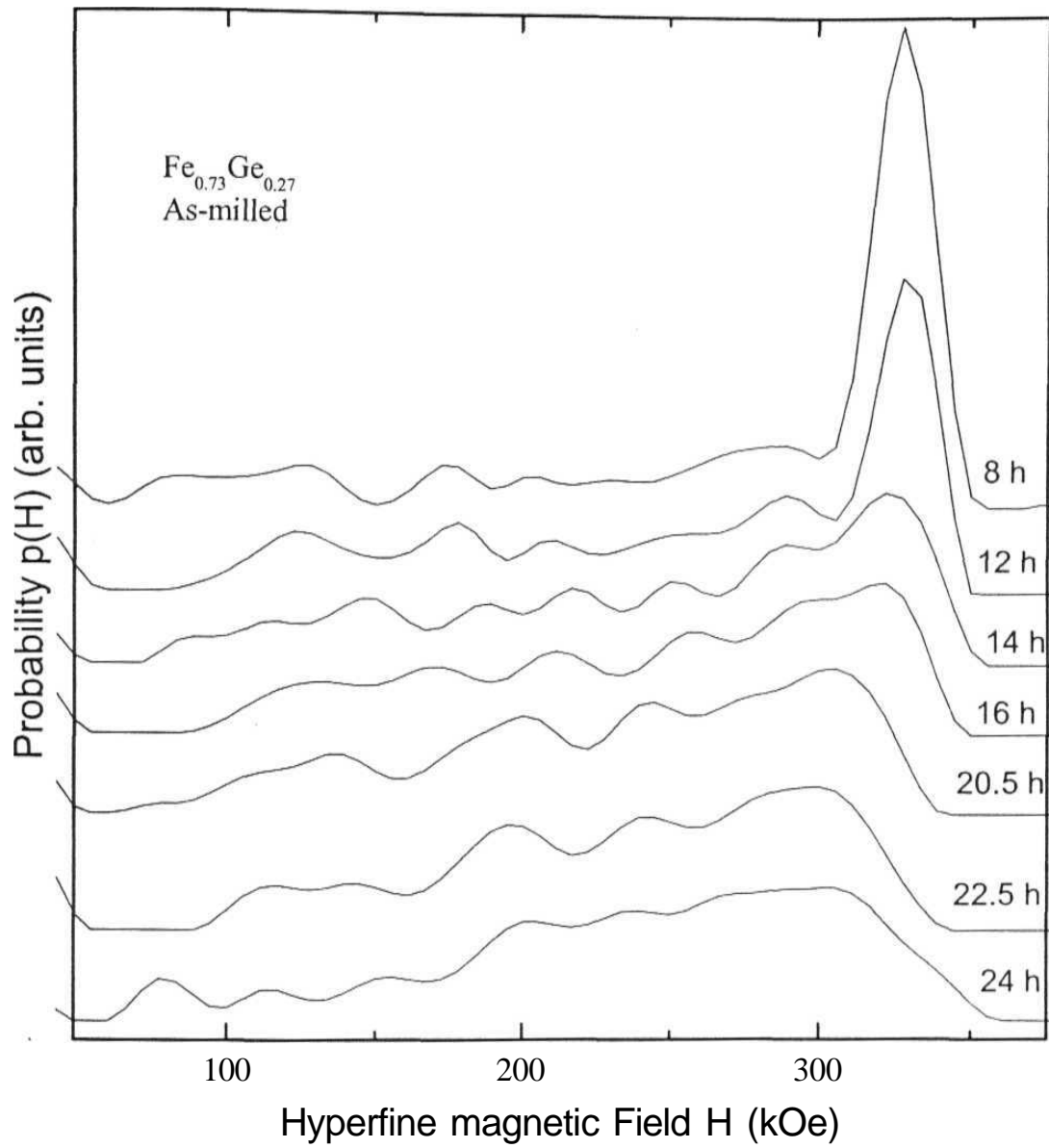


Figure 2.2: Hyperfine magnetic field distributions evaluated from the Mossbauer Spectra recorded after milling of elemental Fe and Ge for different periods of time to see the formation of the solid solution (typically after ~20-24 h) with Fe_{0.73}Ge_{0.27} composition.

composition $\text{Fe}_{0.73}\text{Ge}_{0.27}$ by milling the powder mixture for various periods of time ranging from 8 hours to 24 hours. Samples were drawn after different milling times and Mossbauer spectra were recorded. During the initial stages of milling, up to 14 hours the HMF distributions were narrow and the peak at around 330 kOe arising due to unmixed pure crystalline Fe was prominent. The field distributions started getting broadened with the peak positions shifting towards the lower values after 16 hours of milling and after 20 hours of milling the distribution became broad and did not show any further change. At this stage the field distribution corresponded very well with the binomial distribution characteristics of a disordered alloy. However for this as well as other subsequent Fe-based alloys studied in this thesis we have continued the milling up to 24 hours, if not mentioned otherwise, to obtain disordered bcc (A2 structure) phase alloys (solid solutions) in the as-milled state. Similar alloying behavior was also observed in the case of Fe-20 at. % Cr alloys and will be discussed in chapter 4 later.

Mechanical milling (refinement of structure) and disordering as studied in case of $\text{Fe}_{3-x}\text{Mn}_x\text{Si}$, with $x = 0.3$ (hereafter will be referred as FeMnSi), alloy are shown in figures 2.3 and 2.4. The FeMnSi alloy was prepared earlier by arc melting in the arc-melting furnace, model AF-92C from MRC, NY with a LINCOLN dc arc welder model IDEALARC R3R-400. The arc-melted button was milled for periods from 45 minutes up to 17 hours in succession (i.e. the same button was milled and after every stage of milling sample was taken out to record Mossbauer and powder XRD data). The grain size reduction (figure 2.3a) with milling is similar to that observed earlier in various systems [ref 6 and 47 of chapter 1]. Nano-meter sized grains resulted after 45 minutes of milling with a slow decrease in grain size with further milling. The presence of peaks in the Mossbauer hyperfine field distribution (figure 2.4a) instead of a broad distribution indicates that the arc melted sample was formed in partially DO3 ordered state. This partial ordering was completely destroyed after 45 minutes

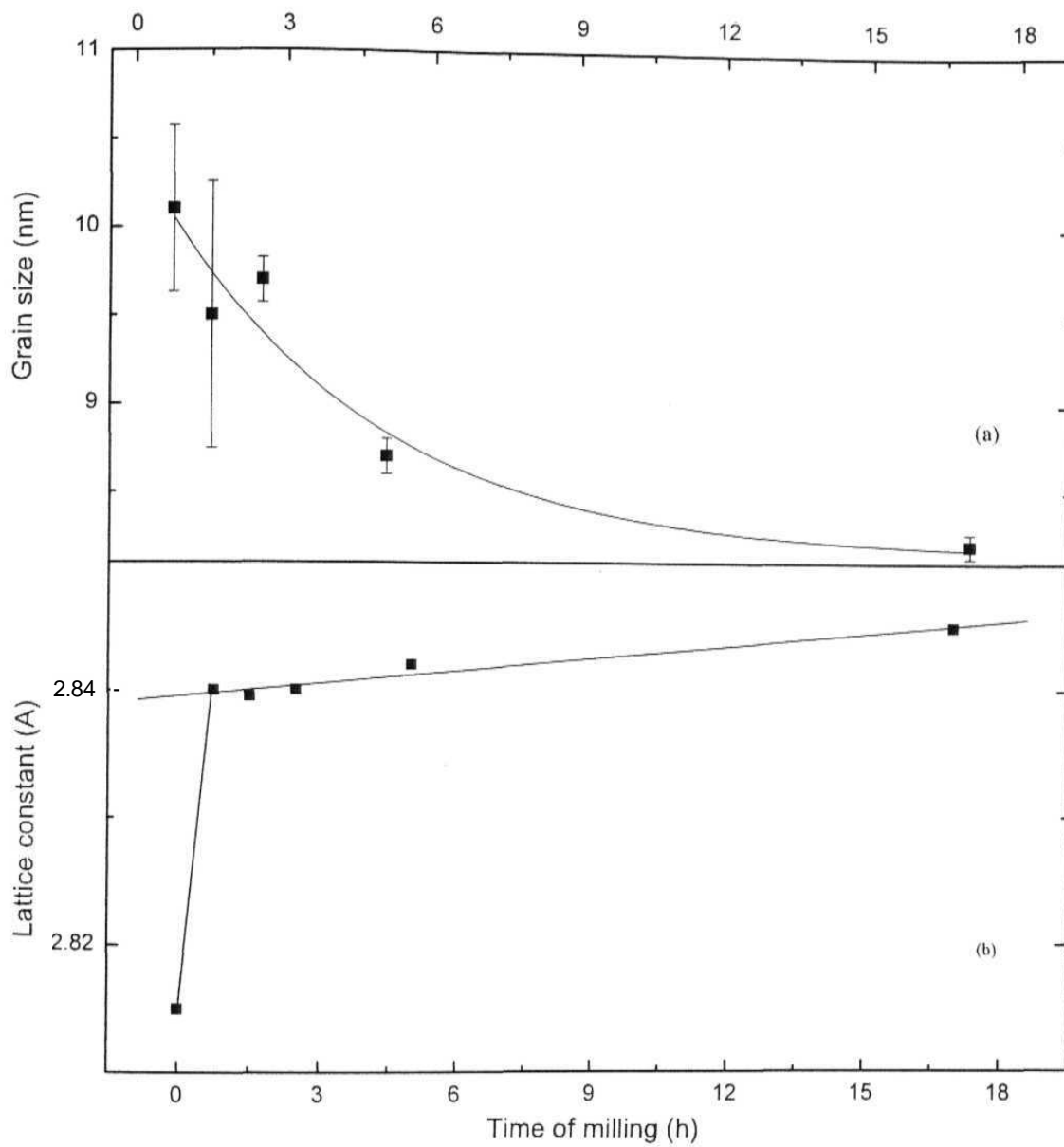


Figure 2.3: Evolution of the grain size and lattice constant with milling time, showing the structural refinement and disordering taking place in a partially ordered $\text{Fe}_{2.7}\text{Mn}_{0.3}\text{Si}$ alloy.

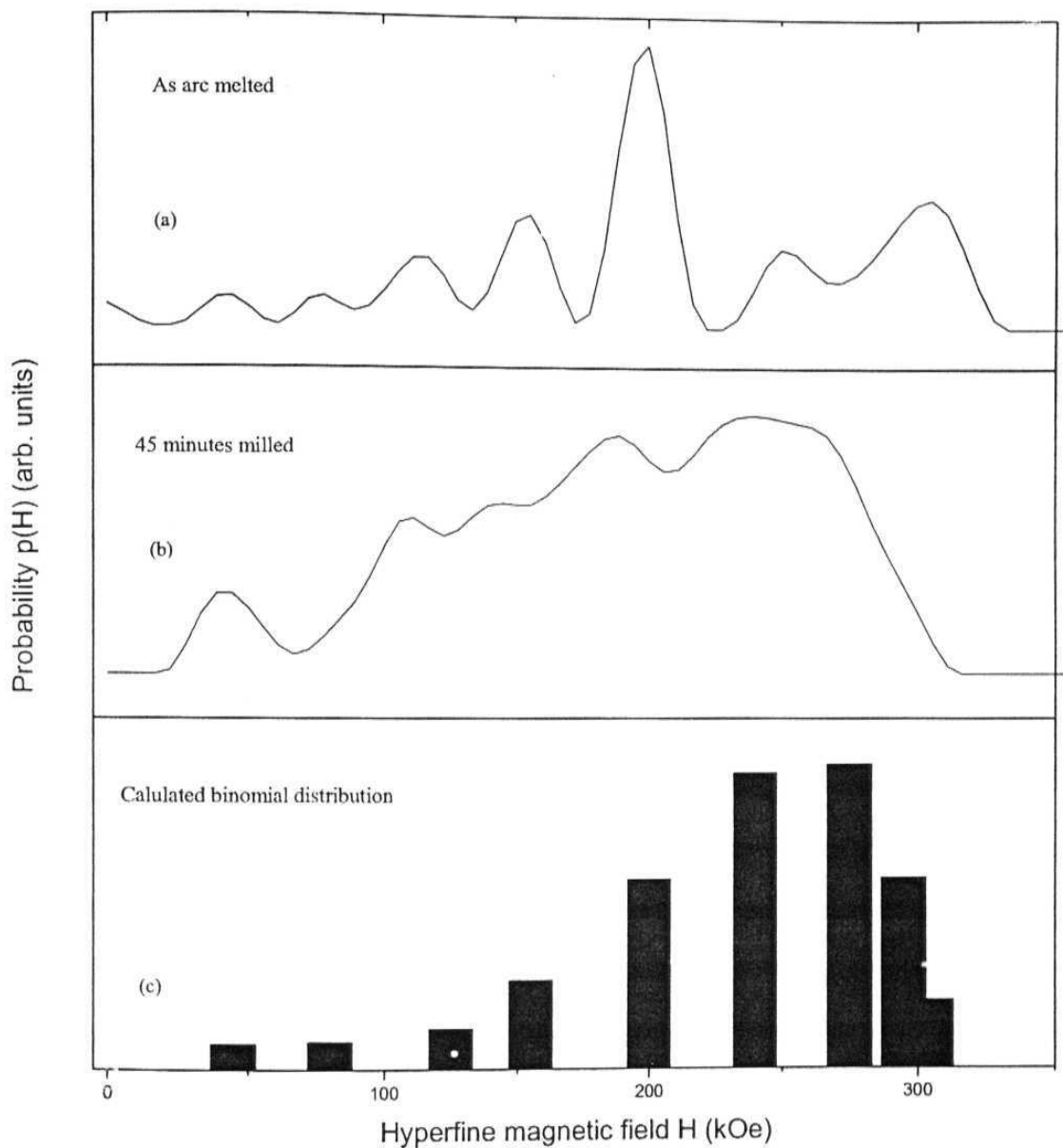


Figure 2.4: HMF distributions of (a) partially ordered and (b) disordered (by milling) $\text{Fe}_{2.7}\text{Mn Si}$ alloy. The calculated binomial random probability distribution is shown in (c). The reasonably good match between (b) and (c) shows the formation of the disordered alloy by just 45 minutes of milling.

of milling and a disordered bcc alloy resulted having a broad distribution (figure 2.4b) matching very well with the binomial probability distribution (figure 2.4c) applicable for the solute configurations around Fe atoms in a disordered alloy. The field values assigned to various solute configurations of Fe atoms in the random distribution were according to 1st nn perturbation model (equation 2.1a, discussed later). The details of DO₃ ordered structure; the HMFs characteristics of DO₃ order will be discussed in chapter 3. This disordering process is also supported by the sharp increase in the lattice constant after 45 minutes of milling (figure 2.3b) followed by asymptotic increase with time indicating anti site disorder [Ref 6 of chapter 1]. Thus the process of grain size reduction and disordering in a pre alloyed powder (MM and MD) is taking place just within 45 minutes which is order of magnitude lesser than the time required, of the order of 20 hours, for MA, which was mentioned in chapter 1.

2.2 Heat treatments

Various phase transformation behaviors and the stability of the nano-phase alloys against grain growth was studied by subjecting the as-milled supersaturated metastable alloys to equilibrium heat treatments. By equilibrium heat treatment we mean that the alloy samples were annealed at temperatures corresponding to the equilibrium phase diagrams to see the desired phase transformation. The samples were heat treated at different temperatures ranging from 250°C- 520°C in borosilicate glass tubes for different periods of time ranging from few minutes to few hours. In case of Fe-Mo alloy (chapter 5) one heat treatment was carried out at 1100°C in fused quartz tube. The as-milled samples were sealed in borosilicate glass tubes under Argon (IOLAR II grade) atmosphere with pressure of nearly 0.05 Torr before putting in the furnace to avoid any oxidation. The furnace temperature was monitored by a Chromel (Cr-Ni)- Alumel (Al-Ni) thermocouple with one end of the thermocouple at room temperature (RT) and the other end at high temperature inside and near the

middle of the furnace without touching the inner wall of the muffle of the furnace. The required temperature was maintained by a temperature controller connected with the thermocouple and the temperature was measured by the corresponding emf generated by the thermocouple with the help of a millivoltmeter. The sample carrying glass tube was put as close as the thermocouple hot junction tip but without touching the tip. After the required time of heat treatment the samples were directly taken out of the furnace without reducing the furnace temperature and quenched in air.

2.3 Energy dispersive X-Ray (EDAX) composition analysis - attached to SEM

The compositions of the as-milled samples were determined by EDAX analysis. The EDAX detector and electronics assembly was attached to SEM, model ESEM XL 30, from Philips. In this procedure the characteristic X-Rays emitted by the elements (by electron jump from higher energy shells to lower energy K-shell once the original K-shell electrons were knocked out by the energetic accelerated primary electrons beam) were detected by the proportional counter detector operated at liquid nitrogen (LN₂) temperature. The derived energy profile was plotted and the presence of different elements in the sample studied gave rise to different peaks at the corresponding X-ray energies over the background. The energy scale of the spectrometer was calibrated by recording ultra pure Cu and Al samples spectra, which determined the two ends of the energy scale precisely. From the position of the peaks the element was recognized and from the intensity the atomic as well as weight percent of the elements were determined using conventional ZAF (Z= atomic number, A = atomic weight and F= fluorescence) matrix method.

The Fe contamination estimated was within 1-3 at. % for most of our as-milled samples and for Fe-Cr systems it was less than even 1 at. %.

2.4 Powder X-ray Diffraction

Most of our X-ray diffraction studies were carried out using a Philips PW 1830 diffractometer employing Cu K_{α} radiation. Occasionally in some cases we have used INEL CPS 120 diffractometer employing Co K_{α} radiation. In case of Phillips machine both Cu- $K_{\alpha 1}$ and $K_{\alpha 2}$ wavelengths were present and we have considered the weighted average wavelength value of 1.5418 Å for all our calculations. In case of INEL machine we were able to separate out Co- $K_{\alpha 1}$ and $K_{\alpha 2}$ wavelengths and used the value of $K_{\alpha 1}$ (i.e. 1.78997 Å) in all calculations. It will be discussed through chapter 3-5 that all our as milled and heat treated samples were of bcc structure. Hence the average grain size was determined from the line width of the fundamental (110) line using the Scherrer formula (grain size (S) = $(K\lambda) / (B\cos\theta_B)$), where K is constant, λ , is the X-ray wavelength, B is the FWHM (measured in radians) of the X-ray peak, and $2\theta_B$ is the position of the peak) with the values of 'K' in the formula taken to be 0.9 [1]. To obtain the experimental line width we have fitted the (110) line of our X-Ray data using both Lorentzian and Gaussian functions and found that Lorentzian line shape was better fitting the spectra with small grain sizes whereas Gaussian and Lorentzian fits were comparable when grain growth up to certain extent took place. However the actual values of the widths obtained using these two functional forms were not very different from each other. This was consistent with the earlier observations [1-3]. The line width due to instrumental broadening was determined by recording the diffraction pattern for microcrystalline pure Fe powder and fitted the pattern with Gaussian line shapes. Figures 2.5a and 2.5b show the representative X-ray diffraction patterns of the actual sample and that of pure Fe along with the fits to the spectra. The signature of the peak coming from Cu $K_{\alpha 2}$ radiation is present as the hump (at $2\theta \sim 44.8^\circ$) in the pure Fe X-ray pattern. Because of this hump, in principle this spectrum should be fitted to two Gaussian instead of one, but practically it was

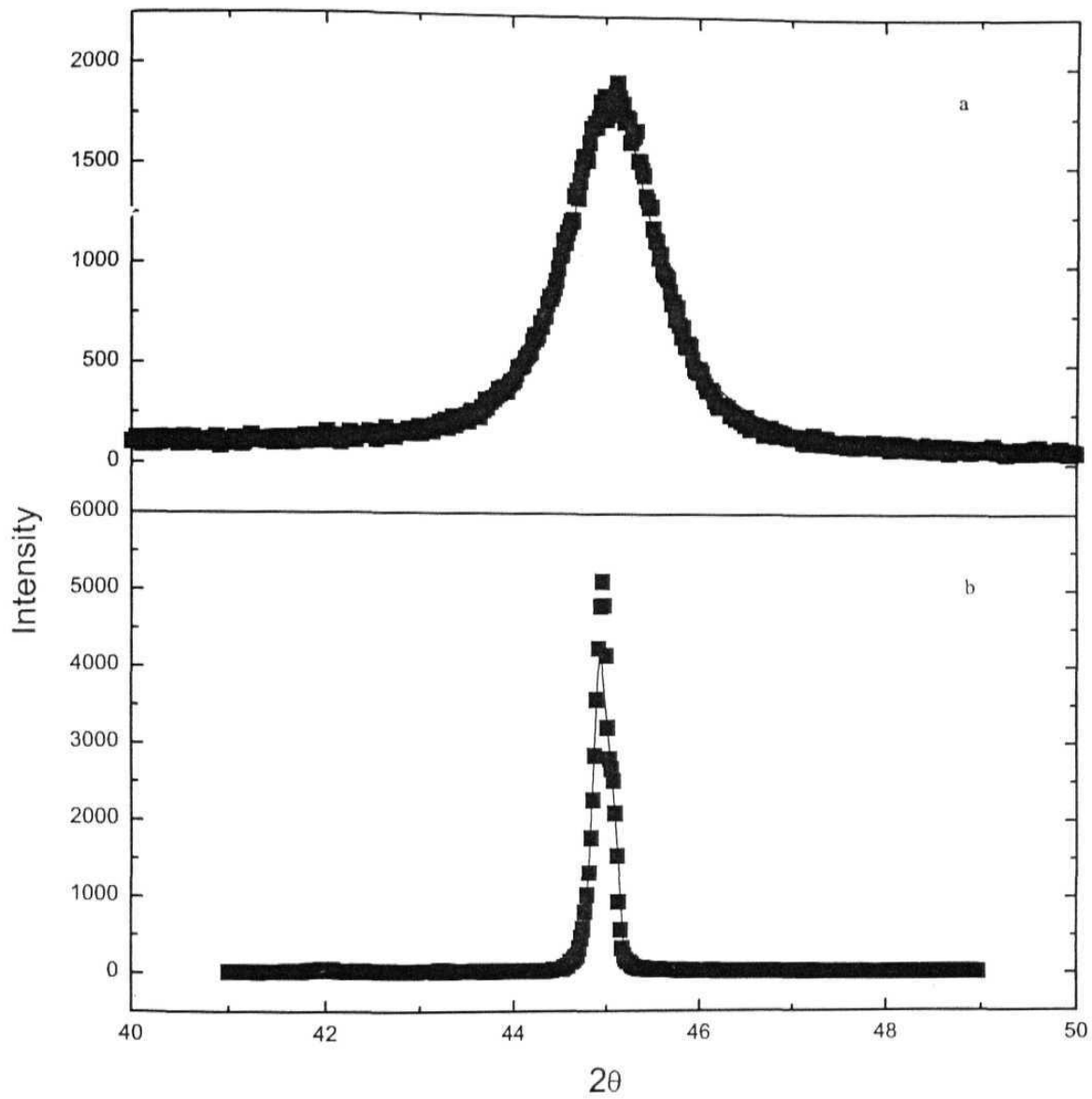


Figure 2.5: The fundamental (110) X-ray peaks arising from the bcc structured (a) as-milled and (b) pure Fe samples and the corresponding Lorentzian and Gaussian fits to the peaks are shown.

very difficult to resolve such closely spaced Gaussian and by trying to fit with two Gaussian, the results emerging out were unphysical. We therefore restricted the fitting to one Gaussian only and as a result in figure 2.5b though the top portion of the experimental data is little bit off-fitted but even then the overall fitting and the estimate of FWHM from the fitting is reasonable within experimental errors. No separate signature of any peak arising from $K\alpha_2$ radiation was observed for the case of nanocrystalline alloys because of the broadness of the peak. The instrumental broadening was subtracted in quadrature from the observed line widths of the nanocrystalline alloys to determine the actual line widths to find the grain size. The lattice strain determination through Williamson-Hall (AK vs. K) method [1] was not possible in our case due to insufficient number of lines. However the maximum lattice strain of the as-milled alloys with similar compositions as ours was determined earlier by Bansal et.al. [ref 173 of chapter 1]. The strain was within 1% and which was released once the samples were subjected for ordering heat treatments. No attempt was made to study the evolution of long-range order from X-Ray diffraction due to small intensities of the broad superlattice lines arising from ordered domains and hence the insensitivity of the diffractometer to detect these lines properly. It was expected that if the ordered domain size is in few nanometer range [ref 24 of chapter 1] than the detection of the corresponding broad superlattice lines attributed to these ordered domains over the background would be very difficult and mostly impossible unless an extremely sensitive diffractometer (not the Phillips machine what we used) is employed.

2.5 Mossbauer Spectrometer

Mossbauer spectra can be recorded most commonly in two ways: 1) employing a single line source with an absorber having different hyperfine interactions generated nuclear energy level splitting or 2) employing a single

line absorber with source having nuclear energy level shift. In either of the two ways the nuclear energy level splitting have to be matched with the recoil free γ -ray energy to record the resonance spectra. One immediate and convenient way of matching these energies is to impart a Doppler velocity to the single line source or absorber and hence giving an first order energy shift (ΔE_γ) to the incident γ -ray energy (E_γ) equals to $\Delta E_\gamma = (v/c) E_\gamma$, where v is the relative velocity between source and absorber. Depending on the variations of the Mossbauer natural line widths (FWHM) and energy level splitting [4] the range and precision of the Doppler velocities has to be selected. For example for the standard Mossbauer absorbers such as pure Fe (where HMF ~ 330 kOe at RT), Fe_2O_3 (HMF ~ 515 kOe at RT), Fe_3O_4 (HMF ~ 455 and 495 kOe at RT), Sodium Nitropruside or stainless steel a velocity range of ± 9 , ± 12 , ± 12 , ± 4 and ± 2 respectively will be sufficient to record a spectra with good baseline and Fe source. Some other ways of recording Mossbauer spectra and designs of spectrometer depending on specific application are summarized in [5].

In our laboratory the Mossbauer spectrometer is operated in the constant acceleration mode and it has the following four basic building blocks (also shown in figure 2.6):

- a Mossbauer source
- b Velocity drive and associated feedback systems
- c γ -Radiation detector system with associated electronics and
- d PC based Mossbauer data acquisition system.

a Mossbauer Source: The Mossbauer source was prepared by Du Pont Pharmaceuticals, USA by electrodepositing Co^{57} nuclei in $6\ \mu\text{m}$ thick Rh matrix and annealing at 1050°C for 72 hours under hydrogen atmosphere. The source has been sprayed with an acrylic coating. The strength of the source was $25.9\ \text{mCi}$ (958.3MBq) with a half life of 270 days.

b Velocity drive and feedback system: The velocity drive unit was fabricated locally by Nucleonix (model MD 575) following the design of Kankeleit [6]. It is an electromechanical transducer and consists of a coil connected to a rod, carrying the source. This coil is made of phosphor-bronze. This coil carries the driving velocity signal and is the energizing coil. The coil and rod assembly moves in a magnetic field produced by two permanent magnets. Another phosphor-bronze coil, known as the pick-up coil is also connected rigidly to the rod, and the rod is held with the transducer at either end with springs.

The magnetic flux (Φ) linked with the pick-up coil is given by $\Phi = \int_A \mathbf{n} \cdot \mathbf{B} \cdot d\mathbf{A}$, where n is the number of turns in the coil, B is the magnetic flux density and A is the area of the loop. When this coil moves in the magnetic field, then according to Lenz's law, an induced emf is produced which is proportional to the rate of change of flux ($d\Phi/dt$) linked with the coil. This induced emf is a replica of the driving waveform and this is fed to the error stage of the feedback and power amplifier where it is compared with the reference velocity waveform. The reference velocity waveform is triangular (constant acceleration) in shape and is obtained by integrating the square input to the Mossbauer drive unit. The feedback network adjusts to produce zero difference between the driving waveform and the reference waveform. Figure 2.7 shows the velocity drive assembly. Apart from triangular wave form the other form possible is sawtooth wave to produce constant acceleration. The specific velocity range required for different absorbers is obtained by changing the amplitude of the velocity waveform.

c γ -Radiation detection system and associated electronics: A gas-filled proportional counter from LND.1INC, USA was used as the Mossbauer γ -ray detector. The gas mixture used was 97%Xe + 3% CO₂ at a pressure of 2 atmosphere with a Beryllium window 0.005" thick and having areal density

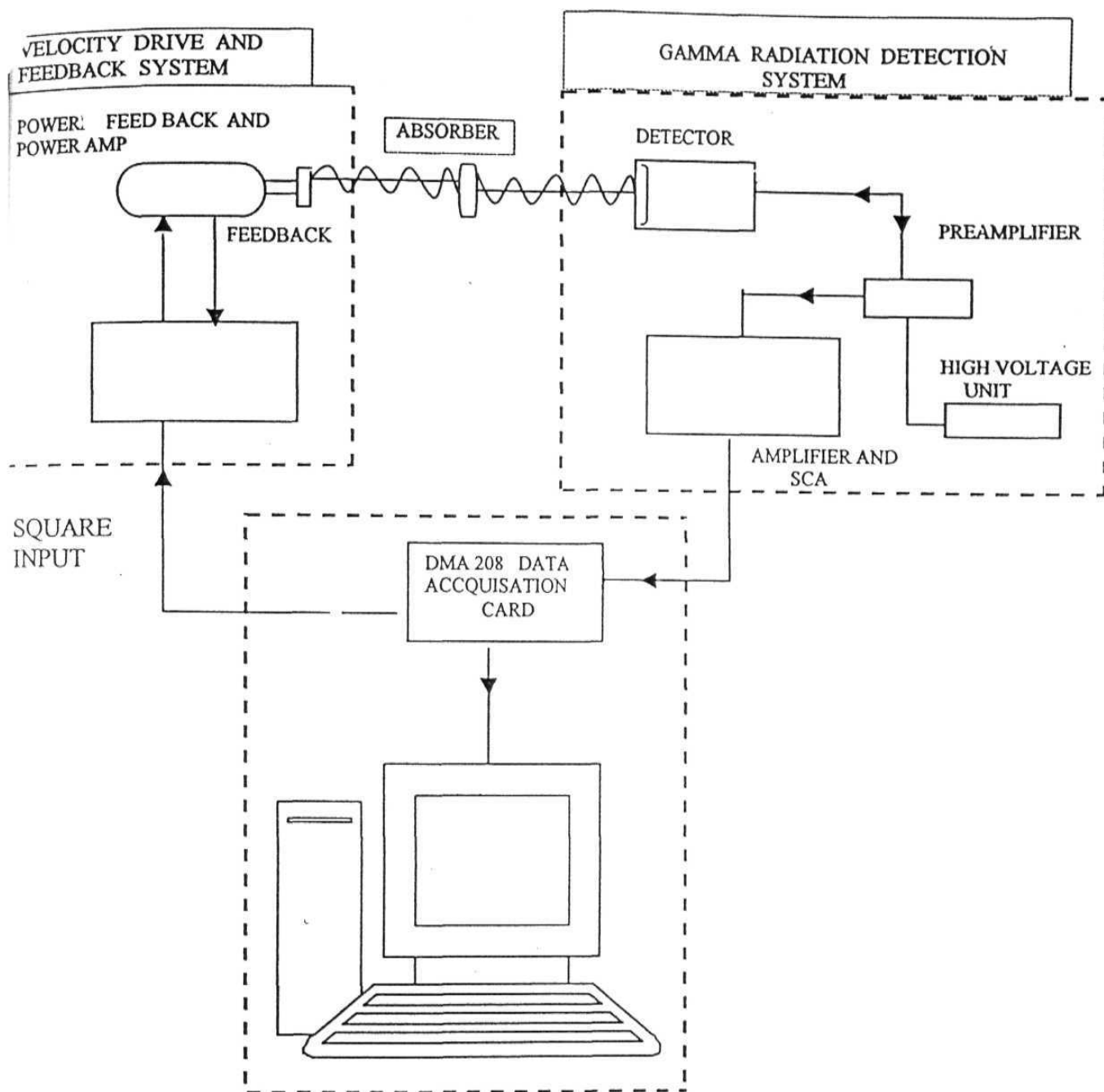


Figure 2.6 Schematic representation of the Mossbauer spectrometer set-up.

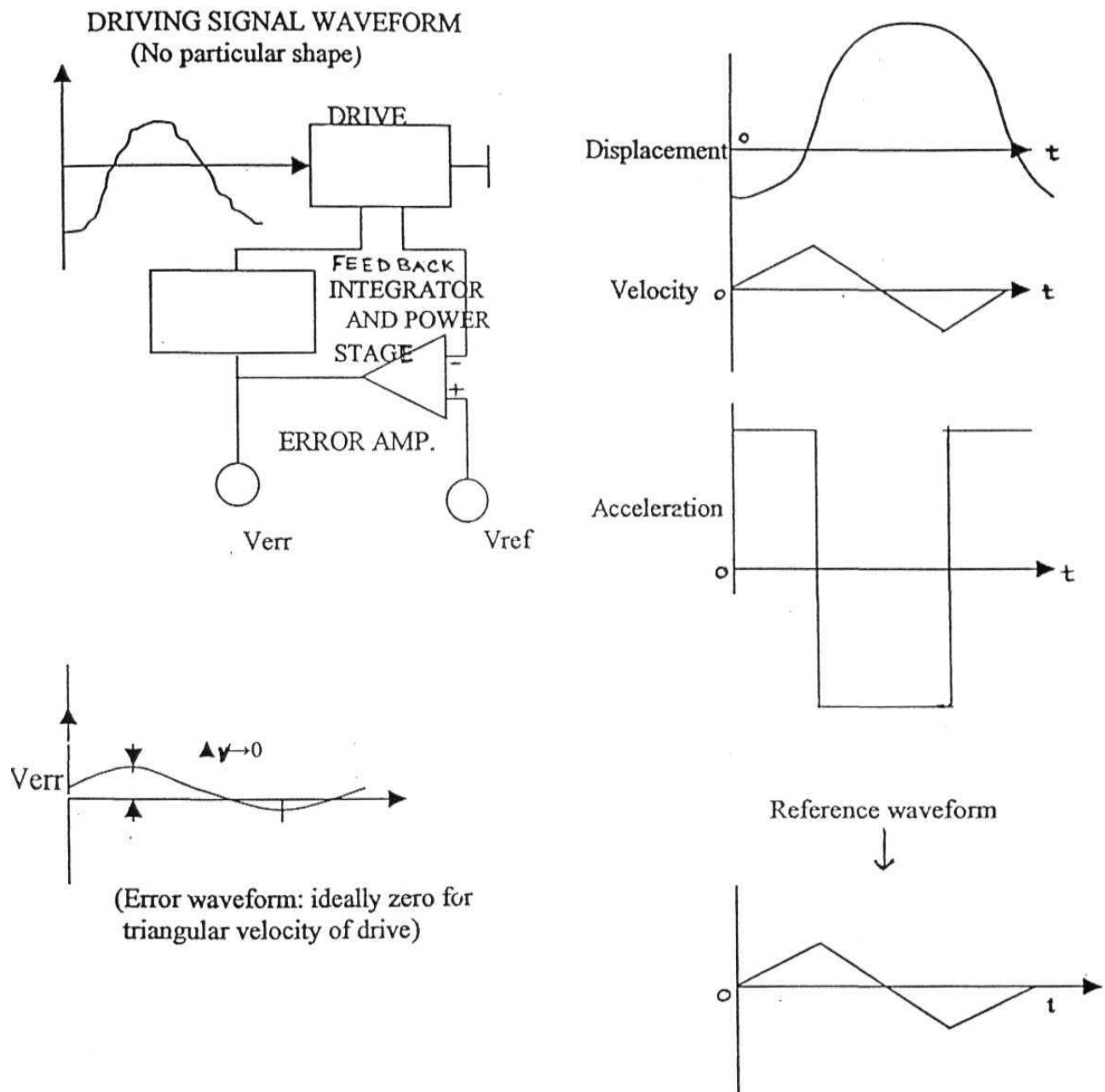


Figure: 2.7 Schematic representation of the process of generation of constant acceleration mode of the Mossbauer drive by the closed loop control method.

22.5 mg/cm². The detector bias was produced by a high voltage unit; model HV 211 from ECIL, India. A preamplifier with very high input impedance and low output impedance was used, which was acting as a buffer (impedance matcher) between the detector and the spectroscopy amplifier. This FET input charge sensitive preamplifier was made by EG & G, ORTEC, USA. Spectroscopy amplifier, model PA572 from ECIL-India, was used for amplifying and shaping the detector output pulses. The output pulses from the spectroscopy amplifier were fed to a single channel analyzer (SCA), model SC6048 from ECIL-India and the TTL output pulses of the SCA were fed to the ADC card for counting purpose. The detector bias, which was fed through the preamplifier, was selected from the plateau region of the number of counts (pulses) from the detectors vs. applied voltage curve with the Mossbauer source directly facing the detector. The bias voltage was set between 2600-2700 volts. This high voltage is achieved by using an oscillator coupled step-up transformer - a voltage multiplier- in the output stage and a feedback system to maintain the oscillator current and hence secondary voltage.

Mossbauer spectra were recorded in transmission geometry with γ -rays, collimated using lead block. The radiations emitted from the Mossbauer source were 6.3 keV X-rays. 14.4 keV and 136 keV γ -rays. The high-resolution proportional counter was detecting all these three radiation and corresponding pulses were produced. However we were interested only in the 14.4 keV γ -rays. So for obvious reasons we had to block the pulses produced by other radiations to enter in to the counting system. This was achieved by setting the SCA input voltage gates appropriately. Before setting these gates we recorded the so-called pulse height spectrum (PHS) without putting any absorber between the source and the detector and by keeping the SCA in the 'WINDOW' mode, in which the difference between the upper and lower level voltages is fixed. The spectroscopy amplifier gain, pulse shaping time, base line restoration and polarity were properly set by observing the amplified detector pulses on the

oscilloscope. Care was taken in choosing these parameters of the spectroscopy amplifier so that there were not many saturated output pulses. In the PHS we observed well-resolved two peaks (apart from the low voltage escape peak) in different voltage intervals proportional to the 6.3 and 14.4 keV incident radiation. The sum peak corresponding to the (6.3 keV+14.4 keV) was also observed with low intensity. The SCA lower and upper voltage levels were set to the voltage values close to starting of 14.4Kev peak and ending of the sum peak respectively and it was put in the NORMAL mode (where pulses between the upper and lower level only were accepted and all other pulses were rejected). In this way 14.4 keV γ -ray pulses were chosen and hence the signal to noise ratio was improved.

d PC based Mossbauer data acquisition system

In designing the Mossbauer data acquisition system one need to use a multi channel analyzer (MCA) operating in the multi channel scaling (MCS) mode, the mode in which different channels are accessed at different time intervals. The time intervals correspond to the times during which the drive is moving with velocity ' v ' to ' $v + dv$ '. In implementing this operation it is convenient and cost effective to use a microprocessor based data acquisition system (MPDS) rather than a conventional MCA with involved hardware [7]. What all one has to do is to open a memory bank (channels) to store the counts (standard pulses from the output of the SCA) in synchronization with the velocity of the drive. Different channels correspond to different velocities of the source and in turn different energies. Thus the counts vs. channel number data represent the Mossbauer spectrum. Standard samples (e.g. pure Fe) Mossbauer data are recorded to calibrate the channel numbers to velocities from the known separations of the Mossbauer lines in terms of velocity from other sources [ref 198 of chapter 1]. In principle we can increase the number of channels to have better resolution of velocity but not up to *ad-infinitum* as it may *detoriate* the

spectrum quality due to even marginal non-linearity in the drive velocity waveform. Most commonly 256, 512, or 1024 channels are addressed.

Our design of the data acquisition system was based on the PCL208 High Performance Data Acquisition Card (or ADC card) of Dynalog Microsystems India. The card was plugged into the expansion slot of a PC to implement MCS function of a MCA. The I/O card has an AD converter, an Intel 8254 programmable interval timer, and a DA converter on board. The timer IC has three 16 bit down counters/timers. The counters were set to binary counting mode to enable them to count from 0 up to 65535. The counter registers and the counters control register were configured to get the following counter operations. Counter 1 was internally coupled with a clock of frequency 1 MHz and is used to generate the dwell time of 100 μ -seconds. We organized 1024 (512 + 512) channels for our spectrometer. To implement this, Counter 2 was set to down count by 1024 and give the current channel position by reading its contents on the fly [8] to reduce the dead time in the MCS to the order of 0.5 μ -second. The third timer (Counter 0, internally coupled with 100 kHz clock) keeps track of the number of SCA TTL output pulses that come from the radiation detector. For the purpose of synchronization the square wave to drive the Mossbauer velocity drive is obtained by software checking the counter, which divides the dwell time by 1024. If there is a channel advance then the DAC is output with zero for a current timer value greater than 512 and FF for a value less than 512. The frequency of this square wave, fed to the Mossbauer drive unit, was 10 Hz.

Mossbauer spectra with good counting statistics (~ 0.5 M counts/channel) were recorded. The spectrum recorded in the first 512 channels was the mirror image of the spectrum recorded in the next 512 channels. Therefore the spectra in these two halves were added by folding the overall spectrum w.r.t the zero velocity channels in both the halves to increase the statistics of each spectrum

(~1M counts/channel in the folded spectrum). SC A gates were set to get very good signal-to-noise ratio.

e Mossbauer absorber preparation

There are various ways of preparing Mossbauer absorber. It can be in the form of a foil or in the form of powder - either compacted in the form of pellet or as it is. In our studies absorbers were prepared by spreading the fine powder as uniformly as possible in the central hole (~12 mm diameter) of a copper plate fixed on cello tape; in this way the sample was also stuck to the cello tape. Another piece of cello tape was fixed from top so that there was no chance of the sample to fall and the copper plate with sample were firmly stuck to cello tape pieces from both side. The amount of powder for the absorber was calculated so that the natural Fe contents in the absorbers were closed to 10mg/cm², which is ideally required according to Margulies and Ehrman [Ref 205 of chapter 1]. Hence we could safely assume no correction in the lines due to thickness broadening and that all our absorbers were within the thin absorber limit.

f Various methods of Mossbauer data analysis

Mossbauer spectra can be analyzed depending on the kind of interactions resulting the spectra. If the spectrum results out of a single interaction or a well resolved superposition of two or three interactions then the methods of Fast Fourier Transformation (FFT) or % lest square fitting are adopted to fit the spectrum. In these methods most commonly Lorentzian lines are generated at different velocities/channel numbers and the simulated and experimental spectra are compared by minimizing the quantity

$$S = \chi^2 = \sum_{i=1}^N W_i (C_e(i) - C(i))^2 \quad (2.1)$$

till the best fit with minimum χ^2 value is obtained. In the above expression W_j 's are the weight factors, $C_e(i)$ and $C(i)$ are the experimental and calculated intensities in channel i .

Complicacy arises when the spectra (such as our as-milled and heat treated samples spectra) are unresolved and consist of strongly overlapping and widely distributed hyperfine parameters from elementary component spectra. These kinds of spectra very commonly arise for magnetically disordered or amorphous systems, where hyperfine parameters change from Fe site-to-site resulting in the distribution of hyperfine parameters. There are various methods suggested to obtain relevant information from this kind of unresolved spectra [9-19].

According to Vincze [16, 17] the basic assumptions to resolve these overlapped spectra are:

- i) The distribution of the hyperfine parameter concerned is independent to the distributions of the other parameters.
- ii) The intensity ratios and line widths of the component spectra (also called elementary spectra) of the distribution are known.

Most commonly the component spectrum is built from Lorentzian peaks in the thin absorber approximation. But other peak shapes are also assumed occasionally depending on the specific interaction present, e.g. when quadrupole interaction was present as a perturbation to the hyperfine magnetic field interaction [18]. Price has described an empirical line shape suitable for fitting a wide variety of spectra [20].

The underlying concept to these model independent methods is to consider a probability distribution $p(x)$ of the hyperfine parameter (X) such that

$$\int_0^{\infty} p(x) dx = 1 \quad (2.2)$$

and the spectrum can be generated as

$$C(i) = C_{\infty} - \int_0^{\infty} p(x) F(i, x) dx \quad (2.3)$$

or in more physical way close to reality as

$$C(i) = C_{\infty} - \int_0^{x_{\max}} p(x) F(i, x) dx \quad (2.4)$$

Where C_{∞} is the background far from resonance and $F(i, x)$ defines the contribution in channel i of the elementary component which is single line, a doublet and a sextuple according to the nature of X . If hyperfine magnetic field interaction (H) is considered then the requirements that without any external magnetic field the probability distribution $p(H) = p(-H)$ and that there is an upper cut-off field H_{\max} beyond which $p(H)$ goes to zero smoothly [13, 19] gives $(dp(H) / dH)_{at H=0}$ and $H-H_{\max} = 0$.

With a probability distribution $p(H)$ the spectrum generated at velocity v is given by

$$S(v) = \int_0^{H_{\max}} p(H) L_6(v, H) dH \quad (2.5)$$

Where

$$L_6(v, H) = \sum_{i=1}^6 (1/\pi) [(\Gamma_i/2) / ((\Gamma_i/2)^2 + (v - \alpha_i H)^2)]$$

is the normalized Lorentzian shape function of the lines of elementary spectrum arising due to hyperfine magnetic field H . Γ_i are the line widths of the six lines of the component spectrum and $\alpha_i H$ are their positions.

In his method Window [13] has expanded $p(H)$ in the form of

$$p(H) = \sum_{n=1}^N a_n f_n(H) \quad (2.6)$$

where

$$f_n(H) = \cos(n\pi H/H_{\max}) - \cos(n\pi)$$

and N is the total number of elementary spectra giving rise to the hyper magnetic field distributions. Using equations (2.6) equation (2.5) becomes

$$S(v) = \sum_{n=1}^N a_n S_n(v) \quad (2.7)$$

where

$$S_n(v) = \int_0^{H_{\max}} f_n(H) L_6(v, H) dH \quad (2.8)$$

is the spectrum created by the term $f_n(H)$. If the experimental spectrum at velocity v is denoted by $W(v)$, then coefficients a_n of the field distribution can be found by minimizing the function

$$\Phi = \sum_v (S(v) - W(v))^2 \quad (2.9)$$

by the non linear least square fit method w.r.t the parameters a_n or other parameters like IS, if necessary. But if we assume IS to be independent of the HMF, then the minimization of equation (2.9) boils down to the solution of N linear simultaneous equations of the form [19]

$$\sum_{m=1}^N a_m X_{mn} - \sum_v W(v) = 0 \quad (2.10)$$

Where

$$X_{mn} = \left[\sum_v S_m(v) S_n(v) \right]$$

These equations are solved to find the coefficients a_n [13, 19]. The advantage of the Window method is the possibility of fitting the background of the spectrum, for this purpose one defines $S_0=1$ in equation (2.7) and the corresponding a_0 represents the background.

In the method of Hesse and Riibartsch [14] the range of hyperfine parameters in question is divided into N equal intervals ΔH [12] with $H_{\max} - N$

ΔH and $H_h = h \Delta H$ and the integral of equation (2.5) is replaced by a discrete sum

$$S(v) = \sum_{h=0}^N p(H_h) L_6(v, H_h) \quad (2.11)$$

Which could also be represented as

$$S_v = P_h L_{h,v}$$

considering the fact that spectrum is collected in discrete number of channels.

The probability distribution is obtained using the generalized method of numerical solutions of integral equations of 1st kind [21-23] adding a smoothing parameter. The criteria to find the correct smoothing parameter was defined by the parameter

$$X = \left(\sum_{i=1}^N [S(v_i) - S_m(v_i)]^2 \right) / \left(\sum_{i=1}^N (\text{number of counts in channel } i) \right) \quad (2.12)$$

Where m is the number of coefficients and ideally $X=1$, whereas $X>1$ or $X<1$ determine smoothing chosen is either too strong or too weak.

The problem of the above two last methods were:

- i) Only smooth and broad distributions could be found correctly but large errors were introduced if sharp peaks were present [table 2 and 3 of 14]
- ii) Unphysical oscillations with negative values were present in the distribution due to ill- defined background [figure 1-3 of 14].

In the method of Le Caër and Dubois [which was essentially a modification of the H-R method] the probability distribution was assumed to be as a continuous distribution and a discrete term of the form

$$f(x) = p(x) + \sum_{l=1}^L p_l \delta(x - x_l) \quad (2.13)$$

$$\text{with } \int_0^{\infty} f(x) dx = 1$$

The integral of equation (2.4) was replaced by the discrete sum

$$C(i) = C_{\infty} - \sum_{k=1}^K \alpha_k (\Delta x) p_k F_k(i) - \sum_{l=1}^L p_l F_l(i) \quad (2.14)$$

with $p_k = p(x_k)$ and $F_m(i) = F(i, x_m)$

Hence unlike H-R method, background is also included in Le Caer method [18]. The unknown parameters C_{∞} , p_k can be determined by the least square minimization of S in equation (2.1). It became obvious in their argument that there must be a step Δx_c (AH for H-R) of the h - parameter below which the problem is improperly posed in the sense that small changes (e.g. noise in the collected spectrum) in the input parameters produce large changes in the solution, which presents an oscillatory behaviour. For large Δx_c overlapping between the H parameters will be less and it will corresponds to the case of Vanet [10].

The solutions of equation (2.1) were obtained, similar to H-R analysis, by the generalized least square method with smoothing parameters but using constrained optimization process of numerical analyses [24]. The criteria (equation 2.12) to determine the smoothing parameter holds good in this case also. The advantage gained by Le Caer method over the other methods (H-R, Window, Bansal) was that we were able to obtain sharp peaks also correctly apart from broad continuous distribution by choosing proper Δx_c and smoothing parameter (SM) values. The unphysical negative oscillations were removed from the probability distributions. We were able to generate distribution consists of only sharp peaks by putting $SM=0$ hence avoiding over smoothing. The solutions are much more stable with respect to fluctuations in data by using proper Δx_c . We could fit spectra with line intensity ratios other than 3:2:1 present due to texture effect.

g Mossbauer data analysis procedure adopted by us

Calibration spectra (with ~0.05-0.1M counts/channel) were recorded with Fe (99.85% pure) foil, enriched SS foil, and Sodium Nitroprusside (SNP with

chemical formula $\text{Na}_2(\text{CN})_5\text{NO}\cdot 2\text{H}_2\text{O}$) button. These spectra were fitted by FFT method by using the program supplied by Prof. V. Spijkerman of Ranger Scientific Corporation, USA. The value of the velocity calibration obtained was in the range of 0.0363-0.0367 mm/sec/channel. The zero velocity channel was chosen to be the one for which pure natural Fe Isomer Shift (IS) was nearly ~ -0.106 mm/sec with respect to Fe/Rh (source) matrix. Hence all our **IS values reported will be with reference to Fe/Rh**, if not mentioned otherwise. The average line width (FWHM) of the Fe lines was found to be 0.276 mm/sec.

All other spectra consisting of superposition of HMFs were fitted by the method of Le Caër & Dubois with a smoothening parameter value of 20. The increment in field (ΔH) chosen was nearly around 5.5 kOe. The intensity ratio of the absorption lines used was 1:2:3. A linear relationship between the IS (I) & HMF (H) is assumed of the form $I = aH + b$, where a, b are the parameters optimized to obtain the best fit with minimum χ^2 . In most of our spectra the value of 'a' was negative and that of 'b' was positive and typical values of 'a' and 'b' were -0.001 mm/sec/kOe and 0.30 mm/sec respectively. But in the cases of Fe-Cr, Fe-Mo, and FeCo-W alloys the signs of 'a' and 'b' were needed to be reversed in order to fit the experimental intensity ratios of the absorption lines. This type of correlation is justified because the isomer shift in the Mossbauer spectrum is directly proportional to the total S-shell electron density at the nuclear site whereas the magnetic field is proportional to the difference between the spin up and spin down S-shell electron density at the nuclear site. Changes in HMF arise from a change in the spin up or spin down s electron density, which also changes the total s electron density and hence the isomer shift proportionally. This general systematic between isomer shift and the HMF works very well in a wide variety of alloy systems [ref 173 of chapter 1]. FWHM of the elemental lines were varied in the range of 0.25-0.35 mm/sec to obtain minimum χ^2 . If a well-defined hyperfine field component with specific IS and QS value arising from a distinct phase is present in the Mossbauer

spectra it can also be separated out from the broader distribution using the above method. For instance in the case of DO₃ order (discussed in the next chapter) in a alloy system with $\sim\text{Fe}_3\text{X}$ stoichiometry (X= non magnetic solute atoms for which the 2nd and higher nn perturbation is negligible in comparison to 1nn perturbation), there are two kinds of Fe atoms, one which is surrounded by 4 Fe and 4 solute (e.g. Ge) 1nn atoms and the other surrounded by 8 1nn Fe atoms giving rise to HMF values of ~ 200 and 330 kOe with IS equals to ~ 0.25 and 0.05 respectively. The QS values for both these field components are zero. A typical spectrum of this kind arising in case of Fe-Ge system is shown in figure 2.8. If only a field distribution is fitted to the spectrum (figure 2.8 a) the fits are not satisfactory because of the large and definite spectral components coming from the DO₃ phase. It was therefore found necessary to introduce two fixed hyperfine fields, isomer shifts, and FWHM values for these components. These hyperfine parameters for the well-defined components were also optimized to get the minimum χ^2 . A remarkable improvement in the fitting was obtained as shown in figure 2.8b.

The HMF distributions obtained by this method were fitted to Gaussian functions [25] peaked at the field positions corresponding to HMFs seen by a Fe atom with different 1nn and 2nn (wherever applicable, e.g. FeCo-W and Fe-Mo alloys) solute configurations [26]. In determining the HMF values corresponding to different nearest neighbour configurations of Fe atoms we used the simple additive perturbation model [26-32] according to which the HMF at a Fe site is given by:

$$H = H_0 + n (\Delta H_1) + m (\Delta H_2) + kC \quad (2.15)$$

and the IS is given by

$$I = I_0 + n (\Delta I_1) + m (\Delta I_2) + kC \quad (2.16)$$

Where 1 and 2 refer to 1st and 2ⁿ nearest neighbours, n and m refers to number of 1st and 2nd nn, ΔH and ΔI correspond to the perturbation in the field and isomer shift over that of unperturbed values H_0 and I_0 (without any solute atoms

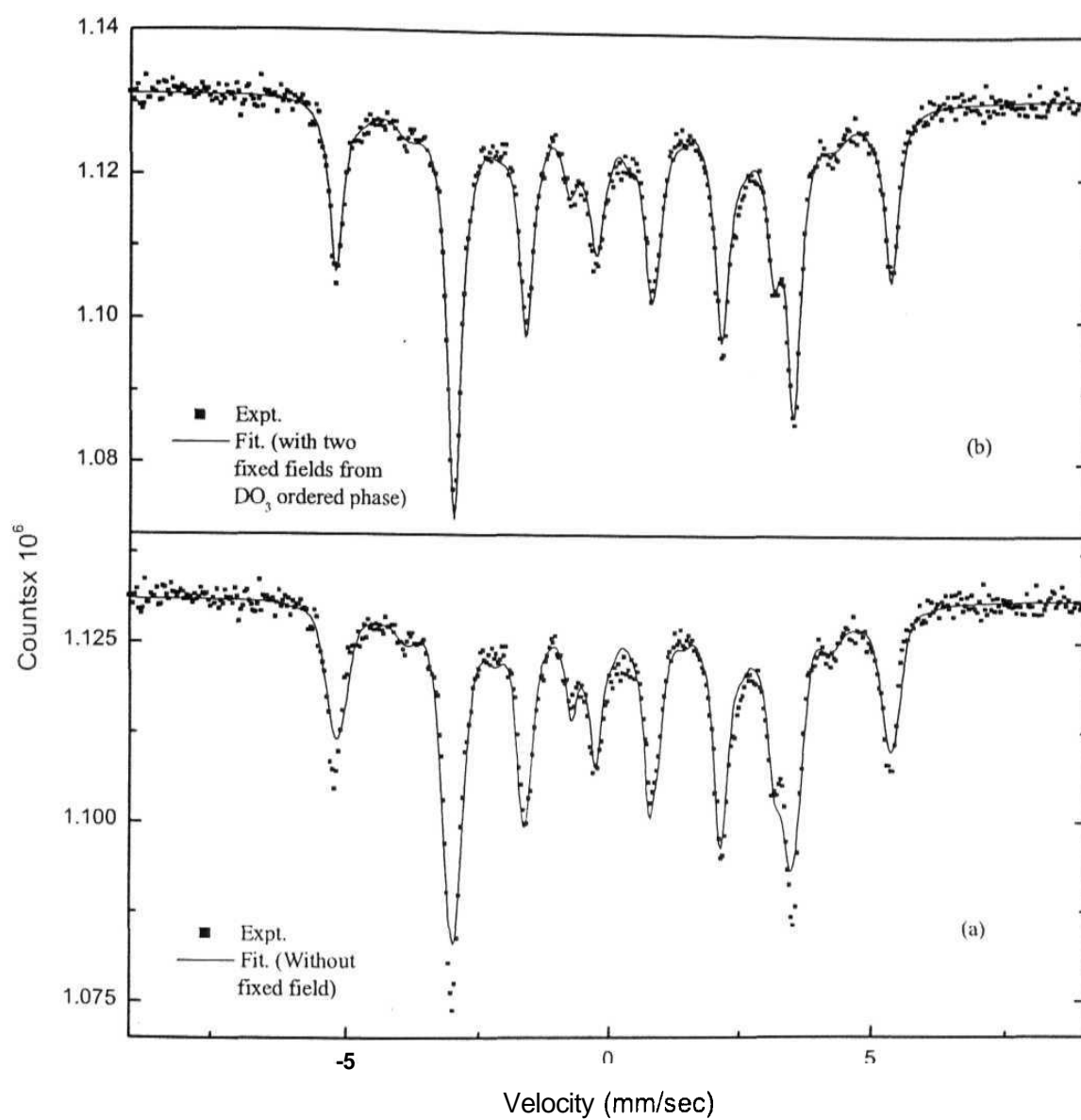


Figure 2.8 Mossbauer spectrum for Fe₃Ge alloy heat treated at 350 °C for 24 hours and fits to spectrum. In (a) only a field distribution was used to fit the data whereas in (b) fixed hyperfine field components at around 330 kOe and 200 kOe were introduced together with a field distribution.

around Fe atoms) due to the presence of solute atoms in the neighbourhood of Fe atoms, and kC is the average and almost negligible contribution from distant neighbours. In our analysis we have considered up to first two nearest neighbour contributions. Figure 2.9 shows the Gaussian fit to the HMF distribution obtained for the Fe_{0.73}Ge_{0.27} as-milled alloy taken as a representative system. The Gaussian fit to the field distribution arising from a heat-treated ordered sample is not shown here, as it is similar kind but of much simpler type because the peaks arising from specific Fe environments are well resolved than in comparison to as-milled alloy where the overlapping between the fields is strong.

Two important points are to be noted before we proceed further:

- 1) The approximate average sizes of the powder particles of our as-milled samples, as determined e.g. in case of Fe₃Ge, using a Wild Photomakroskop Model M400 optical microscope with a magnification of 320, were found to be in the range of 0.5 μm to 1.0 μm . This particle size is large and no superparamagnetic relaxation effects are expected. Accordingly none of our Mossbauer spectra indicates the presence of any relaxation effects at room temperature and the observed field distribution can be attributed to a different near neighbour configurations of Fe atoms.
- 2) Our Mossbauer spectra of the as-milled alloys did not show any separate contribution, which could be attributed to ⁵⁷Fe atoms residing near or at grain boundaries. In the case of nanocrystalline Fe [33, 34] as well as in some concentrated binary Fe alloys [35] separate HMF contributions were observed for grain boundary atoms, which were about 10-20 kOe less than the in-grain field. However in all these systems the grain size obtained was of the order of 8 nm or less and it has been observed by Fultz et.al. [35] that the contributions from grain boundary Fe atoms are insignificant when the grain size is 10 nm or more because at this grain size the grain boundary width is negligible in comparison to the size of the crystalline grains. As the grain sizes were ~ 10 nm

for most of our as-milled samples except Fe-Ge and Fe-Mn-Ge systems so we also did not observe any separate HMF component arising from grain boundary Fe atoms. In case of Fe-Ge and Fe-Mn-Ge systems GB Fe atoms field component if present would merge with the broad distribution arising due to random atomic arrangements of the disordered structure.

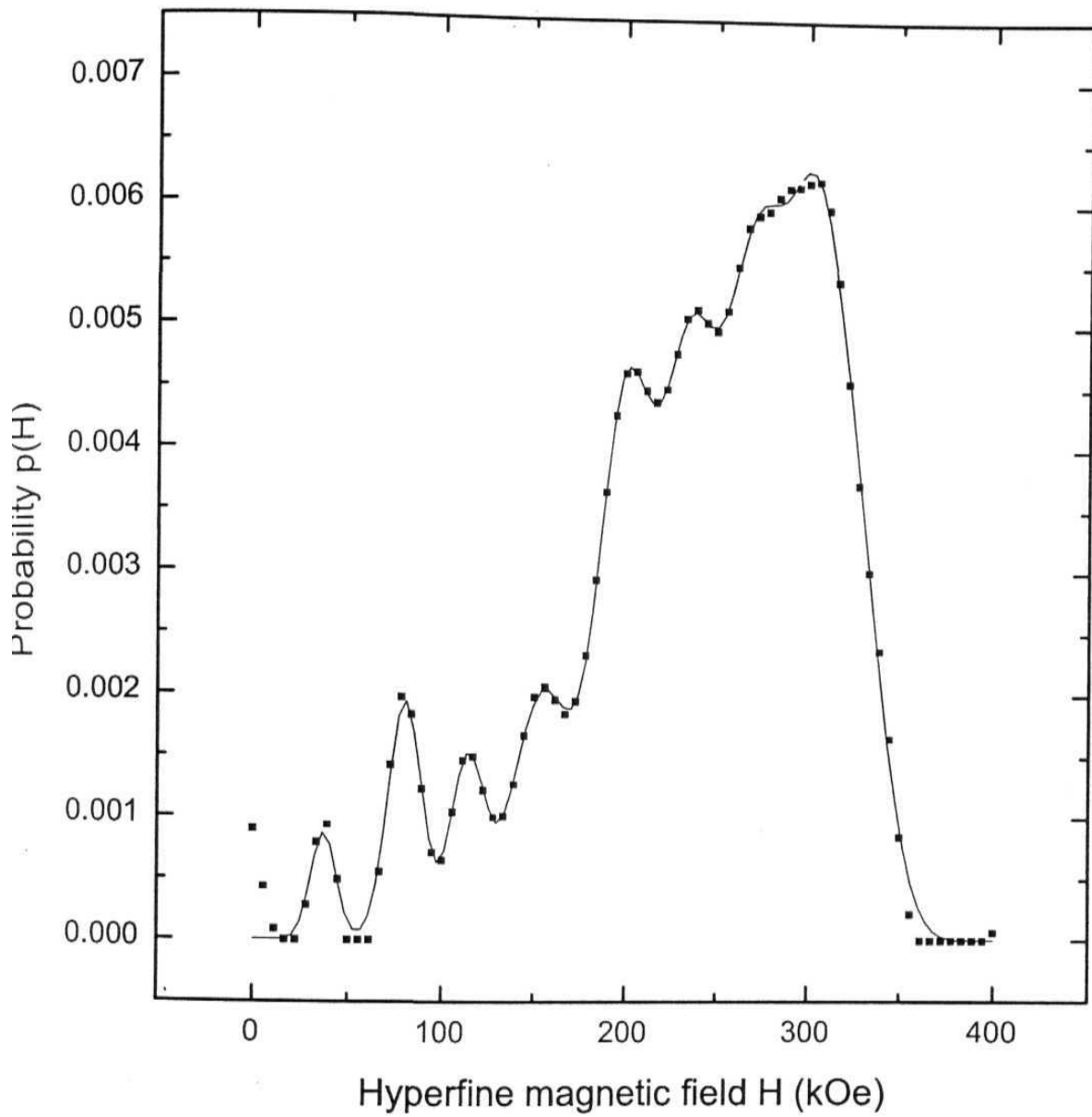


Figure 2.9: Gaussian fit to HMF probability distribution of the 24 h milled $\text{Fe}_{0.73}\text{Ge}_{0.27}$ alloy (taken as a representative system). Symbols: Exp, Solid line: Fit.

References

- [1] H. P. Klug and L. E. Alexander, X-Ray Diffraction Procedures for Polycrystalline and Amorphous Materials, 2nd Edition, (John Wiley and Sons, New York, 1974).
- [2] B. D. Culity, Elements of X-Ray Diffraction, 2nd ed. (Addison-Wesley Publishing Company Inc., Philippines, 1978).
- [3] B. E. Warren, X-Ray Diffraction (Addison-Wesley, Reading, Massachusetts, 1969).
- [4] T. E. Cranshaw, in Mossbauer Effect: Current Applications to Physical Sciences, edited by L. S. Kothari, J. S. Bajjal and S. P. Tewari (Academic Publications, India, 1984).
- [5] Mossbauer Spectroscopy I and II, Topics in Appl. Phys., edited by U. Gonser, Vol. 5, and Topics in Current Phys. Vol. 25 Springer (1975 and 1981).
- [6] E. Kankeleit, in Mossbauer effect methodology, edited by I. J. Gruverman (Plenum Press, NY, 1965), Vol 1.
- [7] J.T.T. Kumaran, Ph. D Thesis, University of Hyderabad, 1990.
- [8] J. T. T. Kumaran and C. Bansal, Nucl. Instrum. and Methods in Physics Research **B61**, 357 (1991).
- [9] A. H. Muir, Jr., Mossbauer effect methodology, Vol. 4 (Ed. I. Gruverman), Plenum Press, NY (1967), p. 75.
- [10] F. Varret, A. Gerard, and P. Imbert, Phys. Stat. Solidi **B43**, 723 (1971).
- [11] T. E. Sharon and C. C. Tsuei, Phys. Rev. **B5**, 1047 (1972).
- [12] J. Hesse and U. Schossow, Int. J. Magnetism 5, 187 (1973).
- [13] B. Window, J. Phys. E4, 401 (1971); *ibid*, J. Phys. F: Metal Phys. 4, 329 (1974).
- [14] J. Hesse and A. Rübartsch, J. Phys. E7, 526 (1974).
- [15] P. Mangin, G. Marchal, M. Piecuch, and C. Janot, J. Phys. E9, 1101 (1976).
- [16] I. Vincze, Solid State Commun. 25, 689 (1978).
- [17] I. Vincze and E. Babic, Solid State Commun. 27, 1425 (1978).
- [18] G. Le Caer and J. M. Dubois, J. Phys. **E12**, 1083 (1979).
- [19] C. Bansal, Bull. Mater. Sci. 6, 1047 (1984).
- [20] D. C. Price, Austr J. Phys. **34**, 51 (1981).
- [21] D. L. Phillips, J. Ass. Comput. Mach. 9, 84 (1962).
- [22] S. Twomey, J. Ass. Comput. Mach. 10, 97 (1963).
- [23] P. Paatero, S. Manninen, and T. Paakkari, Phil. Mag. 30, 1281 (1974).
- [24] M. Avriel, Nonlinear Programming: Analysis and Methods, Prentice-Hall, NJ (1976).
- [25] D. G. Rancourt and J. Y. Ping, Nucl. Instrum. and Methods in Physics Research **B58**, 85 (1991).

- [26] B. Fultz, Z. Q. Gao, H. H. Hamdeh, and S. A. Oliver, Phys. Rev. **B49**, 6312 (1994).
- [27] M. B. Stearns, Phys. Rev. 129, 1136 (1963); Phys. Rev. B6, 3326 (1972).
- [28] B. Fultz, in Mossbauer Spectroscopy Applied to Magnetism and Material Science, edited by G. J. Long and F. Grandjean (Plenum Press, New York, 1993), Vol. 1, p. 1.
- [29] B. Fultz and Z. Q. Gao, Nucl. Instr. and Methods in Phys. Res. B76, 115 (1993).
- [30] B. Fultz, Z. Q. Gao, and H. H. Hamdeh, Hyperfine Interact. 54, 799 (1990).
- [31] B. Fultz, Z. Q. Gao and L. Anthony, Mater. Res. Soc. Symp. Proc. 186, 187(1991).
- [32] I. Vincze and I. A. Campbell, J. Phys. F3, 647 (1973).
- [33] U. Herr, J. Jing, R. Birringer, U. Gonser, and H. Gleiter, Appl. Phys. Lett. 50,472(1987).
- [34] P. Sinha and G. S. Collins, Hyperfine interactions 92, 949 (1994).
- [35] B. Fultz, H. Kuwano, and H. Ouyang, J. Appl. Phys. 77, 3458 (1995).

Chapter 3

Chemical Order-Disorder Transformations

INTRODUCTION

Order-disorder transformation in binary and ternary alloy systems is one of the fascinating and extensively studied fields for many years [1-10]. The formations of different ordered phases governed by the thermodynamic equilibrium conditions and the kinetics of their formation decided by the atomic diffusion as well as activation energy barriers have been studied by various researchers. The ordered phases between two metals are known as intermetallics. The high temperature properties of the intermetallics, like better strength, corrosion/oxidation resistance are very promising for their wide applications [ref 6 of chapter 1]. Frequently the disadvantage of the intermetallics is their low ductility and fracture toughness at low temperatures. The method of high energy ball milling to produce alloys is found to be suitable to overcome these drawbacks by refining the grains to smaller sizes, introducing atomic disorder in the lattice and in some cases stabilizing higher symmetry structure than the equilibrium relatively lower symmetry structures [11, ref 43 of chapter 1]. It has also been long known that partially ordered phases are stronger than those wholly disordered or fully ordered (because at a certain value of the long-range order parameter, L , superdislocations separate into unlinked singles). It was shown that the microhardness of mechanically milled Ni_3Al powders exhibited a pronounced sharp maximum corresponding to $L = 0.5$ [Ref 65 of chapter 1]. This work suggests that the greater is the ordering energy; the steeper will be this maximum of strength (or hardness). Thus, it is of interest to study the mechanical behavior of materials in various states of partial order. Disordering phenomena of ordered alloys have also been studied to understand the mechanism of disordering and also to produce the disordered material that has a higher ductility/formability than the ordered alloy. The atomic disorder in an intermetallic can be manifested in three different ways [12]. Firstly, the two atomic species involved can occupy the

"wrong" sublattices and this is referred to as anti-site disorder. This introduces strain into the lattice but maximum upto 3 % [ref 46 of chapter 1]. This type of disorder was observed in a number of mechanically milled compounds with the $L1_2$ structure, e.g., Ni_3Al , Ni_3Si , Fe_3Ge and those with the B2 structure, e.g., $CoGa$ and $AlRu$. Secondly, triple-defects can be generated. In an equiatomic compound such as $CoGa$, for example, the transition metal Co atoms can substitute on the Ga lattice, and this is anti-site disorder. But, the Ga atoms stay on their own lattices. This leads to the presence of vacancies in the Co lattice to maintain the stoichiometry. Thus, vacancies on the Co -sublattice in combination with Co anti-site atoms in a ratio of 2:1 constitute the triple defects. Third, there could also be redistribution of interstitials wherein the interstitial atoms in the octahedral sites are transferred to the tetrahedral sites, e.g., Mn_3Sn_2 , Fe_3Ge_2 . Alloys can be disordered by irradiation [13, 14], rapid solidification [ref 22 of chapter 1], or heavy plastic deformation through MM/MA [15]. Large amounts of plastic deformation result in the generation of a variety of defect structures (dislocations, vacancies, stacking faults, grain boundaries, etc.) and these destabilize the ordered nature of the lattice leading to the formation of a disordered (crystalline) or amorphous phase. If the enthalpy of ordering is high then in some cases alloys tend to become amorphous after they are chemically disordered [ref 56, 57 of chapter 1, 16, 17]. In some cases such as Al based transition metal alloys [18-25] and different brass compositions [26, 27] ordered alloys were produced by MA. It may also be mentioned in passing that all order states ($L = 0$ to 1) cannot be accessed by traditional methods of disordering. For example, in equilibrium, the order parameter for Cu_3Au jumps discontinuously from 0.8 to zero at the critical ordering temperature. But, mechanical milling can be used to obtain different degrees of order so that the effect of order parameter on structure and mechanical properties of alloys can be investigated. Ermakov et al. reported the first observation of disordering of an ordered compound $ZnFe_2O_4$ by MM in

1982 [28]. Disordering of Fe_3Si by mechanical grinding was reported later [29, 30]. It has been noted that upon milling, the long-range order parameter (L) in the intermetallic is gradually reduced and, in many cases, the material may become totally disordered ($L = 0$), e.g., Ni_3Al [31, ref 65 of chapter 1]- this is a permanently $L1_2$ ordered intermetallic and sustain its order structure under other commonly used disordering process but under severe plastic deformation disordering of the alloy takes place within a milling time of 8 hours. In other cases, L is reduced with milling time but does not reach $L = 0$, i.e., partial order and partial disorder co-exist, e.g., CuTi [32] and AlRu [ref 64 of chapter 1]. In other cases, the L value does not decrease at all and is maintained at $L = 1$; but, with continued milling the material becomes amorphous, e.g., CoZr [ref 60 of chapter 1].

Among the various techniques (e.g. powder X-ray diffraction, measurement of superconducting transition temperature, specific heats, magnetic susceptibility, determining coefficient of thermal expansion, differential scanning calorimetry, etc.) used to study the order-disorder transformations, Mossbauer spectroscopic technique is very powerful (as we will see shortly) to determine the short-range order (SRO) parameter with high accuracy.

There have also been several studies on reordering of disordered phases [33-36]. For the nanocrystalline disordered alloys we need to consider grain growth also apart from ordering. It was reported that on heating the milled powder in a differential scanning calorimeter (DSC), two distinct exothermic peaks were observed. The transformations that occurred were irreversible. The low-temperature low-intensity peak is attributed to the re-establishment of short-range order. This was confirmed by the results obtained from electron energy loss fine structure studies. The absence of such a peak during reheating of mechanically milled elemental powders also indirectly confirms this hypothesis since chemical reordering cannot occur in pure metal powders. The

second major peak is associated with the simultaneous evolution of ordering and grain growth. The apparent activation energy for the transformation is found to be lower than expected during ordering of a conventional alloy. The explanation could be that the high density of point defects such as vacancies and anti-site defects, generated during milling, assist the diffusive processes and help in achieving reordering easily.

Most of the mechanically milled disordered intermetallics exhibit these two peaks in their DSC plots, with the difference that the actual temperatures and peak shapes and heights could be different depending on the nature and composition of the alloy and milling time. In ternary intermetallics, however, a third low intensity peak, often overlapping the second major peak, is observed. Although a clear explanation is not available for this it is thought that this could be due to annealing out of dislocations, usually not mobile at temperatures as low as those of the first two peaks.

In this chapter we will discuss the temporal evolution of SRO parameter in various Fe based binary and quasi and pseudo binary nanocrystalline alloys from an initial disordered state. The so-called 'kinetic path' (the path spanned in the space of two order parameters) approach will be discussed and used. The grain growth behavior in these alloys will also be discussed. An attempt will be made to correlate ordering, microstructure formation and grain growth behaviours. In section 3.1 binary Fe-Al, Fe-Ge alloy systems will be discussed, in section 3.2 pseudo binary Fe-Mn-Ge alloy system and in section 3.3 quasi binary Fe-Co-X (X = Mo, Ge, W) systems will be discussed.

3.1 Binary systems

The Fe_3X (X= Al, Si, Ge) alloy systems have been intensively investigated for **their** ordering behavior both in the microcrystalline [37, ref 27

of chapter 2, 38] and nanocrystalline states [39, ref 173 of chapter 1]. The various ordered structures for bcc alloys of A_3B stoichiometry have been enumerated and analyzed by Cahn and his group [40]. Depending on chemical compositions and signs and strengths of the first and second nearest neighbour (1nn and 2nn) interactions there are three possible ordered structures (figure 3.1). These structures can be understood by considering a unit cell of lattice parameter twice than that of the original bcc unit cell. The A and B atoms can then occupy four possible interpenetrating fcc sublattices α , β , γ , and δ (figure 3.2) in different ways to form these ordered bcc structures which are designated as B32, B2, and DO₃. The disordered bcc phase is labeled as A2.

If we consider for example Fe_3Al system then in the B32 structure the adjacent α and γ sites are occupied by Fe atoms exclusively and the β and δ sites are randomly occupied by 50% Fe and 50% Al atoms. For DO₃ order Fe atoms occupy the three sublattices (α , γ and δ) whereas Al atoms occupy the fourth one (β). In case of B2 order two non-adjacent sublattices α and δ are occupied by Fe atoms only whereas the other two β and γ are randomly occupied by 50% Fe and 50% Al atoms. These arrangements are shown in figure 3.3. We can also calculate the probability distributions of solute atom (Al) occupancy in the 1st nearest neighbour (1nn) shell of solvent atoms (Fe) for different ordered phases and also of the disordered phase in the following manner.

In the A2 structure the random distribution of the atoms over the lattice sites gives rise to a binomial distribution:

$$PA_2(X) = {}^8C_x (0.25)^x (1 - 0.25)^{1-x} \quad (3.1)$$

where $x = 0, 1, 2, \dots, 8$ are the number of 1nn Al atoms surrounding a given Fe site.

For the B32 ordered structure, the Al atoms are distributed randomly on four sites, instead of all 8 sites, in the 1nn shell of Fe. The other 4 sites are

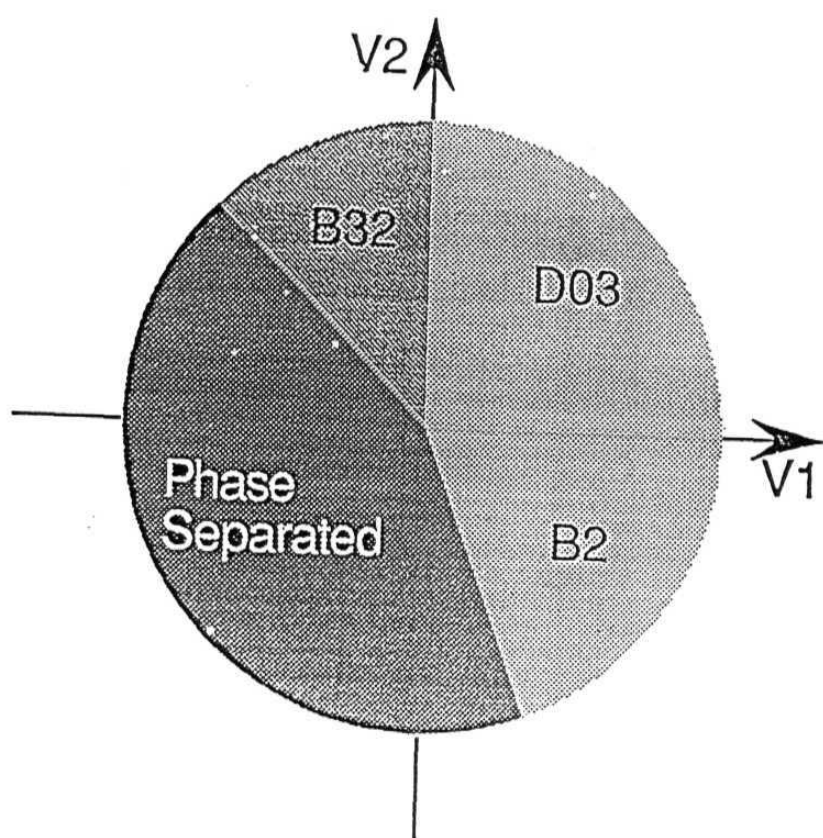


Figure 3.1 Ground states for bcc binary alloys of the A_3B stoichiometry and with different 1nn and 2nn interatomic interactions, V_1 and V_2 respectively.

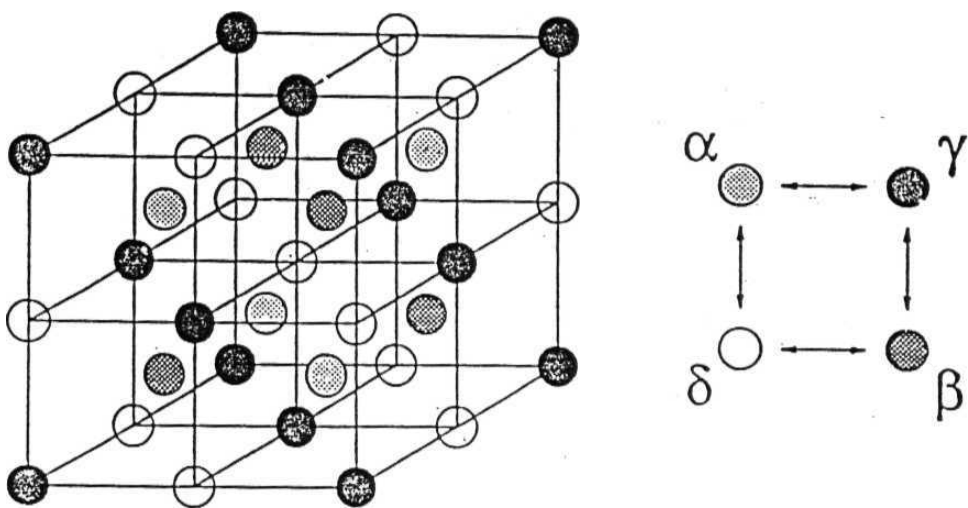
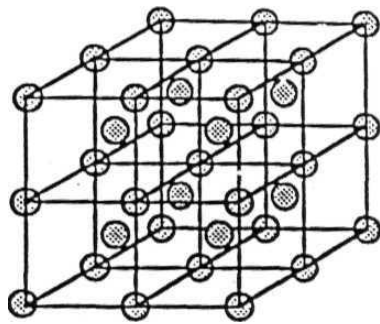
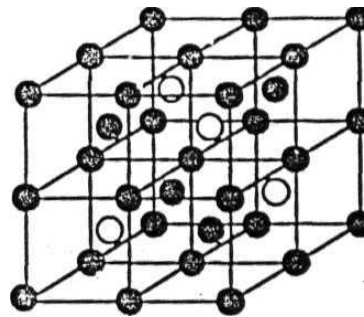


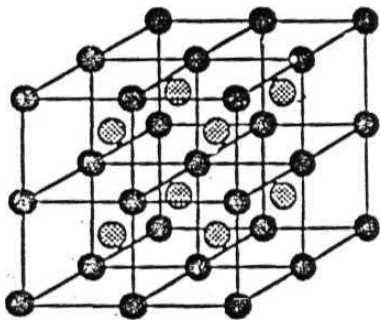
Figure 3.2 Four sublattice model for bcc lattice. A bcc lattice is divided into four interpenetrating fcc sublattices. The arrows indicate the nearest neighbor relations between pairs of sublattices.



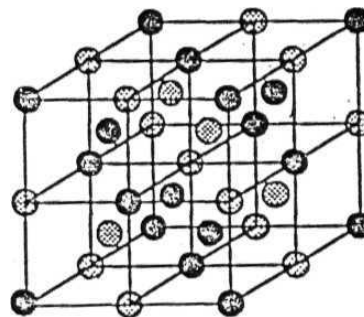
(a): A2 or bcc disorder



(b): D03 order



(c): B2 order



(d): B32 order

Figure 3.3 Four possible ordered states for bcc lattice of A_3B stoichiometry.

(●: pure Fe atom; ⊗: 50% Fe atom and 50% solute atom randomly; ⊙: 75% Fe atom and 25% solute atom randomly; and ○: pure solute atom.)

occupied by other Fe atoms, so the probability distribution for B32 order is still a binomial distribution but involving only 4 sites of the form:

$$P_{B32}(x) = {}^4C_x (0.5)^x (1-0.5)^{4-x}, x = 0, 1, \dots, 4 \quad (3.2)$$

In the B2 structure, one third of the Fe atoms (e.g. y site) are surrounded by 8 Fe atoms and two third of the Fe atoms (e.g. a and (3 sites) are surrounded by four Fe atoms and four Al atoms distributed randomly giving rise to the distribution:

$$P_{B2}(X) = \frac{2}{3}({}^8C_x (0.5)^x (0.5)^{8-x}) + \frac{1}{3} 5(0), x = 0, 1, \dots, 8. \quad (3.3)$$

Finally the DO3 order is characterized by the presence of two distinct near neighbour environments of Fe. One (e.g. Fe atoms at y site), which is surrounded by 8 Fe atoms, and the other (e.g. Fe atoms at a and (3 sites), which is surrounded by 4 Fe and 4 Al atoms. The distribution is

$$P_{DO3} = \frac{2}{3} 8(4) + \frac{1}{3} 5(0) \quad 3.4$$

The three non-equilibrium sites in the DO₃ ordered structure are labeled as 4(a), 4(b), and 8(c) in Wyckoff notation [41]. Ge atoms occupy the 4(a) sites whereas Fe atoms occupy the 4(b) and 8(c) sites. The 4(b) sites have 8 Fe near neighbours whereas the 8(c) sites have 4 Fe and 4 Ge near neighbours. This gives rise to two distinct HMFs for the Fe atom: around 330 kOe for Fe atoms at 4(b) sites having 8 Fe 1nn and around 200 kOe for Fe atom at 8(c) sites having 4 Fe and 4 Ge 1nn [42]. There are twice as many 8(c) sites as 4(b) sites giving rise to intensity of 200 kOe field to be double of the intensity of the 330 kOe field.

The probability distribution of Al atoms in the first nearest neighbour (1nn) shell of Fe for these structures is shown in figure 3.4. There is a distinct probability distribution for each of these ordered structures and the presence of these structures can be unambiguously observed using a technique such as Fe-57 Mossbauer spectroscopy, which is sensitive to the local environment around the Fe atom.

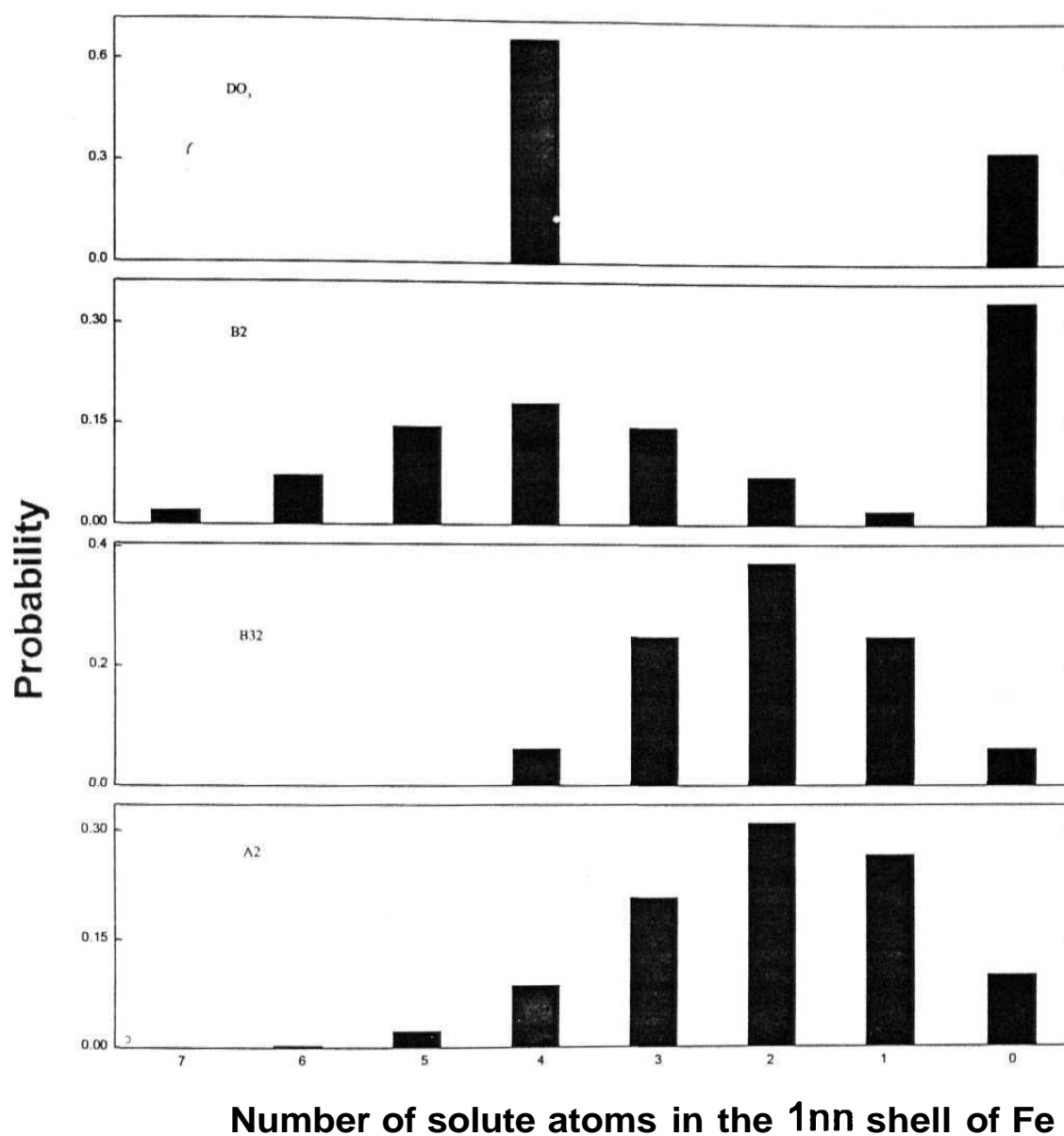


Figure 3.4: The calculated probabilities of Fe atoms having different no. of 1nn solute atoms for the A2, B32, B2, and DO₃ structures.

3.1.1 Fe-Al system

a Introduction

The Fe-Al alloy system near Fe_3Al stoichiometry shows very interesting order-disorder phase transformation behavior. The phase diagram of the Fe-Al alloy system is shown in figure 3.5 [43]. Near Fe_3Al stoichiometry it shows the disordered A2 phase (α) at temperature above 800°C , B2 ordered phase (α_2) between 800° and 530°C and the DO_3 ordered phase (Fe_3Al) below 530°C . There were several studies of ordering kinetics in the Fe_3Al system near the $\text{B2} \rightarrow \text{DO}_3$ critical ordering temperature [44, 40, 45-48]. X-ray diffraction studies of the $\text{B2} \rightarrow \text{DO}_3$ phase transformation showed the DO_3 long-range order parameter in agreement with Bragg-Williams theory [46]. The transformation was observed to proceed by nucleation and growth process with third degree order reaction kinetics. The temporal growth of DO_3 domains size (ϵ) was found similar to the growth of grains in metals in the form $\epsilon = k t^n$ with $n = 0.3$ and $k = \text{a constant}$.

In another set of measurements [37] the growth of DO_3 order was studied in alloys formed by piston-anvil quenching technique to retain the disordered A2 phase. In this case the alloys, heat treated at 300°C to develop DO_3 order, showed the transient formation of B32 order during the early stages of ordering when the DO_3 ordered domains were small. After long time annealing the equilibrium DO_3 order developed. This was interesting because neither there is any B32 ordered region in the equilibrium phase diagram nor it was expected from the work of Richard and Cahn or Allen and Cahn [40] assuming predominating $1nn$ interaction over $2nn$ favouring alloying with unlike atom pairs (e.g. B2 or DO_3 order) preferred over like atom pairs (e.g. B32 order). This observation was interpreted as a kinetic effect dependent on the initial state of the as-milled alloys. The evolution of long-range order parameter (LRO) in Fe_3Al was studied at different temperatures and it was

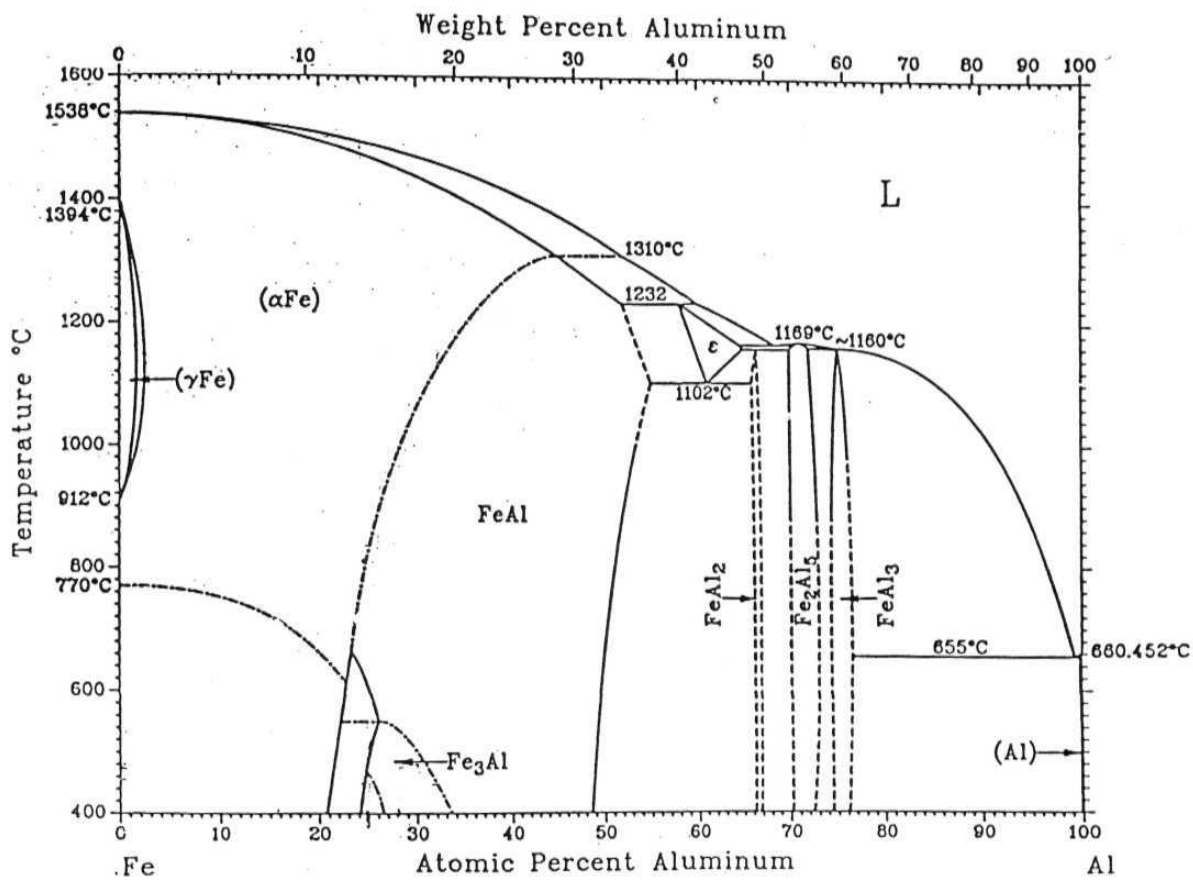


Figure 3.5 Thermodynamic equilibrium phase diagram
For Fe-Al alloy

Phase	Composition (at. % Al)	Structure	Prototype
αFe	0 to ~45	A2	W
FeAl	23.3 to ~55	B2	CsCl
Fe_3Al	~23 to ~34	DO_3	BiF_3

found that the LRO parameters for DO₃ order and B2 order developed at different rates depending on the temperature [49]. This was interpreted with the help of theoretical model calculations using the kinetic master equation in the point as well as the pair approximation formalism [49] and by Monte Carlo simulations [50]. Theoretical calculations for short-range order (SRO) parameter also showed transient B32 phase formation in agreement with the above experiments [49]. There was another report of observing B32 order in Fe-20 at. % Al, [51] but the heat treatment of the sample was not well controlled.

In the present work we study the ordering transformation behaviour of nanocrystalline Fe-Al alloys prepared by mechanical alloying in an initial disordered bcc state far from thermodynamic equilibrium. It is shown that the presence of small grain sizes and large grain boundary regions has a significant influence on order-disorder phase transformation. We find that in the nanophase Fe-Al alloys the development of ordered structures as well as the ordering kinetics are different as compared to the coarse grained microcrystalline alloys.

b Experimental

Fe_{1-x}Al_x (x=0.31 and 0.27) alloys were prepared by direct mechanical alloying of the elemental Fe (99.99 % + purity, fine gray powder from Aldrich-Sigma chemicals) and Al (Aluminum shot, 3.2 mm m3N5 from Ventron-Alfa division) metal powders. Fe contamination from the vial and the balls was found to be 2-3 atomic % from the chemical analysis of the as-milled alloy which gave rise to final composition of the as-milled alloys as Fe_{0.72}Al_{0.28} and Fe₃Al. The as-milled alloys were subjected to ordering heat treatments at 300° C and 450° C for various periods of times ranging from few tens to few hundred of hours. Powder XRD and Mossbauer spectroscopic techniques were

used to study the grain growth and order disorder phase transformation behavior of the alloy.

c Results and Discussion

Figure 3.6 shows the X-ray diffraction pattern of the as-milled Fe_3Al alloy. The X-ray spectrum shows the formation of single disordered bcc phase (A2) alloy. The average grain size estimated from the line width of the fundamental (110) line was about 10 nm. Similar results were obtained from the X-ray study of $\text{Fe}_{0.72}\text{Al}_{0.28}$ alloy. The Mossbauer spectra of the as-milled alloys are shown in figures 3.7 and 3.8 respectively for the 25 and 28 at. % Al alloys. These spectra are in excellent agreement with disordered Fe-Al alloys prepared by piston-anvil quenching [37]. The HMF distributions of the as-milled alloys as shown in figures 3.9-3.12 are also in good agreement with earlier reported results.

The HMF seen by Fe in Fe-X alloys was analyzed [ref 28 of chapter 2] in terms of the number of first and second neighbour solute atoms (X). The effect of the more distant neighbours was taken in terms of an average concentration dependence of all the fields. Ignoring the effect of second neighbours, which are very small in the Fe-Al system, the fields at Fe were found to be mainly dependent on the number of first neighbour Al atoms. The estimated fields for Fe atoms with different number of Al first neighbours are shown in figure 3.9.

The observed HMF distribution was fitted to a set of Gaussian functions centered at the field positions corresponding to different Al first neighbours configurations. The intensities of these Gaussian peaks corresponded very well to the probabilities of occurrence of these configurations as calculated using binomial distributions. This unambiguously shows that the initial state of the as-milled alloys is atomically disordered and the HMF assignments to different number of Al first nearest neighbour (1nn) are justified.

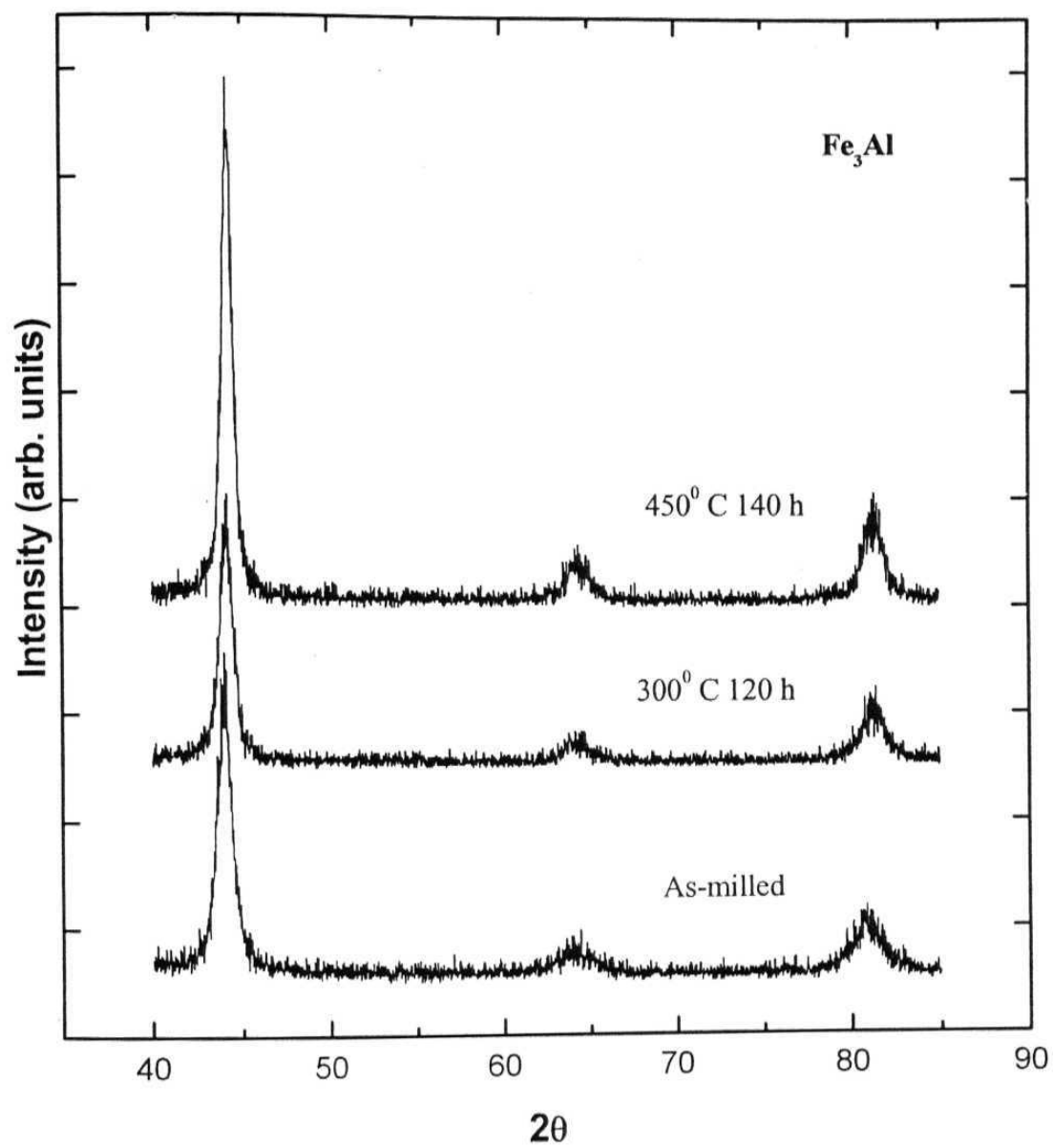


Figure 3.6: Typical X-ray diffraction patterns for as-milled and heat-treated Fe_3Al alloys.

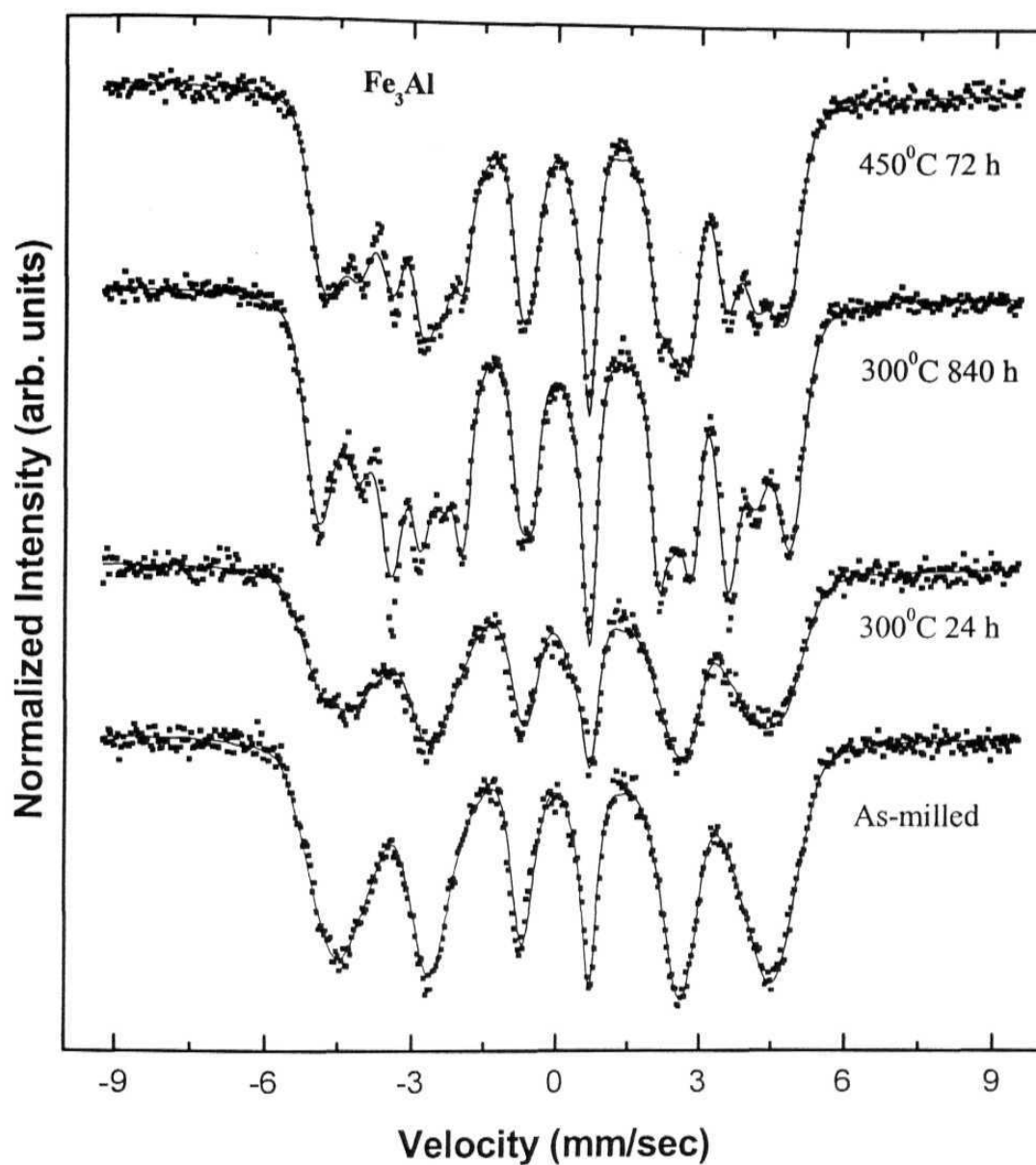


Figure 3.7: Representative Mossbauer spectra for the as-milled and heat treated Fe_3Al alloys and fits to data using model independent field distribution analysis (solid symbols: data, solid lines:fits).

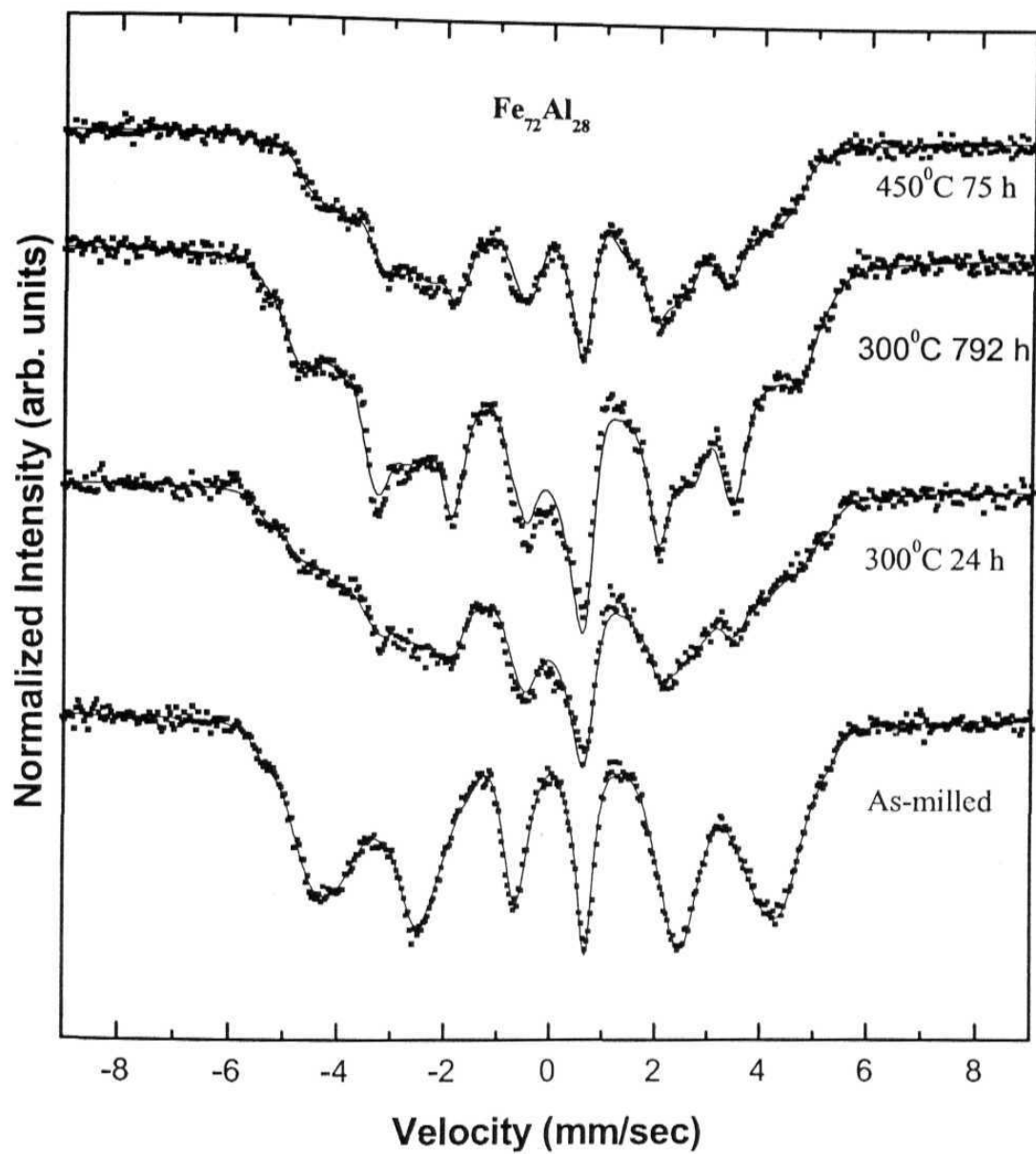


Figure 3.8: Typical Mossbauer spectra for the as-milled and heat treated $\text{Fe}_{0.72}\text{Al}_{0.28}$ alloys (solid symbols: data, solid lines: fits).

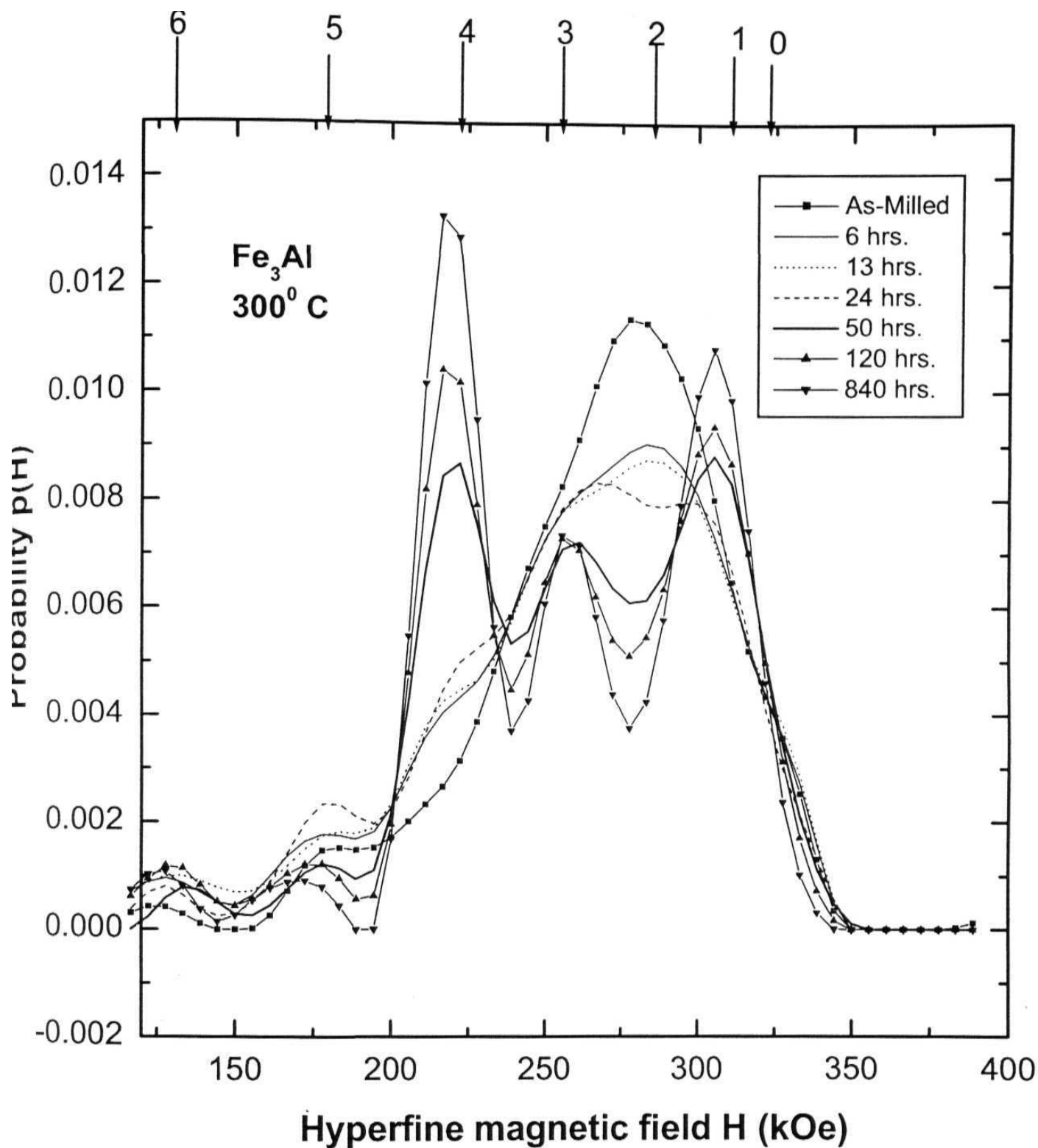


Figure 3.9: HMF distributions evaluated from the Mossbauer spectra of as-milled and 300°C heat treated samples for Fe_3Al stoichiometry alloy. The hyperfine field values of Fe atoms for different number of 1nn Al atoms are shown marked by arrows.

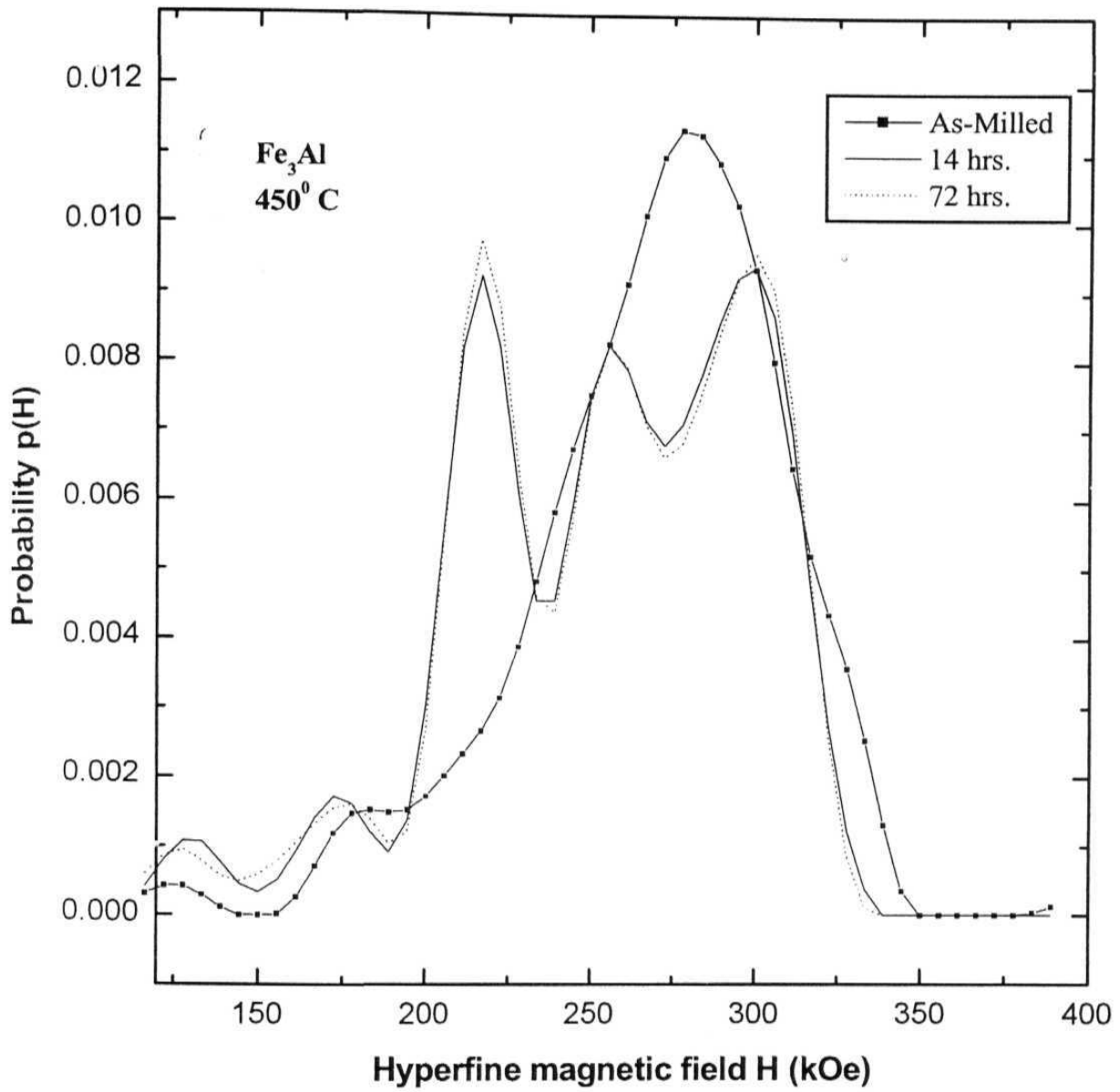


Figure 3.10: HMF distributions evaluated from the Mossbauer spectra of as-milled and 450 C heat treated sample of Fe Al composition alloy.

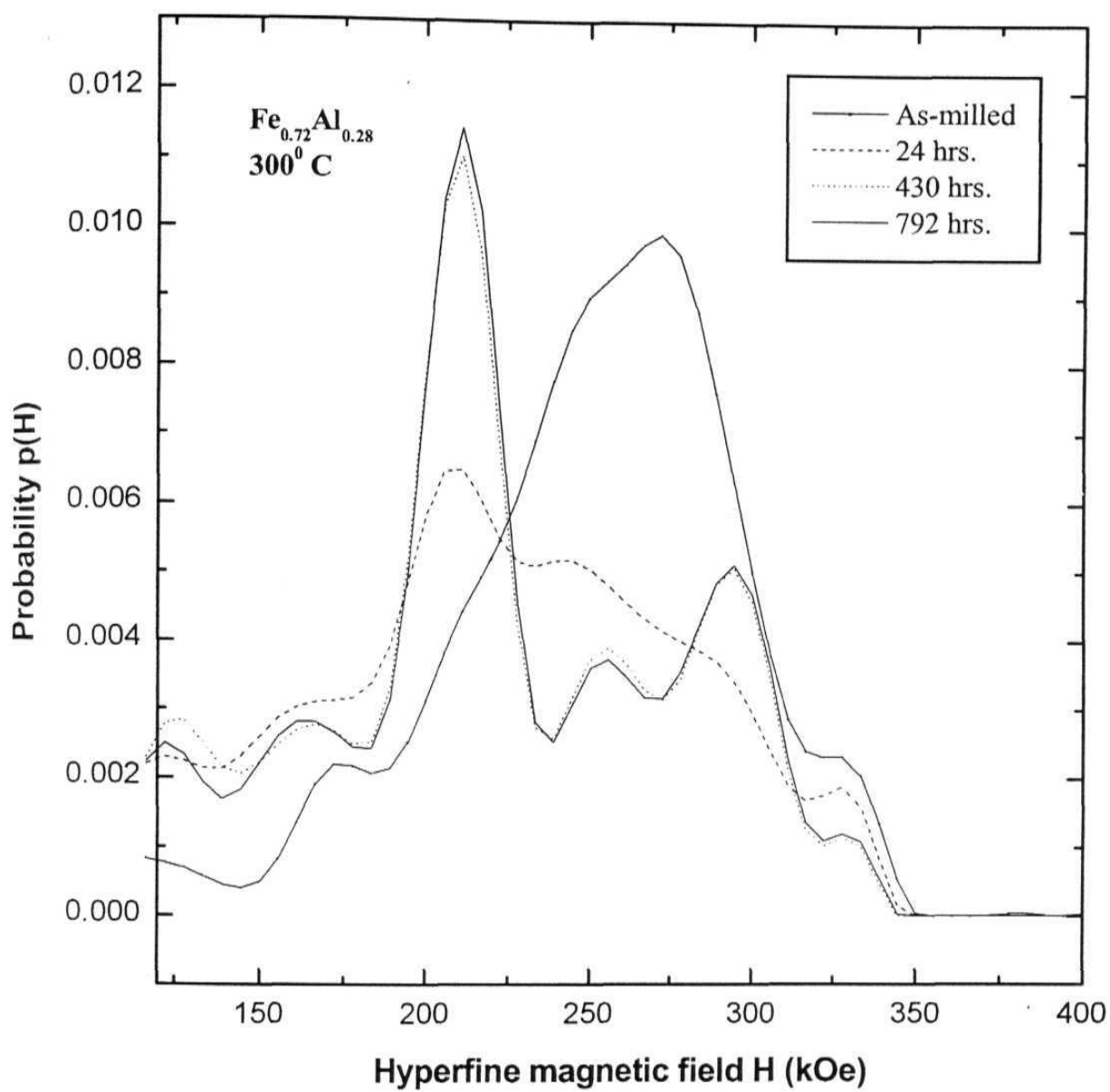


Figure 3.11: HMF distributions evaluated from the Mossbauer spectra of as-milled and 300°C heat treated sample of $\text{Fe}_{0.72}\text{Al}_{0.28}$ composition.

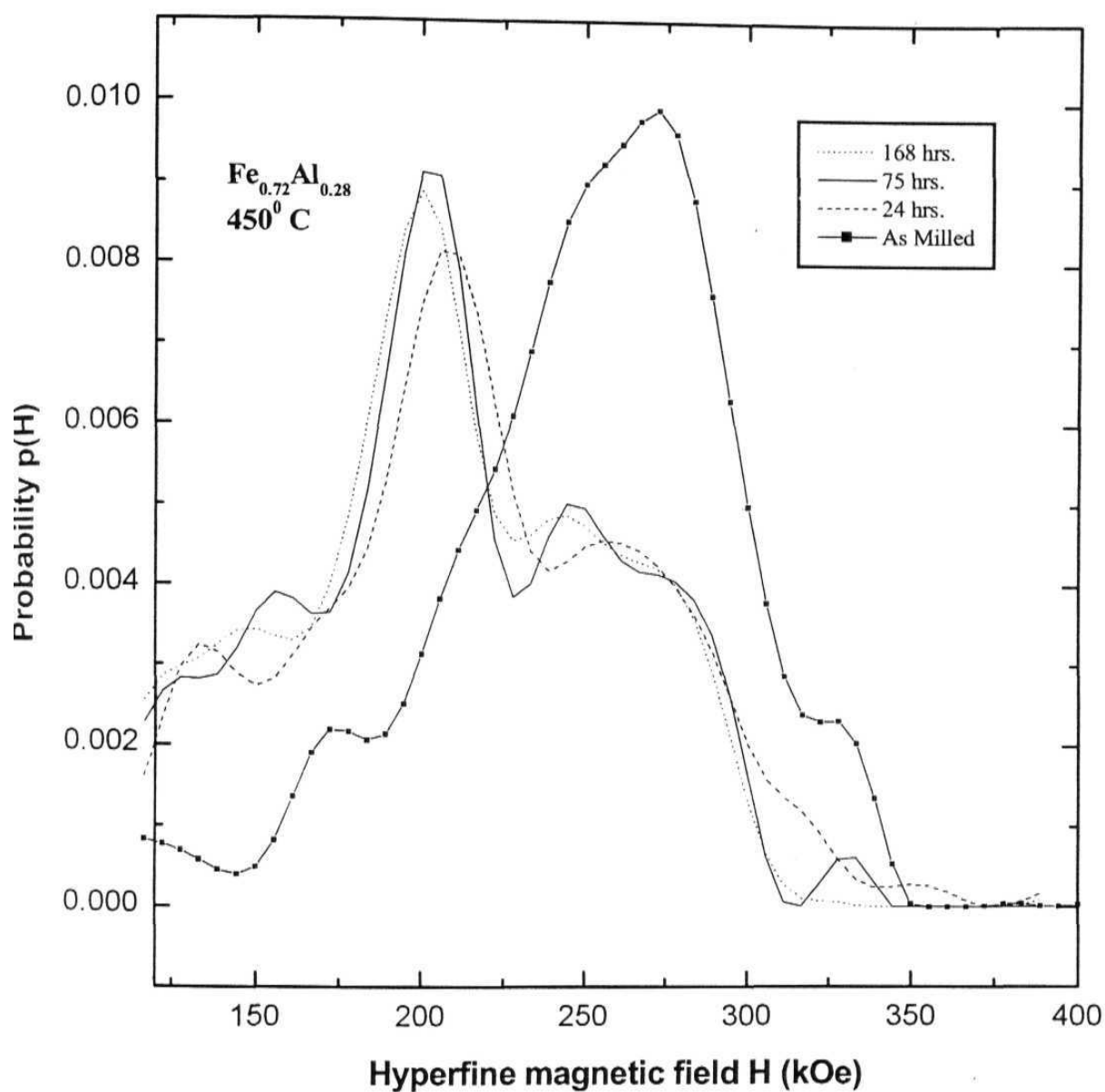


Figure 3.12: HMF distributions evaluated from the Mossbauer spectra of as-milled and 450°C heat treated samples of Fe-Al composition alloy,

The evolution of short-range order in the system is reflected in the change in intensities of the various peaks in the HMF distributions. Figures 3.9 to 3.12 show the evolution of the peaks of the as-milled alloys heat treated at 300° and 450° C for different periods of time. At 300° C the Fe₃Al composition alloy shows a rapid increase in intensities of the 0 and 4 Al neighbour peaks and a decrease in the intensities of 2 and 3 Al neighbour peaks (figure 3.13). As seen from figure 3.4 the 0 and 4 Al peaks correspond to the growth of DO₃ ordered phase. The probability of 2 and 3 Al neighbour configurations is high for B32 order and we see from the evolution of the intensities of these peaks that they saturate to a substantially high value after the initial fast decrease. For DO₃ order these intensities should be ideally zero. These observations show that there is a rapid growth of DO₃ order from the A2 matrix in the initial stages followed by the stabilization of B32 phase along with the DO₃ phase. However as seen from figure 3.4 the probability distributions for the disordered A2 and the B32 ordered phases are similar. To confirm the presence of B32 order, we plotted the kinetic path followed by the system in the space spanned by two order parameters [37]. Figure 3.14 shows such a plot wherein the intensity of the 0 Al 1nn peak is plotted against the intensity of the 4 Al 1nn peak. Also shown in the figure, are the calculated kinetic paths for DO₃ order alone, for (50% DO₃ + 50% B32) order and for (50% DO₃ + 50% B2) order assuming that the growth of a region of ordered structure occurs at the expense of the disordered A2 structure. The slope of these paths is given by

$$m = \Delta p(0) / \Delta p(4) \quad (3.5)$$

where $\Delta p(j)$ is the change in the probability of Fe atoms with j Al atoms in their 1nn shell, w.r.t the probability in the disordered structure:

$$\Delta p(j) = f_{DO3}[p_{DO3}(j) - p_{A2}(j)] + f_{B2}[p_{B2}(j) - p_{A2}(j)] + f_{B32}[p_{B32}(j) - p_{A2}(j)]$$

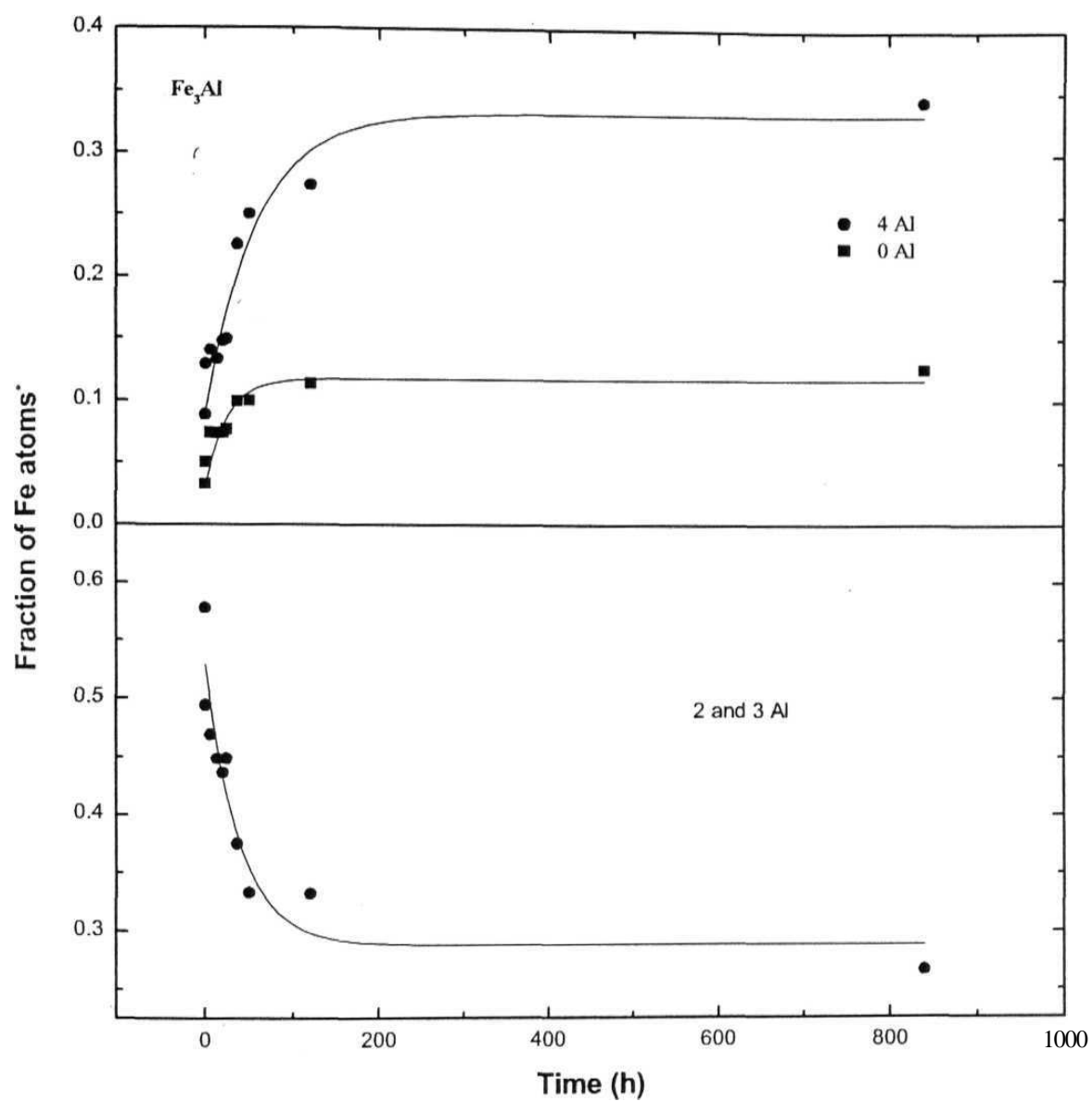


Figure 3.13: Temporal evolution of fraction of Fe atoms with 0, 4, and (2+3) first near neighbour Al atoms at 300° C (symbols: experimental fractions evaluated from the HMF distributions; solid lines: fits to data using Eq. (3.11)).

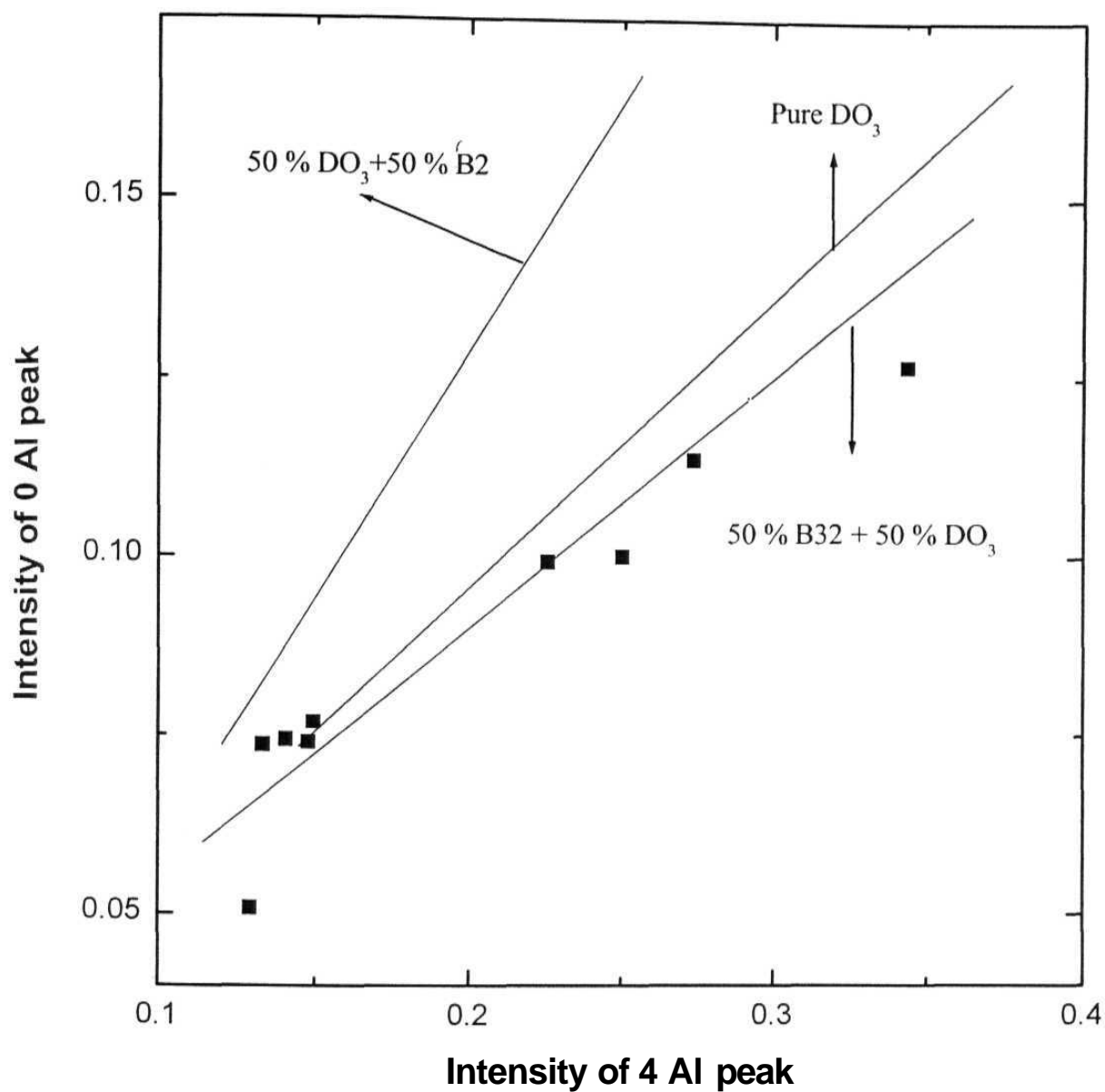


Figure 3.14: Kinetic path at 300° C for the Fe_3Al alloy showing the evolution of the 0 Al vs. 4 Al 1nn peaks. Also shown in the figure (solid lines) are the calculated paths assuming growth of pure DO_3 order, (50% DO_3 + 50% B2) order, and (50% DO_3 + 50% B32) order from the disordered A2 matrix.

where f_{DO3} , f_{B2} , and f_{B32} are the fractions of the three ordered structures that grow from the disordered A2 structure, and

$$f_{\text{DO3}} + f_{\text{B2}} + f_{\text{B32}} + f_{\text{A2}} = 1 \quad (3.7)$$

because $p_{\text{DO3}}(j)$, $p_{\text{B2}}(j)$, $p_{\text{B32}}(j)$, and $p_{\text{A2}}(j)$ are constants, the slope of the kinetic path depends only on the fractions (f) of these structures.

As seen from figure 3.14 there is a growth of DO3 order initially followed by an admixture of both DO₃ and B32 ordered phases. Essentially a similar behaviour is observed for the Fe₇₂Al₂₈ alloy heat treated at 300° C (figure 3.15) and for both the alloys heat treated at 450° C (figures 3.16 and 3.17) except that the 0 Al peak is not resolved from the 1 Al peak. It was not possible to make a plot of the kinetic path similar to the one shown in figure 3.14, in these cases, as the intensity of the 0 Al peak is very small and large errors are observed in the fits to the field distributions using Gaussian peaks at the field value corresponding to the 0 Al configuration. This can also be attributed to the presence of more B32 ordered phase, which results in larger intensity of 1 Al 1nn peak as compared to 0 Al 1nn peak.

A comparison of the behaviour of nanocrystalline Fe-Al alloys with that of coarse-grained Fe-Al alloys prepared by piston-anvil quenching [37] shows that for the nano- grained alloy there is no transient B32 phase formation but a rapid growth of DO3 order directly. This can be attributed to the fast diffusion paths provided by the grain boundary regions. The growth of DO3 ordered regions could however extend only up to the size of the nanocrystalline grains. Davies [52] also observed that in fine-grained cold rolled Fe-Al alloys the DO3 domains stopped growing beyond the grain size of 15 nm. In our nanocrystalline alloys the grain growth as shown in figures 3.18 and 3.19 is very small and saturates to a maximum size of about 15 nm. This also explains the presence of substantial B32 order in later stages of the transformation. The

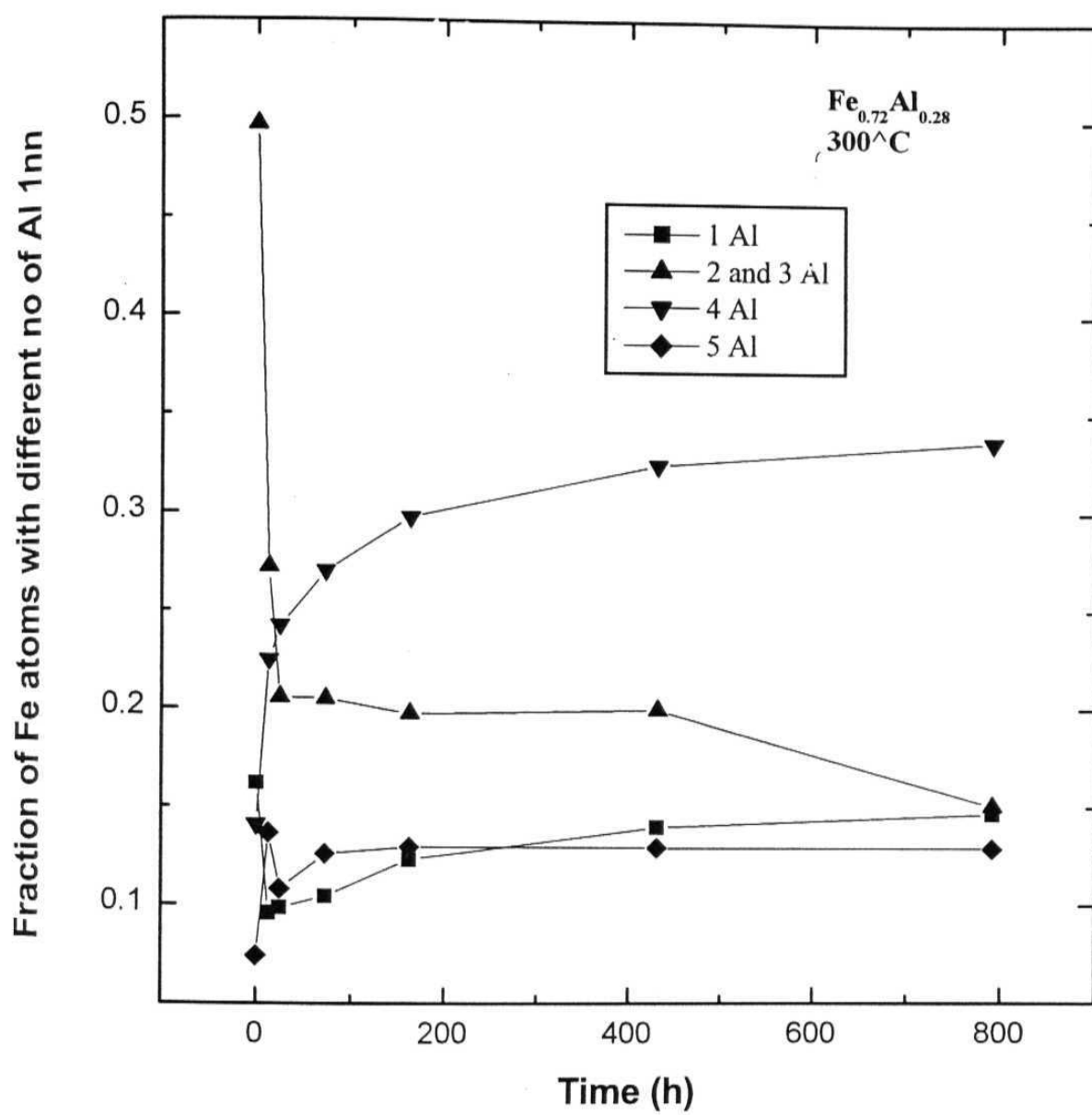


Figure 3.15: Temporal evolution at 300 C of fraction of Fe atoms with different number of 1nn Al atoms for the Fe_{0.72}Al_{0.28} alloy system.

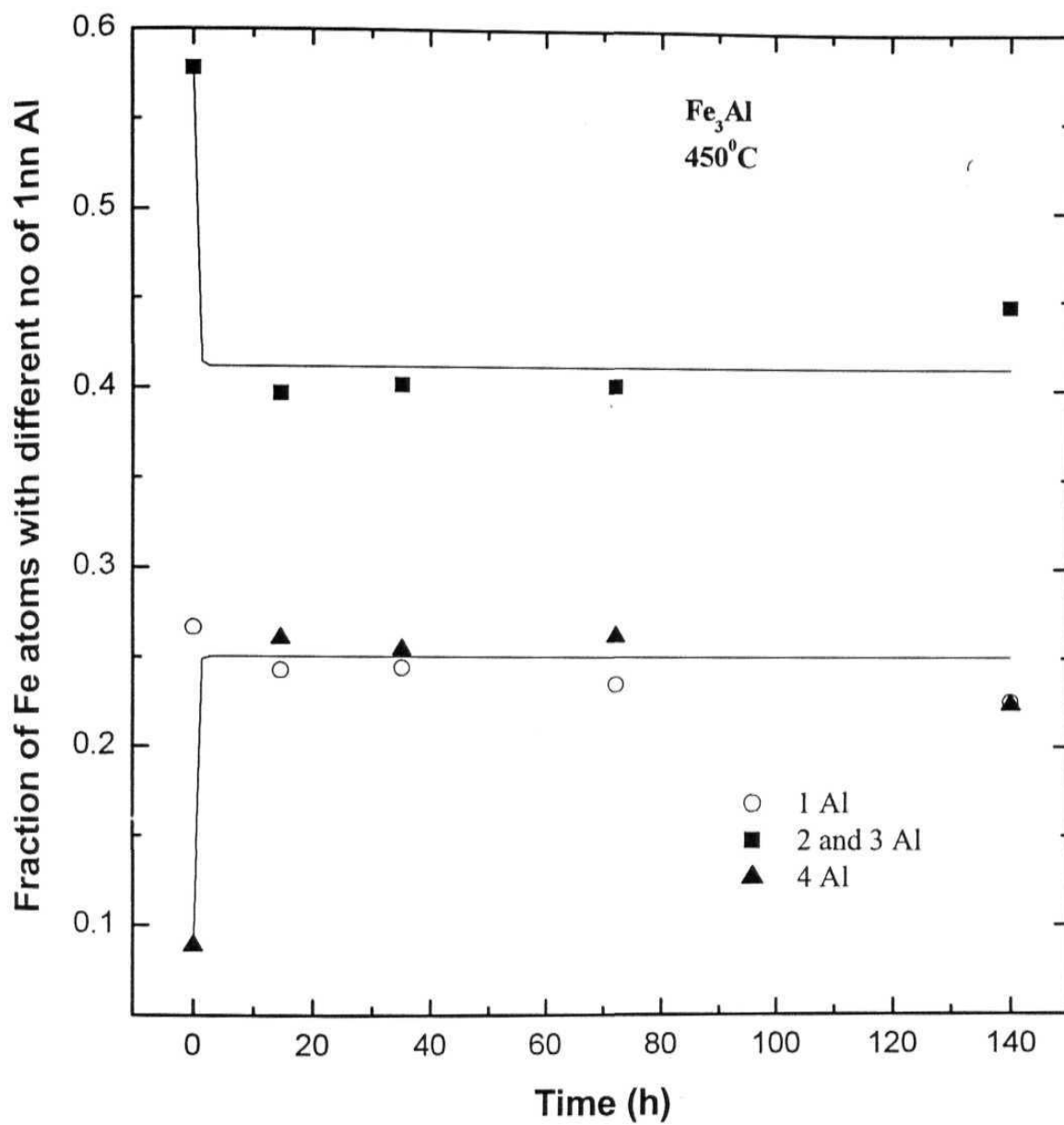


Figure 3.16: Temporal evolution at 450°C of fraction of Fe atoms with 1, 4, and (2+3) 1nn Al atoms for Fe_3Al (symbols: experimental fractions; solid lines: fit).

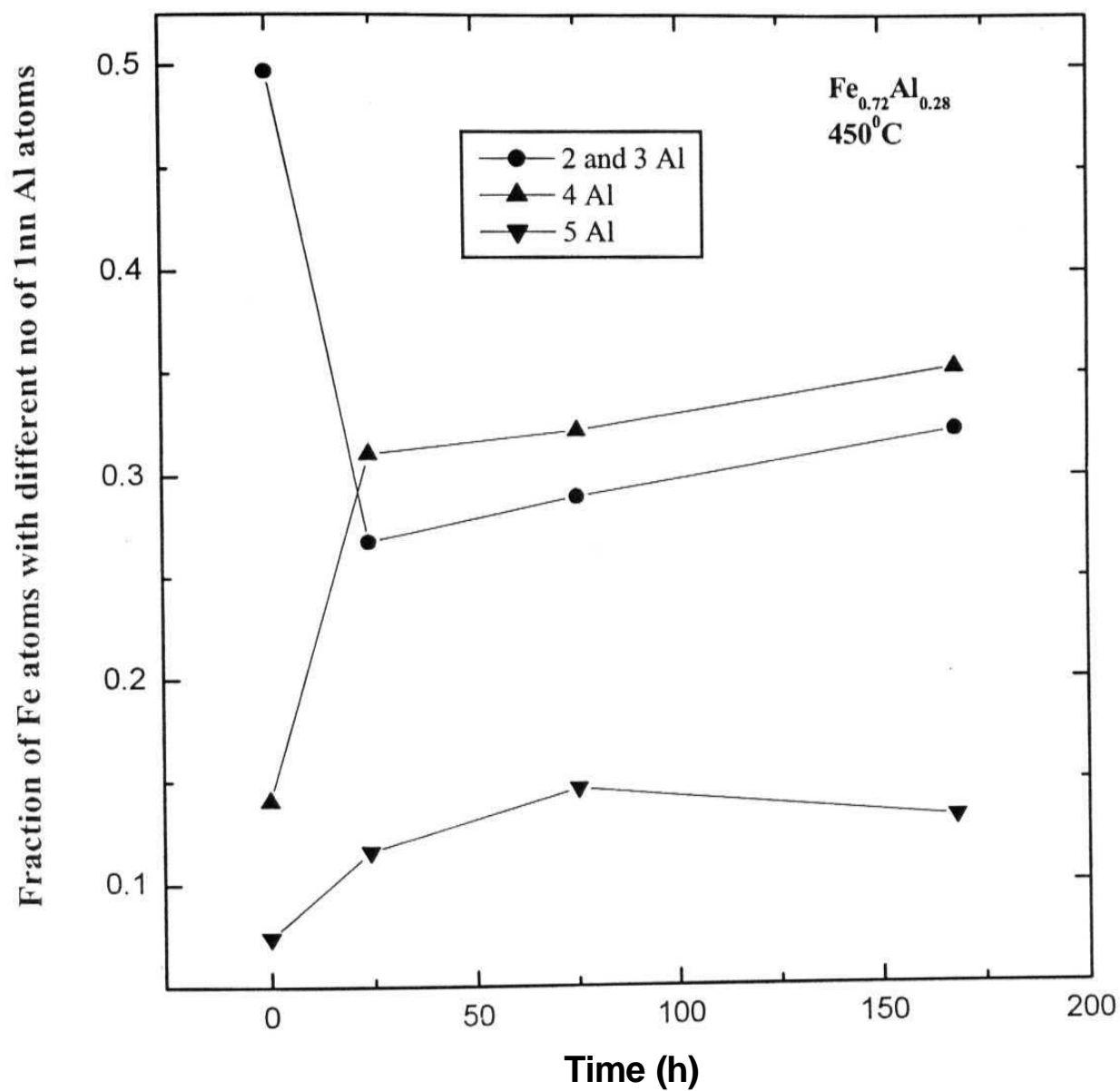


Figure 3.17: Temporal evolution at 450° C of fraction of Fe atoms with different number of 1nn Al atoms for the Fe_{0.72}Al_{0.28} alloy system.

B32 ordered regions are possible to arise in the anti-phase domain boundary (APDB) regions between DO₃ ordered domains [ref 194 of chapter 1]. This was also the explanation given for the transient formation of B32 order between small DO₃ ordered domains (approximately 3 nm) which grew initially in the coarse grained alloy [37]. In the nanophase alloy the maximum growth of DO₃ domain size is limited by the grain size and the grain boundary regions also constitutes the B32 ordered APD boundaries for the system.

Figures 3.20 and 3.21 show the kinetic evolution of the short range order parameter, $S(4)$, defined in terms of the intensities $p(4)$ of the 4 Al 1nn peaks, as follows:

$$S(4) = [p_{\text{expt}}(4) - p_{\text{disord}}(4)] / [p_{\text{DO}_3}(4) - p_{\text{disord}}(4)] \quad (3.8)$$

where $p_{\text{expt}}(4)$ is the experimentally observed intensity, $p_{\text{disord}}(4)$ is the intensity for the disordered alloy calculated from the binomial distribution, $p_{\text{DO}_3}(4)$ is the intensity for fully ordered alloy. The kinetics of order evolution in an alloy system can be treated in terms of the model proposed by Khachaturyan [53], which relates the kinetics of the transformation to the thermodynamics. According to this model the temporal rate of change of order parameter, $r|(t)$, is assumed proportional to the sensitivity of the Gibbs free energy change w.r.t the order parameter:

$$\frac{d\eta(t)}{dt} = - \frac{L}{kT} \frac{dG(\eta)}{d\eta} \quad (3.9)$$

where L is a mobility factor which depends on the kinetic mechanism of ordering. Expanding $G(r|)$ in a Taylor series about equilibrium, $\eta = \eta_{\text{eq}}$, and retaining only terms up to second order derivative of G ($\frac{dG}{d\eta} = 0$ at $\eta = \eta_{\text{eq}}$) one

gets

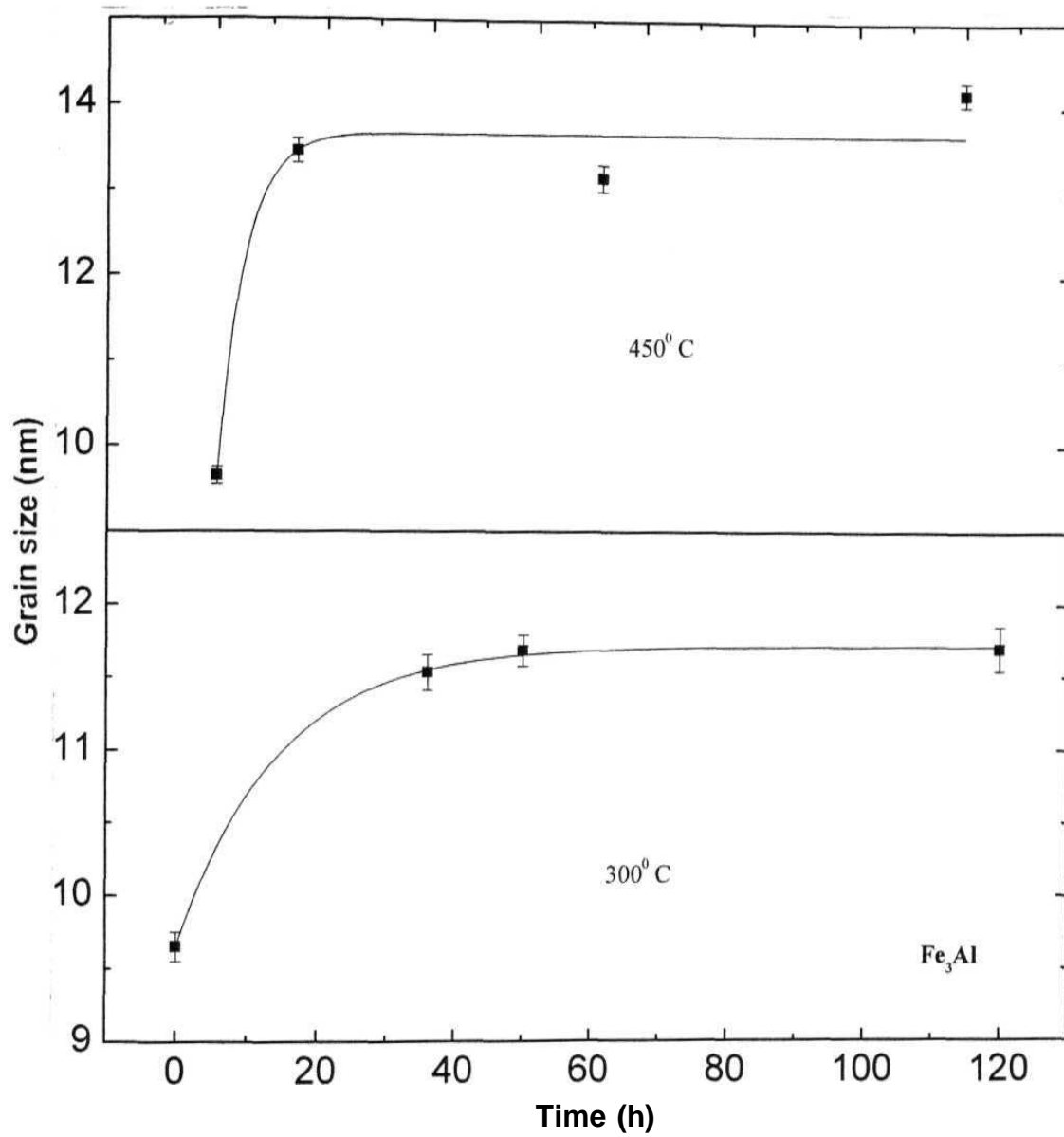


Figure 3.18: Grain growth kinetics at 300°C and 450°C for the Fe_3Al alloy. (Symbols: experimental grain size; solid lines: fits to data as explained in text).

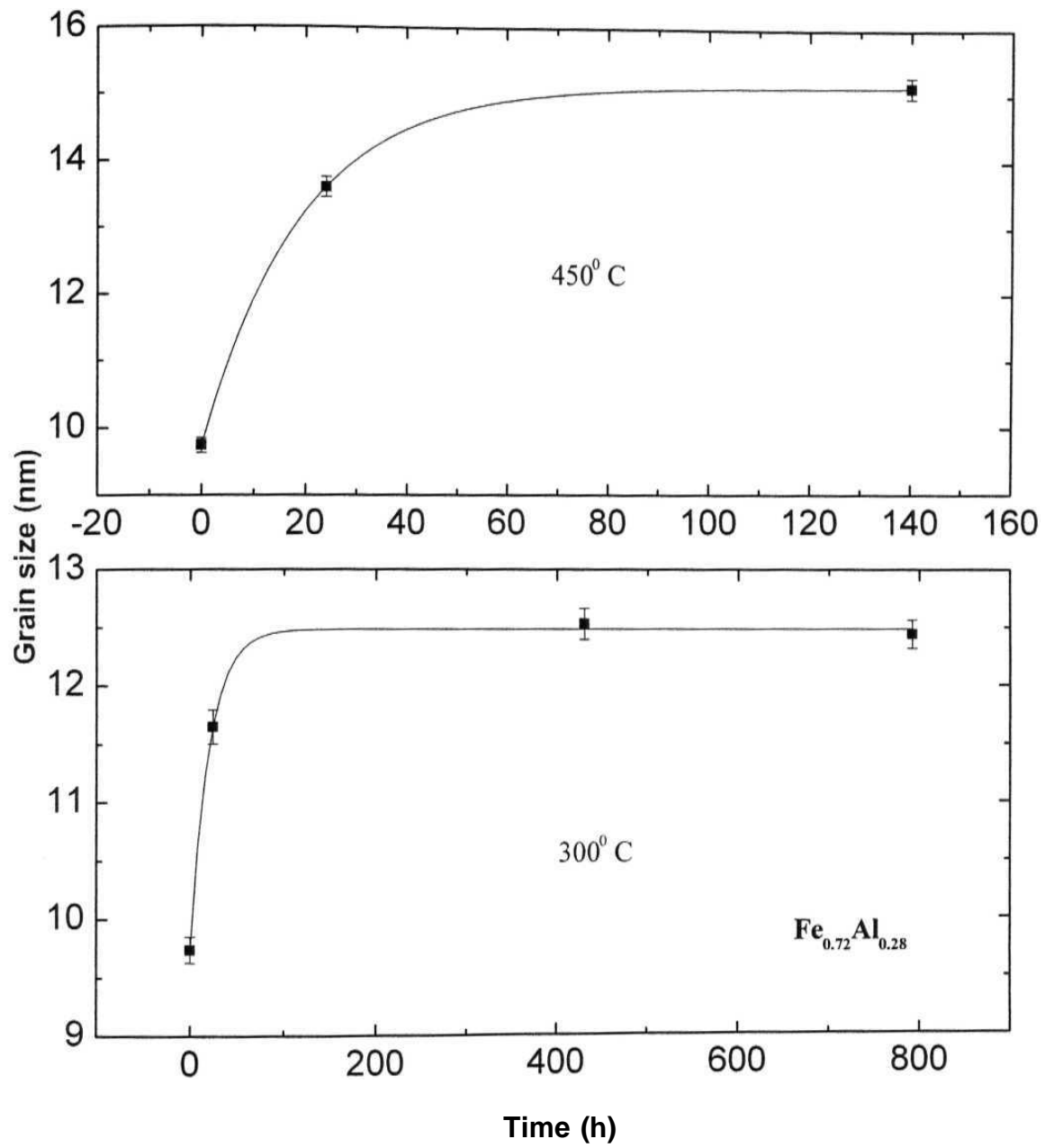


Figure 3.19: Grain growth kinetics at 300° and 450°C for the $\text{Fe}_{0.72}\text{Al}_{0.28}$ alloy (symbols:exp; solid line: fit using Eq. (3.11)).

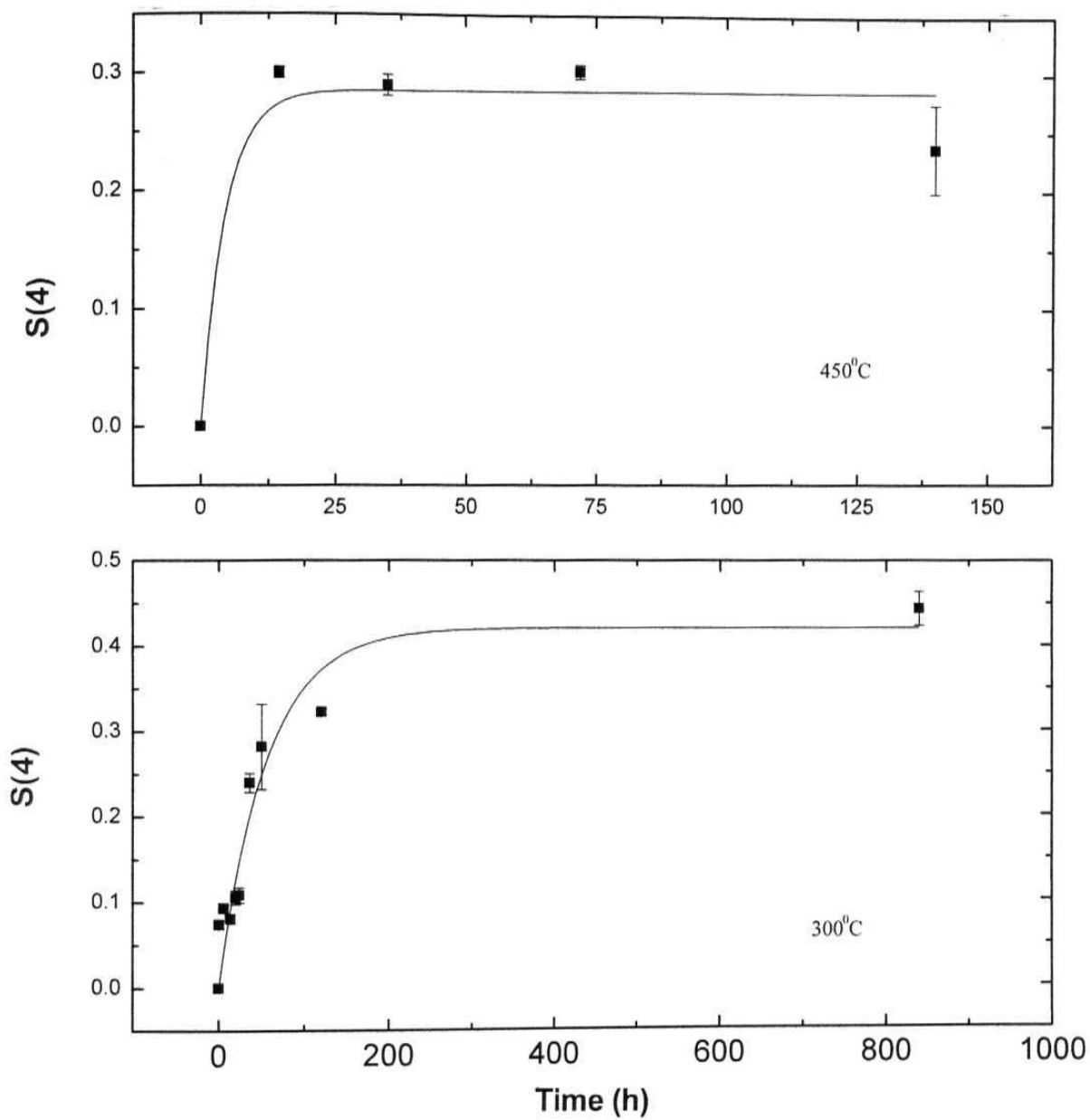


Figure 3.20: Evolution of the short-range order parameter, $S(4)$, with time at 300°C and 450°C for the Fe_3Al alloy (symbols:exp, solid lines:fits).

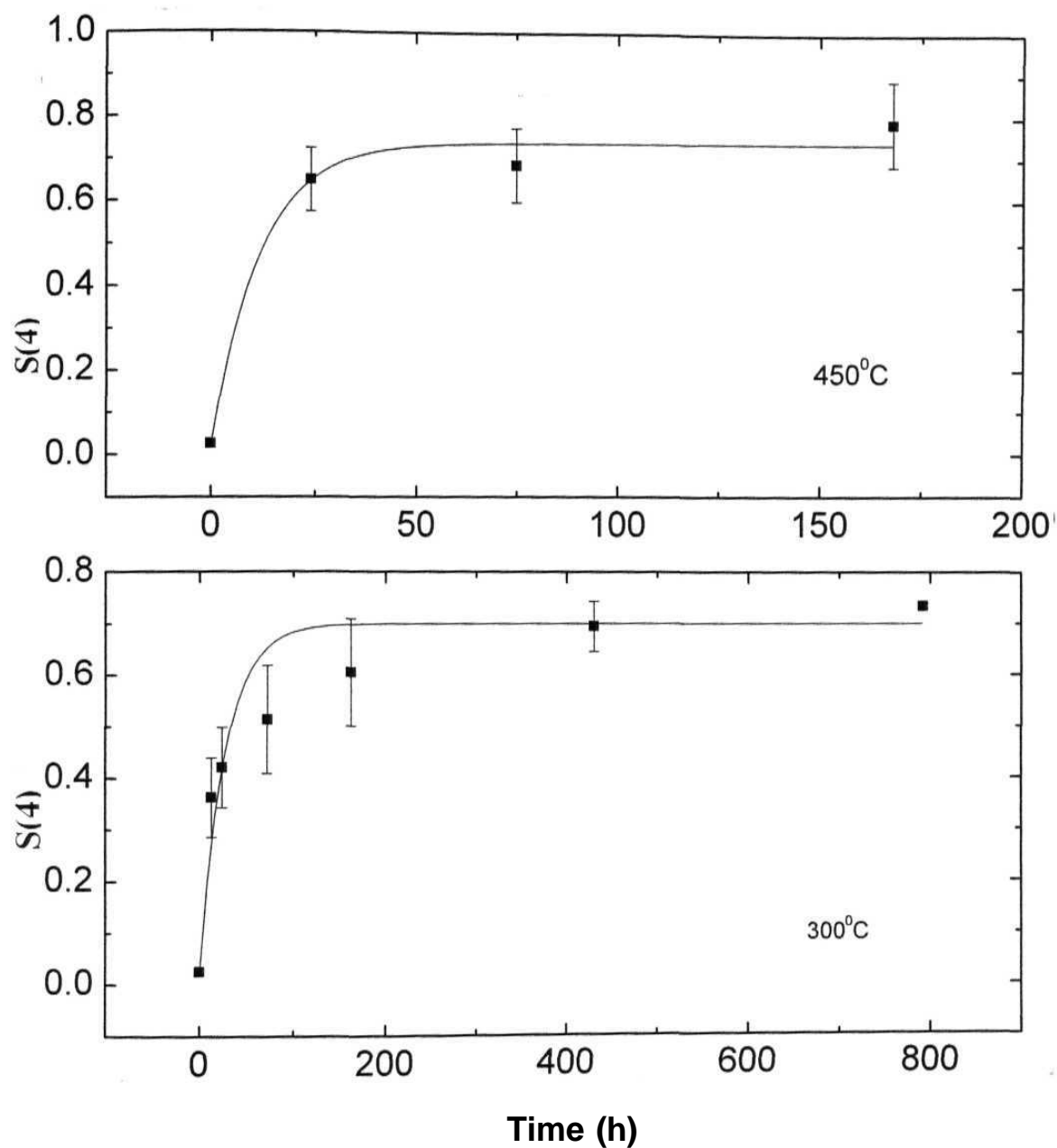


Figure 3.21: Evolution of short range order, $S(4)$, with time at 300°C and 450°C for the Fe-Al alloy (symbols:expt; solid line:fit using Eq. (3.11)).

$$\frac{d\eta(t)}{dt} = -A(\eta - \eta_{eq})$$

where

(3.10)

$$A = \frac{L}{kT} \left(\frac{d^2G}{d\eta^2} \right)_{\eta = \eta_{eq}}$$

The solution of this equation is

$$\eta(t) = (\eta_0 - \eta_{eq}) \exp(-At) + \eta_{eq} \quad (3.11)$$

where η_0 is the order parameter at time $t = 0$

The fits to the S(4) data using this equation (with $\eta = S(4)$) are also shown in figures 3.20 and 3.21. The parameters obtained from the fits are shown in Table 1. As seen from the table the ordering relaxation time ($1/A$) is small at higher temperature as expected. The equilibrium order parameter reached is seen to be less than unity. This also reflects the presence of residual B32 order as mentioned earlier. Another important point to note is that in polycrystalline coarse grained alloys the B2 \rightarrow DO₃ transformation was found to proceed as a third order reaction [46] whereas our equation to describe the order evolution corresponds to a first order reaction. This indicates that the ordering mechanism in the nanocrystalline alloys is different from the coarse grained alloys due to the presence of extensive grain boundary regions. As observed in our measurements on kinetics of ordering in nanophase FeCo-X alloys [in section 3.3] the grain boundary regions provide short circuited diffusion paths which give rise to faster diffusion relative to coarse grained systems.

The kinetics of grain growth as shown in figures 3.18 and 3.19 also do not follow a conventional curvature driven grain growth mechanism as observed for bulk systems. Interestingly the grain growth behavior in our system could also be fitted to equation (3.11) with η replaced by average grain size. This is not totally unexpected because the mechanism of grain growth as well as atomic ordering may be the same viz. diffusion through grain

boundaries. Such correlation between grain growth and chemical ordering was also observed in nanocrystalline $\text{Fe}_{3-x}\text{Mn}_x\text{Si}$ alloys [54] where the chemical ordering was seen to influence the grain growth behavior significantly. It was observed in these alloy systems that the atomic order proceeded very rapidly and this resulted in impeding of grain growth and once atomic ordering took

Table 1

Values of different order parameters and relaxation times obtained by fitting the $S(4)$ data of figures 3.20 and 3.21 to Eq. (3.11).

Alloy Stoichiometry	Temperature	Order parameter, $S(4)$, at time $t = 0$	Equilibrium order parameter, $S(4)$, attained	Ordering relaxation time ($1/A$) (h)
Fe_3Al	300° C	0.0	0.42	56
	450° C	0.0	0.28	4.5
$\text{Fe}_{0.72}\text{Al}_{0.28}$	300° C	0.02	0.68	27
	450° C	0.02	0.72	12

place there was no further growth of grains.

It is relevant to mention here that we have assumed a fixed mobility factor (L) in Eq. (3.9), instead of a time varying L due to change in vacancy and defect concentration during annealing, i.e. a linear response theory, to analyze the temporal evolution of $S(4)$ and grain growth. We feel this assumption is justified because in these nanocrystalline systems the atomic diffusion is taking place through grain boundary regions occupying a large volume fraction as compared to the coarse-grained materials. This grain boundary diffusion gives rise to large L and therefore the change in L with time due to change in concentration of defects and vacancies with annealing time is

expected to be only a small perturbation and hence this assumption of constant mobility factor is valid.

In conclusion we observed that the nanophase nature of the Fe_3Al alloys influenced the atomic order evolution as well as the kinetics of the ordering process very significantly. The observed behaviour was attributed to the nano size of the grains and the grain boundary regions in these nanocrystalline alloy systems.

3.1.2 Fe-Ge System

a Introduction

The disorder-order phase transformation in Fe-Ge alloy system is also equally interesting similar to Fe-Al system. The phase diagram of Fe-Ge alloy system is shown in figure 3.22 [43]. There are various phases present with different Ge concentrations and temperature ranges. At low temperatures (up to 400°C), the equilibrium phase for Fe_3Ge composition is a two-phase mixture ($\alpha_1 + \beta$); while at higher temperatures it assumes an ordered closed-packed structure (fcc at temperatures below 700°C , and hcp at temperatures above 700°C). Because of these diverse phase structures, Fe-Ge system was of interest for various phase transformation studies [55-61, ref 171 of chp I]. The large regions of DO_3 order at low Ge concentrations ($\sim 10\text{-}20$ at.%), and the high critical temperature for the DO_3 ordered structure (up to the melting point), imply that there is a strong tendency of ordering for this alloy. In fact this aspect of Fe-Ge phase diagram in comparison to that of Fe-Al (figure 3.5) implies that the interatomic interactions favouring order in Fe_3Ge are stronger than in Fe_3Al . In this section we will discuss the ordering transformations in this system in the nanocrystalline state below 400°C . In chapter 6 the massive structural transformation from disordered bcc \rightarrow ordered fcc (L1_2) phase at temperatures above 400°C will be discussed.

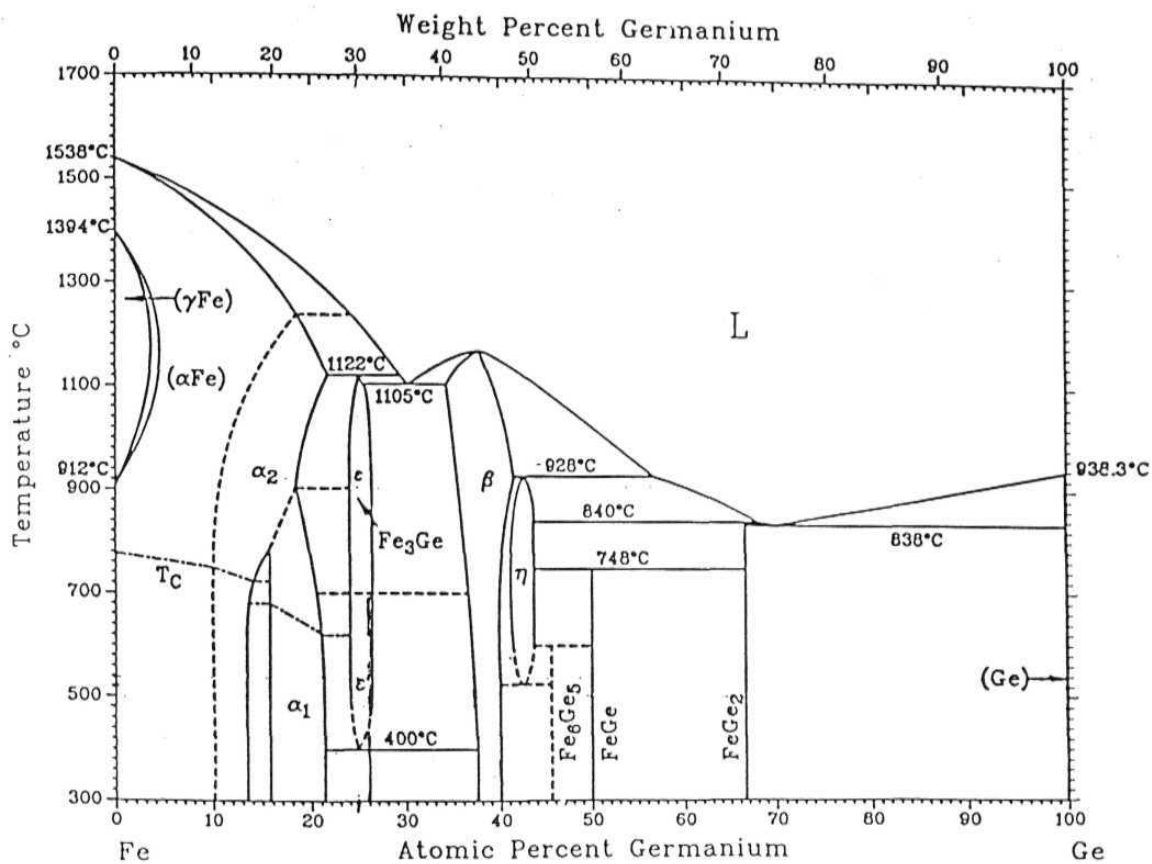


Figure 3.22 Thermodynamic equilibrium phase diagram
For Fe-Ge alloy

Phase	Composition (at. % Ge)	Structure	Prototype
αFe	0 to 17.5	A2	W
α_1	15.2 to 21.0	DO ₃	BiF ₃
ϵ' (Fe ₃ Ge)	23.7 to 25.7	L1 ₂	AuCu ₃
β	33.5 to 41.0	B8 ₁	NiAs

b Experimental

$\text{Fe}_{1-x}\text{Ge}_x$ alloys in the composition range $0.17 < x < 0.39$ were prepared by mechanical alloying of elemental Fe and Ge powders of 99.99%+ purity (Aldrich-Sigma Chemicals). The Fe contamination due to ball milling was typically about 1 to 2 atomic percent as determined by EDAX and chemical composition analysis.

c Results and Discussion

Figures 3.23 and 3.24 show the X-Ray diffraction patterns for the as-milled alloys with compositions close to Fe_3Ge , and $\text{Fe}_{0.83}\text{Ge}_{0.17}$ respectively. All the lines are indexed to disordered bcc (A2) phase. The average grain size obtained for the samples near Fe_3Ge stoichiometry was approximately 6.0 nm, The grain size of the as milled $\text{Fe}_{0.83}\text{Ge}_{0.17}$ was found to be approximately 8.3 nm. The Mossbauer spectra of the above as-milled samples are shown in figure 3.25 and the corresponding probability distributions are shown in LHS of figure 3.26; the calculated probability distributions using equation 3.1 is shown in the RHS of figure 3.26. Very good agreement between these experimental and calculated probability distributions confirms the formation of the as-milled alloys in the A2 phase, which is also supported by the XRD results. The field distributions were in good agreement with those of disordered Fe_3Al prepared by piston and anvil quenching [37], disordered Fe_3Si prepared by milling of Fe and Si [ref 26 of chp 2] and for Fe-22 At. % Ge deposited on quartz substrate by ion beam sputtering [ref 26 of chp 2]. The formation of only disordered bcc (α) phase in the as milled alloys for $x=0.17$ and ~ 0.25 composition, in spite of the fact that at these compositions either pure DO_3 or $\text{DO}_3 + \text{B81}$ phases should stabilize according to the phase diagram, therefore implies that ball milling inhibits the formation of hexagonal (β) phase and favours only the development of the bcc structure with anti-site disorder [ref 6 of chp 1]. The

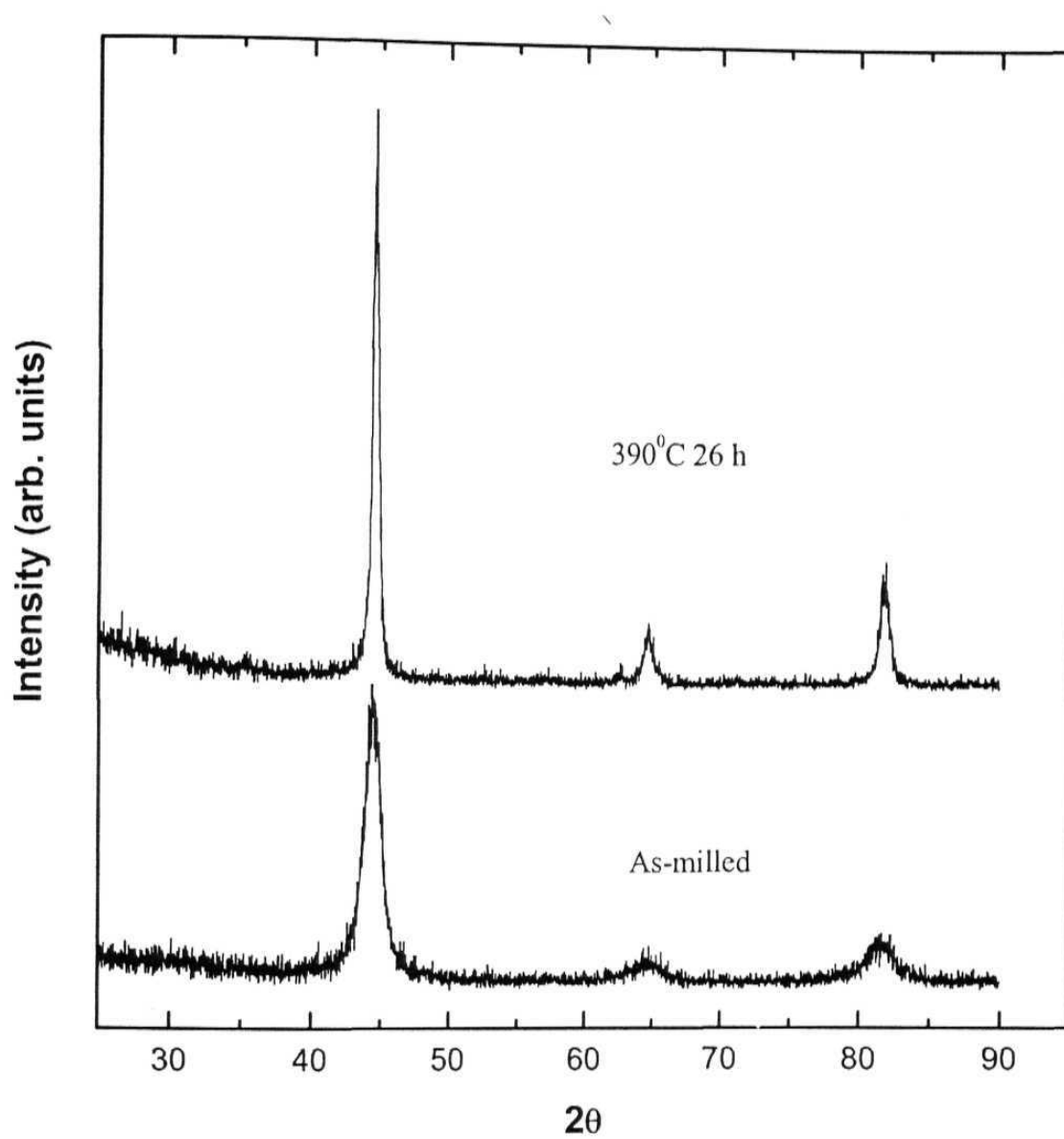


Figure 3.23: Representative X-ray diffraction patterns of the as-milled and heat treated samples with $\sim\text{Fe}_3\text{Ge}$ composition.

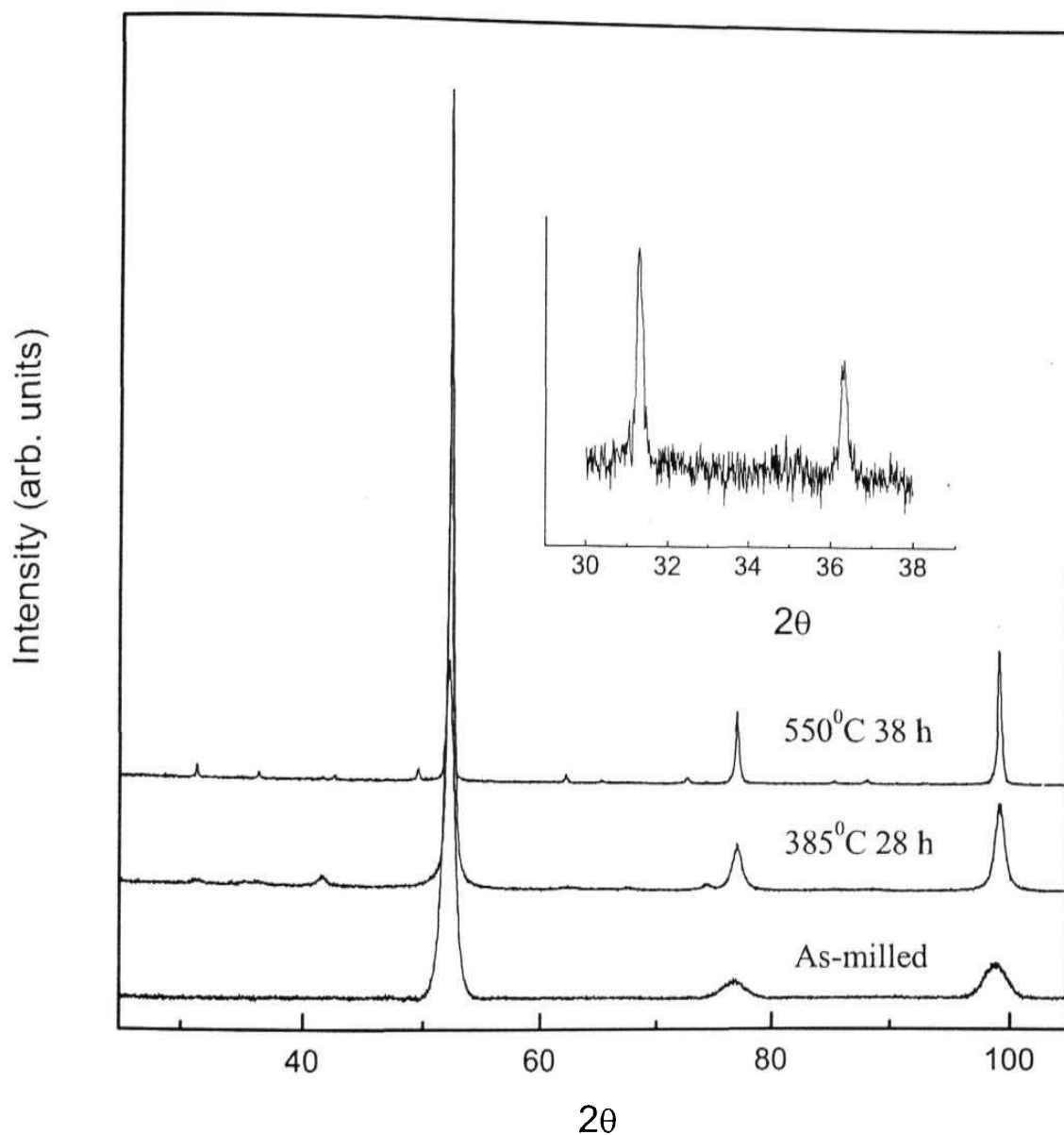


Figure 3.24: X-ray diffraction patterns recorded using INEL CPS 120 diffractometer for as-milled and heat treated samples with $\text{Fe}_{0.83}\text{Ge}_{0.17}$ composition. The formation of the alloy in a phase and the ordering to DO_3 order upon heat treatment is evident from the patterns. The presence of superlattice lines are seen (shown separately in the inset). Growth of bcc grains is indicated by the decrease of FWHM of the lines.

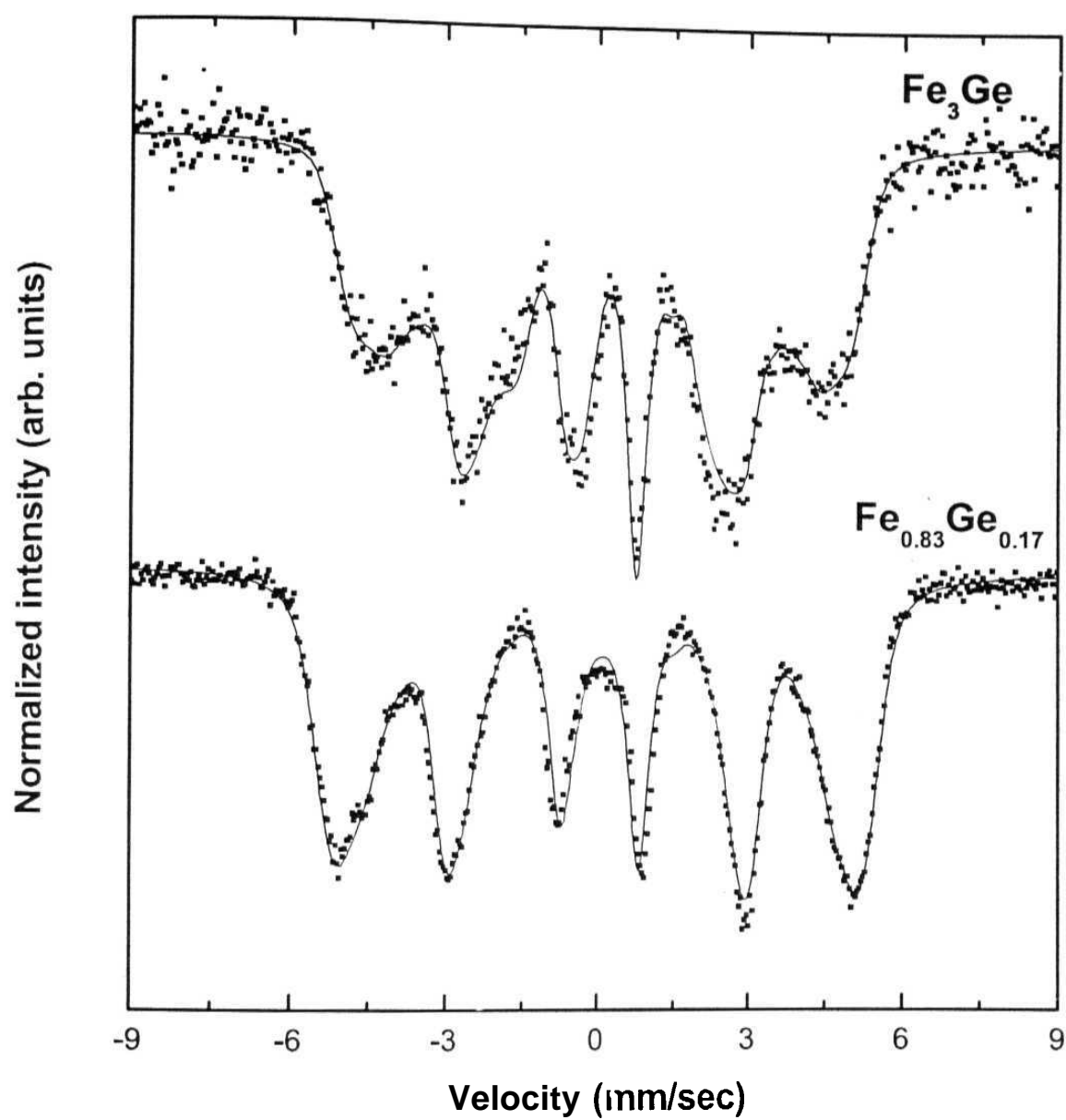


Figure 3.25: Experimental (symbols) and fitted (lines) Mossbauer spectra of the as-milled Fe-Ge alloys with compositions indicated.

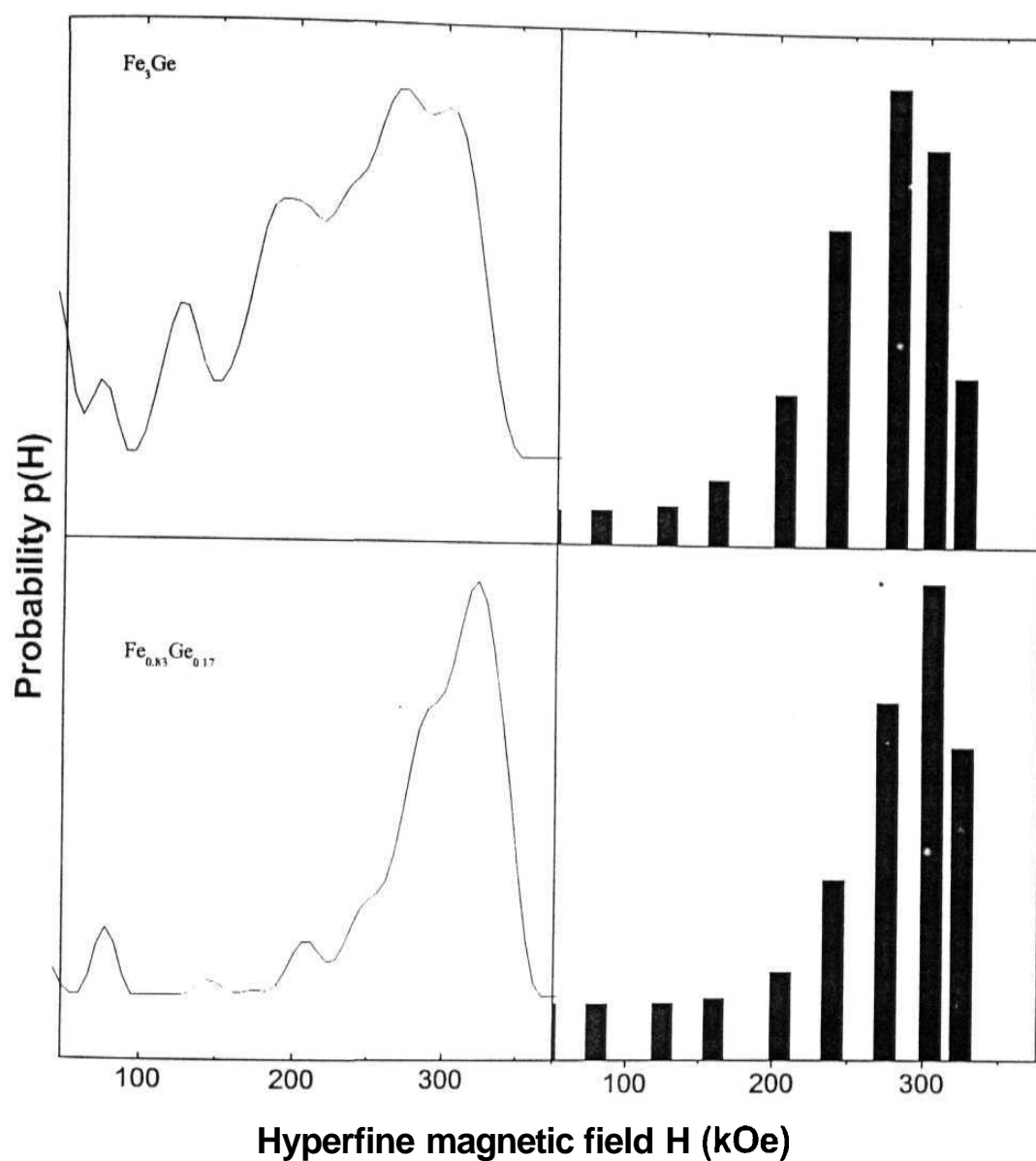


Figure 3.26: HMF distributions evaluated from the Mossbauer spectra of figure 3.25 are shown in LHS. The corresponding calculated probability distributions using Eq. (3.1) are shown in RHS. The analogy between the experimental and the calculated probability distributions shows the formation of the alloy in a phase.

observed increase in lattice constant by 0.2-0.4 % on disordering indicates that anti-site disordering is taking place.

The samples were subjected to heat treatments at 350° C, 375° C and 390° C for periods of time ranging from few hours to few hundreds of hours to see the formation of the equilibrium phases as expected from the phase diagram [figure 3.22]. $\text{Fe}_{0.83}\text{Ge}_{0.17}$ alloy was also heat treated at 550° C to see the evolution of DO_3 ordered phase. Representative XRD patterns from the heat-treated samples are shown in figures 23 and 24. Evolution of only ordered bcc phase is indicated in the XRD patterns. Typical Mossbauer spectrum is shown in figure 2.8. LHS of figure 3.27 and figure 3.28 show the probability distributions evaluated from the Mossbauer spectra of heat treated $\text{Fe}_{0.83}\text{Ge}_{0.17}$ and $\sim\text{Fe}_3\text{Ge}$ alloys. The probability distributions of the as-milled samples are also shown once again for comparison. The $\text{Fe}_{0.83}\text{Ge}_{0.17}$ sample is off-stoichiometry as far as perfect DO_3 order (ideally in Fe_3Ge composition) evolution is concerned; some of the 4(a) sites are also occupied randomly by Fe atoms, therefore giving rise to a distribution of the form

$$P_{8c}(4,n,x) = {}^4C_n(x)^n(1-x)^{4-n}, n = 0, 1, 2, 3, 4 \quad (3.12)$$

for the 8(c) sites Fe atoms with a multiplicity factor of 2 / 3.32. In this distribution 4 is the number of 4(a) 1nn sites of an 8(c) site Fe atom, n is the number of Ge atoms substituting this site in an alloy with Ge concentration x. 4(b) site Fe atoms have all Fe (8(c) sites) 1nn giving rise to 8(0) distribution with a multiplicity factor of 1 / 3.32. This distribution is shown in RHS of figure 3.27. The good agreement between the experimental and calculated probabilities (figure 3.27) of different HMF values arising from various 1nn configuration of Fe atoms show the evolution of only DO_3 order in the system. The evolution of DO_3 order is also shown in the XRD pattern (inset of figure 3.24) by the presence of $(\frac{1}{2}\frac{1}{2}\frac{1}{2})$ and (100) lines in nearly 2:1 ratio. In case of

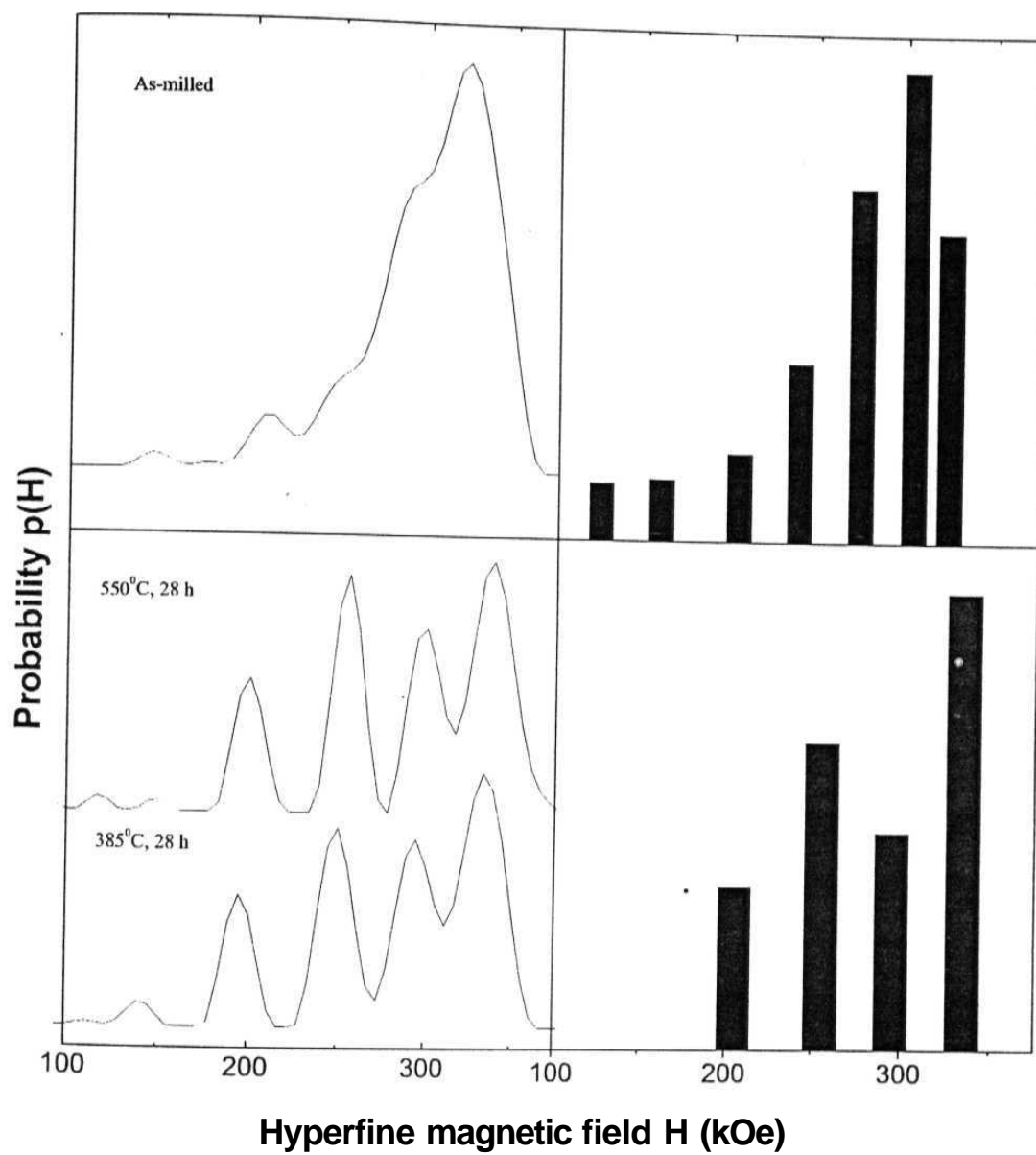


Figure 3.27: Experimental (line graph) and calculated (bar graph) field distributions of as-milled and heat treated samples with $\text{Fe}_{0.83}\text{Ge}_{0.17}$ composition are shown. The evolution of DO_3 order (as discussed in text) is clearly seen by the emergence of peaks in the distribution.

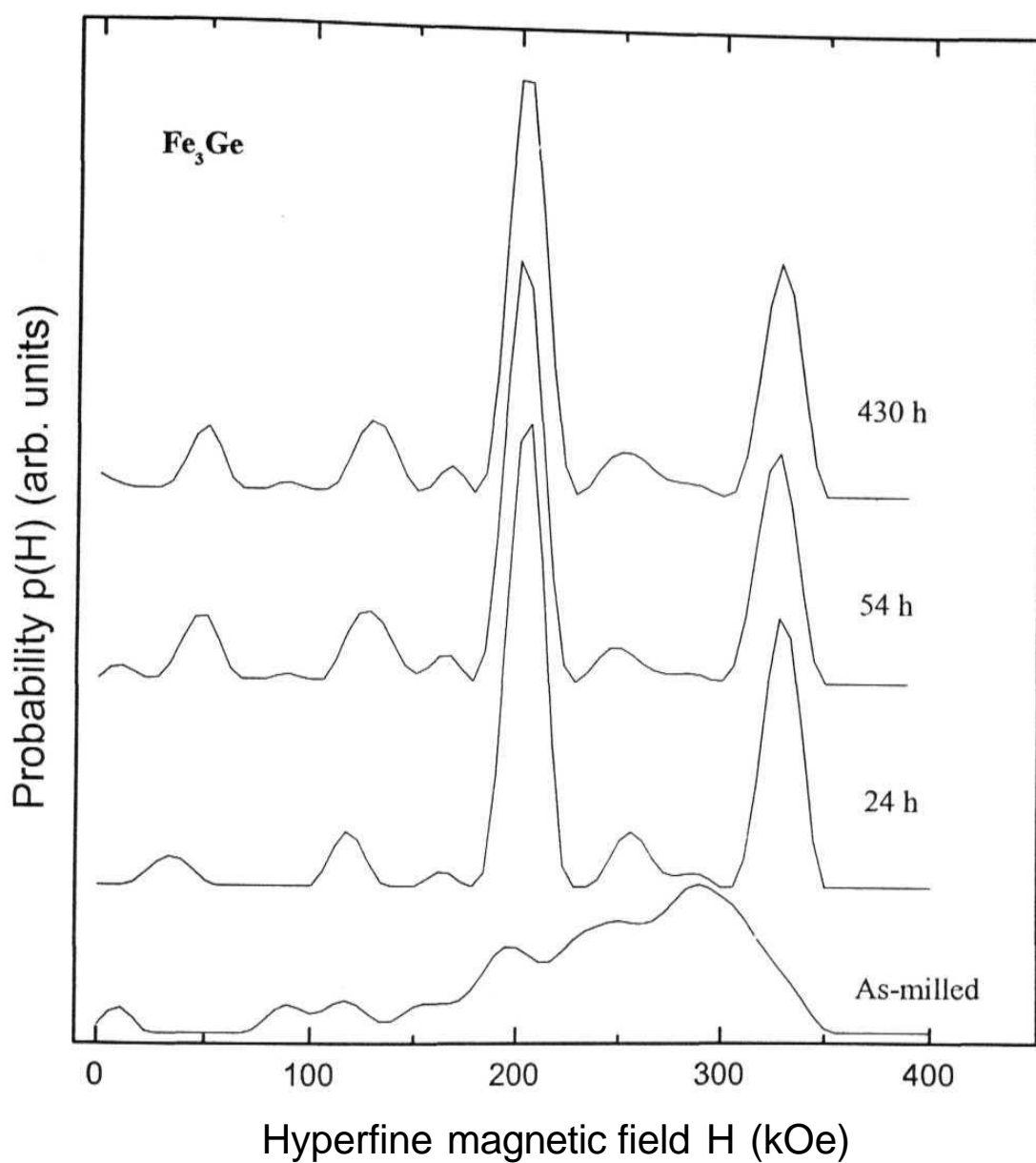


Figure 3.28: Evolution of DO_3 order in Fe_3Ge heat treated at 350°C as seen by the development of peaks in HMF distributions at ~ 205 kOe and 330 kOe corresponding to the 8(c) and 4(b) Fe sites, respectively.

$\sim\text{Fe}_3\text{Ge}$ alloys the evolution of fields at 330 and 205 kOe (figure 3.28) in the ratio 1:2 indicate the growth of only DO₃ order in the system supported also by XRX) results. No signature of the β phase was observed although it was expected. These observations are in good agreement with the work of Gao [37, ref 24 of chapter 1]. The grain sizes of the $\text{Fe}_{0.83}\text{Ge}_{0.17}$ heat-treated alloys were estimated to be approximately 18 and 75 nm respectively at 385 and 550°C. The SRO parameter evolution was $\sim 97\%$ and 99% respectively at these two temperatures. In case of $\sim\text{Fe}_3\text{Ge}$ alloys the grain growth and S(4) evolution was up to around 25 nm and 75% below 400°C. The temporal evolution of grain size and S(4) near Fe_3Ge stoichiometry will be shown in the next section and compared with the behavior in case of Fe-Mn-Ge alloys. Similar to Fe-Al system in this system also a first order evolution kinetics was observed. However there was no intermediate or permanent B2 or B32 order phases developed in this system as was seen in case of Fe-Al alloys, most probably because of much stronger ordering interactions in this system due to which DO₃ order is stabilized in the boundary regions also.

β phase (B81 (hcp) structure) region in the Fe-Ge phase diagram is characterized by two different Fe atoms tetrahedrally and octahedrally bonded with the Ge atoms [figure 6 of reference 61]. The populations of tetra and octahedrally bonded Fe atoms are in 1:2 ratio. Tetrahedral Fe sites having 4 Ge 1nn give rise to HMF around 200 kOe and octahedral sites surrounded by 6 1nn Ge atoms give rise to HMF at around 120 kOe in the Mossbauer $p(H)$ distributions ideally with the intensity ratios of these two fields as 1:2. To check the ordering process in the β phase, an alloy with starting composition of $\text{Fe}_{0.61}\text{Ge}_{0.39}$ in the β phase region of the phase diagram was synthesized by milling of elemental powders. The composition after milling became $\text{Fe}_{0.62}\text{Ge}_{0.38}$. Figures 3.29 and 3.30 show the XRD and Mossbauer spectrum along with field probability distribution of the as-milled sample. The as-milled

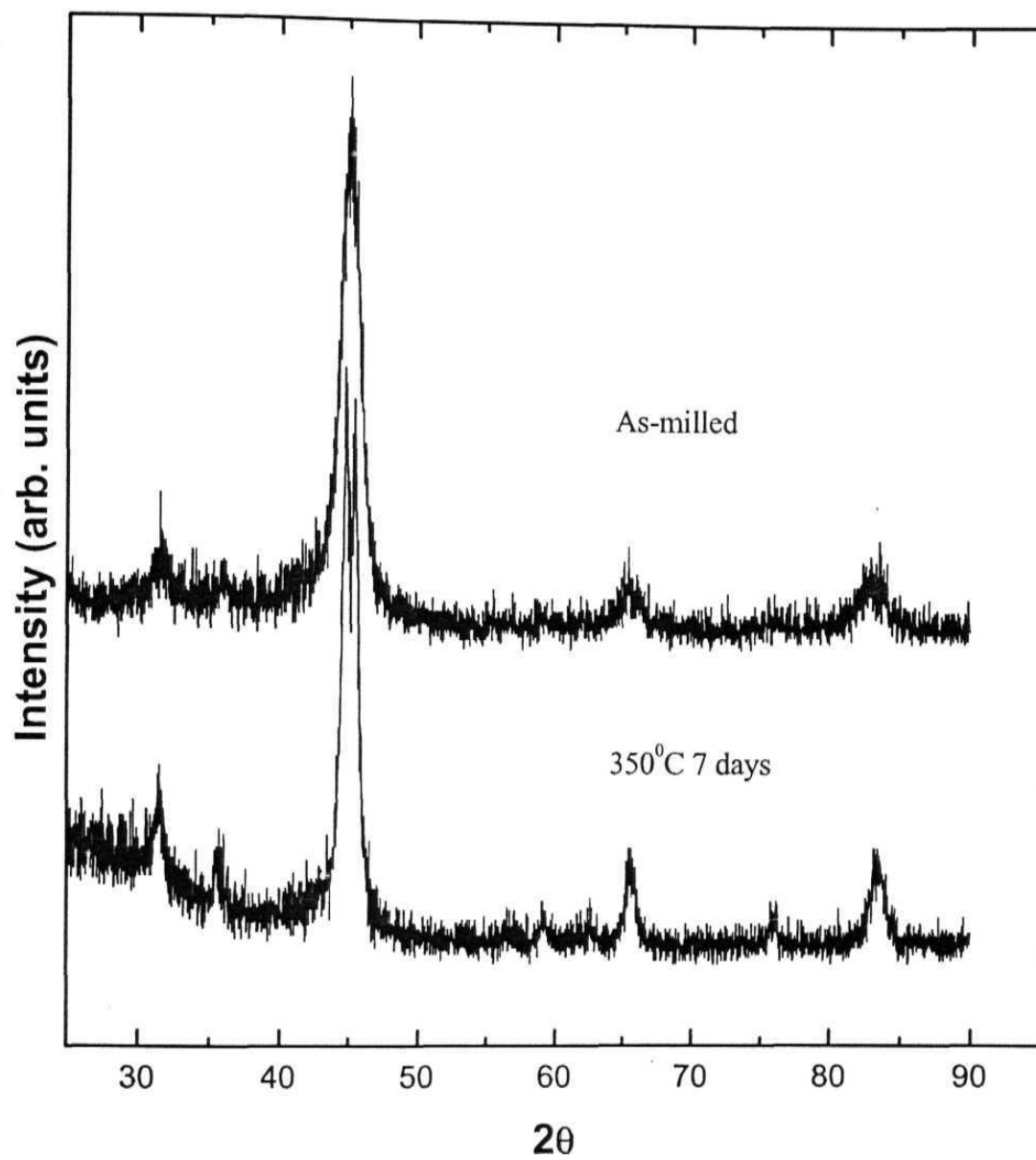


Figure 3.29: XRD patterns showing the formation of the disordered p phase Fe Ge composition alloy in the as-milled state. The evolution of ordered p phase is seen after heat treatment.

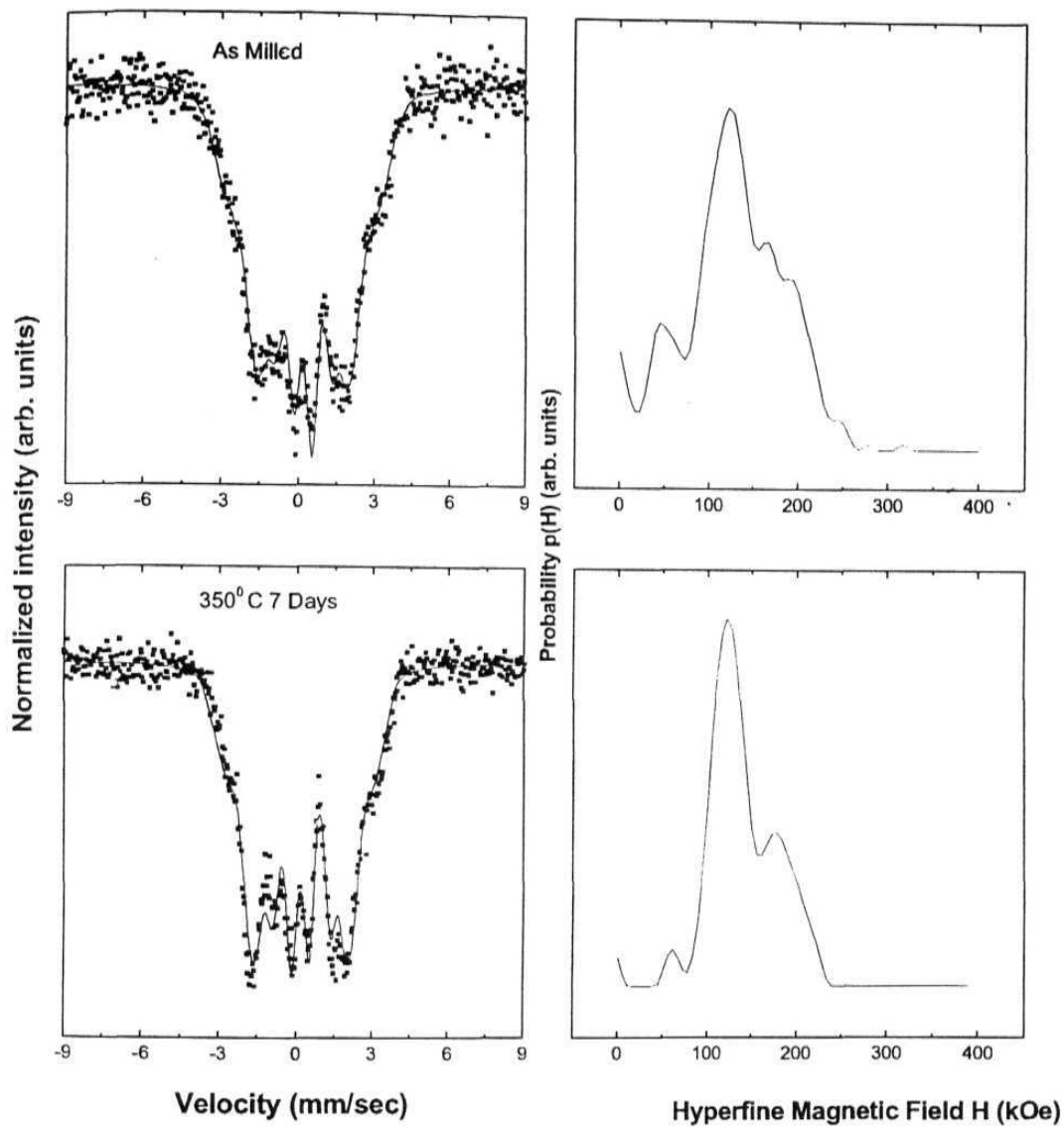


Figure 3.30: Mossbauer spectra and HMF distributions for $\text{Fe}_{0.62}\text{Ge}_{0.38}$ alloy composition (p phase) in as milled state and after heat treatment at 350 C for 7 days. The evolution of atomic ordering giving rise to Fe atoms with specific Ge 1nn configurations instead of a random configurations of the as-milled alloy is evident from the spectrum as well as field distribution.

alloy was formed in the nanocrystalline (grain size ~ 5.5 nm) disordered B81 phase giving rise to only one broad peak at around 45° (2 θ) and broad peaks (indicating distribution of Ge atoms around Fe) at HMF values of nearly 200 and 120 kOe but not in the ratio of 1:2. The as-milled sample was heat treated at 350° C for 1, 3, and 7 days to see the evolution of the equilibrium β phase. The XRD pattern and Mossbauer spectrum with field distribution for the 7 days heat-treated sample is also shown in figures 3.29 and 3.30. The presence of two distinct peaks in the XRD pattern at 44.68 and 45.40 (2θ -values) indicates the ordering process and grain growth, which is taking place in the system. The lattice constants values of $a = 3.995$ and $c = 5.007$ Å are in good agreement with the literature data [JCPDS- International Center for Diffraction Data, PDF Numbers 18-0556, 72-1472, and 35-1183, 1999.] available for this alloy. The grain size obtained was 14 nm. The peaks in the HMF distribution of the heat-treated sample (figure 3.30) correspond to octahedral and tetrahedral Fe sites with 2:1 ratio. The area of the 120-kOe field peak is a good representation of the SRO in the system. The temporal evolution of this peak area is shown in figure 3.31 with the solid line representing a first order ordering reaction kinetics according to equation 3.11. This study therefore constitutes an example of an alloy that can be disordered only by mechanical milling.

3.2 Pseudo Binary System (Fe-Mn-Ge)

a Introduction

Ternary solute additions to the binary systems have been used to improve the high temperature strength and several studies have been made to observe the site substitution behavior. Neutron diffraction studies on $\text{Fe}_{3-x}\text{Mn}_x\text{Si}$ [62] alloy system revealed the preferential 4(b) site substitution of Mn atoms in the DO3 structure. Later it has been observed from spin echo NMR [63], Mossbauer Spectroscopic [42] and X-Ray diffraction studies [41] of the

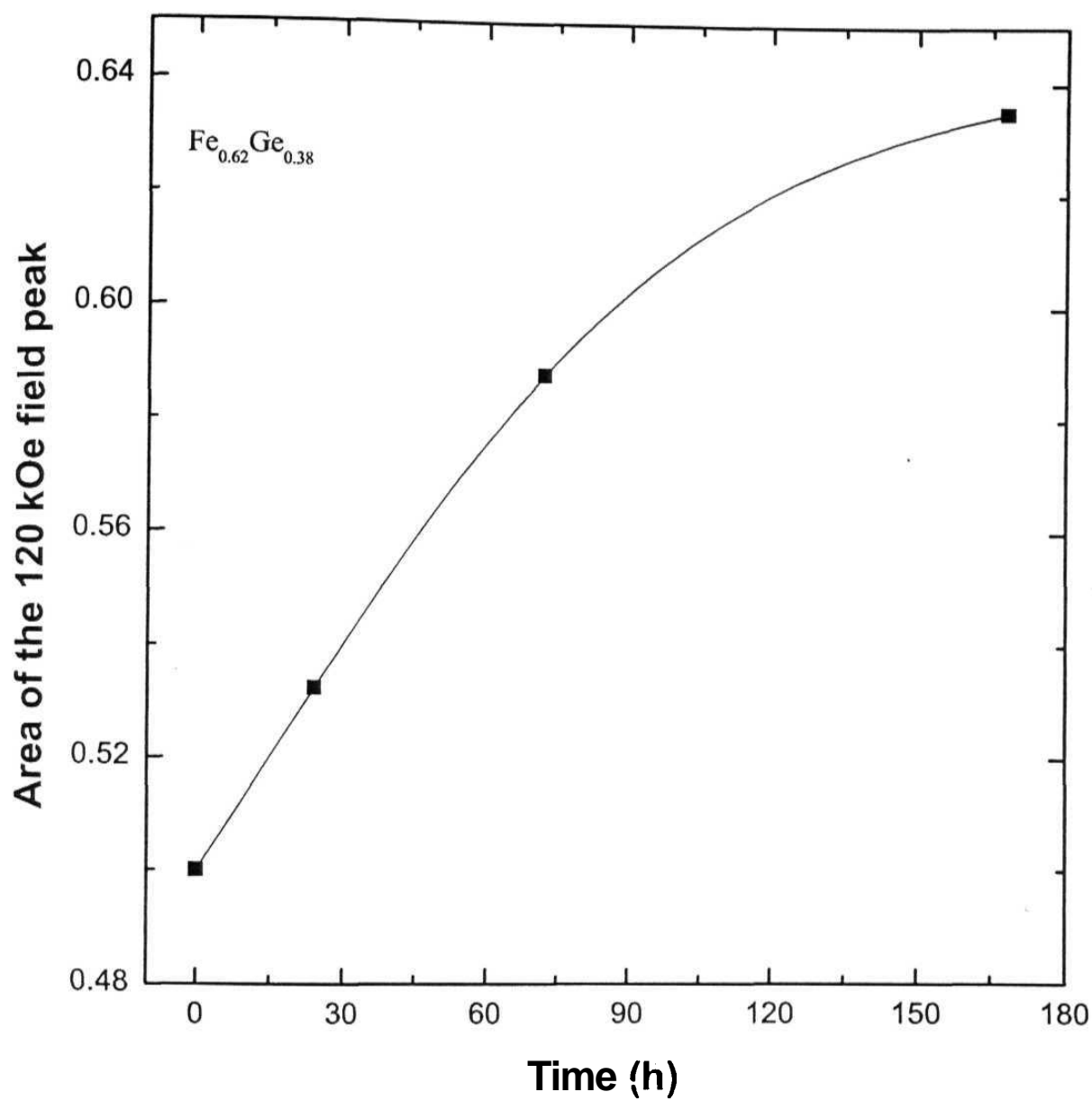


Figure 3.31: The temporal evolution of the 120-kOe field peak area representing short-range-ordering that is taking place in the system.

microcrystalline alloys that solutes to the left of Fe in the periodic table (e.g. Ti, Mn, W, Nb, and Mo) occupy preferentially the 4(b) sites whereas solutes to the right of Fe (e.g. Co and Ni) occupy 8(c) sites in the DO₃ ordered structure. However for the nanocrystalline Fe_{3-x}Mn_xSi system it was found that an ordering heat treatment to develop DO₃ order leads to a segregation of Mn atoms in the grain boundaries and simultaneously the growth of DO₃ grains is suppressed [54].

In this work we studied the effect of Mn addition to the binary Fe₃Ge alloys to understand the site substitution and chemical ordering behavior in the nanocrystalline state. It was observed that in nanocrystalline Fe_{3-x}Mn_xGe alloy systems for $0.0 < x < 0.75$ compositions the Mn atoms get homogeneously alloyed in the as-milled state but do not substitute in the equilibrium DO₃ phase which forms when the as-milled alloys are heat treated.

b Experimental

Fe_{3-x}Mn_xGe alloys ($0 < x < 0.75$) were prepared by mechanical alloying of elemental Fe (Aldrich Sigma 4N), Ge (Aldrich Sigma 4N) and Mn (Alpha Ventron m3N7) powders. The Fe contamination estimated was 1-2 at %.

c Results and discussion

Figure 3.32 shows the X-ray diffraction data for the as-milled alloy samples. The presence of predominantly bcc phase lines in the X-ray pattern shows the formation of homogenous single-phase bcc alloys (a) for all Mn concentrations. The additional very low intensity Bragg peaks present in the as-milled patterns were indexed to trace amount of Iron Manganese Oxide phase [JCPDS- International Center for Diffraction Data, PDF Number 77-2362,

1999]. The average grain sizes obtained for the **as-milled alloys** were approximately 6 nm.

Figure 3.33 shows the Mossbauer Spectra of the as-milled alloys with different Mn concentrations. The corresponding Hyperfine Magnetic Field (HMF) distributions obtained by Le Caer analysis are shown **in the left hand** side of figure 3.34. In fitting the HMF distributions using Gaussian functions it was considered that the **1nn** HMF perturbation caused either by a Ge atom or by an Mn atom is of equal magnitude of nearly 25 kOe and that caused by the **2nn** Ge or Mn atom is negligible in comparison to the **1nn** [ref 32 of chp 2], With increase in the concentration (x) in $\text{Fe}_{3-x}\text{Mn}_x\text{Ge}$ the HMF value corresponding to the maximum probability in the distribution shifts to lower values relative to Fe_3Ge . The probability distributions of the as-milled alloys for different near neighbour configurations (with 0 to 8 Fe **1nn** of Fe) correspond very well with the calculated probabilities (shown in right side of figure 3.34 as bar graph) using the distribution of equation 3.1 with all the Constituent atoms substituting randomly at the bcc lattice sites. The HMFs corresponding to different number of **1nn** solute configurations to Fe atoms was in accordance with the earlier work of Fultz et. al. [ref 26 of chp 2] based on the additive perturbation model [ref 28 and 32 of chapter 2]. The good agreement between the experimentally obtained and theoretically calculated probability distributions shows that Mn enters **substitutionally** in the disordered bcc structure (A2) and forms a homogeneous alloy in the as-milled state, which is also supported by the X-ray data. As it was the case for Fe-Ge alloys the Mn substituted alloys were also formed in the disordered bcc **a** phase although the equilibrium phase diagram for Fe-Ge (figure 3.22) shows a two-phase region (**DO₃ + B81**) at this composition and temperature.

The samples were heat treated at 350°C for periods of time ranging from 7 to 24 hours to see the development of the equilibrium order. Figure 3.35 shows the representative X-ray patterns for the 350°C heat-treated samples.

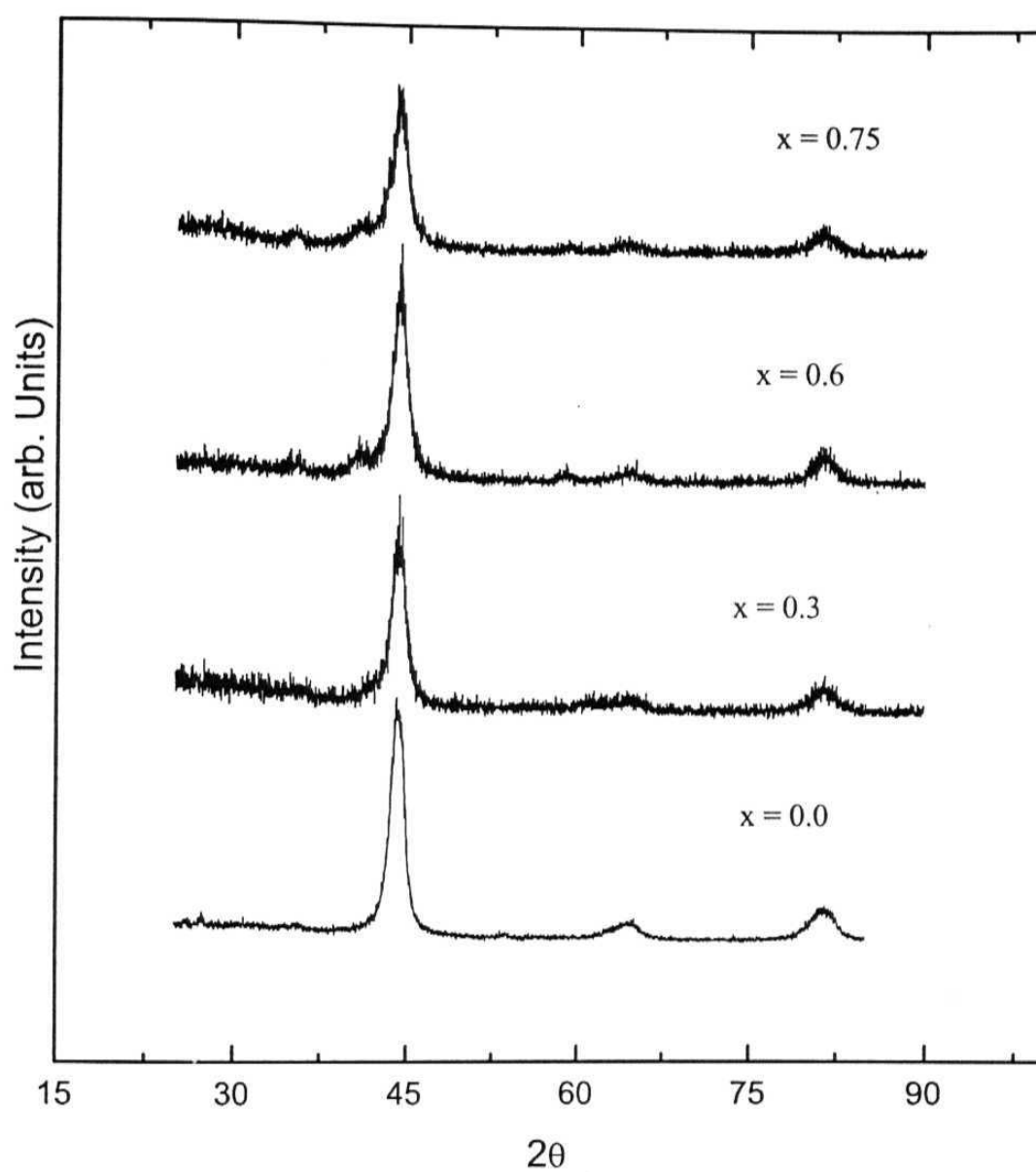


Figure 3.32: X-Ray diffraction patterns for the as-milled samples with different Mn concentrations (x).

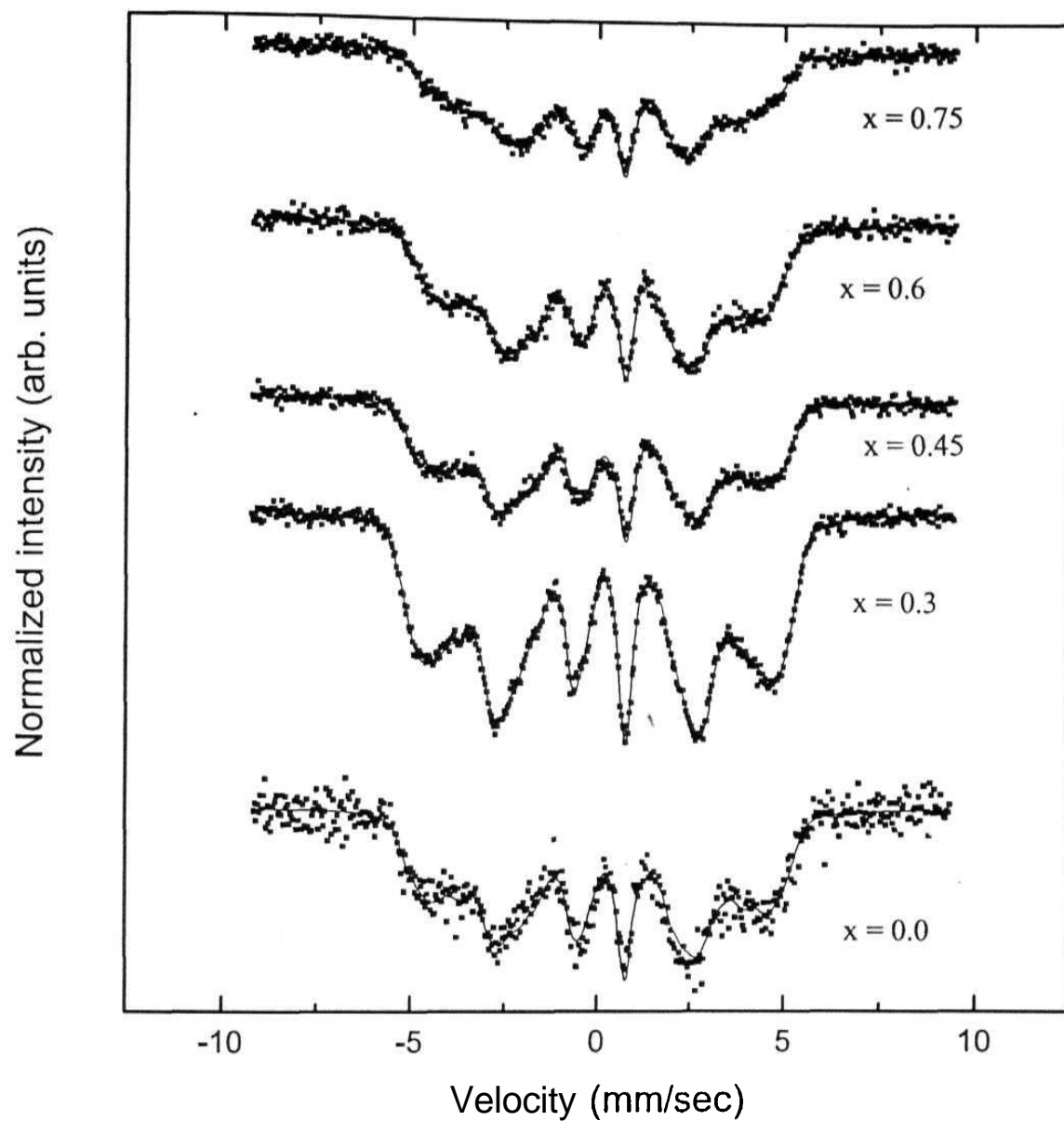


Figure 3.33: Mossbauer Spectra of the as-milled samples. Scattered points: experimental data; solid line: fit to the data by Le Caër method.

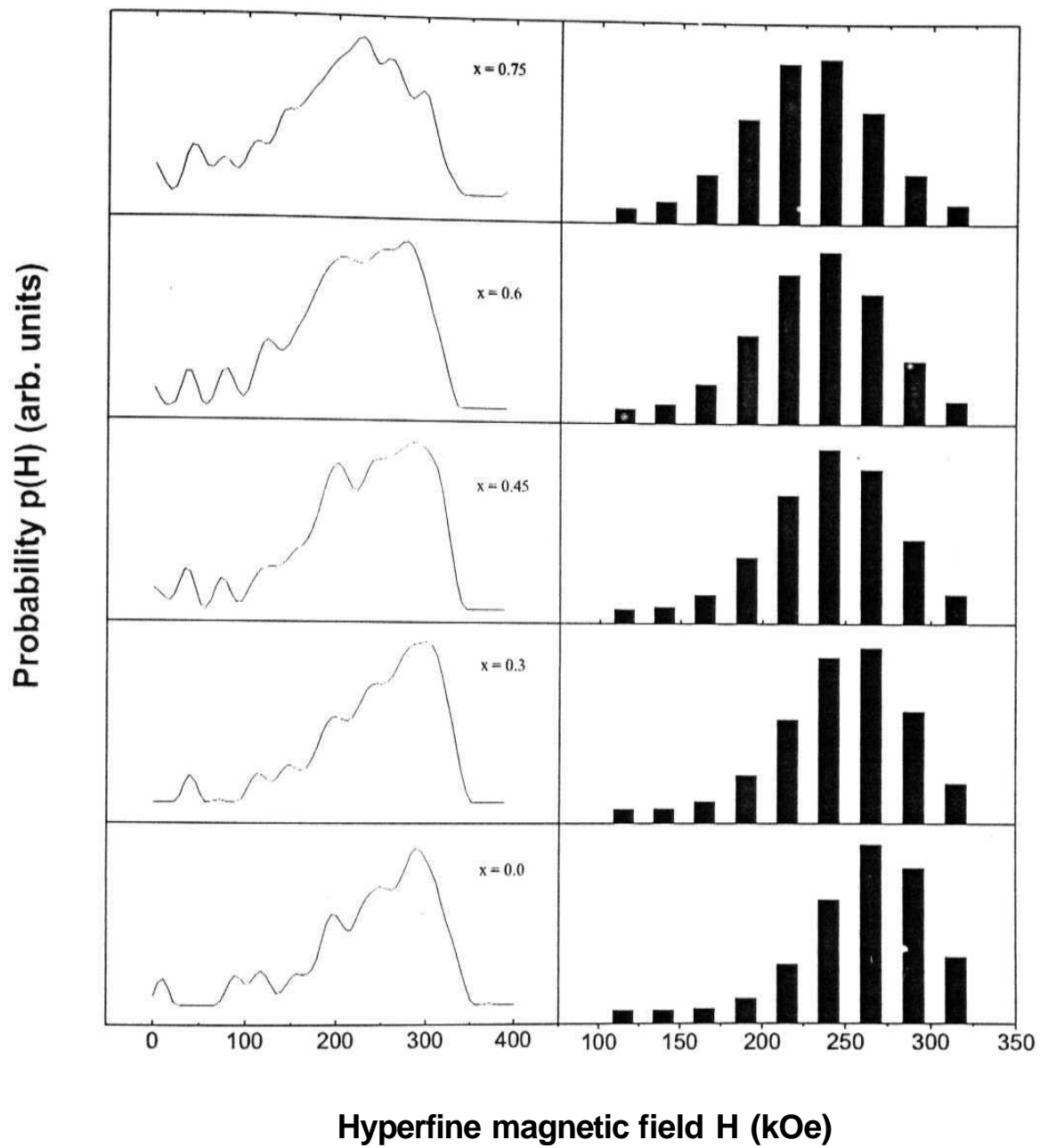


Figure 3.34:(LHS) Experimentally obtained HMF distributions from the Mossbauer spectra of the as-milled alloys. (RHS) Binomial probability distributions calculated for the as-milled alloy compositions.

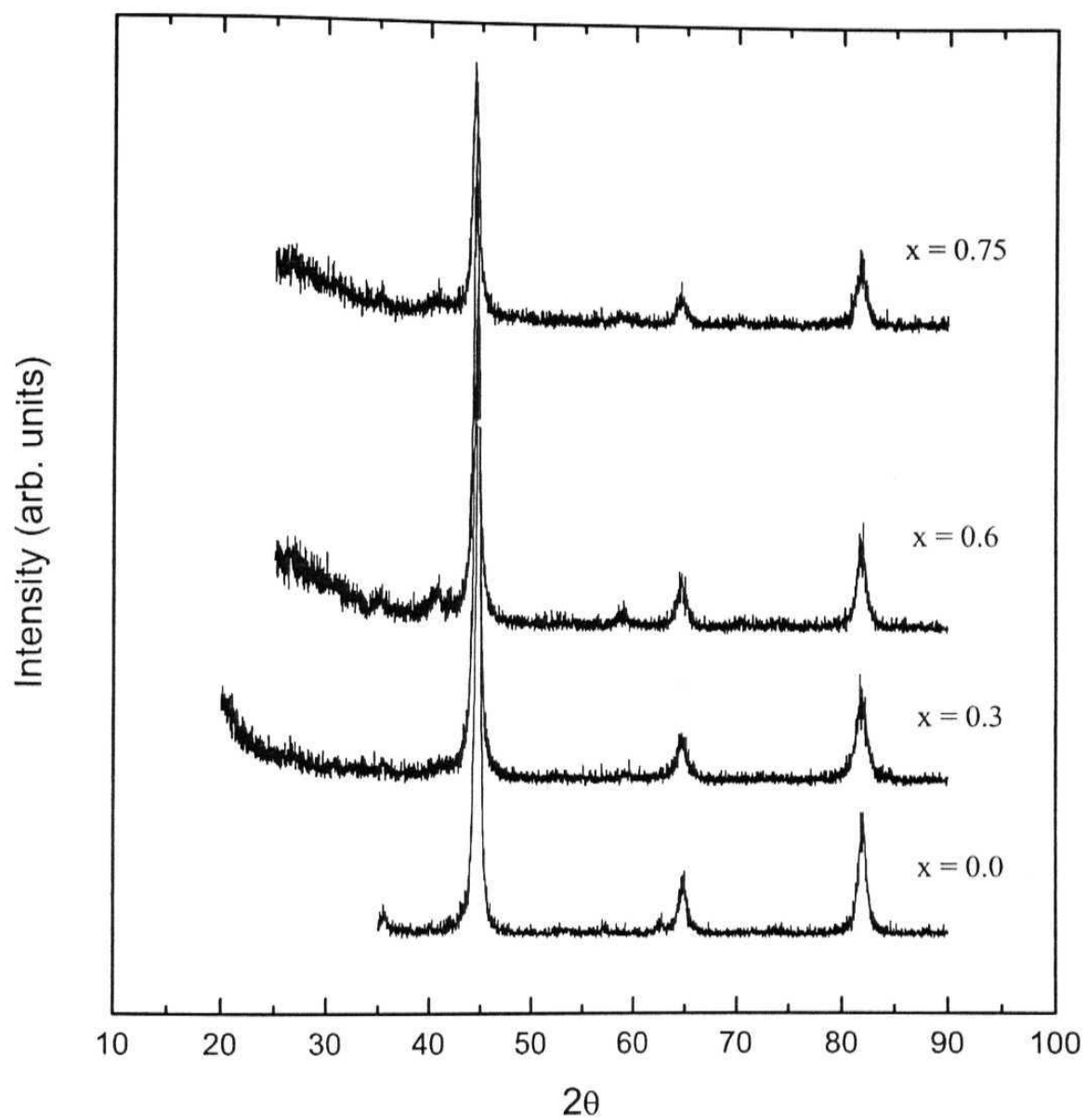


Figure 3.35: X-Ray patterns for the representative 350 C, 24 h heat-treated samples with different Mn concentrations.

Narrowing of **line** widths of the bcc phase lines in comparison to the **as-milled** patterns shows the grain coarsening and no other lines were present except **the** very weak lines due to the oxidation phase. Grain growth behavior of the 350 C heat- treated samples with different Mn concentration are shown in figure 3.36. Similar grain growth behavior is observed for pure Fe-Ge as well as different Mn substituted alloys. Representative Mossbauer Spectra and the corresponding HMF distribution of these heat-treated samples are shown in Figures 3.37 and 3.38. The development of DO₃ ordered phase from the evolution of two main magnetic hyperfine field peaks (at around 200 kOe and around 330 kOe) can be seen clearly. The other very less intense peaks in the P(H) distribution may be arising from the remaining disorder matrix [ref 27 of chapter 2 and ref 24 of chapter 1] or it could be attributed to disorder arising from off-stoichiometry i.e. the deviation from perfect DO₃ order, which is possible only for Fe_{0.75}Ge_{0.25} composition.

The superlattice peaks ($\frac{1}{2}$ $\sqrt{2}$ $\frac{1}{2}$ and 100) in the X-Ray patterns at around 26.5 and 31° 2 θ values arising from the DO₃ order are observed to be very weak and broad (figure 3.35). This may be due to the small size of the ordered domains.

If Mn atoms randomly substitute [64- 54] for Fe in the 4(b) sites of the DO₃ structure then the 1nn environment of Fe atoms in the 4(b) sites remains unchanged (because these consist of Fe atoms at 8(c) sites) but the 1nn environment of 8(c) site Fe atoms will have a distribution of the form of equation 3.12, (i.e. $P_{8c}(4,n,x) = {}^4C_n(x)^n(1-x)^{4-n}$, $0 < n < 4$), but in this case 4 is the number of 4(b) sites of an 8(c) site Fe atom, n is the number of Mn atoms substituting this site in an alloy with Mn concentration x. The weight factor to be multiplied to this distribution to get the probability of a particular Fe configuration is $2 / (3-x)$. The 1nn of the 4(b) sites are 8(c) site Fe atoms and this needs to be multiplied by a factor of $(1-x)/(3-x)$ to get the desired

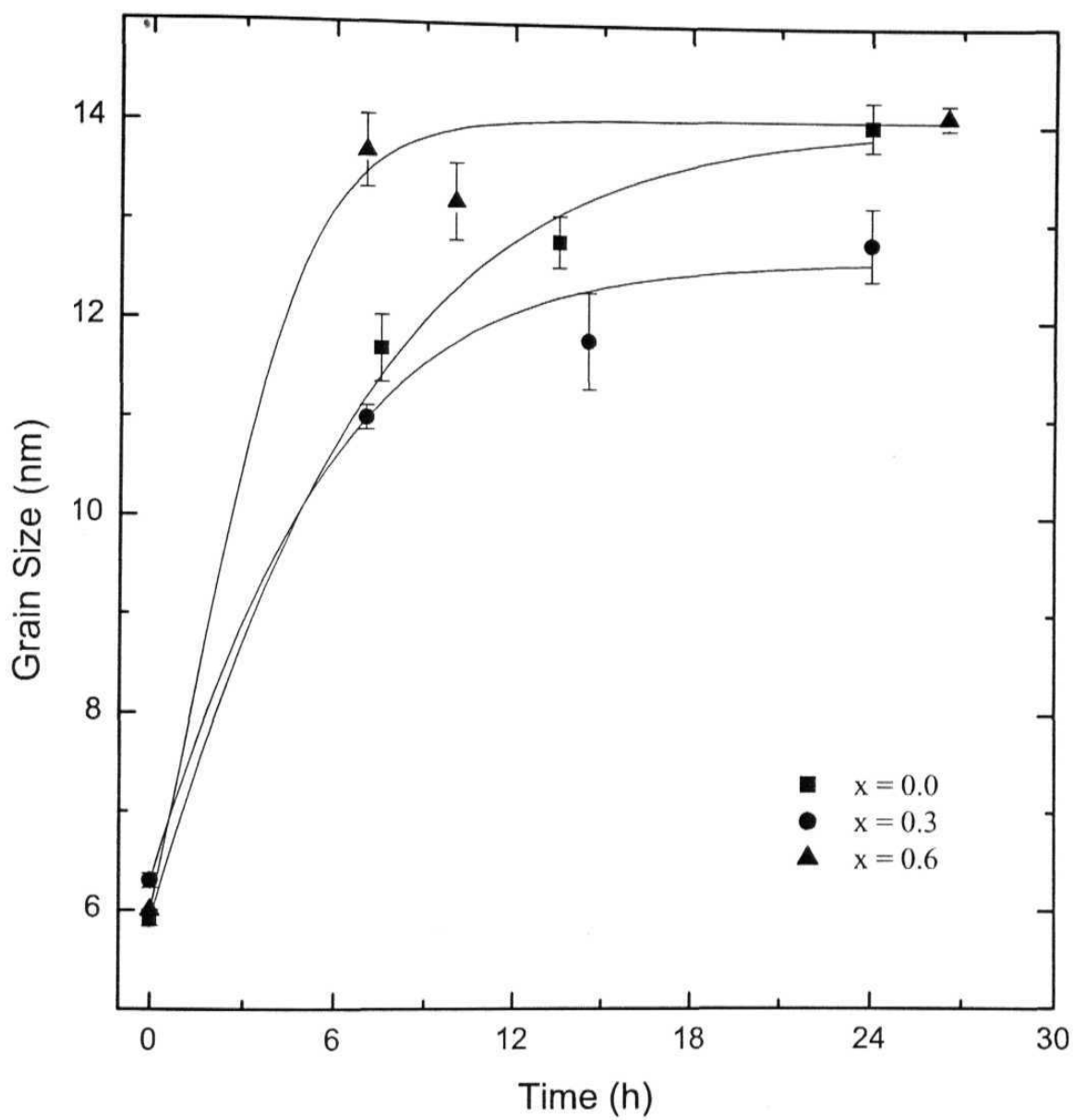


Figure 3.36: Grain growth observed at 350 C for representative Mn concentration alloys.

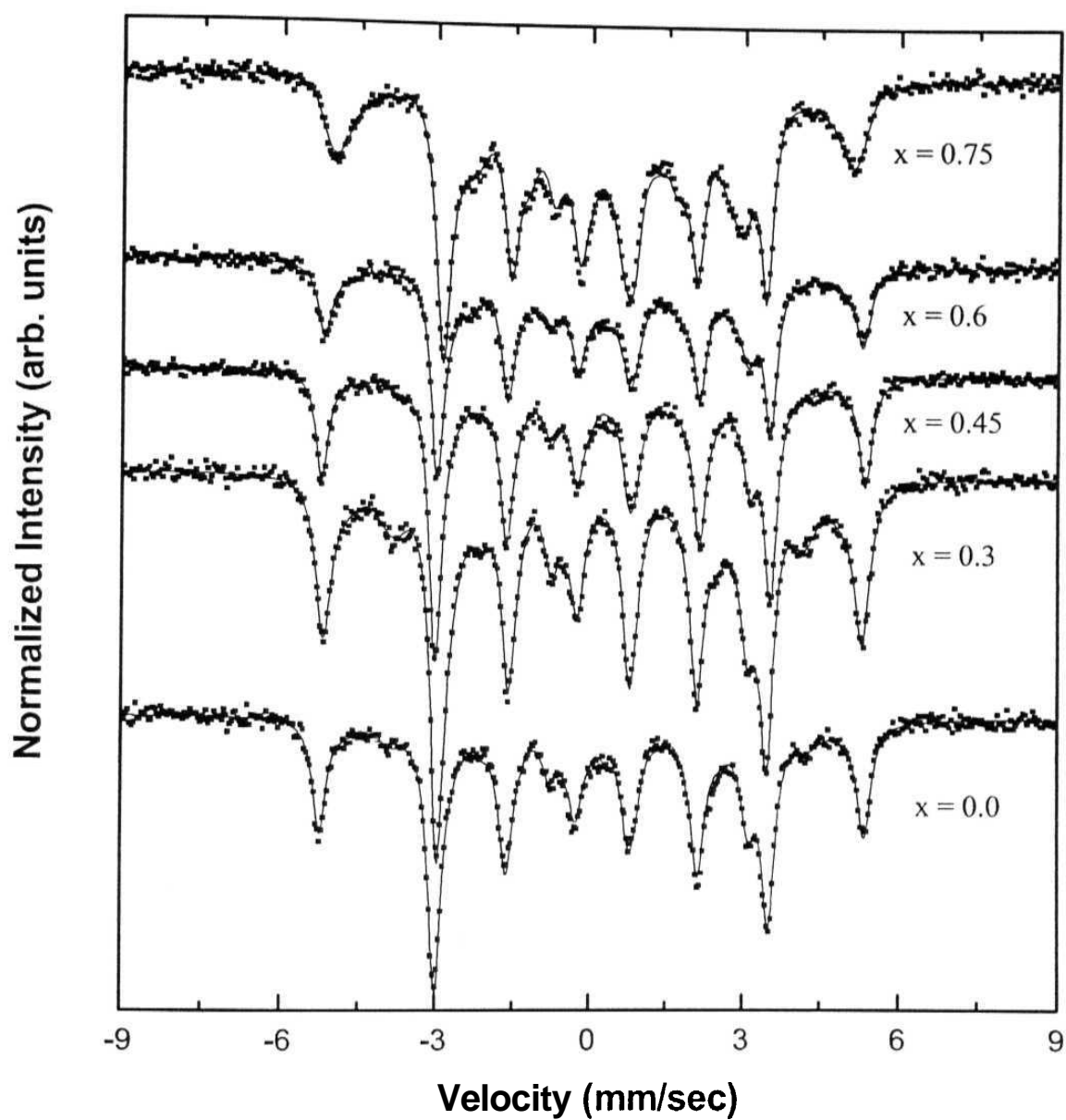


Figure 3.37: Representative Mossbauer spectra of the 350°C, 24 h heat-treated samples with different Mn concentrations.

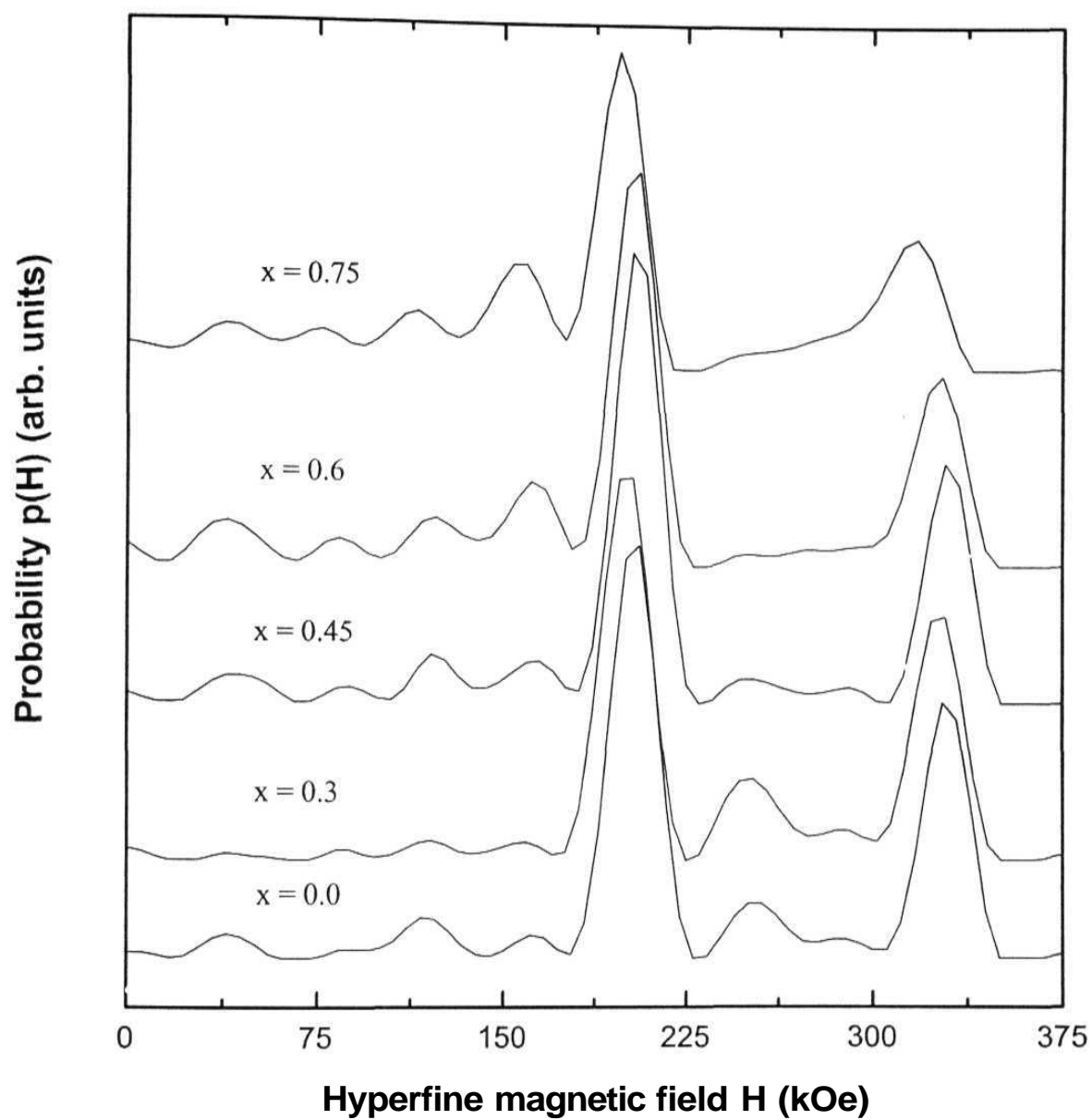


Figure 3.38: HMF distributions obtained from the Mossbauer spectra of figure 3.37.

probability. The calculated probability distribution expected by considering the above argument is shown in the LHS of figure 3.39.

It was argued in case of microcrystalline alloys that Mn atoms substitute into 8(c) sites once all 4(b) sites are occupied in Mn rich alloys [63, 65]. In case of nanocrystalline alloys if Mn atoms randomly substitutes Fe in the 8(c) sites of the DO_3 structure then the 1nn environment of Fe atoms in the 8(c) sites remains unchanged (these are 4(b) Fe sites), but the 1nn environment of 4(b) Fe atoms will have a distribution of the form

$$P_{4b}(8,n,x/2) = {}^4C_n (x/2)^n (1-x/2)^{8-n}, \quad 0 < n < 8 \quad (3.13)$$

where 8 is the number of 8(c) 1nn sites of an 4(b) site Fe atom, n is the number of Mn atoms substituting this site in an alloy with Mn concentration x. The weight factor to be multiplied with this distribution is $1 / (3-x)$ and that to be multiplied with the distribution of the 8(c) site is $(3-x-1)/(3-x)$. The calculated probabilities arising from this kind of site substitution is shown in the RHS of figure 3.39.

The complete mismatch between our experimental probability distribution (figure 3.38) and the probability distributions of figure 3.39 gives clear indication that Mn atoms are not substituting any of the DO_3 ordered sites in contrast to the behavior observed in microcrystalline alloys. There is no indication of Mn rich Fe or Mn rich Ge phases in the Mössbauer spectra or X-ray patterns. This shows that Mn atoms may be clustering within the bcc grains or segregating to the grain boundary (GB) regions. Out of these two possibilities segregation is more likely because of the existence of high diffusivity paths in grain boundaries.

The observed isomer shift values relative to Fe/Rh of 0.24 mm/sec for 8(c) sites Fe atoms and 0.05 mm/sec for 4(b) sites Fe atoms of the DO_3 structure for the Mn substituted alloys are also equal to those for the $x = 0.0$

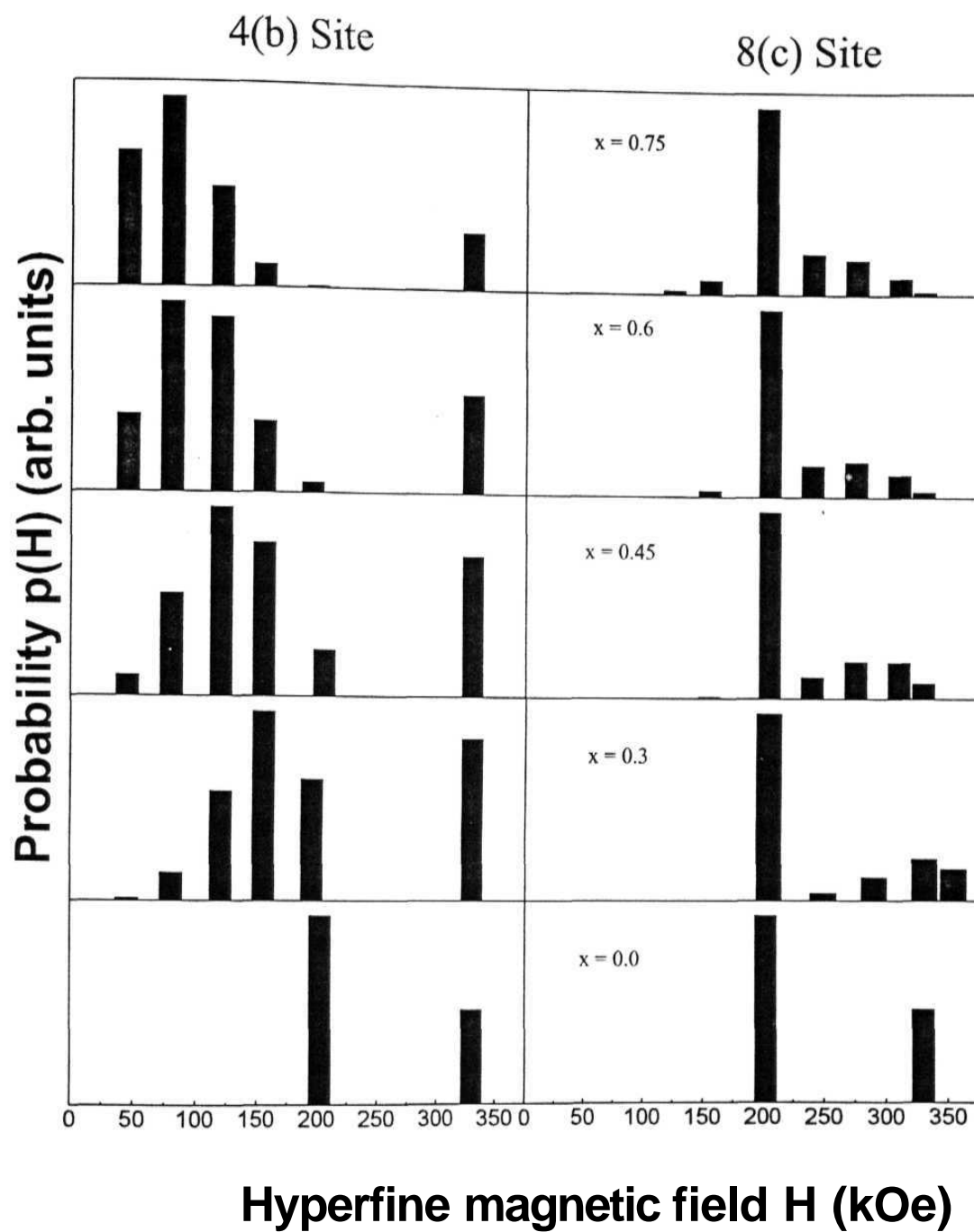


Figure 3.39: Expected HMF distributions assuming Mn atoms substituting either 4(b) or 8(c) sites of the DO_3 structure.

alloy **and** match very well with the previously reported values of $\text{Fe}_{0.79}\text{Ge}_{0.21}$ alloy system [59]. The ratio of Gaussian areas of Mn substituted alloys for **the** 8(c) site **field** and 4(b) site field in the DO_3 structure is close to 2:1, which is expected only for a pure stoichiometric alloy of Fe_3Ge composition. This once again indicates segregation of Mn atoms away from Fe neighborhood. Another evidence of Mn segregation is the comparison of the Isomer shift vs. HMF plots, shown in figure 3.40 between the as-milled and heat-treated samples of the pure and Mn substituted Fe-Ge alloys. The slope of the curves indeed changes after short range ordering takes place in the alloys but both the curves are parallel which would not have been the case if Mn atoms substitute into DO_3 sites and hence give rise to a considerable probability for configurations with different number of Fe 1nn than 4 and 0 Fe 1nn and a measurable change in isomer shift.

The short range ordering process was studied by defining the short range order parameter ($S(4)$) according to equation 3.8. The value of p_{DO_3} was assigned to be 0.67 based on the observed intensity ratio of 2:1 for the 8(c) sites and 4(b) sites peaks. Figure 3.41 shows the kinetic evolution of $S(4)$ parameter in case of representative samples. This behavior is analogous with the behavior obtained in case of nanocrystalline Fe-Al alloy system. The development of the $S(4)$ parameter is similar for the $x=0.0$, 0.3 and 0.45 alloys and it is less for the $x = 0.6$ and 0.75 alloys. Figure 3.42 shows the behavior of the $S(4)$ with Mn composition after 24 hours heat treatment. This behavior is expected for a larger deviation from A_3B stoichiometry due to Mn segregation. Figure 3.43 shows the parametric plot between the evolution of grain size and $S(4)$. It is seen that the growth of the grains and evolution of short-range order are correlated independent of the alloy compositions. Figure 3.44 shows the comparative temporal evolution of $S(4)$ parameter and grain growth in the alloy systems at 350°C . It can be seen that both the processes take place on the

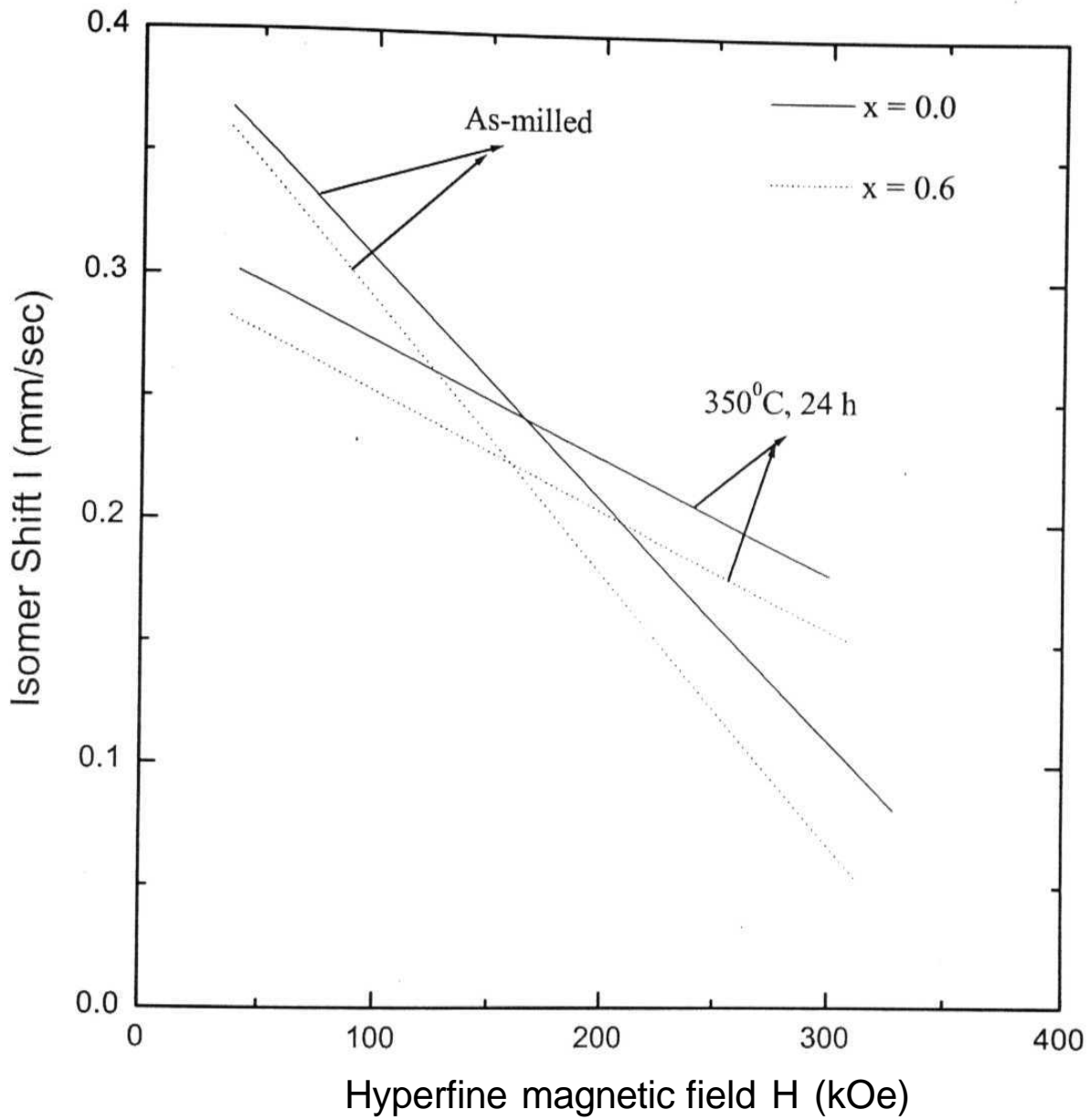


Figure 3.40: Representative I vs. HMF plot showing no change in the slope between $x = 0.0$ and Mn substituted alloy in the as-milled state as well as after ordering heat treatment at 350 C.

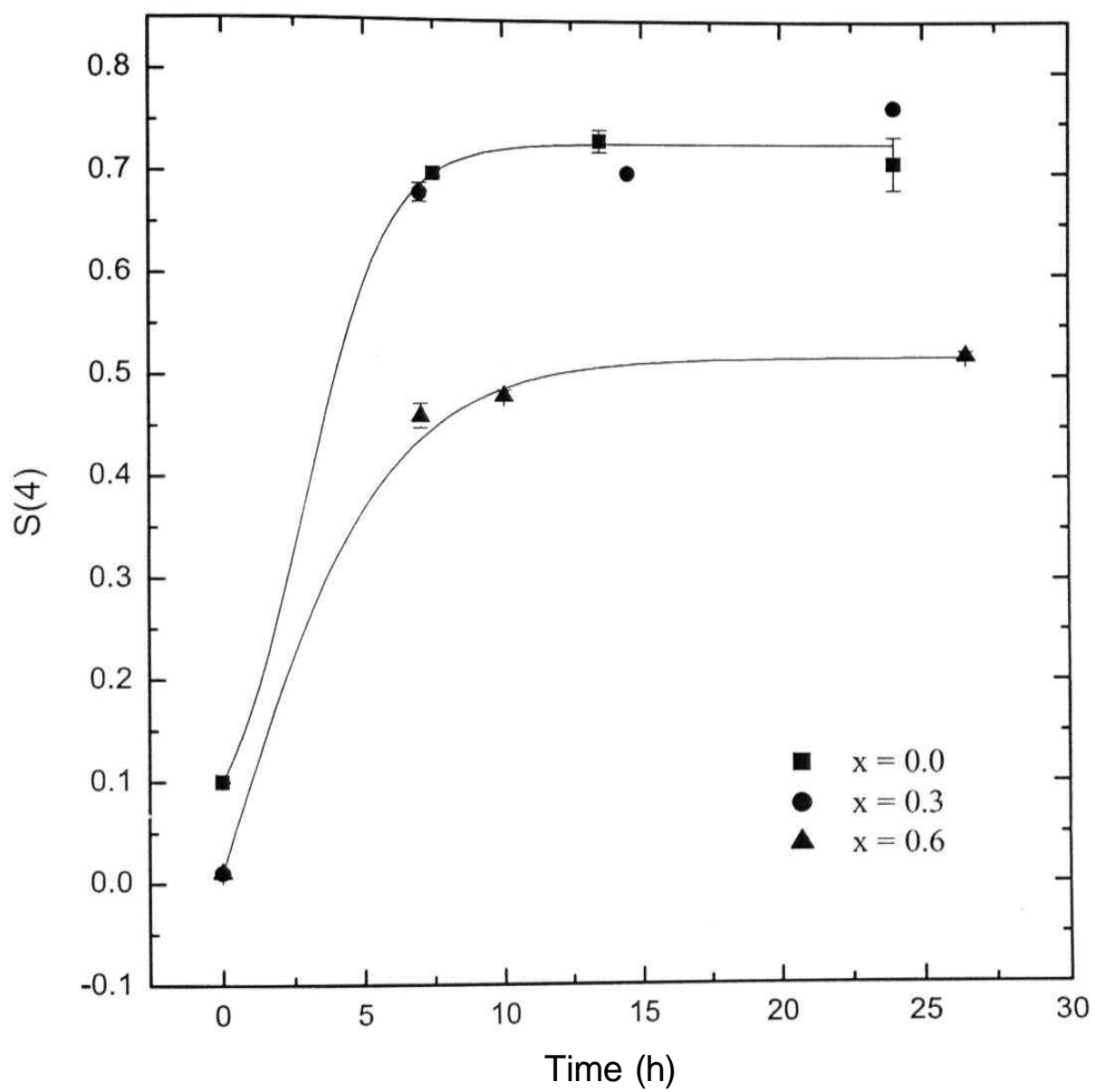


Figure 3.41: Temporal evolution of the short range order parameter at 350 C.

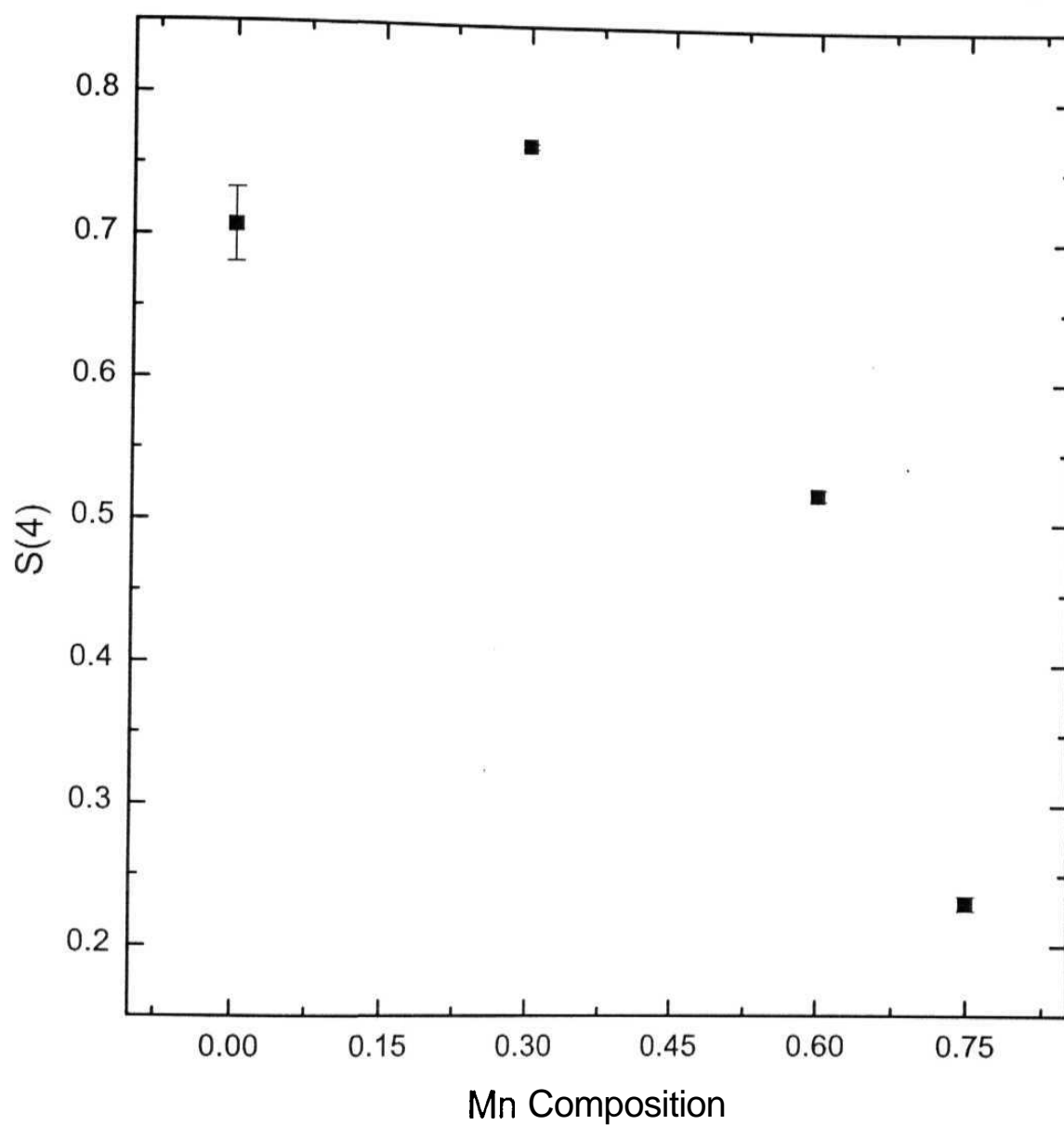


Figure 3.42: The dependence of short range order parameter on Mn concentration after 24 h heat treatment at 350°C.

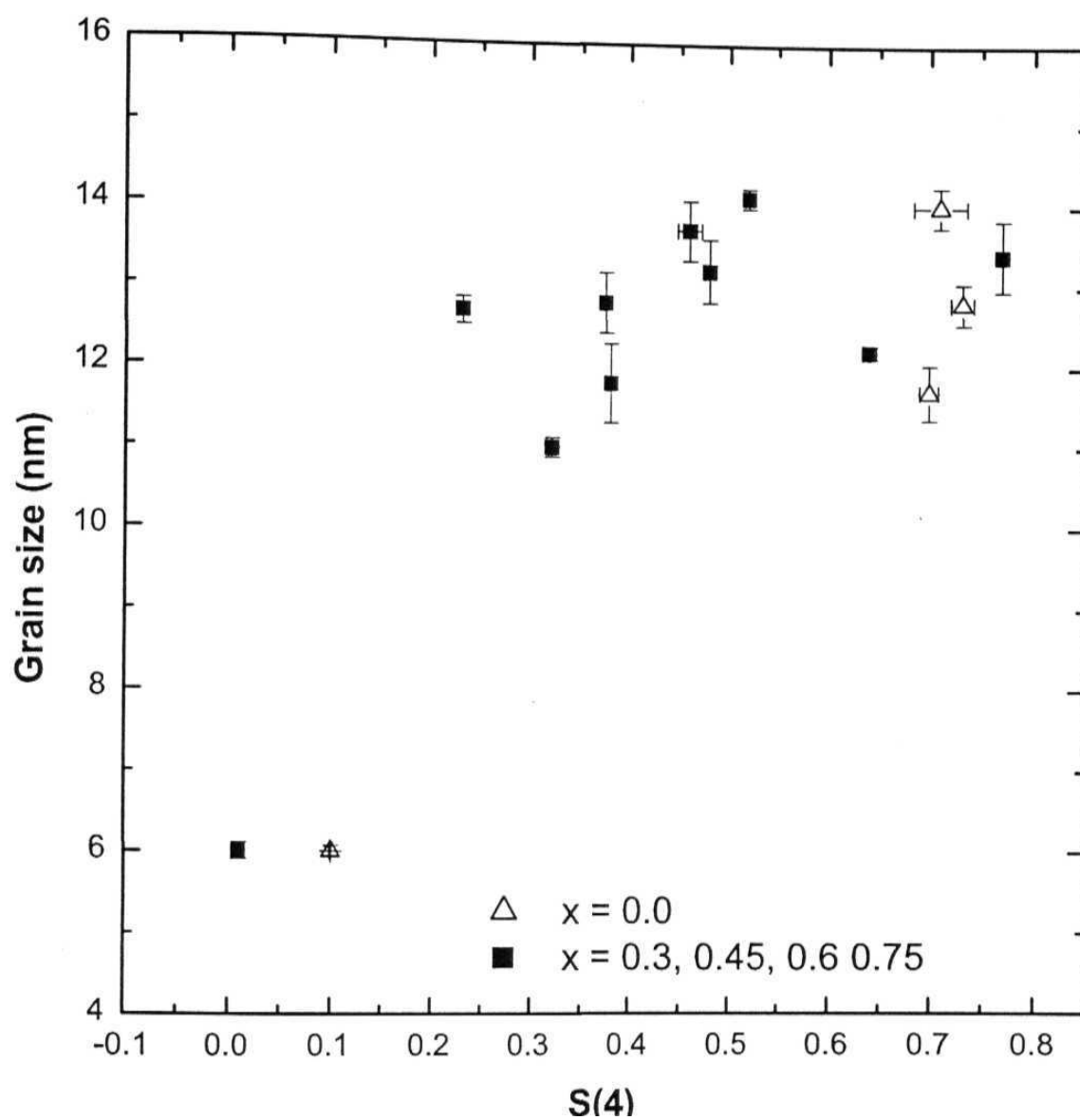


Figure 3.43: Parametric plot between grain size and short-range order parameter at 350 C.

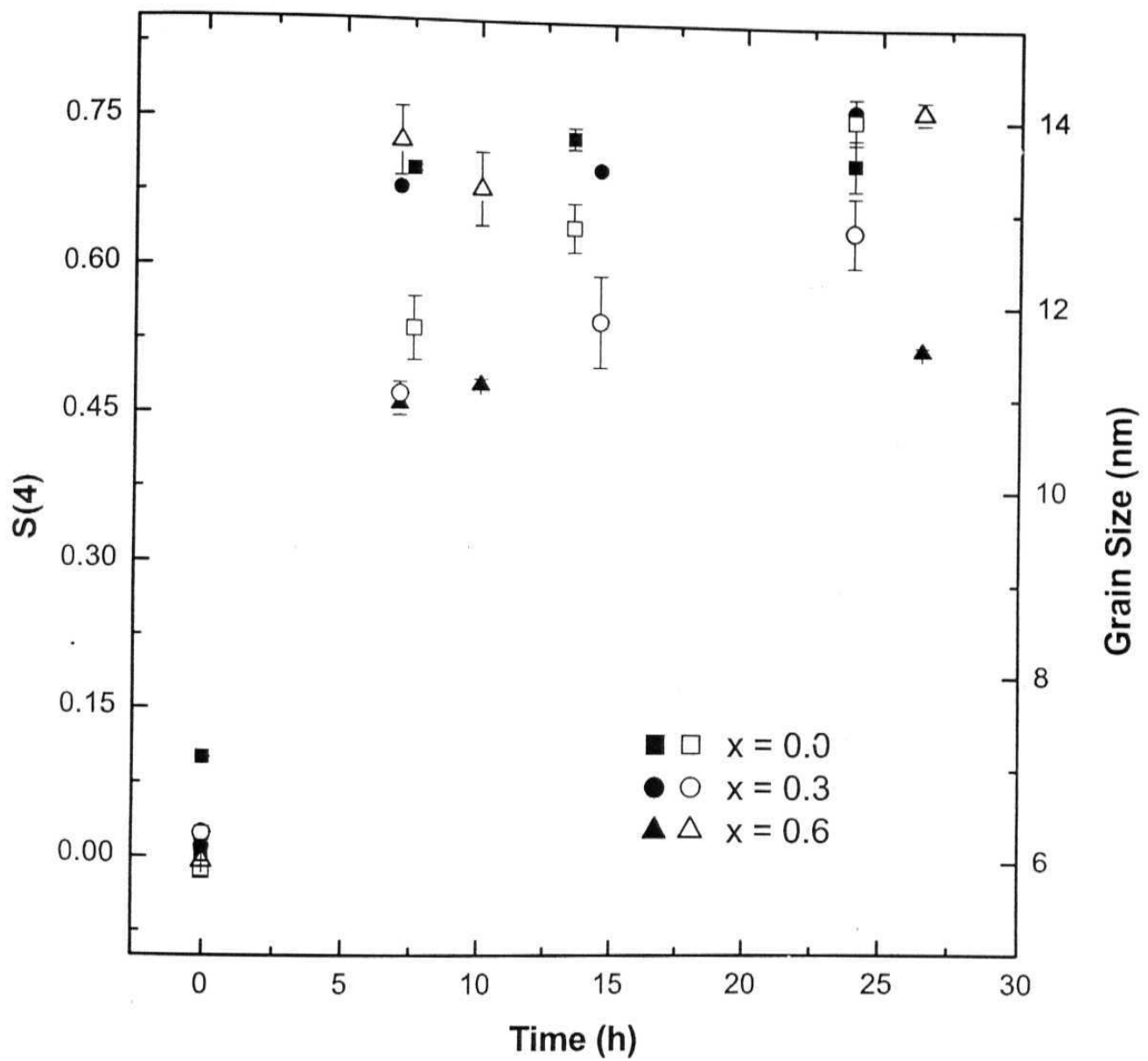


Figure 3.44: Comparative temporal evolution of S(4) parameter and grain growth at 350°C. Solid symbols correspond to SRO parameter and hollow symbols correspond to grain growth.

same time scale. This indicates that the underlying mechanism for atom diffusion is the same for ordering as well as segregation.

In conclusion, it was observed that Mn substitution in the nanocrystalline Fe-Ge alloy system leads to grain boundary segregation of Mn atoms on ordering heat treatments of the initially disordered homogeneous as-milled alloy state. This was in contrast to bulk Fe_3X alloys where Mn substitutes at preferential sites in the DO_3 structure up to a large concentration. The development of DO_3 chemical short-range order and grain growth proceed on the same time scale at 350°C .

3.3 Quasi Binary Systems (FeCo-X, X = 4 at. % Mo, Ge, W)

a Introduction

The kinetic evolution to the chemically ordered equilibrium state of an ordering alloy from its initial disordered state has been a subject of many interesting studies but not fully understood [6, 66]. It has been argued that for a ternary alloy where the state of order is characterized by two order parameters the alloy may develop various combinations of the order parameters in the approach to the final equilibrium state [67]. The initial and final states may be connected by different chains of intermediate states i.e. for a given value of one order parameter, the other order parameter need not have a unique value. It was shown using Master Equation formulation that these chains of kinetic evolution towards the final equilibrium order or '*kinetic paths*' were temperature dependent when the atomic species of the alloy had different activation energy barrier heights for diffusive jumps or different interatomic interactions.

FeCo phase diagram (figure 3.45) shows a large region of B2 order and a Mossbauer spectroscopic study on the kinetics of chemical ordering in several piston-anvil quenched FeCo-X alloys (X = W, Nb, Mo, Cr, Ti, V, and Al) showed that the kinetics of B2 ordering was slowed down for the 4d and 5d solutes but the 3p and 3d series elements did not affect the ordering kinetics

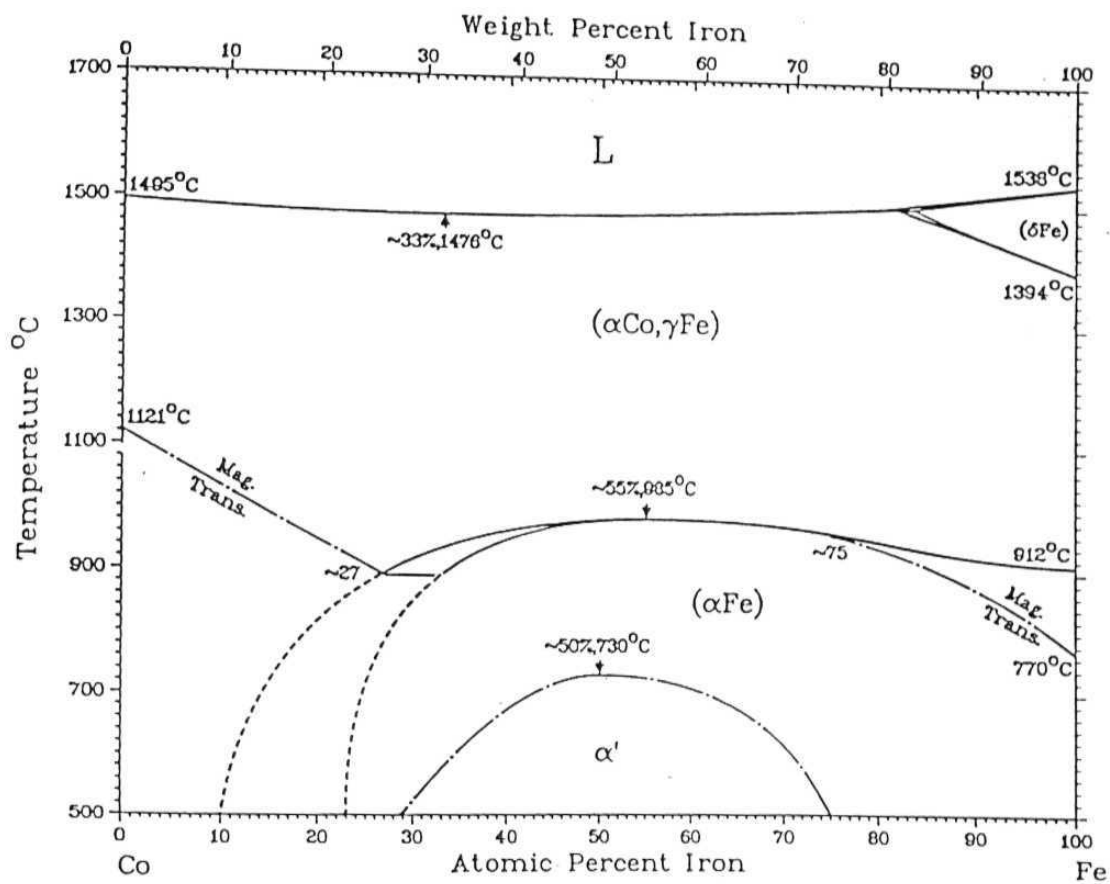


Figure 3.45 Thermodynamic equilibrium phase diagram
For Fe-Co alloy

Phase	Composition (at. % Fe)	Structure	Prototype
α'	25 to 75	B2	CsCl

[68]. This was understood to arise due to the lesser mobility of the W, Nb and Mo solutes. A more detailed investigation of the FeCo-Mo system was subsequently carried out to observe differences in *kinetic paths* of the Warren-Cowley short-range order parameters $\alpha_{\text{Mo/Fe}}$ and $\alpha_{\text{Co/Fe}}$ at different temperatures [69]. The kinetic paths at 350°C and 400°C were indeed observed to be different albeit not as much as predicted from model calculations. The temperature dependence of *kinetic paths* was attributed to the high activation energy barrier for diffusive jump of Mo atoms.

In this section we will discuss our studies on the kinetic behavior of the FeCo-X alloys prepared in the nanocrystalline state by the process of mechanical alloying to see the effect of the nanocrystalline nature of the alloys on the ordering process. The kinetic evolution of B2 order in nanocrystalline FeCo-X alloys was studied at different temperatures using Mossbauer spectroscopy and powder XRD techniques. We found that the *kinetic paths* were essentially the same at different temperatures. This suggests that the larger grain boundary regions in these nanocrystalline alloys act as *short circuited* diffusion paths and give rise to an increased rate of diffusion for all the atomic species constituting the alloys [70, ref 194 of chapter 1].

3.3.1 Fe-Co-Mo

a Experimental

FeCo-4 at. % Mo alloys were prepared by direct mechanical milling of the elemental Fe (99.99% purity, fine gray powder from Aldrich-Sigma Chemicals), Co (m2N8, spherical -325 mesh, from Alfa Products) and Mo (m3N±, -200 mesh, from Alfa Products) powders. The sample was initially milled for 24 hours, but this was not sufficient to produce a completely disordered alloy. It was in partially ordered state as evident from the area of the satellite peak in the Mossbauer spectra, being less than mat expected for a

random distribution. The milling time was therefore increased to 50 hours to obtain a completely disordered alloy with the satellite peak area corresponding to that of a binomial distribution of a random alloy. The as-milled alloys were formed in single-phase disordered bcc structure as confirmed by the X-ray diffraction (XRD) pattern. The average grain size obtained from XRD pattern of the as-milled alloy was about 10 nm. Both the 24 h and 50 h milled samples were heat treated under argon atmosphere in borosilicate glass ampoules at a pressure of 0.05 Torr for various periods of time ranging from few minutes to several hours at 250°, 300°, 350° and 400°C to follow the evolution of B2 order in these samples. Mossbauer spectra with good statistics were recorded and the HMF distributions evaluated from the spectra were fitted to two Gaussian, one corresponding to the main peak and the other corresponding to the satellite peak.

b Results and Discussions

Figure 3.46 shows the Mossbauer spectra for the as milled FeCo and FeCo-4 at. % Mo alloys. Also shown in the figure is the difference spectrum between the two alloy systems. The difference spectrum corresponds to a **hyperfine field** of 54 kOe lower than the average hyperfine field for FeCo. This is attributed to the presence of Mo atoms in the 1st near neighbour (1nn) environment of Fe. The presence of satellite lines in FeCo-Mo at lower field values is similar to that observed by adding a few atomic percent solutes to pure iron in several Fe-X (where X = few atomic percent Si, Al, Mn, Cr, Mo etc.) alloys [71]. The observed field shift of 54 KOe for the satellite line is in good agreement with earlier work [68]. The average hyperfine field perturbation caused by 1 Mo atom either in the 1nn or in the 2nn shells of Fe atoms is around 35 kOe [69]. Hence in calculating the binomial probability

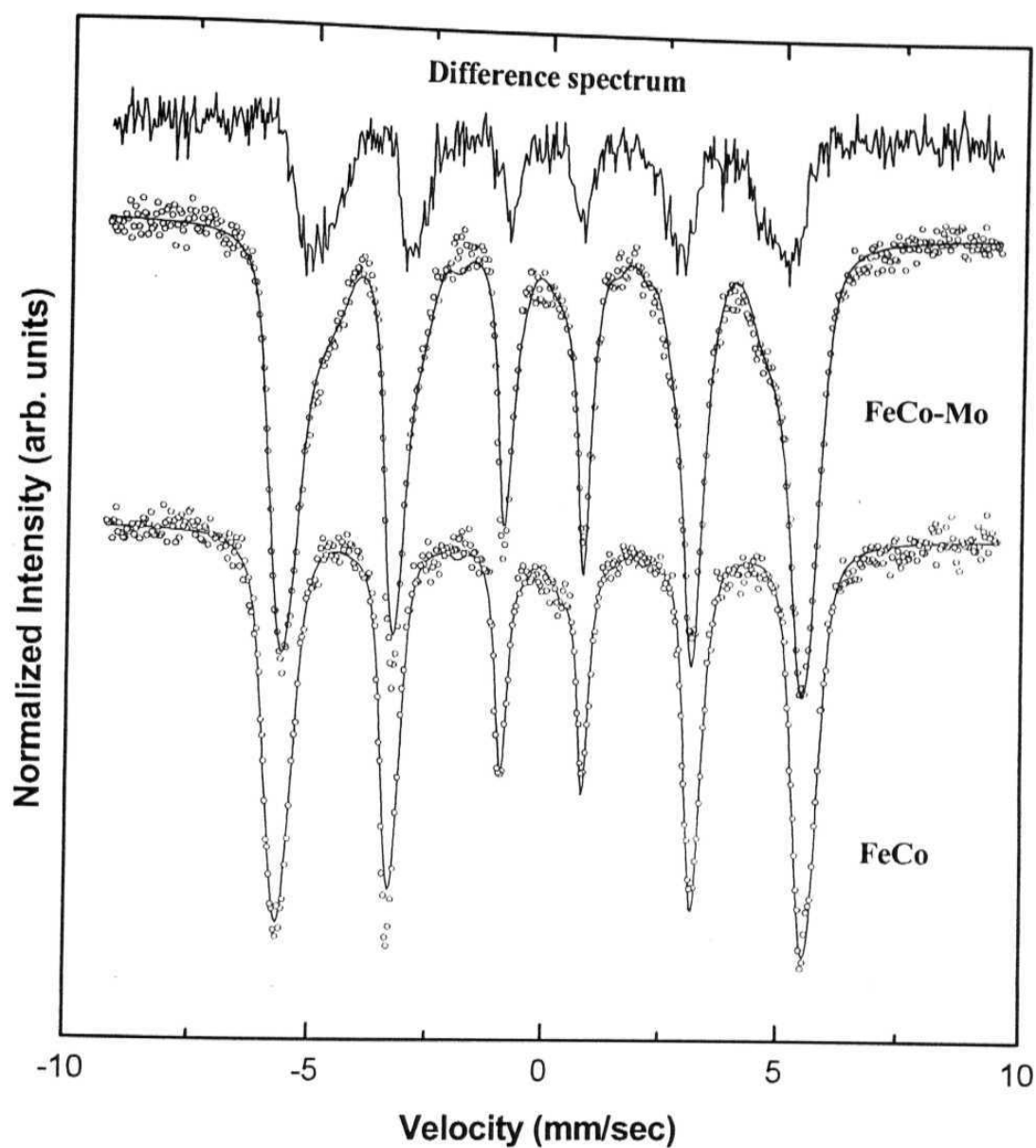


Figure 3.46: Mossbauer spectra for nanocrystalline disordered bcc FeCo and FeCo-4 at. % Mo alloys (symbols: exp, solid lines:fit). The difference spectrum shows that Mo addition to FeCo gives rise to a satellite line corresponding to a reduced hyperfine field value.

distribution for the disordered alloy we considered both the nearest neighbours and probability distribution of the form

$$P_{A2} = \{ {}^8C_x (c)^x (1-c)^{1-x} \} \{ {}^6C_y (c)^y (1-c)^{1-y} \} \quad (3.14)$$

Where c is the concentration of the solute, 8 and 6 are the total possible number of 1st and 2nd nn, and x and y are the number of solute atoms in these nn shells.

The experimentally obtained Mo satellite peak area corresponded well to a random distribution of 1 Mo atom in the first nearest neighbour shell of Fe and 0 Mo atom in the 2nd as calculated using $x=1$ and $y=0$ in the above binomial distribution, which confirmed the formation of a disordered bcc (a phase) homogeneous solid solution in the as-milled state.

After ordering heat treatments the width of the main peak as well as the intensity of the satellite peak decrease as shown in Figure 3.47. The area of the main peak on the other hand increases. The hyperfine magnetic field distributions evaluated from the Mossbauer spectra are shown in Figure 3.48. The Mossbauer Spectrum for as milled FeCo sample shows a six line magnetic hyperfine field split pattern with broadened lines, having outer line width equal to 0.52 mm/sec as compared to 0.30 mm/sec for natural Fe. The hyperfine magnetic field is determined to be 349.4 kOe from the splitting of the outer lines. Ordering of the alloy by heat treatment at 400° C for 24 hours gave narrower lines and a hyperfine magnetic field of 343.8 kOe. These results are in good agreement with earlier reported value for quenched and annealed samples [72]. This shows that B2 ordering in FeCo decreases the magnetic hyperfine field at Fe sites relative to the disordered state of the alloy.

From these observations and also from earlier studies of disorder→B2 order transformation in pure FeCo it is known that the width of the hyperfine distribution decreases with increase in chemical order due to a change in 1nn

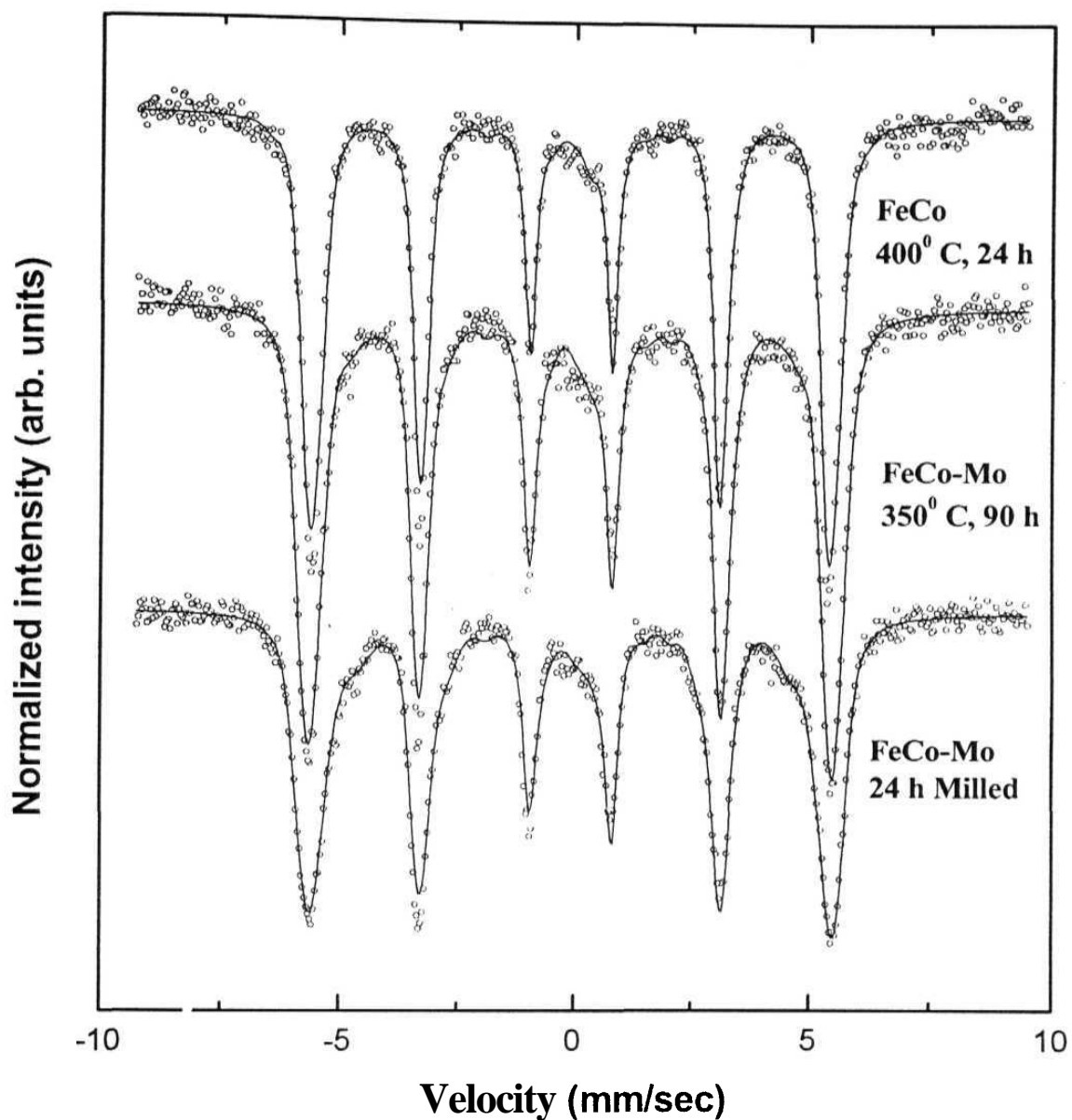


Figure 3.47: Mossbauer spectra showing the effect of ordering heat treatments in FeCo and FeCo-Mo. There is a decrease in line broadening for both systems and also a decrease in satellite line intensity for FeCo-Mo.

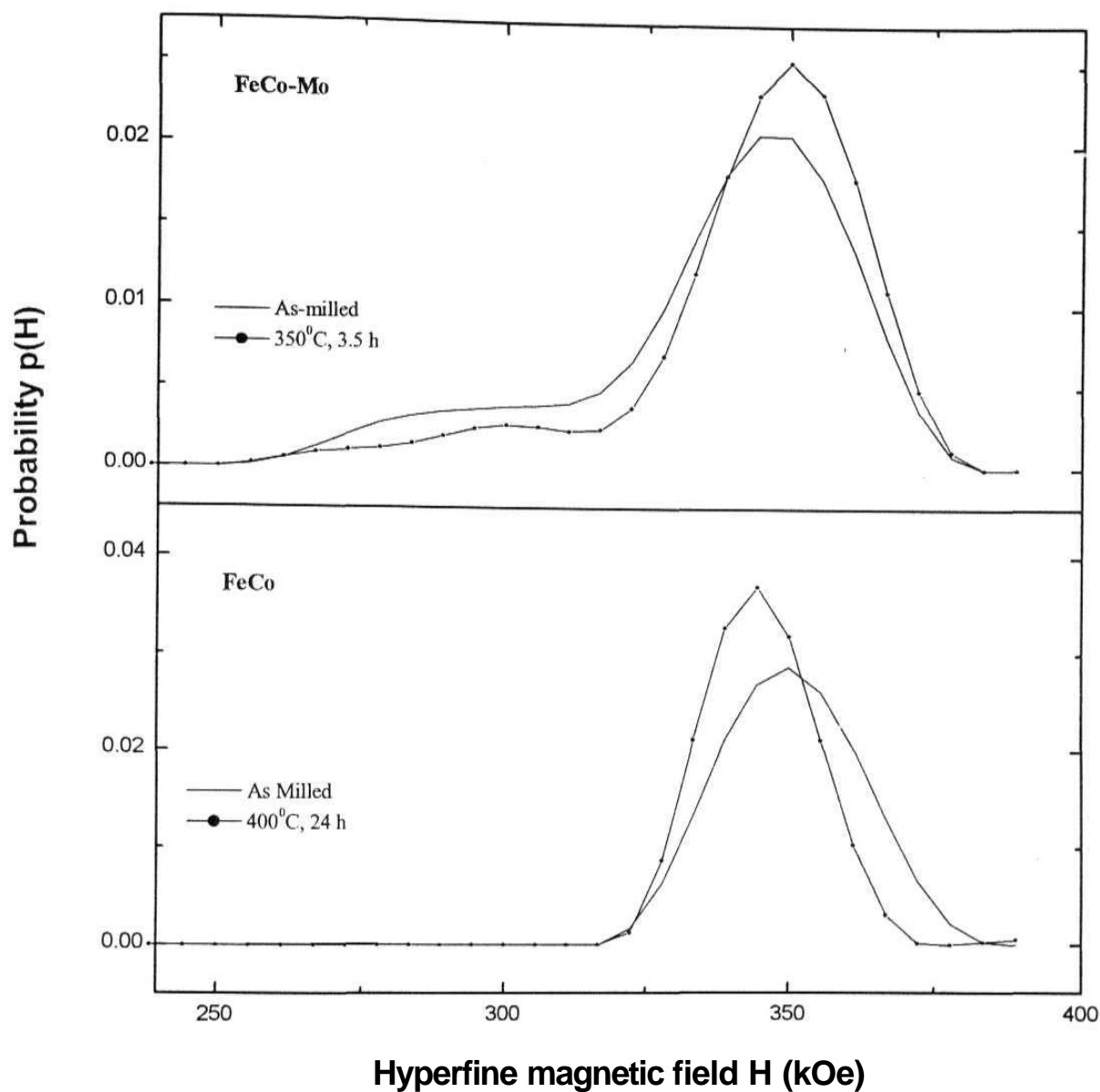


Figure 3.48: Hyperfine magnetic field distributions evaluated from the Mossbauer spectra. The evolution of B2 order is reflected from the decrease in the widths and increase in the intensities of the main peak as well as from the decrease in the intensity of the satellite peak.

environment from a random distribution to that of an ordered arrangement of all Co neighbours. The width of the main peak is therefore an appropriate measure of the $\langle \text{Co/Fe} \rangle$ correlation. Similarly as the order develops more and more configurations correspond to Fe atoms with Co neighbours and the area of the main peak increases; therefore this area can also be considered as a measure of the $\langle \text{Co/Fe} \rangle$ correlation.

The area of the satellite peak corresponds to the $\langle \text{Mo/Fe} \rangle$ correlation. A decrease in Mo satellite area (Figures 3.47 and 3.48) as ordering takes place, shows that Mo atoms move away from 1nn shell of Fe to a Co near neighbour environment. This is in agreement with the metallic bonding theory of Miedema [73] according to which Co-Mo bonding is preferred to Fe-Mo bonding.

Figures 3.49 and 3.50 show the *kinetic paths* for the nanocrystalline FeCo-4 at. % Mo alloy at different temperatures in the space spanned by the order parameters $\langle \text{Mo/Fe} \rangle$ and $\langle \text{Co/Fe} \rangle$. These plots include points for both the 24 h milled and 50 h milled alloys. It is interesting to note that these paths are essentially the same within experimental errors at all the temperatures and for both the initial states of the alloys.

This observation should be compared to the behavior of piston-anvil quenched polycrystalline FeCo-Mo alloys [69], in which these *kinetic paths* were seen to be distinctly different at 350°C and 400°C. The absolute rate of change of these correlations at these temperatures in nanocrystalline alloys were also seen to be substantially faster as compared to those observed in the previous study [69]. This observation prompted us to study the evolution of order at a lower temperature of 250°C to see whether a higher activation barrier for Mo diffusion would give rise to difference in kinetic path at a lower temperature. The rate of change of correlations was observed to be slower, as expected at a lower temperature, but the kinetic path followed was the same as that at 350 and 400°C.

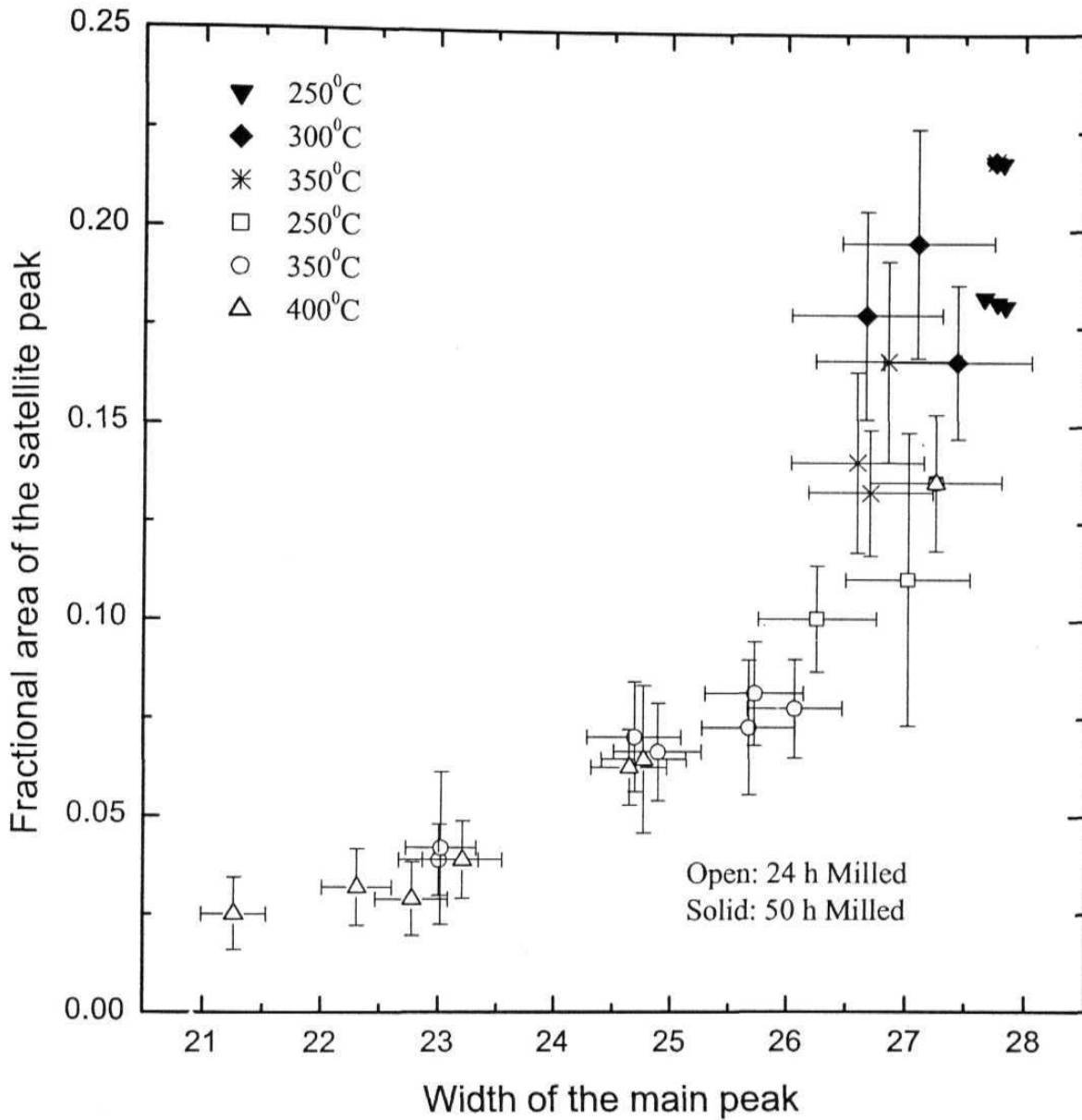


Figure 3.49: Kinetic paths for B2 ordering in nanocrystalline FeCo-Mo at different temperatures. The $\langle \text{Co/Fe} \rangle$ and $\langle \text{Mo/Fe} \rangle$ correlations are measured by the width of the main peak and the intensity of the satellite peak, respectively.

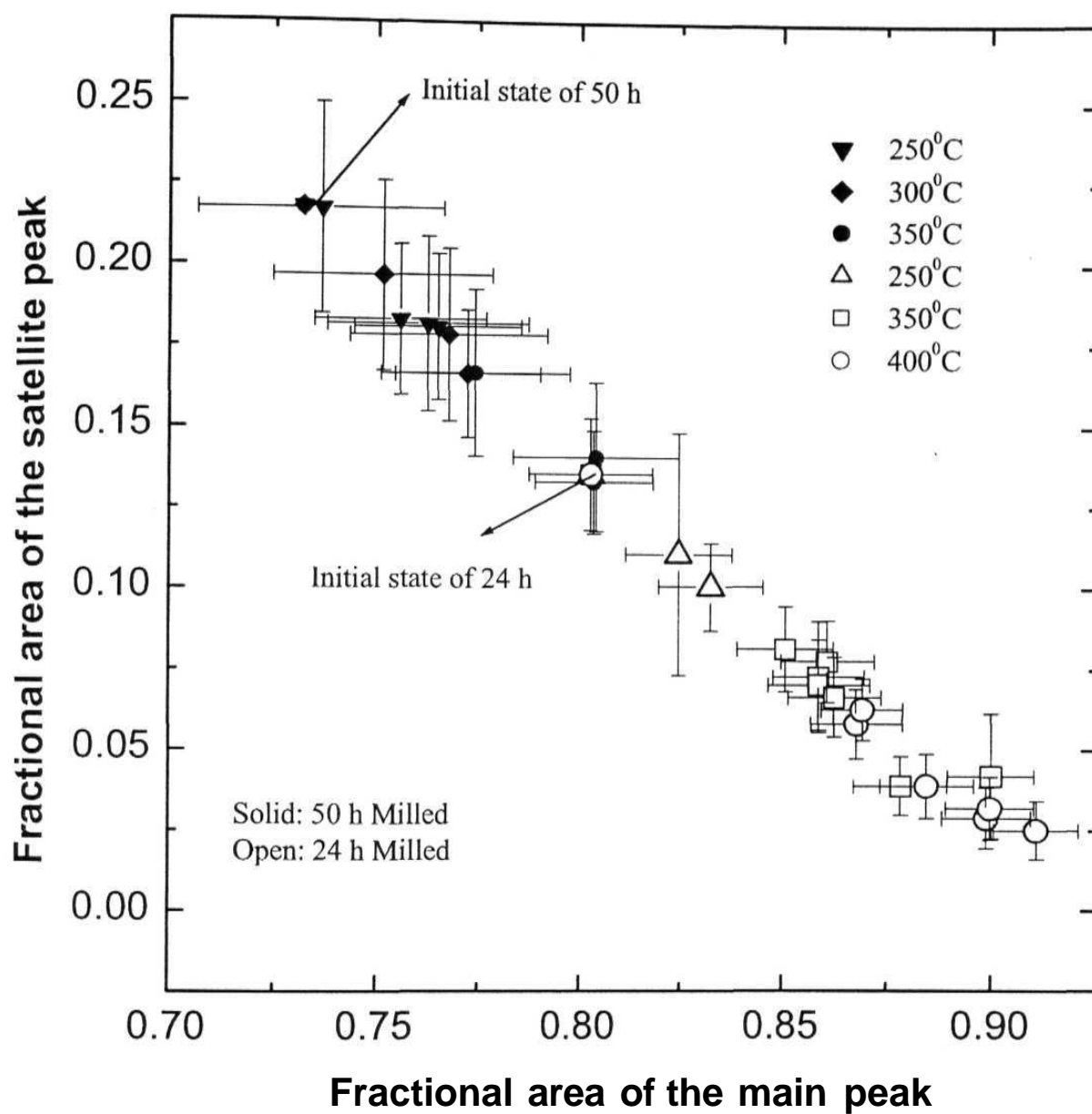


Figure 3.50: An alternative representation of the kinetic paths for B2 ordering in terms of the intensity of the satellite peak and the intensity of the main peak.

We are therefore convinced that the kinetic path behavior of the nanocrystalline system is intrinsically related to the nanocrystalline nature of the ball-milled alloys. The main difference between the macrocrystalline and nanocrystalline systems is the presence of large volume fraction of grain boundary regions. These boundary regions provide *short-circuited paths* for diffusion of atoms [70, ref 194 of chapter 1]. The activation energy of diffusion for the different atoms along these *short-circuited paths* may not be substantially different and thus give rise to identical *kinetic paths* for ordering.

3.3.2 FeCo-Ge System

The evolution of B2 order in a disordered Fe-48 at. % Co- 4 at % Ge alloy was studied. We followed the kinetics of first neighbour $\langle \text{Fe/Co} \rangle$ and $\langle \text{Fe/Ge} \rangle$ correlation and obtained the kinetic paths to determine their temperature dependency. The disordered alloy was prepared by MA and was subjected to heat treatments at 200, 250, 300, 350 and 400° C under Argon atmosphere for various periods of times to study the evolution of B2 SRO in the system. Homogeneous and chemically disordered bcc (a) phase alloy was produced as a result of MA as shown by the Mossbauer Spectra (figure 3.51) and the corresponding HMF distributions (figure 3.52) of FeCo and FeCo-Ge alloys. The presence of the satellite peak for the Fe-48 at. % Co-4 at. % Ge as milled sample is evident (figures 3.51 and 3.52), which is attributed to the presence of Ge in the first nn shell of Fe. The field shift between the main peak and the 1 Ge 1nn peak is 24.9 kOe, in good agreement with the field shift of 24 kOe observed in Fe-6 at. % Ge alloy [74]. The HMF distributions were fitted to two Gaussian, one corresponding to main peak and the other corresponding to satellite peak. The experimentally obtained Ge satellite peak area corresponded well to a random distribution of 1 Ge atom in the first nearest neighbour shell

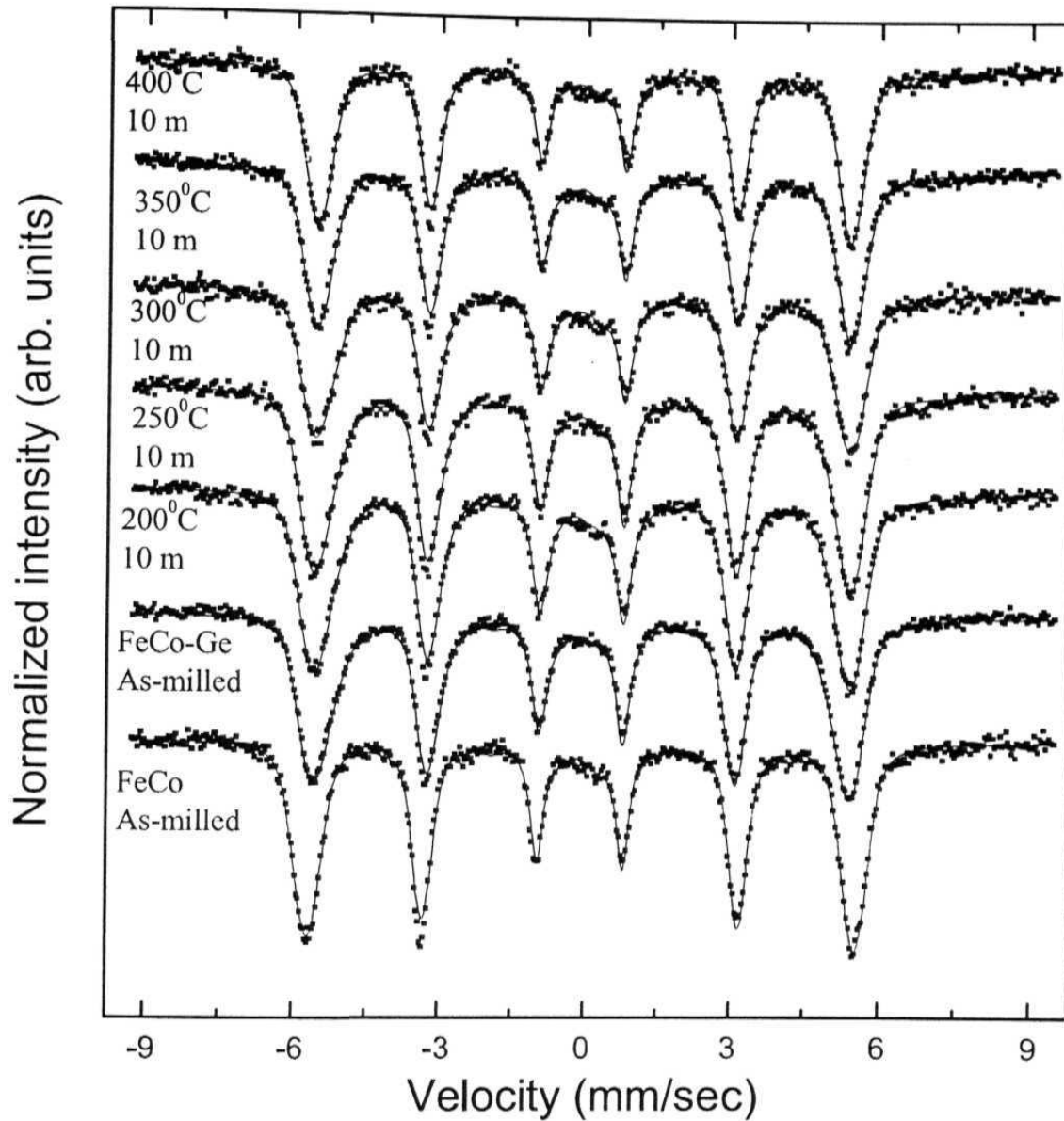


Figure 3.51: Mossbauer spectra of the as-milled Fe-Co and FeCo-Ge alloys, showing the presence of satellite line in the Ge containing sample. Mossbauer spectra of different heat-treated samples of FeCo-Ge alloy showing the evolution of B2 order in the system.

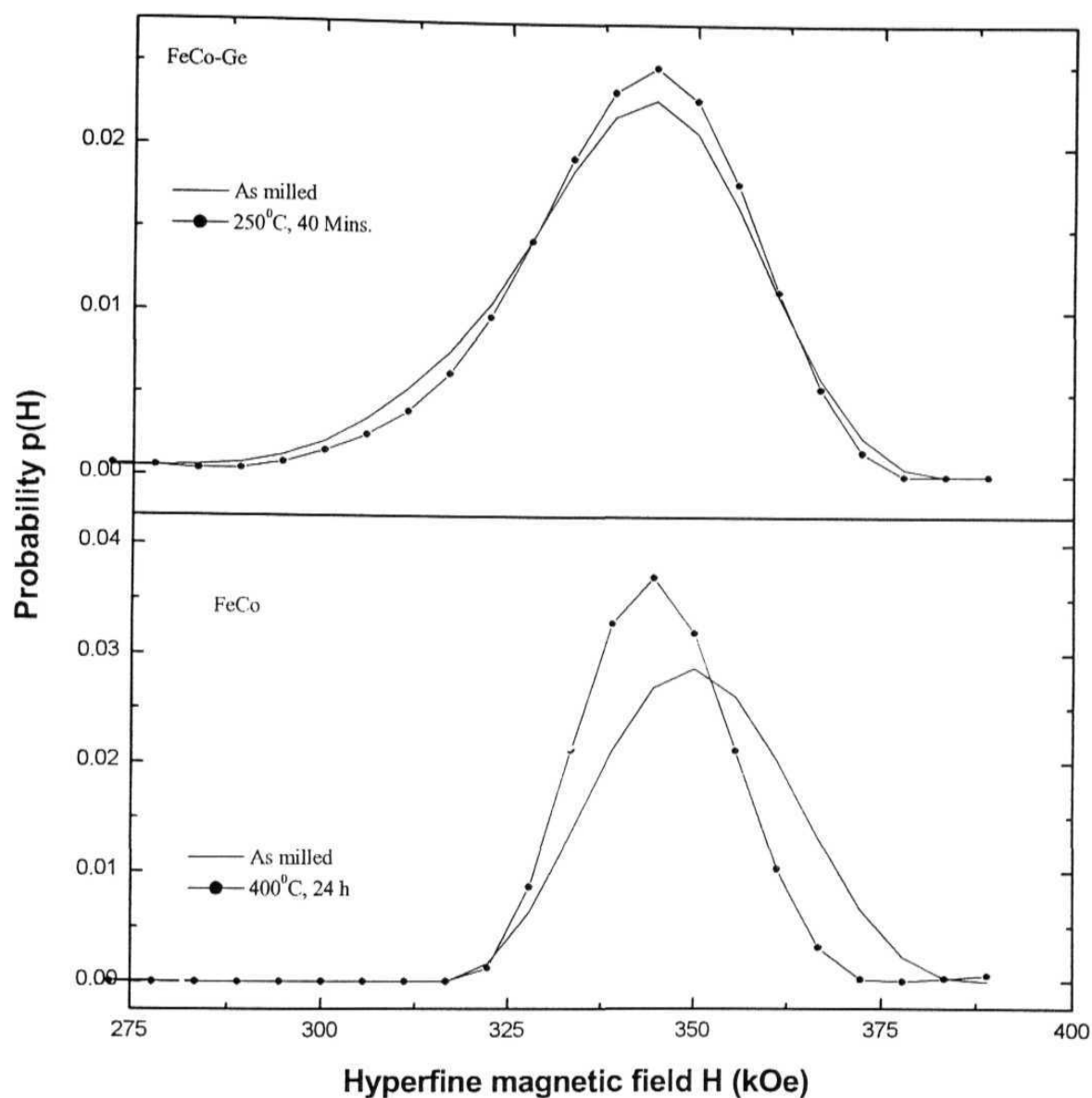


Figure 3.52: HMF distributions of as-milled Fe-Co and FeCo-Ge alloys showing the formation of the alloy in a phase. The evolution of B2 order on ordering heat-treatment accompanied by the depletion of Ge atoms from the 1nn environment of Fe is seen from the decrease in the satellite peak area and increase in the main peak area in the corresponding field distributions of the heat-treated samples.

of Fe (equation 3.1), which confirmed the formation of a disordered bcc (a phase) homogeneous solid solution in the as-milled state. The grain size of the as-milled alloy was determined to be approximately 10 nm.

With the evolution of B2 order on ordering heat treatments the Ge atoms depleted from the Fe nearest neighbour environment causing a decrease in the satellite peak areas as shown in figures 3.51 and 3.52, the area of the main peak on the other hand increased. This behaviour was similar to that of FeCo-Mo. The Ge atoms may either migrate to the grain boundaries or go to the nearest neighbour environment of Co, which are 2nd or more distant neighbours of Fe atoms and hence the effect of Ge atoms on Fe HMF is much less pronounced. Figure 3.53 shows the kinetic paths at 200 and 250 C through the space spanned by the areas of the main and satellite peaks which in turn represent $\langle \text{Fe/Co} \rangle$ and $\langle \text{Fe/Ge} \rangle$ correlations. The kinetic paths were not plotted for other temperatures, as the reduction rate of the satellite peak areas was very high at higher temperatures resulting in situations where satellite peaks were hardly detectable even after 10 minutes of heat treatment. However we observed that the kinetic paths at these two different temperatures fell on the same line. This suggests that the activation barrier for Ge diffusion is similar to that of Fe and Co through *shorted circuited diffusion paths* provided by the grain boundaries in this nanocrystalline alloy.

3.3.3 FeCo-W System

The kinetic evolution of B2 order in disordered FeCo-W system was studied with the idea that whether the bigger size of the Tungsten (W) atoms in comparison to that of Mo or Ge atoms had any effect on the kinetic paths or in other words different microstructure formations towards the attainment of equilibrium ordered structure. An attempt was made to correlate the grain growth behaviour with the ordering process in this alloy system and we will

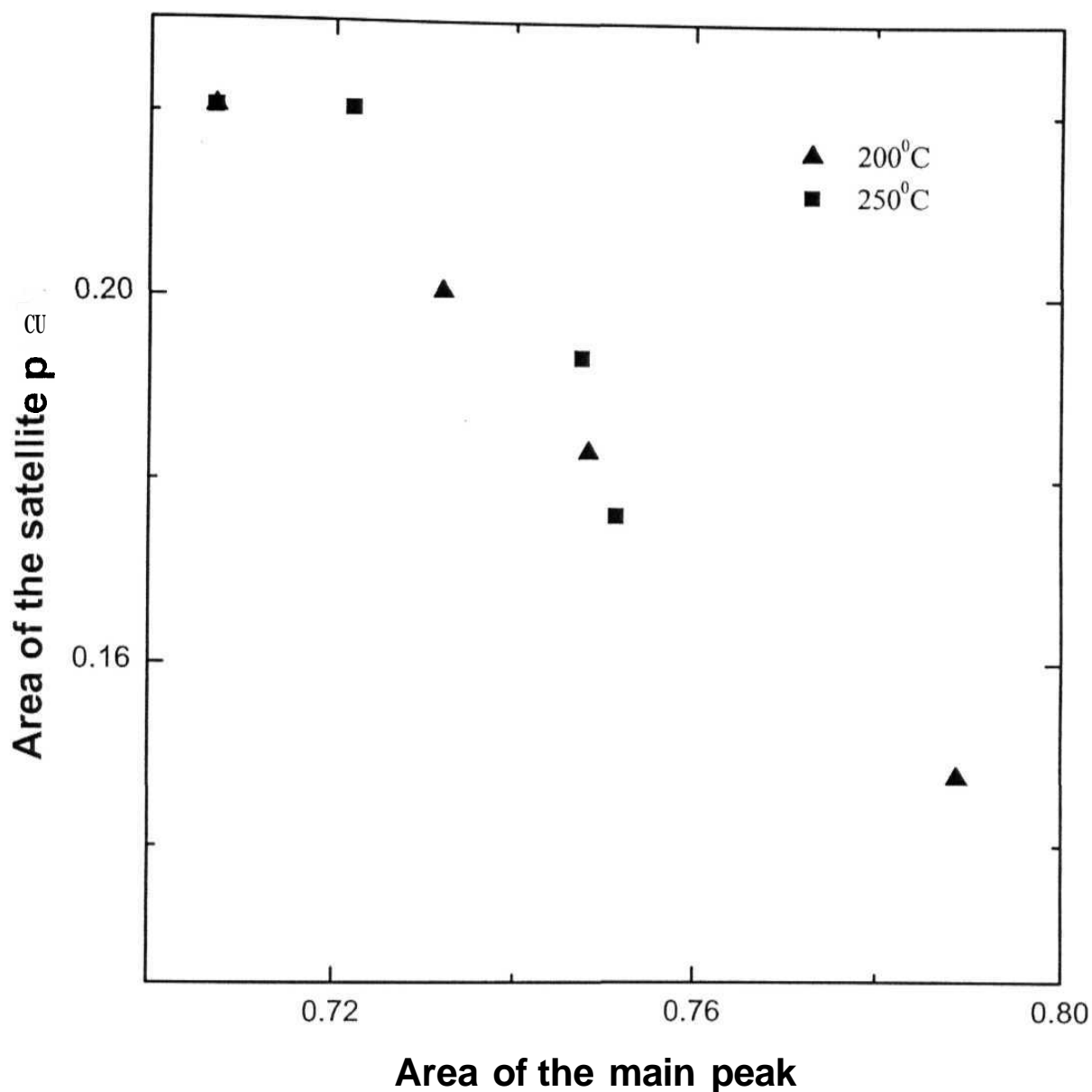


Figure 3.53: Kinetic paths in the space spanned by the $\langle \text{Fe/Ge} \rangle$ and $\langle \text{Fe/Co} \rangle$ correlations (represented by the areas of the 1 and 0 Ge 1nn peaks, respectively) at 200 and 250°C. It is seen that the paths for the evolution of B2 order at these two different temperatures are the same.

see that the underlying atomic diffusion responsible for grain growth as well as ordering process is the same.

Powder mixtures satisfying the composition $\text{Fe}_{0.48}\text{Co}_{0.48}\text{W}_{0.04}$ were subjected to MA. Initially the powder mixture was milled for 24 hours, which was found not to be sufficient for the homogeneous disordered bcc alloy to form. The presence of unmixed W lines in the powder XRD pattern was observed after 24 hours. The unmixed W lines in the X-ray patterns were indexed according to the JCPDS-1CDD (1999) data of pure W with PDF numbers 01-1203, 01-1204 and 04-0806. Hence the powder mixture was milled consecutively up to a total time of 123 hours till the disordered alloy was formed. XRD patterns and Mossbauer spectra were recorded at each stage of milling to monitor the formation of the alloy. Figure 3.54 shows the sequence of XRD patterns for different times of milling. The final composition after milling for 123 hours was $(\text{FeCo})_{0.97}\text{W}_{0.03}$ as determined by EDAX measurement. The Mossbauer spectrum of the final as-milled sample is shown in figure 3.55; the presence of satellite line due to presence of W atoms in the nearest neighbour environment of Fe is evident in the spectrum as well as in the corresponding HMF distribution. The HMF perturbations due to 1nn and 2nn W atoms of Fe atoms were found to be around 46 and 25 kOe respectively from the earlier measurements [ref 32 from chapter 2]. The contributions from both the nn are substantial and in determining the satellite peak area for the disordered alloy we need to use equation 3.14. The field shift of around 50 kOe for the satellite peak (w.r.t to the main peak at around 350 kOe) in our experimental data is in accordance with the 1nn 1 W HMF perturbation. The field distribution was fitted to two Gaussian, corresponding to main and satellite peaks respectively, and the experimental area of the satellite peak after 123 hours of milling matched well with the calculated probabilities with $x=1$ and $y=0$ and $c=0.03$ in equation 3.14. The above findings from XRD and Mossbauer spectroscopic data confirm the formation of the alloy in a

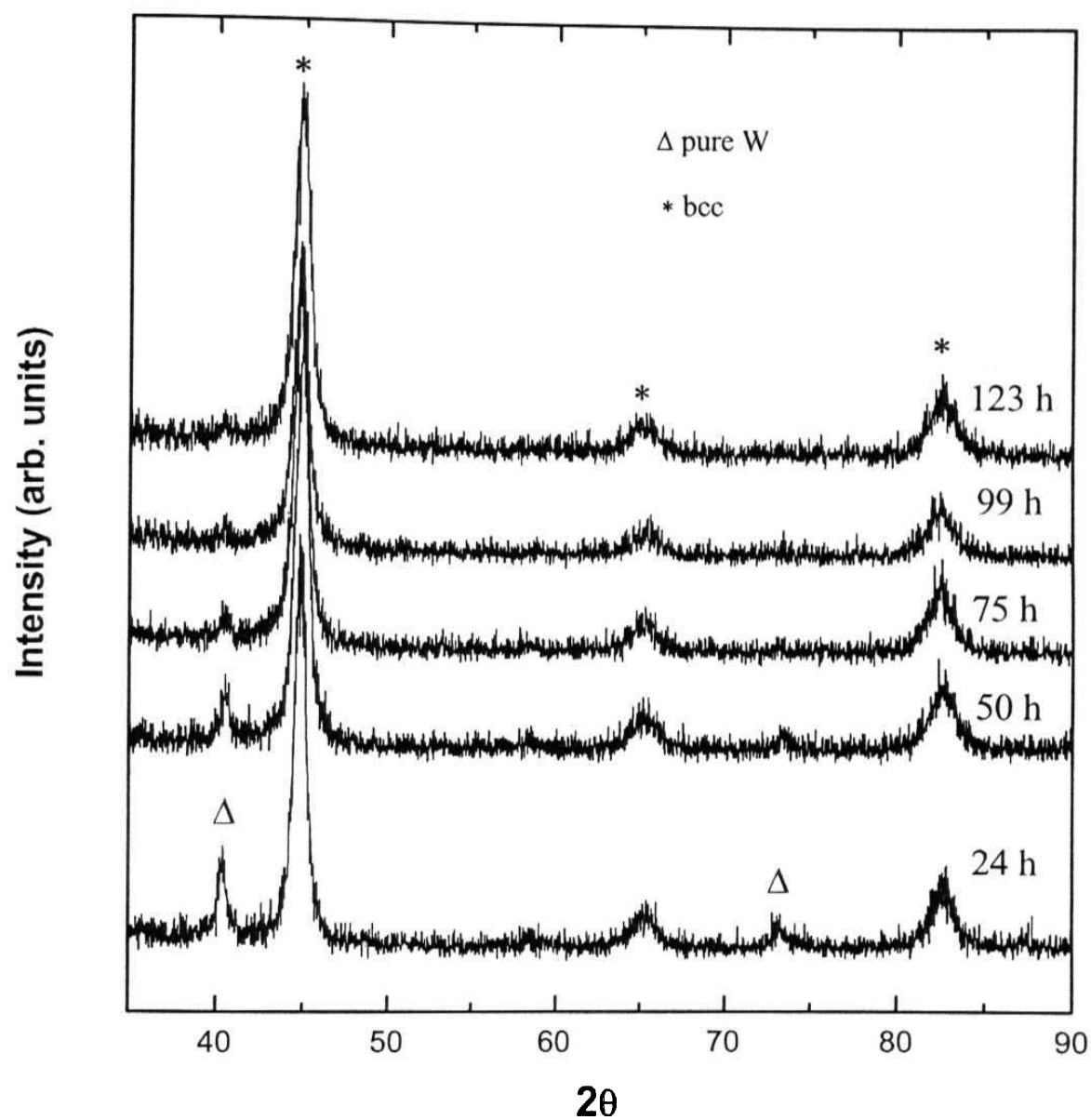


Figure 3.54: XRD patterns recorded at each stage of milling to monitor the formation of the homogeneous FeCo-W alloy.

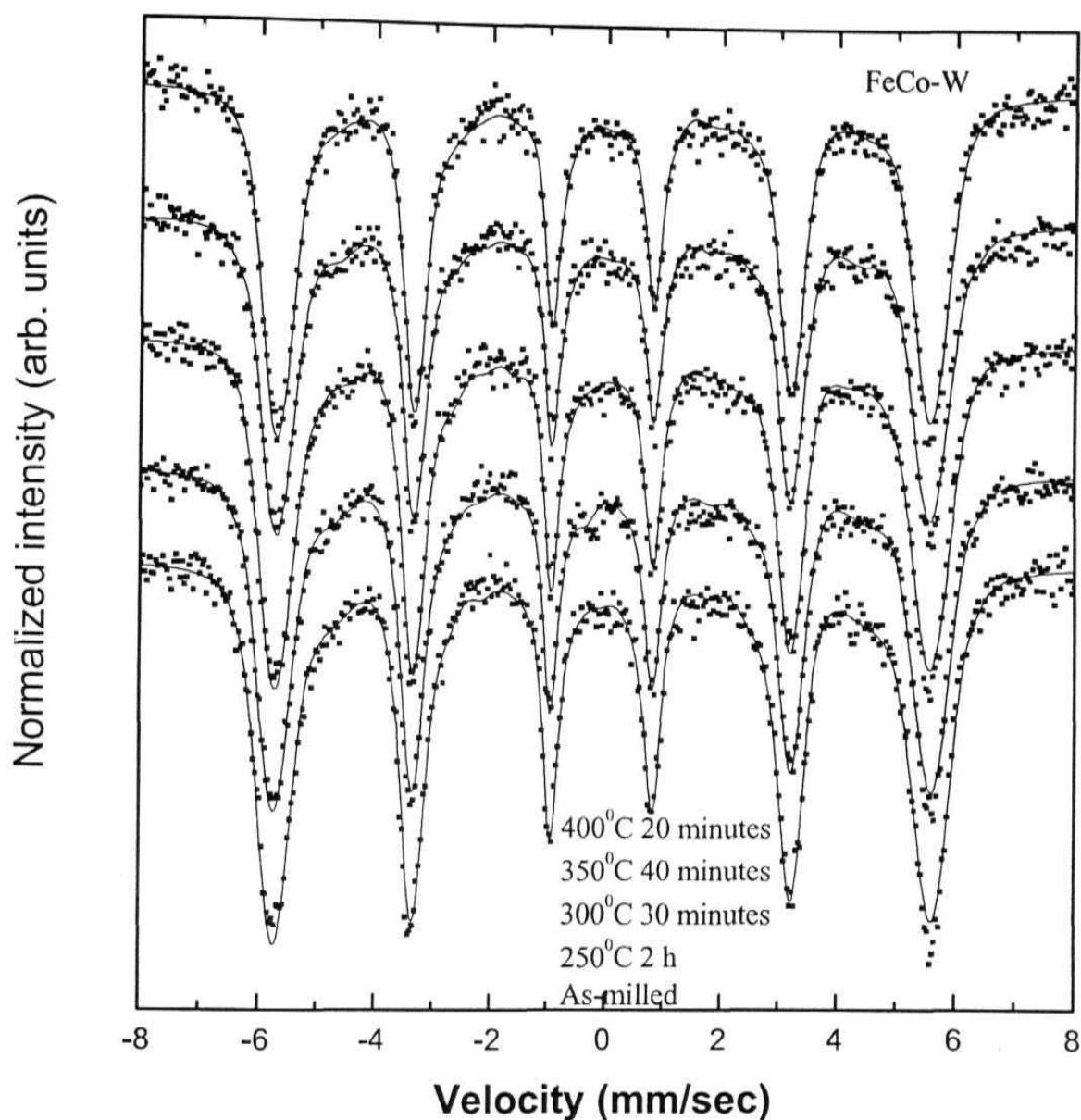


Figure 3.55: Mossbauer spectra of the as-milled and various heat treated samples (symbols:exp; line:fit) show the decrease in the satellite peak intensity and increase in main peak intensity as the B2 order evolves from the disordered matrix. The sequence of the spectra (top-bottom) is according to the sequence of the legends.

disordered bcc (a) phase after 123 hours of milling. The as-milled grain size obtained from the line broadening of the X-ray line was around 9.5 nm.

The as-milled alloy was subjected to ordering heat treatments at 250, 300, 350, and 400°C for periods of times ranging from few minutes to few hours. On ordering heat treatments the W atoms depleted from the Fe nearest neighbour environment causing a decrease in the satellite peak areas as shown in the representative Mossbauer spectra and corresponding HMF distributions in figures 3.55 and 3.56. But there were no extra lines apart from the bcc lines observed in the X-ray spectra, figure 3.57, which indicates that like Ge and Mo atoms W atoms also migrated to GB regions or in the nearest neighbour environment of Co atoms, but no W-Co or pure W phase was precipitated. Figure 3.58 shows the kinetic paths at different temperatures in the space spanned by the Gaussian areas, which represents the $\langle \text{Fe/Co} \rangle$ and $\langle \text{Fe/W} \rangle$ correlations. The kinetic paths are same for all temperatures within experimental errors or rather they are temperature independent. Figure 3.59 shows another representation of kinetic paths in the space spanned by area of the satellite peak ($\langle \text{Fe/W} \rangle$ correlations) and width of the main peak ($\langle \text{Fe/Co} \rangle$ correlations). All the points in this figure lie in the same path independent of temperature. We, therefore, obtained for this system also same kinetic paths at all temperature which shows that different sizes and diffusivities of the constituents atoms does not make any difference on the kinetic paths of ordering as long as the *short circuited diffusion paths* for atomic diffusion through grain boundaries are present in the nano phase.

The narrow wing of X-ray lines (figure 3.57) on heat treatment, show grain growth and the kinetics of grain growth at different temperatures is shown in figure 3.60 by solid symbols. Hollow symbols in this figure depicts the kinetics at different temperatures of the main Gaussian peak area which increases on ordering by W depletion from Fe environment resulting in more and more Co neighbours of Fe. It can be seen from this figure that the grain

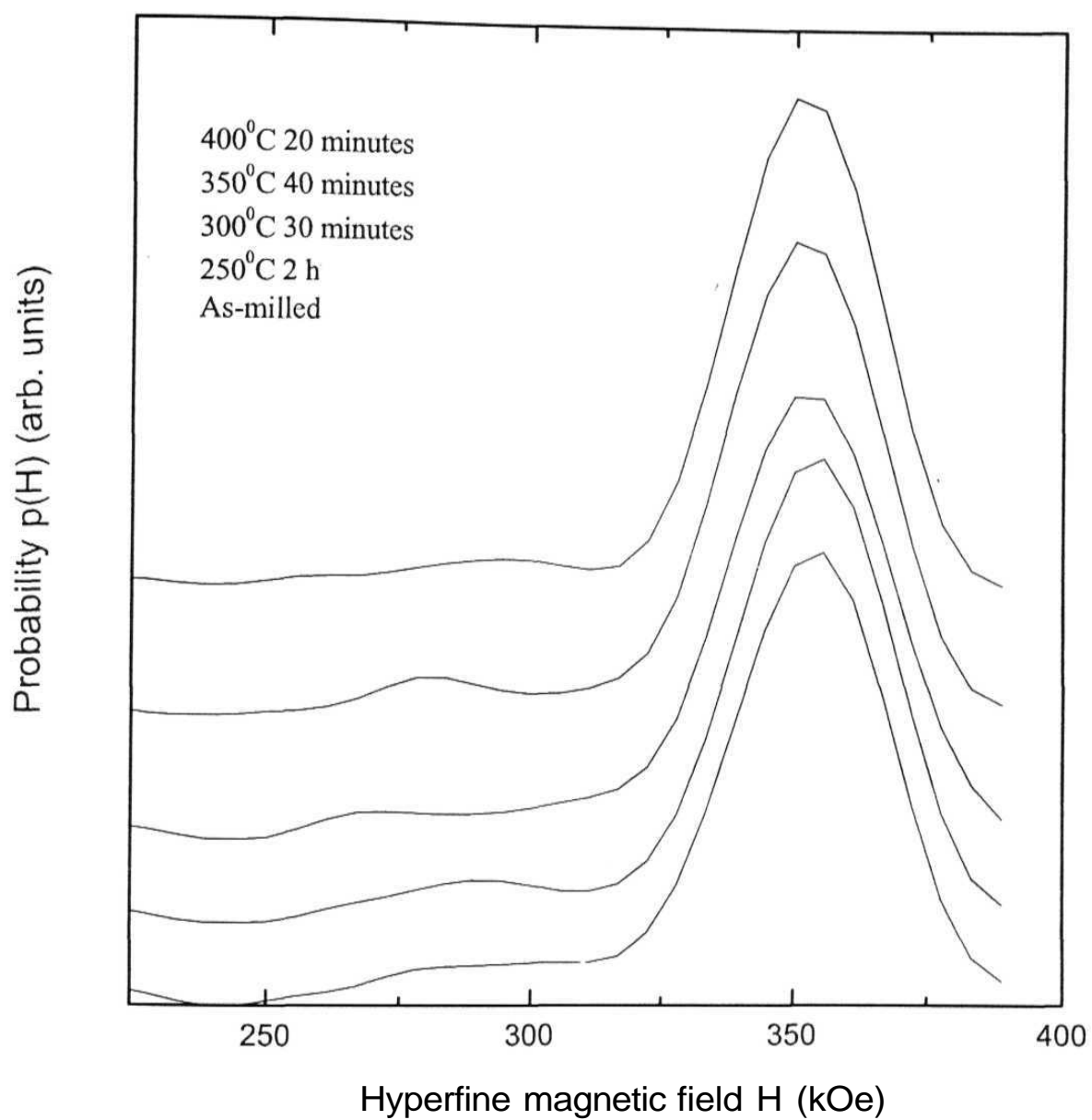


Figure 3.56: HMF distributions showing the depletion of W from Fe neighbourhood as ordering proceeds. The legends correspond to the curves from top to bottom.

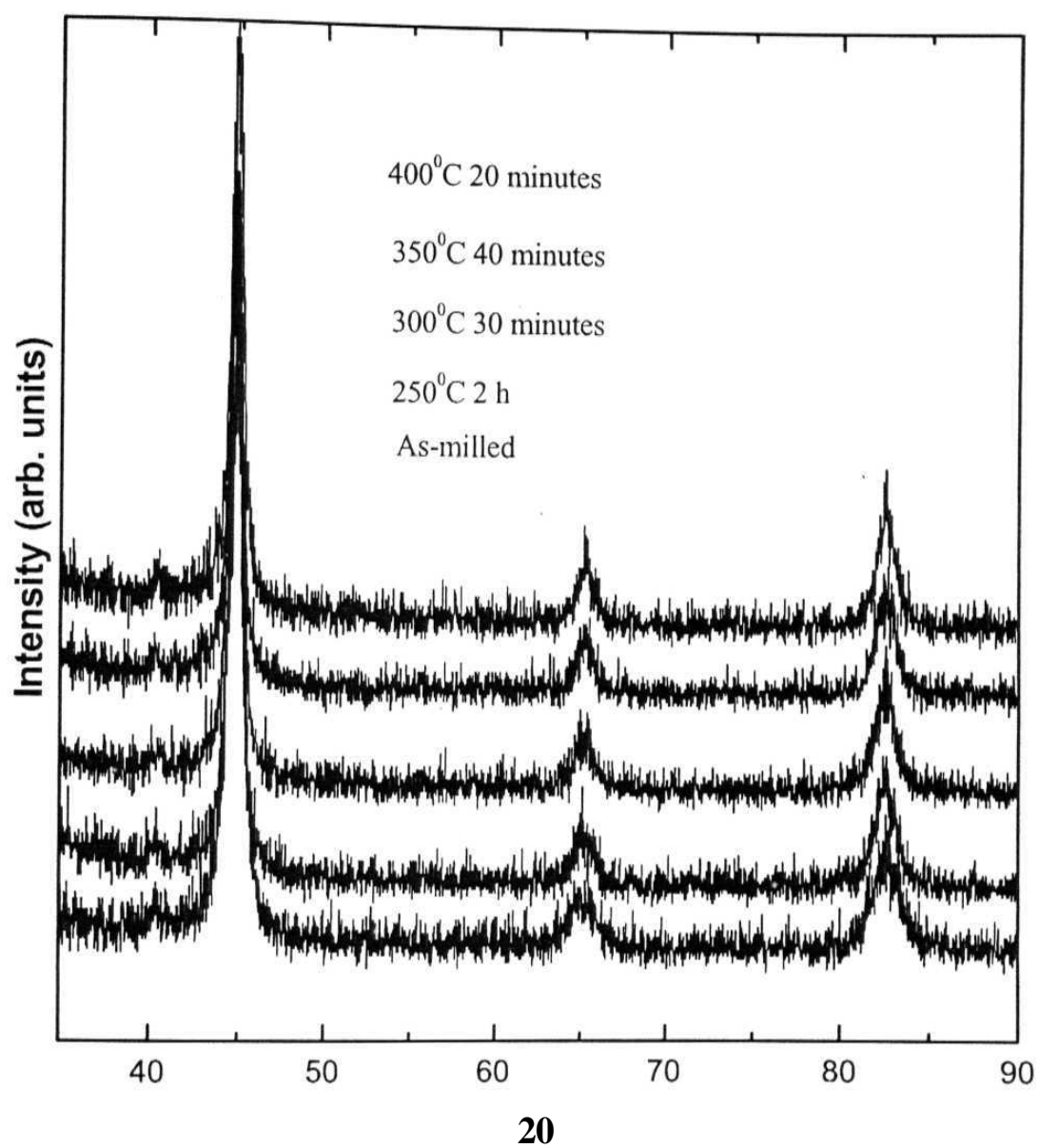


Figure 3.57: XRD patterns (in the sequence of the legends, top-bottom) of the as-milled and heat-treated samples showing the presence of only bcc lines.

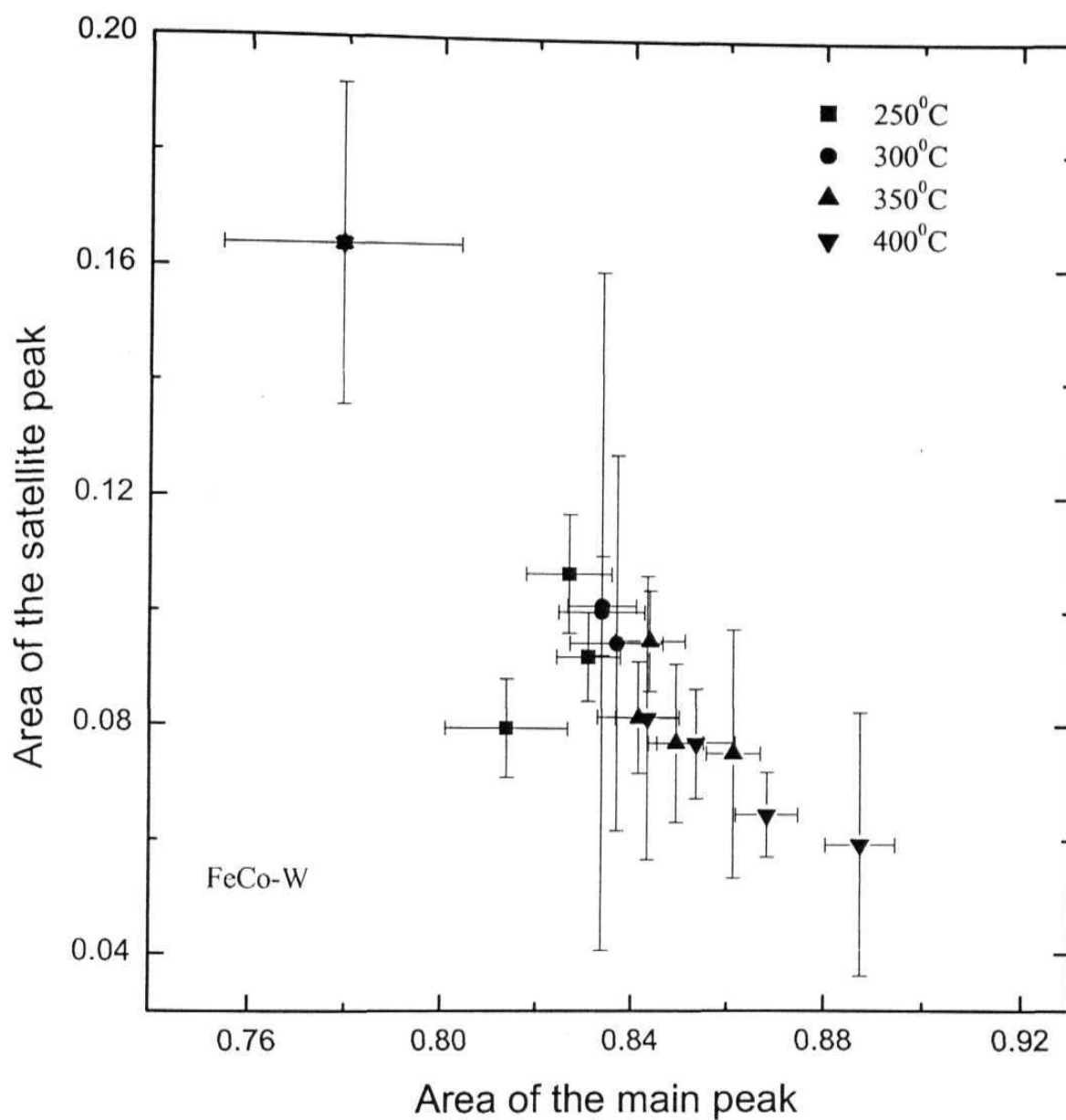


Figure 3.58: Showing same kinetic path at different temperatures for the B2 order evolution.

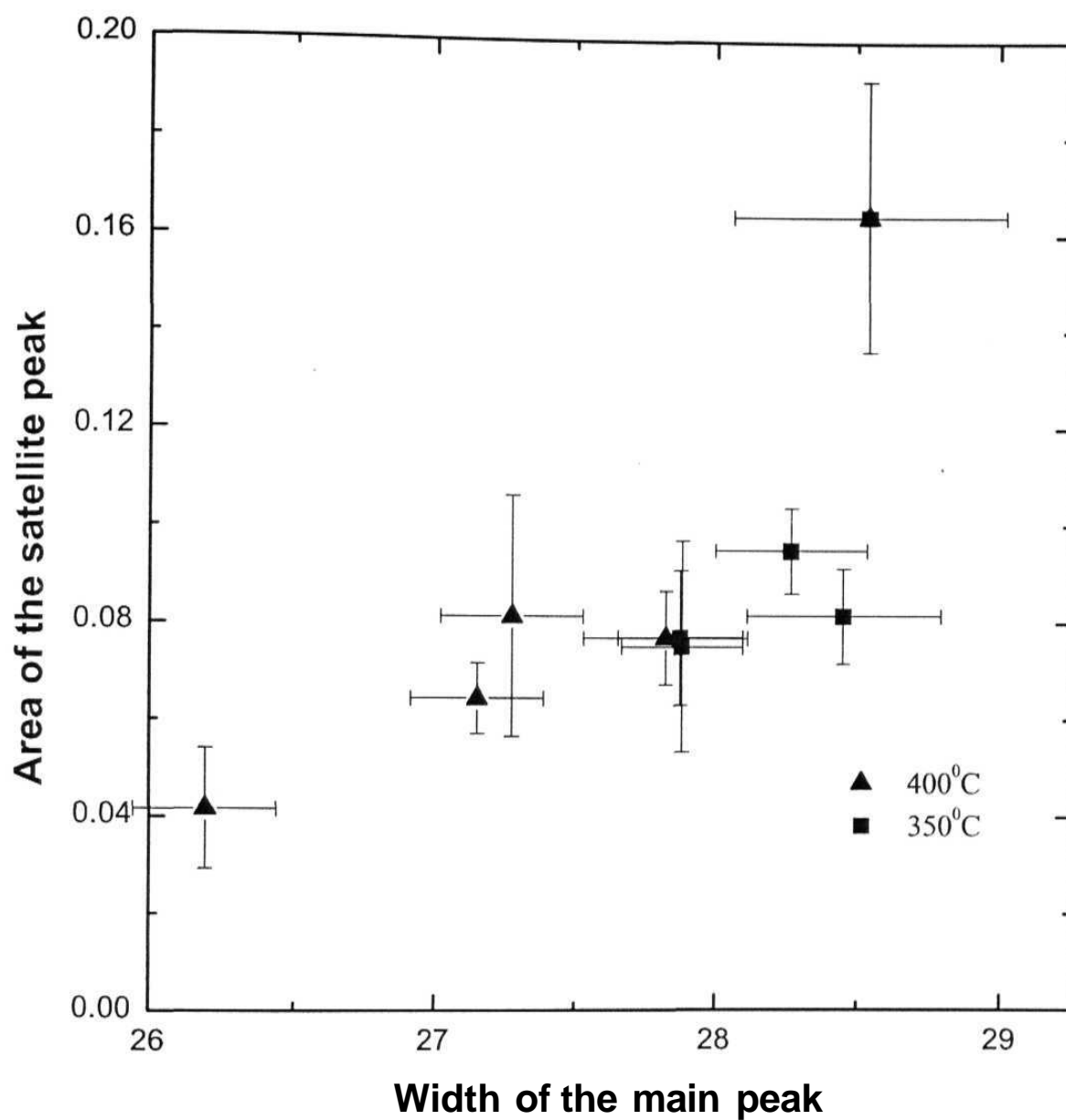


Figure 3.59: Alternative representation of kinetic paths in the space spanned by the area of the satellite peak and width of the main peak shows temperature independent B2 order evolution paths.

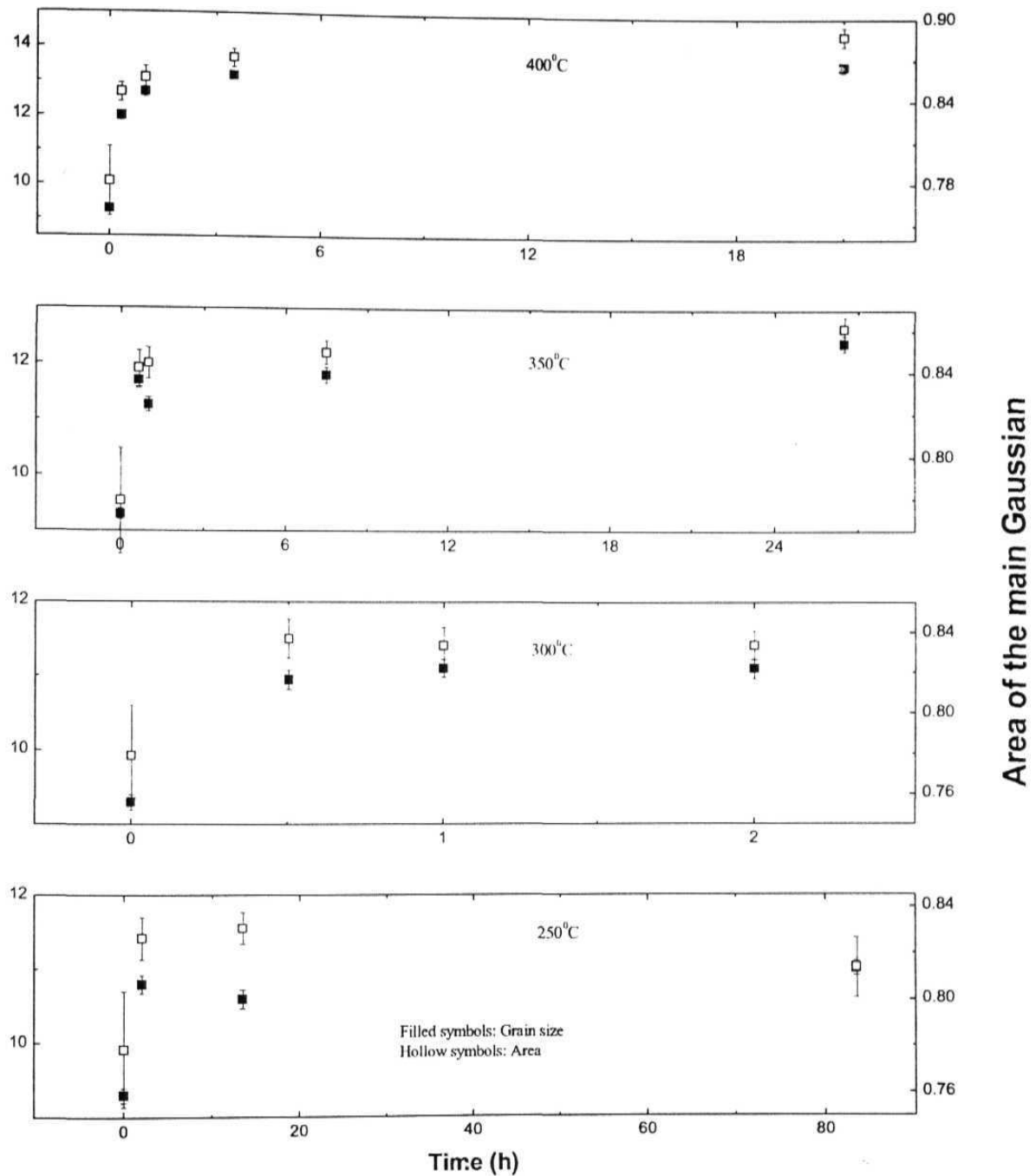


Figure 3.60: Showing the kinetics of grain growth and ordering at different temperatures, for the FeCo-W alloy. Similar kinetics of grain growth and B2 order evolution is seen.

growth and ordering kinetics is essentially the same within experimental errors and they are of first order following equation 3.11. Figure 3.61 shows the important parametric plots between grain size and width and area of the main peak and between grain size and area of the satellite peak. The linear correlation between the grain size and areas of the peaks as well as grain size and width of the main peak independent of temperature and time indicates that the underlying driving force for grain growth and ordering is the same and which is minimization of Gibbs' free energy. The atomic diffusion, which is the underlying mechanism for these two processes, takes place over the same time scale. Figure 3.62 shows the temperature (of heat treatment) dependence of grain growth, main and satellite peak areas, and width of the main peak. It could be seen from the comparative plot (in the middle) of grain size and area of the main peak vs. temperature that the temperature dependence of these parameters are also similar within experimental errors like temporal dependence.

In conclusion our study of the kinetic evolution of B2 order in nanocrystalline FeCo-X (X = Mo, Ge, and W) alloys show that the kinetic paths in the space spanned by the two short range order parameters $\alpha_{\text{Co/Fe}}$ and $\alpha_{\text{X/Fe}}$ (represented by $\langle \text{Co/Fe} \rangle$ and $\langle \text{X/Fe} \rangle$ correlations) were independent of temperature within experimental errors. Hence the B2 ordering proceeded along the same path at different temperatures. It may therefore not be possible to develop new ordered microstructures in the nanocrystalline system by simple thermal processing at different temperatures as was found possible for macrocrystalline FeCo-Mo alloys [69], wherein different kinetic paths at different temperatures were observed. The explanation for this difference in the kinetic behavior lies in the larger grain boundary volume in the nano-system as compared to that of microcrystalline alloys, which provide high diffusivity *short circuited* paths for all constituent atomic species in the alloy. The

activation energy barrier for diffusion of X atoms are comparable to that of the host Fe and Co atoms, giving rise to development of both order parameters at the same rate, if we assume that their interaction energies do not vary substantially.

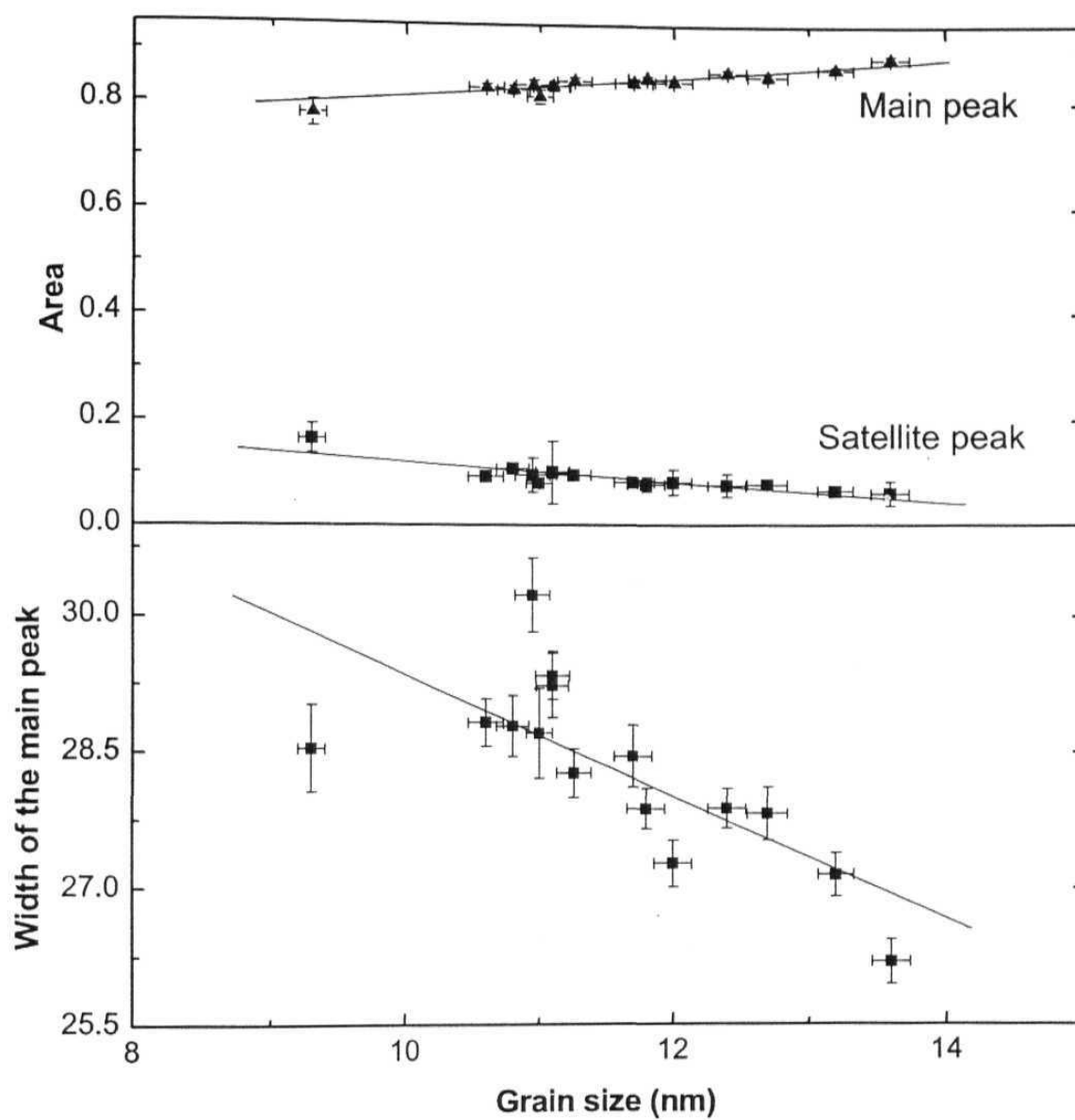


Figure 3.61: Parametric plots showing linear relationship between grain growth and ordering.

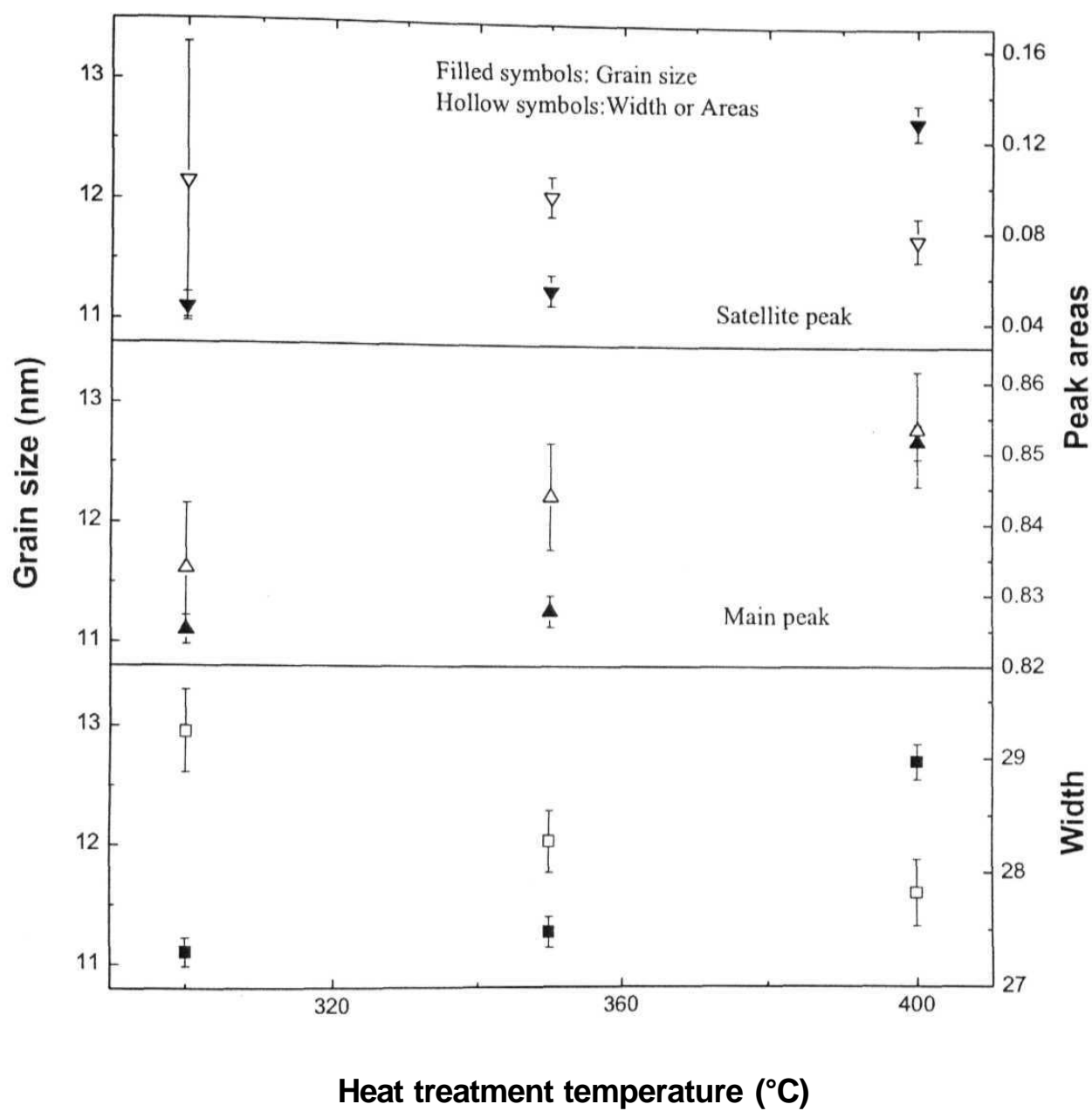


Figure 3.62: Shows the temperature (at which the heat treatment was carried out) dependence of grain growth, main and satellite peak areas, and width of the main peak.

References

- [1] A. Lawley, E. A. Vidoz, and R. W. Cahn, *Acta Metall.* 9, 287 (1961).
- [2] R. Kikuchi, *Ann. Phys.* 10, 127 (1960); *Prog. Theor. Phys. Suppl.* 35, 1 (1996).
- [3] D. W. Clegg and R. A. Buckley, *Matal. Sci.* 7, 48 (1973).
- [4] R. W. Cahn, *Metals, Materials and Processes* 1, 1 (1989).
- [5] L. Anthony and B. Fultz, in *Alloy Phase Stability and Degisn*, edited by G. M. Stocks, D. P. Pope, and A. F. Giamei (*Mat. Res. Soc. Symp. Proc.*, Pittsburgh, PA 1991), Vol. 186, p. 181.
- [6] *Diffusion in Ordered Alloys*, edited by B. Fultz, R. W. Cahn, and D. Gupta (TMS, Chicago, Illinois, 1992).
- [7] B. Fultz, *J. Mater. Res.* 7, 946 (1992).
- [8] R. W. Calm, in *Physics of New Materials- A Status Report*, edited by F. E. Fujita (Springer-Verlag, Berlin, Heidelberg, 1994), p. 179.
- [9] G. D. Mukherjee, C. Bansal, and A. Chatterjee, *Phys. Rev. Lett.* 76, 1876 (1996).
- [10] T. Ziller, G. Le Caër, O. Isnard, P. Cenedese, and B. Fultz, *Phys. Rev.* **B65**, 024204 (2001).
- [11] C. C. Koch, D. G. Morris, K. Lu, and A. Inoue, *MRS Bulletin* 24, 54 (1999).
- [12] H. Bakker, G. F. Zhou, and H. Yang, *Prog. Mater. Sci.* 39, 159 (1995).
- [13] K. C. Russel, *Prog. Mater. Sci.* 28, 229 (1985).
- [14] B. X. Liu, in *Non-Equilibrium Processing of Materials*, edited by C. Suryanarayana (Pergamon, Oxford, 1999), p. 197.
- [15] N. S. Stolo and R. G. Davies, *Prog. Mater. Sci.* 13, 77 (1966).
- [16] R. S. Averback, H. Hahn, H. J. Hofler, and J. C. Logas, *Appl. Phys. Lett.* 57, 1745(1990).
- [17] H. Chang, H. J. Hofler, C. J. Altstetter, and R. S. Averback, *Scripta Metall.* 25, 1161 (1991).
- [18] D. K. Mukhopadhyay, C. Suryanarayana, and F. H. Froes, *Scripta Metall. Mater.* 31,333(1994).
- [19] W. Li, C. Suryanarayana, and F. H. Froes, in *Advances in Powder Metallurgy and Particulate Materials: Part I*, edited by M. A. Phillips and J. Porter (Metal Powder Industries Federation, Princeton, NJ, 1995), p. 145.
- [20] C. Suryanarayana, E. Zhou, Z. Peng, and F. H. Froes, *Scripta Metall. Mater.* 30, 781 (1994).
- [21] S. Srinivasan, P. B. Desch, and R. B. Schwarz, *Scripta Metall. Mater.* 25, 2513(1991).

- [22] R. B. Schwarz, P. B. Desch, and S. Srinivasan, in *Mechanical alloying for structural applications*, edited by J. J. deBarbadillo et al. (Materials Park, OH: ASM International, 1993), p. 227,
- [23] C. Suryanarayana, W. Li, and F. H. Froes, *Scripta Metall. Mater.* 31, 1465 (1994).
- [24] W. Li, C. Suryanarayana, and F. H. Froes, in *Synthesis/Processing of Lightweight Metallic Materials*, edited by F. H. Froes, C. Suryanarayana, and C. M. Ward-Close (TMS, Warrendale, PA, 1995), p. 203.
- [25] H. Schropf, C. Kuhrt, E. Arzt, and L. Schultz, *Scripta Metall. Mater.* 30, 1569(1994).
- [26] B. T. McDermott and C. C. Koch, *Scripta Metall.* 20, 669 (1986).
- [27] S. Martelli, G. Mazzone, S. Scaglione, and M. Vittori, *J. Less-Common Metals* 145,261 (1988).
- [28] A. E. Ermakov, E. E. Yurchikov, and E. P. Elsukov, *Fiz Tverd Tela* 4, 1947(1982).
- [29] E. P. Elsukov, V. A. Barinov, V. R. Galakhov, E. E. Yurchikov, and A. E. Ermakov, *Phys. Metals and Metallogr.* 55, 119 (1983).
- [30] E. P. Yelseekov, G. N. Konygun, V. A. Barenov, and E. V. Voronini, *J. Phys.:Condens. Matter* 4, 75 (1992).
- [31] S. Gialanella, R. W. Cahn, J. Malagelda, S. Surinach, M. D. Baro and A. R. Yavari, in *Kinetics of Ordering Transformations*, edited by H. Chen and K. Vasudevan (TMS, Warrendale, 1992), p. 161.
- [32] Y. Seki and W. L. Johnson, in *Solid State Powder Processing*, edited by A. H. Clauer and J. J. deBarbadillo (TMS, Warrendale, PA, 1990), p. 287.
- [33] A. R. Yavari, *Acta Metall.* 41, 1391 (1993).
- [34] M. D. Baro A, ach S. SurinA, 'and J. Malagelada, in *Mechanical Alloying for Structural Applications*, edited by J. J. deBarbadillo, et al. (ASM International, Materials Park, OH, 1993), p. 343.
- [35] F. Cardellini, V. Contini, and G. Mazzone, *Scripta Metall. Mater.* 32, 641 (1995).
- [36] S. Gialanella, R. Delorenzo, F. Marino, M. Guella, *Intermetallics* 3, 1 (1995).
- [37] Z.Q. Gao and B. Fultz, *Phil. Mag.* **B67**, 787 (1993).
- [38] H. H. Hamdeh, S. A. Oliver, B. Fultz, and Z. Q. Gao, *J. Appl. Phys.* 74, 5117 (1993).
- [39] Z. Q. Gao and B. Fultz, *Nanostructured Materials* 2, 231 (1993).
- [40] M. J. Richards and J. W. Cahn, *Acta Metall.* 19, 1263 (1971); S. M. Allen and J. W. Cahn, *Ibid.* **20**, 423 (1972).
- [41] **L. Anthony and B. Fultz, Acta Metall. Mater. 43, 3885-3891 (1995).**
- [42] J. T. T. Kumaran and C. Bansal, *Solid State Comm.* 69, 779 (1989).
- [43] *Binary alloy phase diagrams*, edited by T. B. Massalski (ASM International, Metals Park, OH, 1990).

- [44] P. R. Swann, W. R. Duff, and R. M. Fisher, *Trans. AIME* **245**, 851 (1969).
- [45] H. Okamoto and P. A. Beck, *Metall. Trans.* 2, 569 (1971).
- [46] K. Oki, M. Hasaka, T. Eguchi, *Trans. Jap. Inst. Met.* **14**, 8 (1973).
- [47] K. Oki, M. Hasaka, and T. Eguchi, *Japan J. Appl. Phys.* **12**, 1522 (1973); *Trans. JIM* 15, 143 (1974).
- [48] B. Park, G. B. Stephenson, S. M. Allen, and K. F. Ludwig, *Phys. Rev. Lett.* 68, 1742 (1992).
- [49] L. Anthony and B. Fultz, *J. Mater. Res.* 4, 1132 (1989). *Ibid* 4, 1140 (1989).
- [50] L. Anthony and B. Fultz, *J. Mater. Res.* 9, 348 (1994).
- [51] W. Schweika, *MRS Symposium Proceedings* (MRS, Pittsburgh, Pennsylvania, 1990), Vol. 166, p. 249.
- [52] R. G. Davies, *Trans. Met. Soc. AIME* **230**, 903 (1964).
- [53] A. G. Khachaturyan, in *Progress in Materials Science*, edited by B. Chalmers, J. W. Christian, and T. Massalski (Pergamon Press, Oxford, 1975), vol. 22, p. 1.
- [54] C. Bansal, Z. Q. Gao, and B. Fultz, *Nanostructured Materials* 5, 327 (1995).
- [55] L. Brossard, G. A. Fatseas, and J. L. Dorman, *J. Appl. Phys.* 42, 1306 (1971).
- [56] G. A. Fatseas, *Can. J. Phys.* 54, 1850 (1976).
- [57] K. Raviprasad, S. Ranganathan, and K. Chattopadhyay, *Scripta Metall. Mater.* **26**, 467 (1992).
- [58] H. H. Hamdeh, M. R. Al-Hilali, N. S. Dixon, and L. S. Fritz, *Phys. Rev.* **B45**, 2201 (1992).
- [59] H. H. Hamdeh, S. A. Oliver, B. Fultz, and Z. Q. Gao, *J. Appl. Phys.* 74, 5117 (1993).
- [60] H. H. Hamdeh, J. Kramer, B. Fultz, Z. Q. Gao, and S. A. Oliver, *Hyperfine Interaction* 94, 2373 (1994).
- [61] G. F. Zhou and H. Bakker, *Materials Transactions:JIM* 36, 329 (1995).
- [62] S. Yoon and J. G. Booth, *Phys. Lett. A* 48, 381 (1974).
- [63] T. J. Burch, J. I. Budnick, V. A. Niculescu, K. Raj, and T. Litrenta, *Phys. Rev.* **B24**, 3866 (1981).
- [64] V. Niculescu, K. Raj, T. J. Burch, and J. I. Budnick, *Phys. Rev.* **B13**, 3167 (1976).
- [65] *Ferromagnetic Materials*, edited by E. D. Wholfarth and K. H. J. Buschow (North Holland, 1988), Vol. IV.
- [66] *Kinetics of Ordering Transformations in Metals*, edited by H. Chen and V. K. Vasudevan (TMS, Warrendale, 1992).
- [67] B. Fultz, *Acta Metall.* 37, 823 (1989).
- [68] B. Fultz, *Hyperfine Int.* 41, 607 (1988).

- [69] B. Fultz, H. H. Hamdeh, and D. H. Pearson, *Acta Metall.* 37, 2841 (1989).
- [70] G. E. Murch, in *Phase Transformations in Materials*, edited by R. W. Calm, P. Haasen, and E. J. Kramer (VCH, Weinheim, 1991), p.90.
- [71] M. B. Sterns, *Phys. Rev.* 147, 439 (1966).
- [72] Ben. DeMayo, *Phys. Rev. B* 24, 6503 (1981).
- [73] A.R. Miedema, P. F. deChatel, and F. R. deBoer, *Physica B.* 100, 1 (1980).
- [74] I. Vincze and A. T. Aldred, *Phys. Rev. B* 9, 3845 (1974).

Chapter 4

Spinodal Decomposition in Nanocrystalline Fe-Cr alloys

4.1 Introduction

Fe-Cr phase diagram is shown in figure 4.1 [ref 43 of chapter 3]. It has a miscibility gap as well as a Spinodal region. There are several earlier studies on Spinodal decomposition (SD) in alloy systems in general and specifically in microcrystalline Fe-Cr alloys [1-5]. It is mentioned in chapter 1 that the SD process initializes over nanometer range spatial regions in bulk alloys having large grains. It is therefore interesting to study the SD process in nanocrystalline alloys where the grain size itself is also in nanometer range. The SD process should be affected or rather limited by the grain growth in this nanocrystalline grains. Our aim was to study the Spinodal decomposition in nanocrystalline Fe-Cr alloys from an initial homogeneous disordered state and to find the correlation between the grain growth and SD process.

4.2 Experimental

Nanocrystalline $\text{Fe}_{1-x}\text{Cr}_x$ ($x = 0.1, 0.2, 0.35, 0.45$) alloys were prepared by mechanical alloying of the elemental high purity Fe and Cr powder. The Fe contamination from milling as determined by EDAX analysis was within the range of 0.2-0.8 at. percent. To study the Spinodal phase decomposition behaviour, the as-milled alloys were heat treated at 475° C, 460° C, 400° C and 300° C for various periods of times ranging from few minutes to hundred of hours.

4.3 Results and discussion

Figure 4.2 shows the XRD patterns of the as-milled alloys with different Cr concentrations. The broadening of the lines in the X-Ray pattern shows the formation of the alloy in the nanocrystalline phase. The average grain size of the as-milled alloys determined was around 10 nm and lattice constant was 2.868Å. To follow the alloying process through milling, the alloy with 20 at. % Cr was milled in steps of 4 hours up to 24 hours. Figure 4.3 shows the XRD

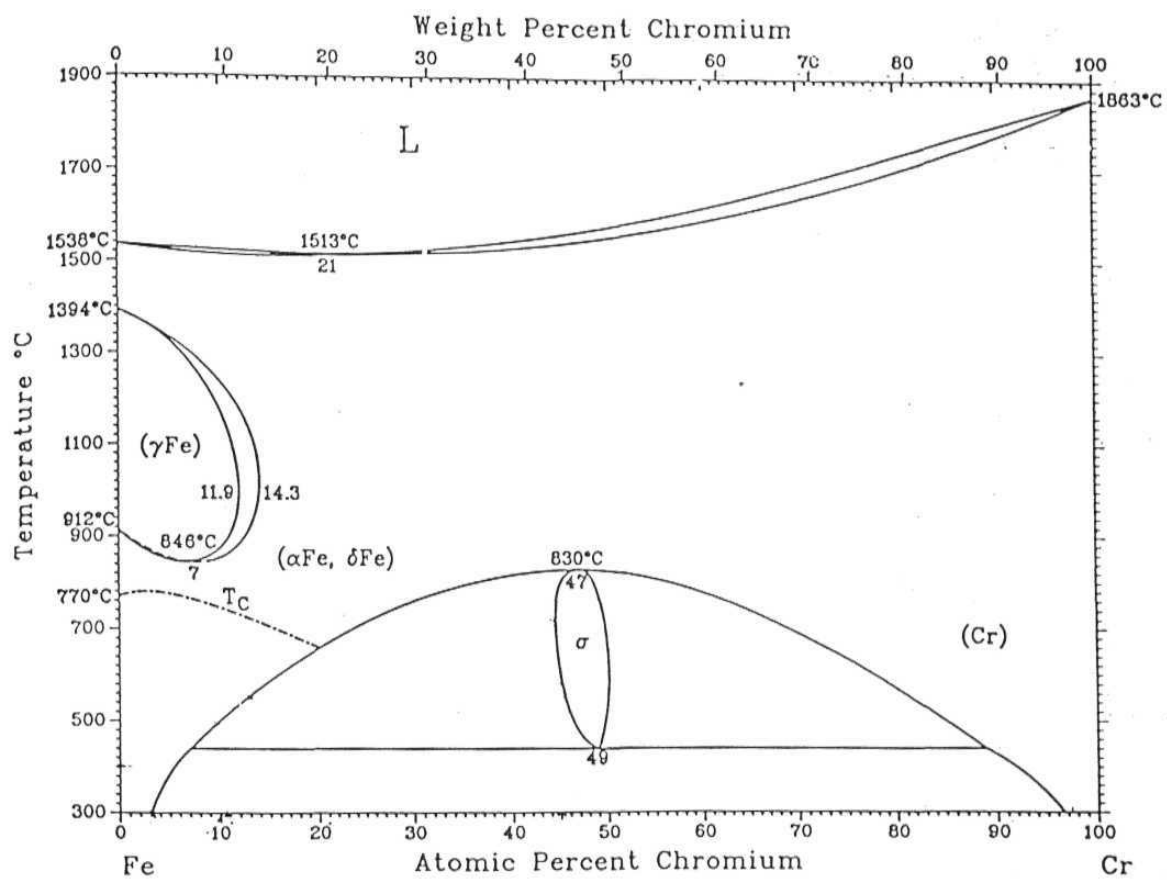


Figure 4.1 Thermodynamic equilibrium phase diagram
For Fe-Cr alloy

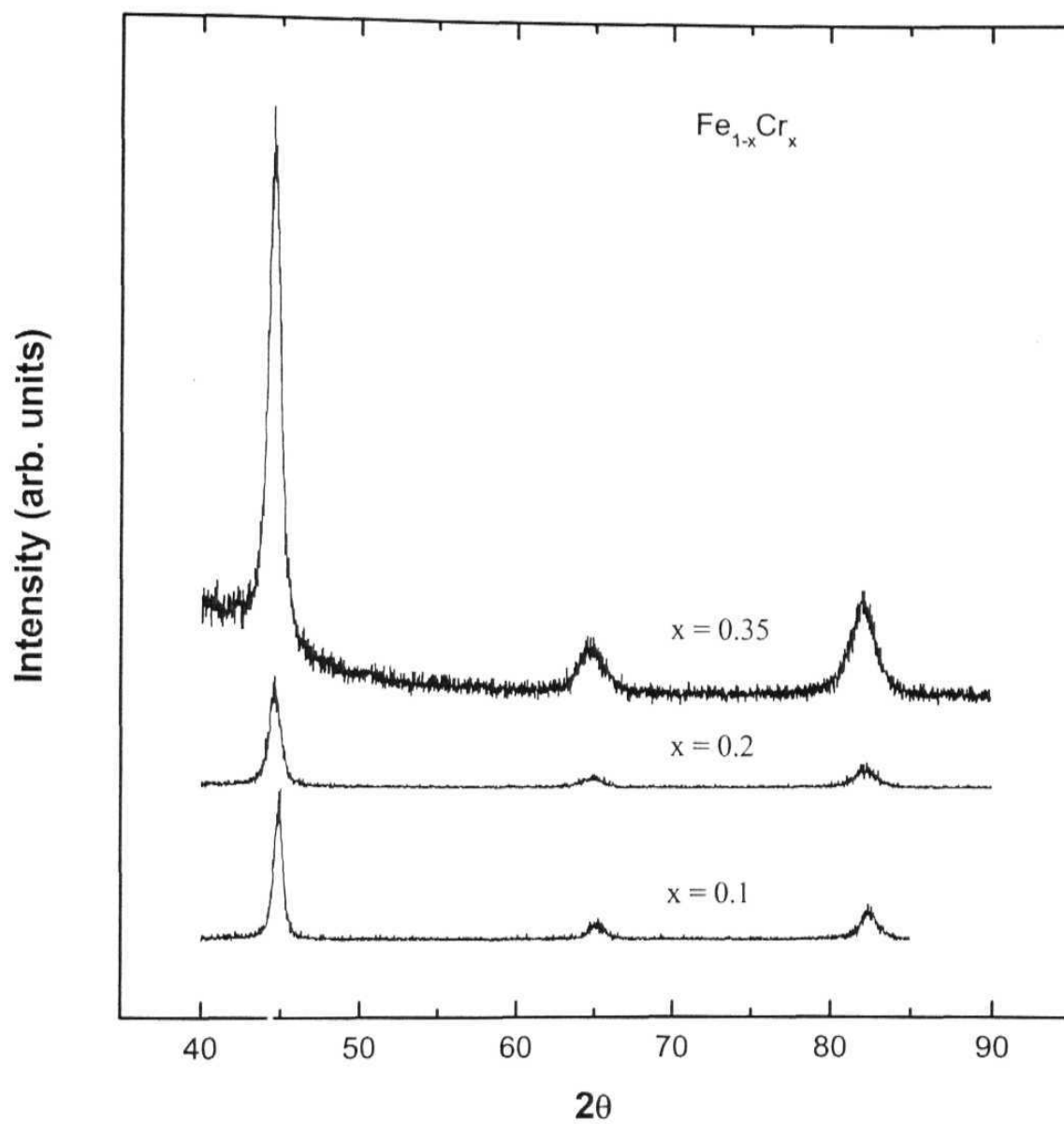


Figure 4.2: X-ray diffraction patterns of the as-milled samples with different Cr concentrations, showing the presence of only disordered bcc (a) phase.

patterns of this milling sequence. Broadening of X-Ray lines due to grain size reduction could be seen from this figure. The presence of separate Fe and Cr lines is not visible even after 4 hours of milling. This may be because of closeness of the positions of the lines of pure Fe and Cr (fundamental lines at 2 θ values of 44.71 and 44.41 with lattice constants being 2.8665 and 2.8847 Å respectively), which hinders the resolution of the lines once they become broad due to grain refinement with milling. It is expected that grain refinement of the individual component take place even after 4 hours of milling. However the HMF distributions of figure 4.4 evaluated from the Mossbauer spectra recorded at each stage of milling show clearly the alloying behavior. It is seen that initially upto 8 hours of milling no alloying took place and only the Fe field (~ 330 kOe) peak was present. After around 12 hours of milling the other peaks due to Cr 1st and 2nd nn of Fe started coming with a field shift of around 10 kOe of the 0 Cr nn peak. The formation of the alloy is complete after 24 hours of milling. The field shift of ~ 10 kOe for the 0 Cr 1st and 2nd nn is in accordance with the earlier results [6, 7]. All the other Cr concentration alloys were milled for 24 hours except the 45 at. % Cr composition, which required a milling time of 30 hours for the formation of a fully disordered homogeneous alloy. Figures 4.5a and 4.5b show respectively the temporal evolution of the broadening of the fundamental (110) X-ray peak and grain size with milling. The grain size determined from the X-ray fundamental peak broadening at the final stages of milling (i.e. 20 hours onwards) is the true nanocrystalline grain size but at the initial stages of milling is not the true grain size of the nanocrystalline alloy as the alloy is not formed at these stages and overall broadening is arising due to superposition of unresolved broad peaks of Fe and Cr. But we can still use this grain size value to see the trend of grain size reduction with milling time irrespective of the absolute values. The solid line through the experimental points of figure 4.5 b is the exponential decay functional fit to the grain size reduction behavior.

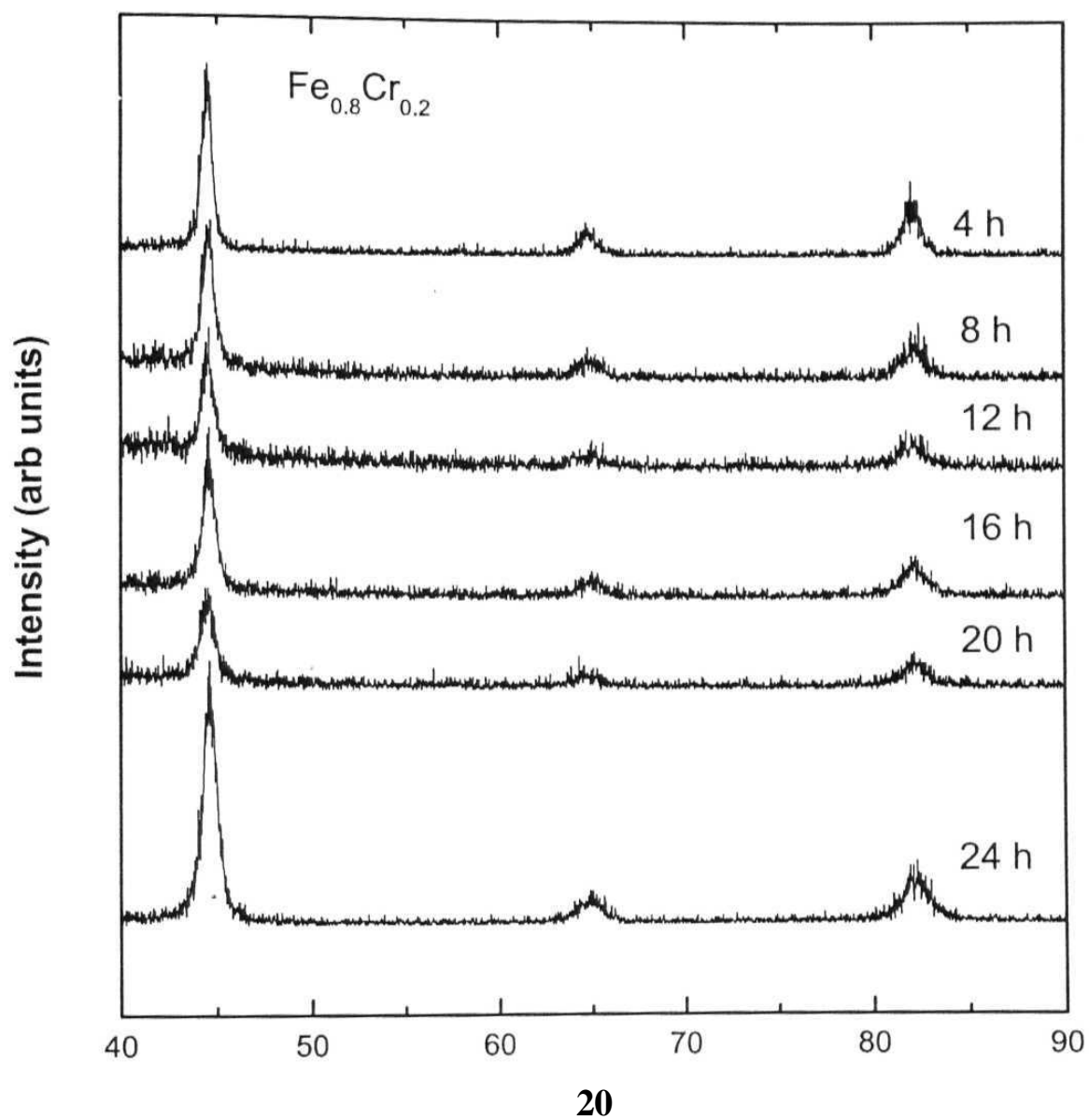


Figure 4.3: X-ray patterns recorded at different stages of milling for the $x = 0.2$ composition alloy.

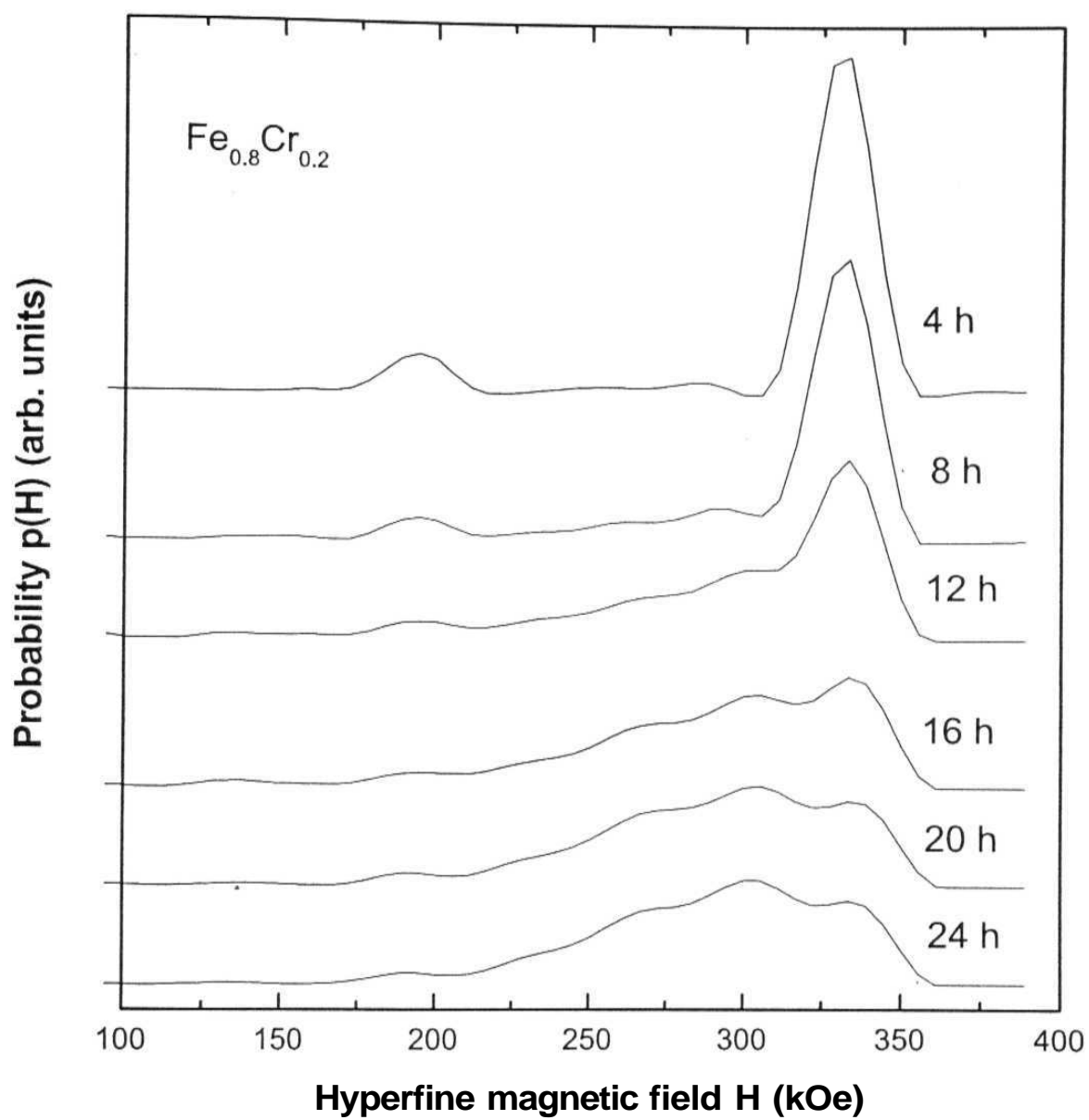
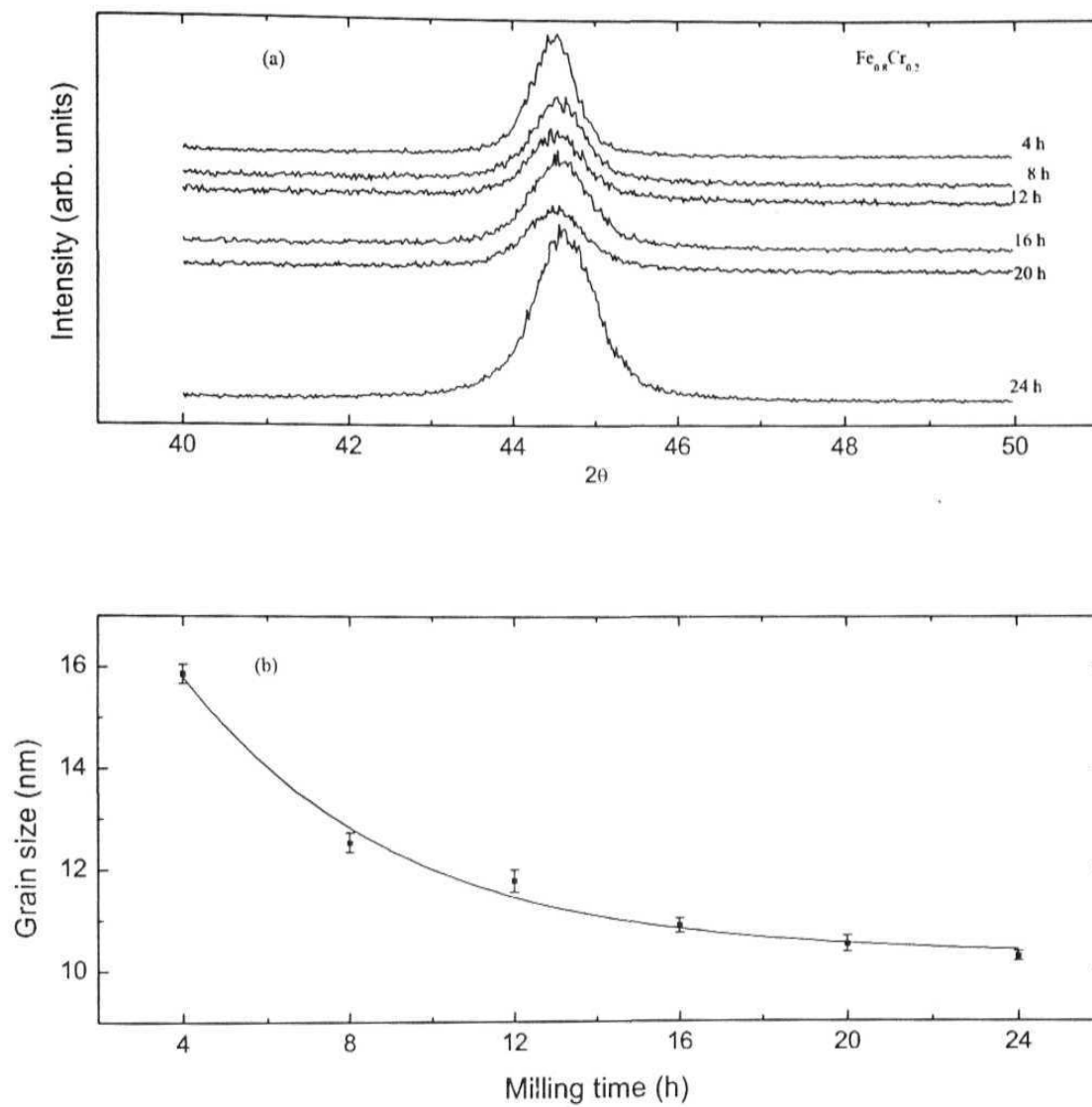


Figure 4.4: Evolution of HMF distributions with milling time, showing the formation of the homogeneous disordered alloy typically after 20-24 h.



Figures 4.5 (a) and (b): Show respectively the temporal evolution of the broadening of the fundamental (110) X-ray peak and grain size with milling time.

The Mossbauer spectra of the final as-milled alloys with different Cr concentration are shown in figure 4.6. No signature of any paramagnetic peak near zero velocity arising from the Cr-rich phase is seen in the Mossbauer spectra. The corresponding HMF distributions evaluated from the Mossbauer spectra of figure 4.6 are shown in LHS of figure 4.7. The calculated binomial probability distributions using equation 3.14, expected for a random configuration of atoms in a disordered bcc alloy are shown in the RHS of figure 4.7. In finding out the binomial distribution the perturbation caused to the Fe nucleus by both 1st and 2nd nearest neighbours (nn) Cr atoms was considered [7]. The values of the 1st nn Cr perturbation (ΔH_1) and 2nd nn Cr perturbation (ΔH_2) were taken to be 31.5 kOe and 22 kOe respectively [7] in using equation 2.15 to find the field values due to different Cr nn of Fe. In this way we get 63 (0 to 8 1st and 0 to 6 2nd nn) different field values and their probabilities. But in the actual experimental distributions the numbers of peaks are much less because many of these peaks with close HMF values cannot be resolved. To incorporate this behavior we have added up the probability values of the fields lying in the range of every 20 kOe and assign the field value for this added-up probability, which is the average of the two extreme field values (e.g. 300 to 320 kOe fields were assigned a value of 310 kOe). This procedure reduced the number of field values and their probabilities to 18 (between 0-360 kOe field range), which is shown in RHS of figure 4.7. The excellent correspondence between the experimentally obtained probabilities and calculated probabilities shows clearly that the as-milled alloy was formed in complete disordered homogeneous state after typical milling times of 24-30 hours. The formation of the disordered homogeneous alloy in otherwise phase separating system is one of the important attributes of MA, as discussed in chapter 1.

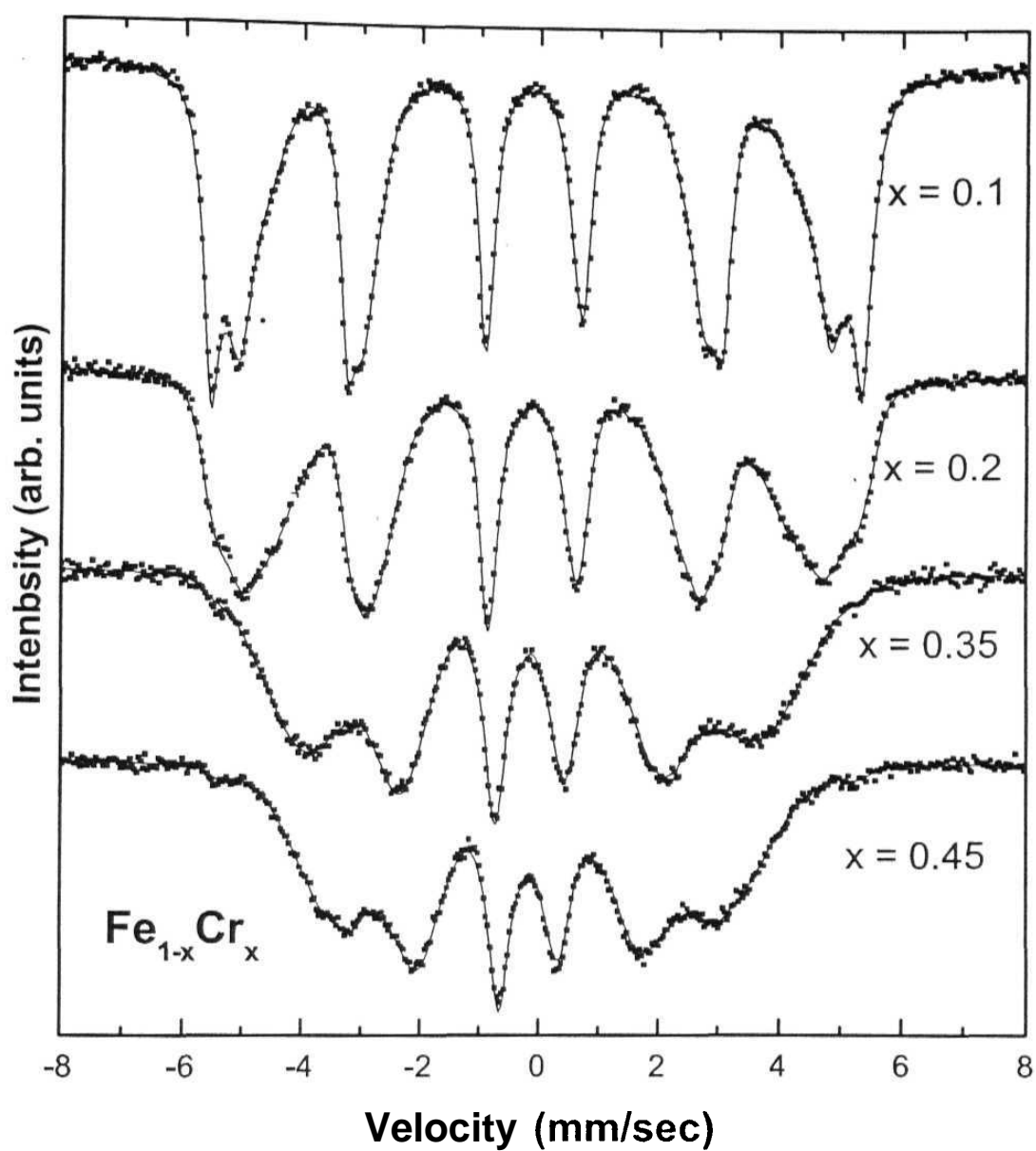


Figure 4.6: Mossbauer spectra of the as-milled alloys with different Cr concentrations. (Symbols: exp, lines:Fit).

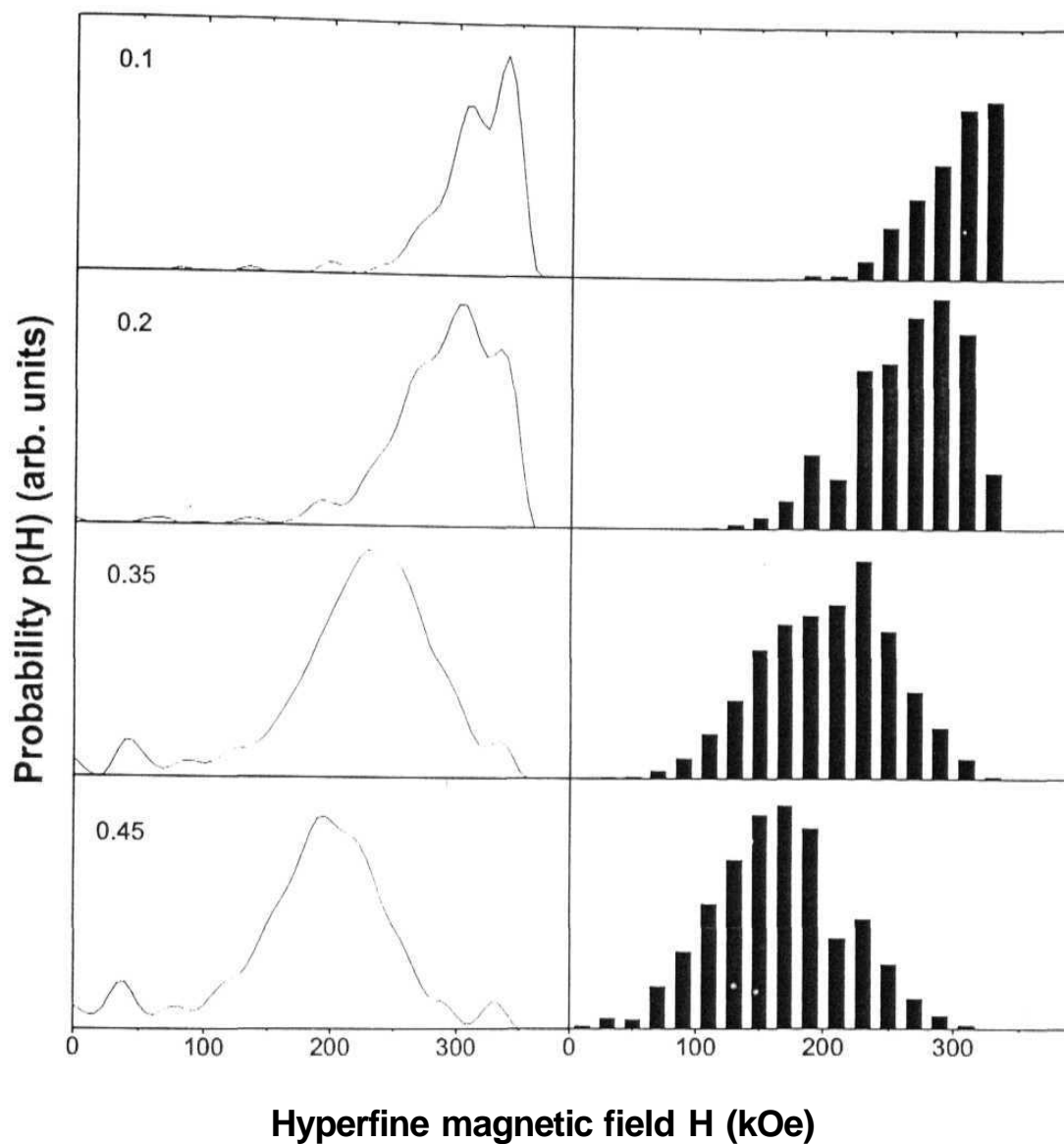


Figure 4.7: HMF distributions evaluated from the Mossbauer spectra of figure 4.6 are shown in LHS. The calculated binomial probability distributions using equation 3.14, expected for a random configuration of atoms in a disordered bcc alloy are shown in the RHS.

The as-milled alloys were heat treated to see the formation of a (Fe-rich) and a (Cr-rich) phases from the A2 phase either by SD or by NG depending on the starting composition of the alloy. The α phase is characterized by the presence of a paramagnetic singlet in the Mossbauer spectrum with IS values of around -0.1 mm/sec w.r.t. pure Fe [6].

Figure 4.8 shows the representative X-Ray patterns for the 20 and 45 at. % Cr samples heat-treated at the temperature and time mentioned in the figure. Figure 4.9 shows only the fundamental (110) X-Ray peaks for the representative heat-treated samples with different Cr concentrations in comparison to as-milled samples. Narrowing of line widths shows grain coarsening.

Figure 4.10 shows the HMF distributions evaluated from the Mossbauer spectra of the 10 at. % Cr alloy heat treated at the temperatures for the periods of times mentioned in the figure. The field distribution of the as-milled sample is also shown in the figure and it can be seen that there is hardly any difference between the as milled and heat treated samples field distributions. This indicates that no phase separation is taking place in this alloy system at these temperatures. According to equilibrium phase diagram this behavior is expected at 460°C (a phase boundary at 12.87 at. % Cr) but at 300°C the system should decompose to α - α' phase. The most probable reason for this kind of no phase separation could be attributed to nano-grain size of the heat-treated sample also. The average grain size of the 300°C, 72 hours heat treated sample was ~17 nm, which increases the solubility of Cr in Fe due to capillary effect. The Mossbauer spectra of the heat-treated samples at this composition are not shown, as they are very similar to the as-milled Mossbauer spectrum shown in figure 4.6.

Figures 4.11 (a) and (b) show the Mossbauer spectra and the corresponding HMF distributions of the 20 atomic percent Cr sample, as-

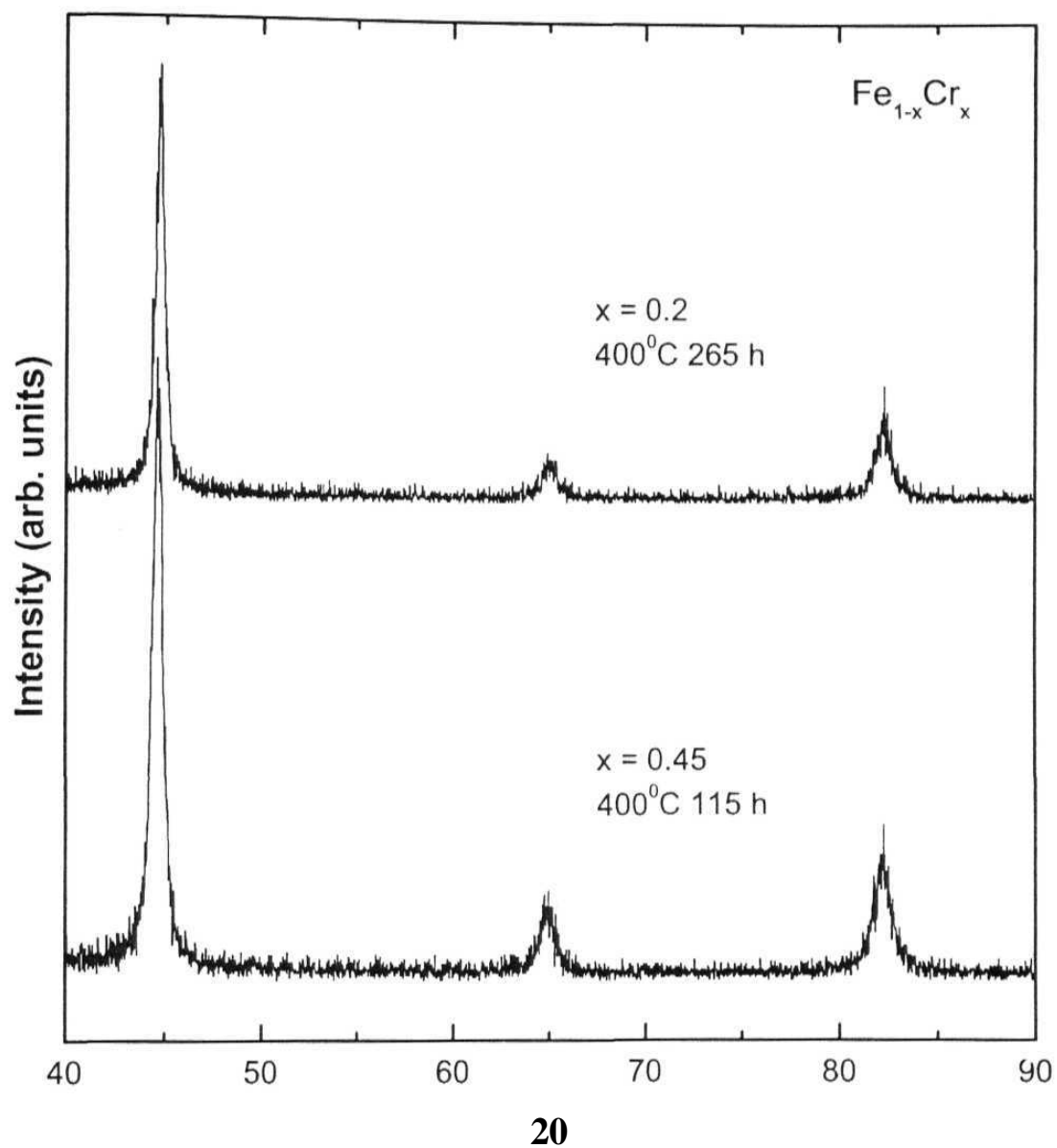


Figure 4.8: Shows the representative X-Ray patterns of the heat treated samples.

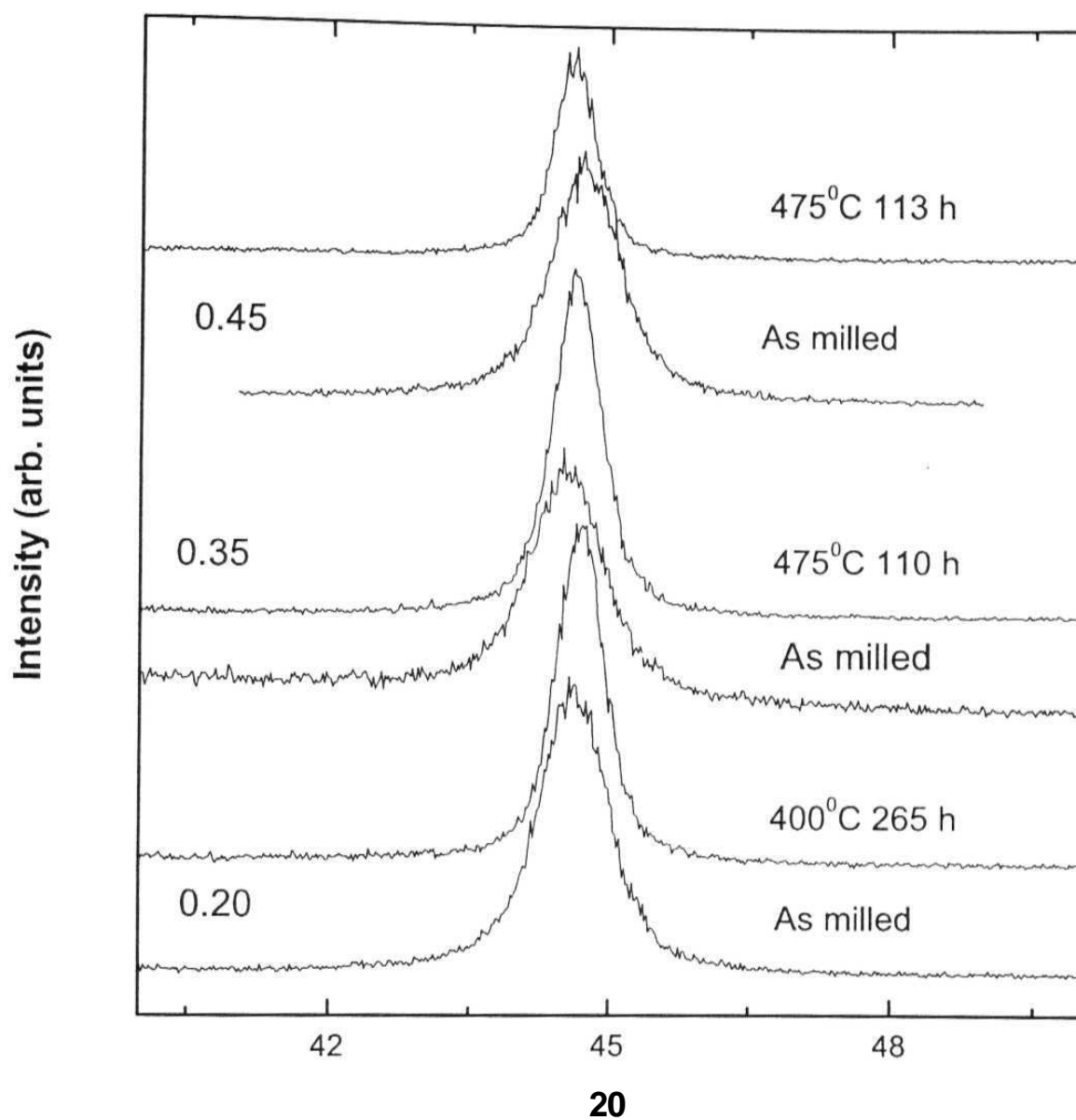


Figure 4.9: Grain coarsening is shown by the narrowing of the fundamental (110) X-Ray peak of the representative heat-treated samples, with different Cr concentrations in comparison to the as-milled samples.

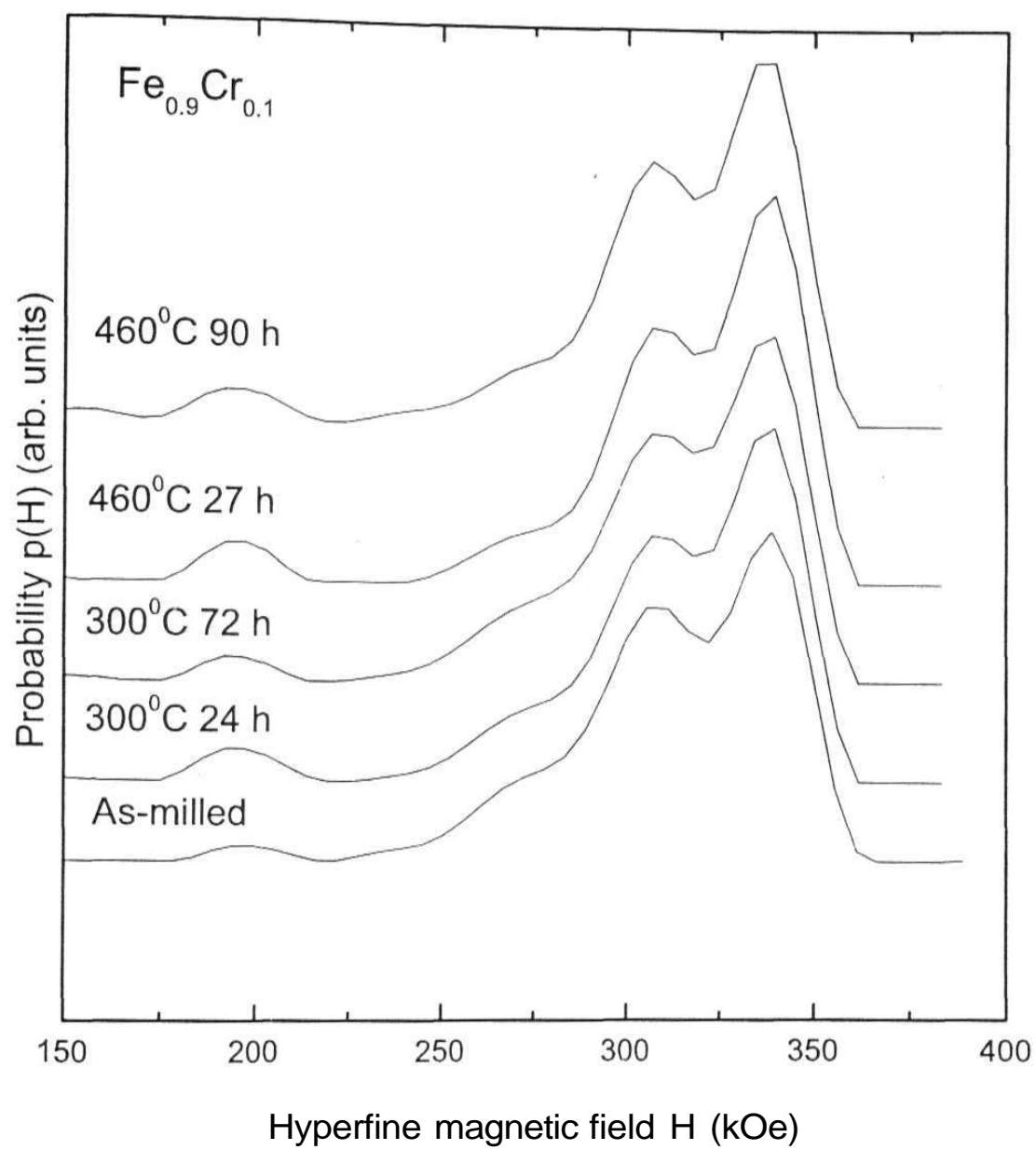
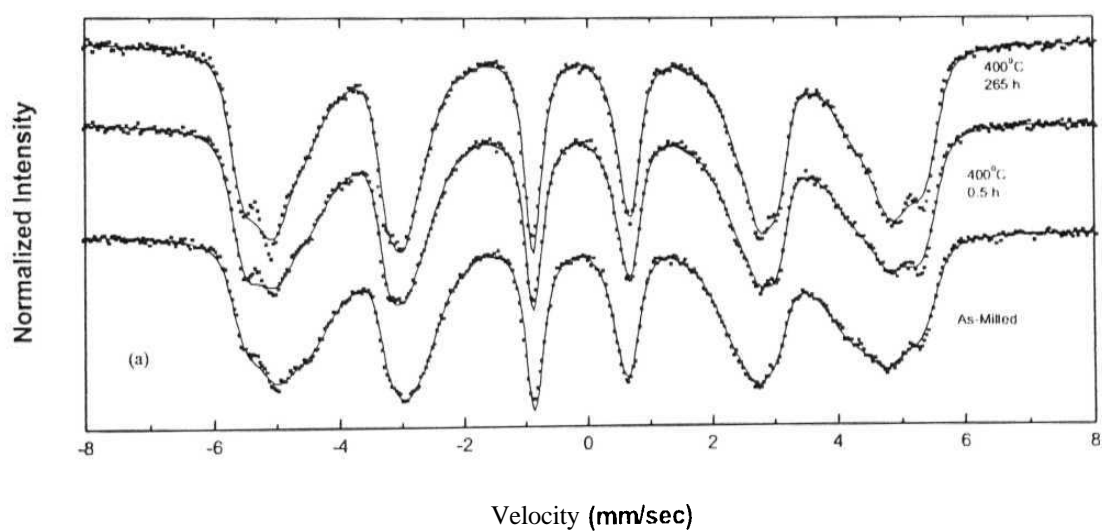
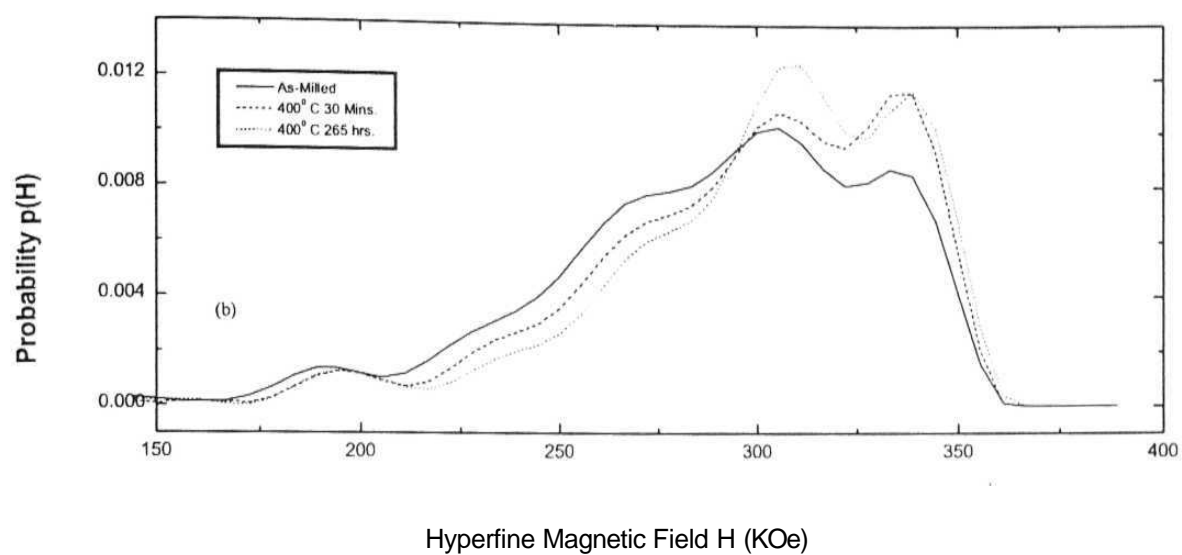


Figure 4.10: Shows similar HMF distributions of the as-milled and heat treated samples.

milled and heat treated at 400°C for 0.5 and 265 hours. The formation of the **Fe-rich** (a) phase is evident from the increase in the intensities of the peaks in the distribution towards higher fields with a corresponding decrease in the intensities of the peaks towards lower field values. This represents configurations with lesser number of Cr atoms in the nearest neighbour environment of Fe due to depletion of Cr from Fe 1st and 2nd nn shells.

Figures 4.12 and 4.13 show respectively the representative Mossbauer spectra of the 35 and 45 at. % ($x=0.35, 0.45$) Cr samples, as-milled and heat treated at 300, 400, and 475°C for periods of times specified in the figures. Figures 4.14 and 4.15 show respectively the HMF distributions of all the heat-treated samples at the above three temperatures for different periods of times including those from the Mössbauer spectra of figures 4.12 and 4.13. As-milled field distributions for both the Cr concentrations are also shown in figures 4.14 and 4.15 for comparison. The phase decomposition towards equilibrium phases is evident from these four figures from the shift of the peaks towards higher field values designating formation of Fe-rich phase with Cr atoms depleting from Fe nearest neighbour environment. In case of samples heat treated at 475°C for 50 hours and above, the formation of Cr-rich phase is also seen in the Mossbauer spectra and field distributions as a paramagnetic peak. To fit this paramagnetic peak better we have adopted the procedure of introducing fixed field component in the distribution with IS values optimized close to the earlier reported value of ~ -0.1 mm/sec w.r.t pure Fe [6]. The presence of this paramagnetic peak is not there in the Mossbauer spectra and field distributions of 300 and 400°C heat-treated samples. The fractions of α phase formed at 475°C after around 110 hours of heat treatments are only $\sim 2\%$ for the $x=0.35$ alloy and $\sim 5\%$ for the $x=0.45$ alloy.

Now the question is whether the phase decomposition is proceeding through Spinodal decomposition (SD) or nucleation and growth (NG). There



Figures 4.11 (a) and (b): Show respectively the Mossbauer spectra and the corresponding HMF distributions of the 20 atomic percent Cr sample, as-milled and heat treated.

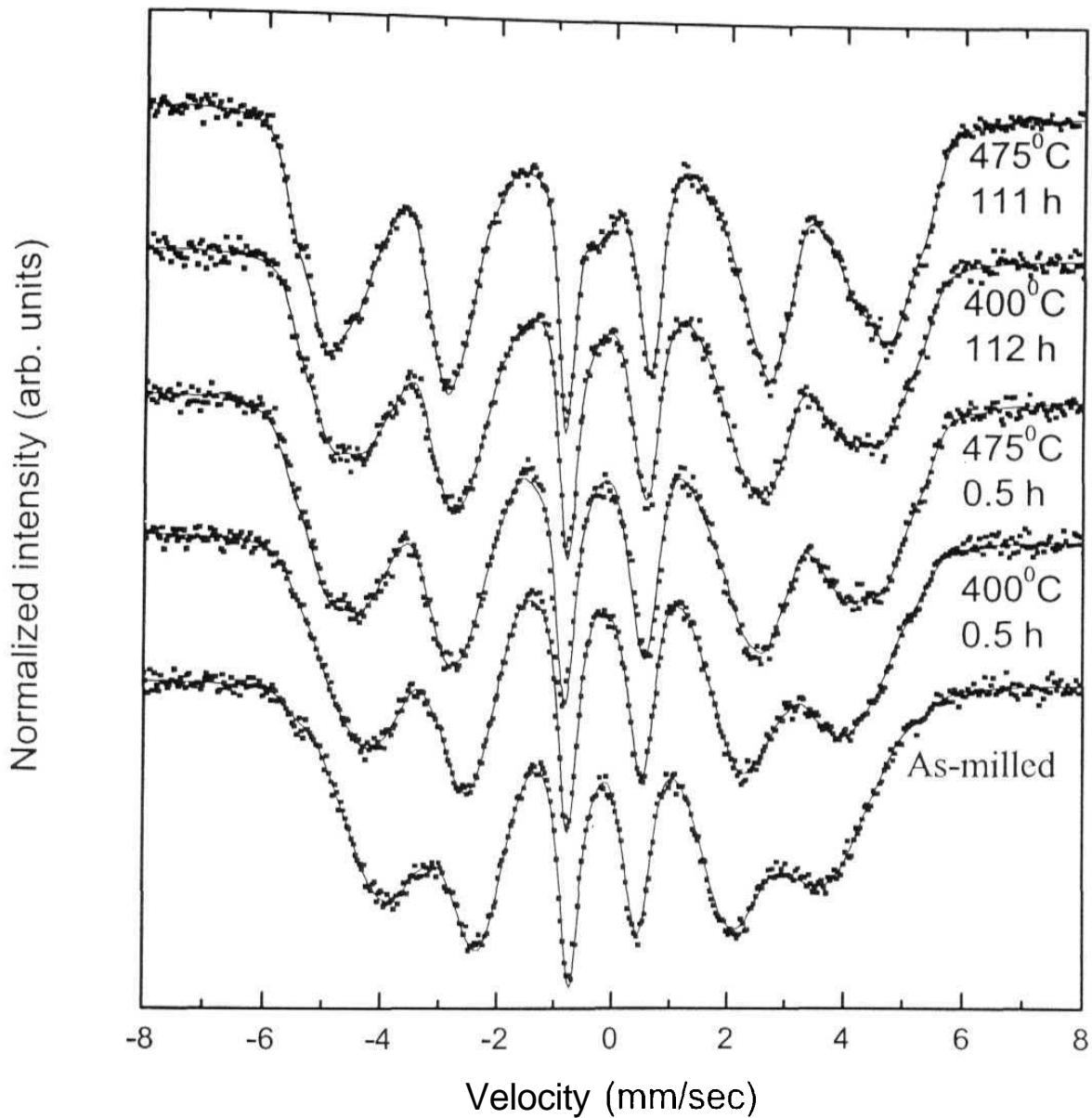


Figure 4.12: Representative Mossbauer spectra of the 35 at. % Cr samples, as-milled and heat treated. The gradual increase in the separation of lines indicates the development of the α phase and the signature of the paramagnetic α phase line is clearly seen in the spectrum corresponding to 475 C, 111 h heat treated sample.

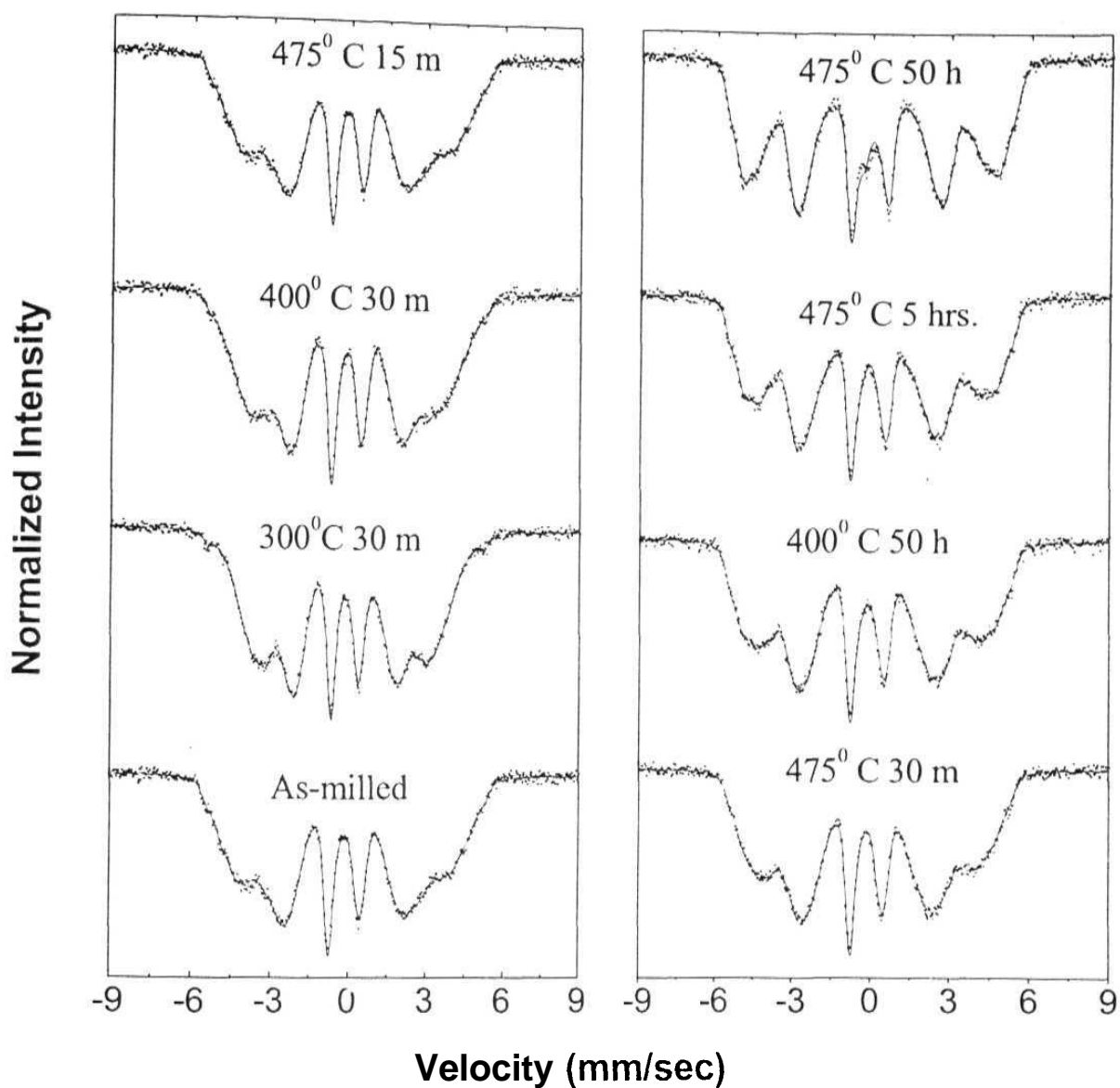


Figure 4.13: Representative Mossbauer spectra of the 45 at. % Cr samples, as-milled and heat treated. The gradual increase in the separation of lines indicates the development of the α phase and the signature of the paramagnetic α phase line is clearly seen in the spectrum corresponding to 475°C, 50 h heat treated sample.

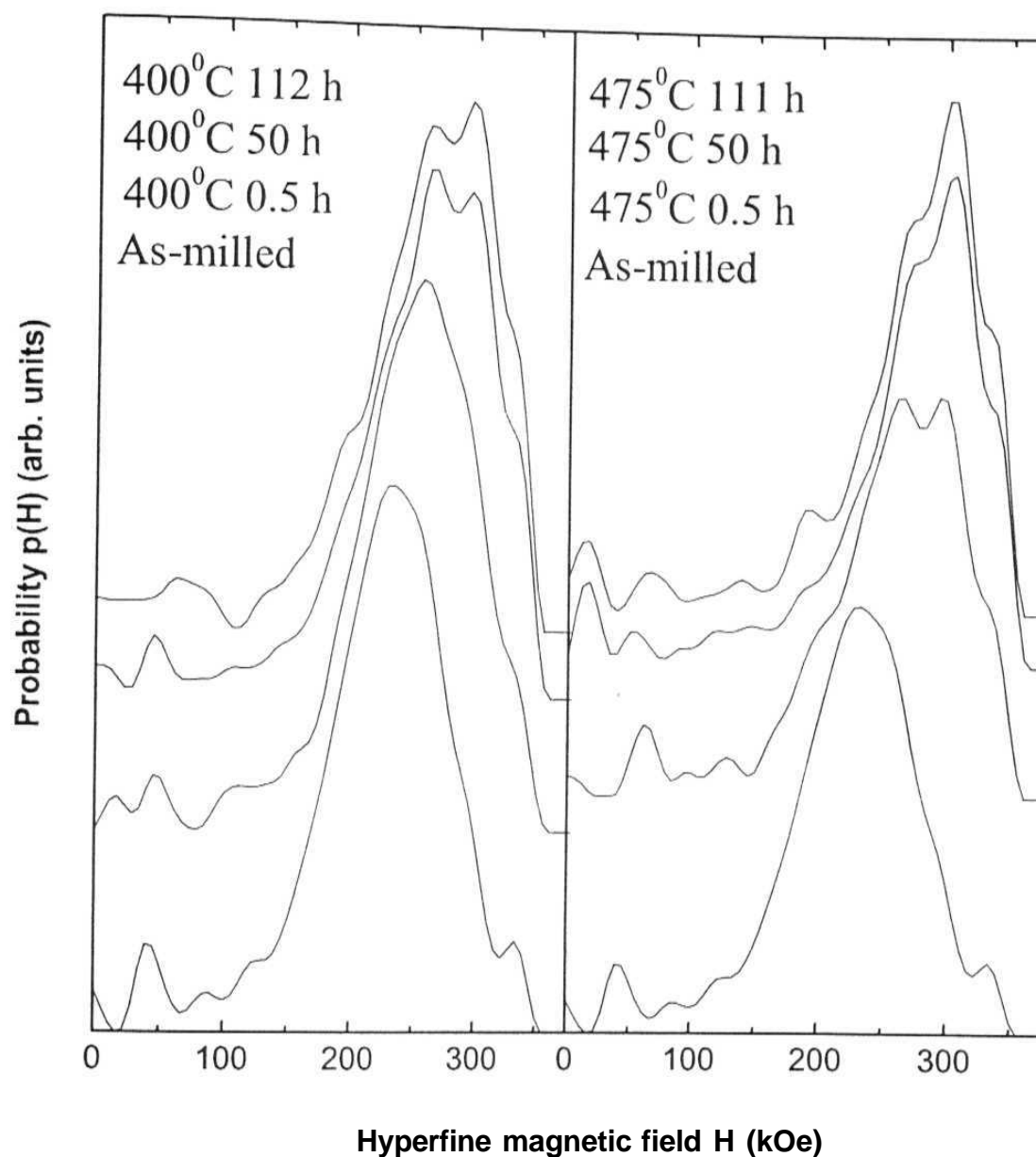


Figure 4.14: HMF distributions evaluated from various heat treated samples and also of the as-milled sample pertaining to the $x = 0.35$ alloy system. The gradual increase in the width of the distribution without the appearance of the peaks towards the extreme field values shows the phase decomposition proceeds through SD process and not through NG.

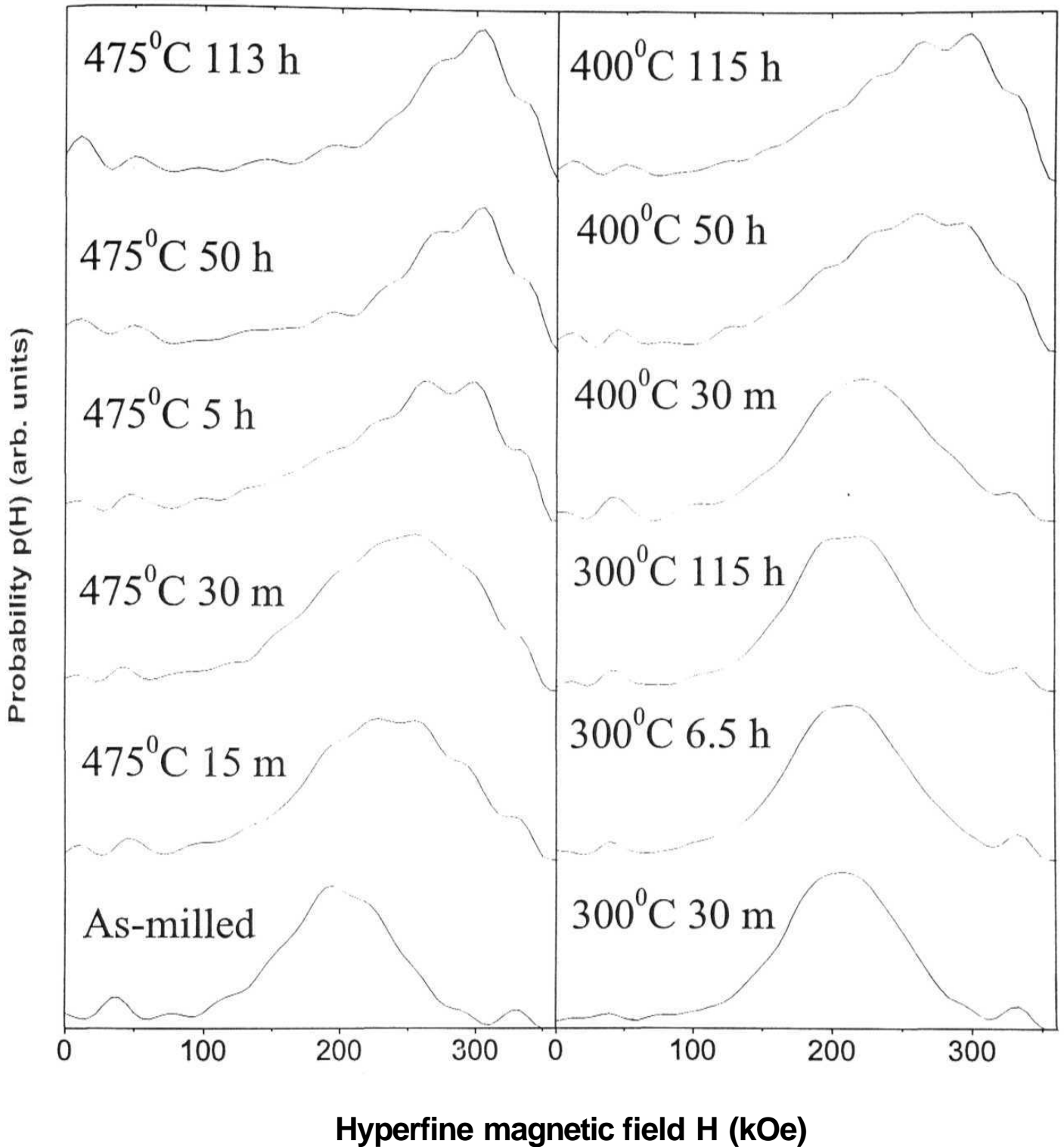


Figure 4.15: HMF distributions evaluated from various heat treated samples and also of the as-milled sample pertaining to the $x = 0.45$ alloy system. The gradual increase in the width of the distribution without the appearance of the peaks towards the extreme field values shows the phase decomposition proceeds through SD process and not through NG.

are two different ways of answering this question using Mossbauer spectroscopic studies. One way is to look at the changes in the hyperfine magnetic field distributions and compare with the expected distribution for the SD or NG process. In our study we adopted a simplified model of composition fluctuation of the form of Gaussian [8] and found out the probability distributions at different stages of the decomposition. The composition differences between the starting composition and the phase boundaries was divided in ten equal intervals and at each of these intervals one Gaussian composition profile was assigned with a typical full width equals to 6 times the square root of the particular composition concerned. The binomial probability distribution for the first two nn shells of Fe obtained using these Gaussian profiles on each composition interval on both sides of the starting composition was added to get the overall probability distribution because of decomposition. RHS of figures 4.16 and 4.17 show such a simulated distribution at different stages of decomposition for the alloy sample with $x=0.35$ at 400 and 475°C respectively. The legends (ϵ_1 , ϵ_2) in the figures denote the stages of decomposition on both sides of the starting composition. RHS of figures 4.18, 4.19, and 4.20 shows such distribution at different stages of decompositions for the alloy sample with $x=0.45$ and at temperatures 300, 400, and 475°C.

The LHS of these (figures 4.16-4.20) figures show the probability distribution calculated by assuming NG decomposition process at the compositions and temperatures mentioned above. In calculating the probability distributions of the figures we have assumed the decomposition process taking place continuously, i.e. the a and α phases nucleate and grow continuously from the disordered matrix. The legends (f) in these figures denote the fraction transformed, e.g. $f = 0.2$ means formation of 20% of the end phases with the remaining 80% disordered matrix.

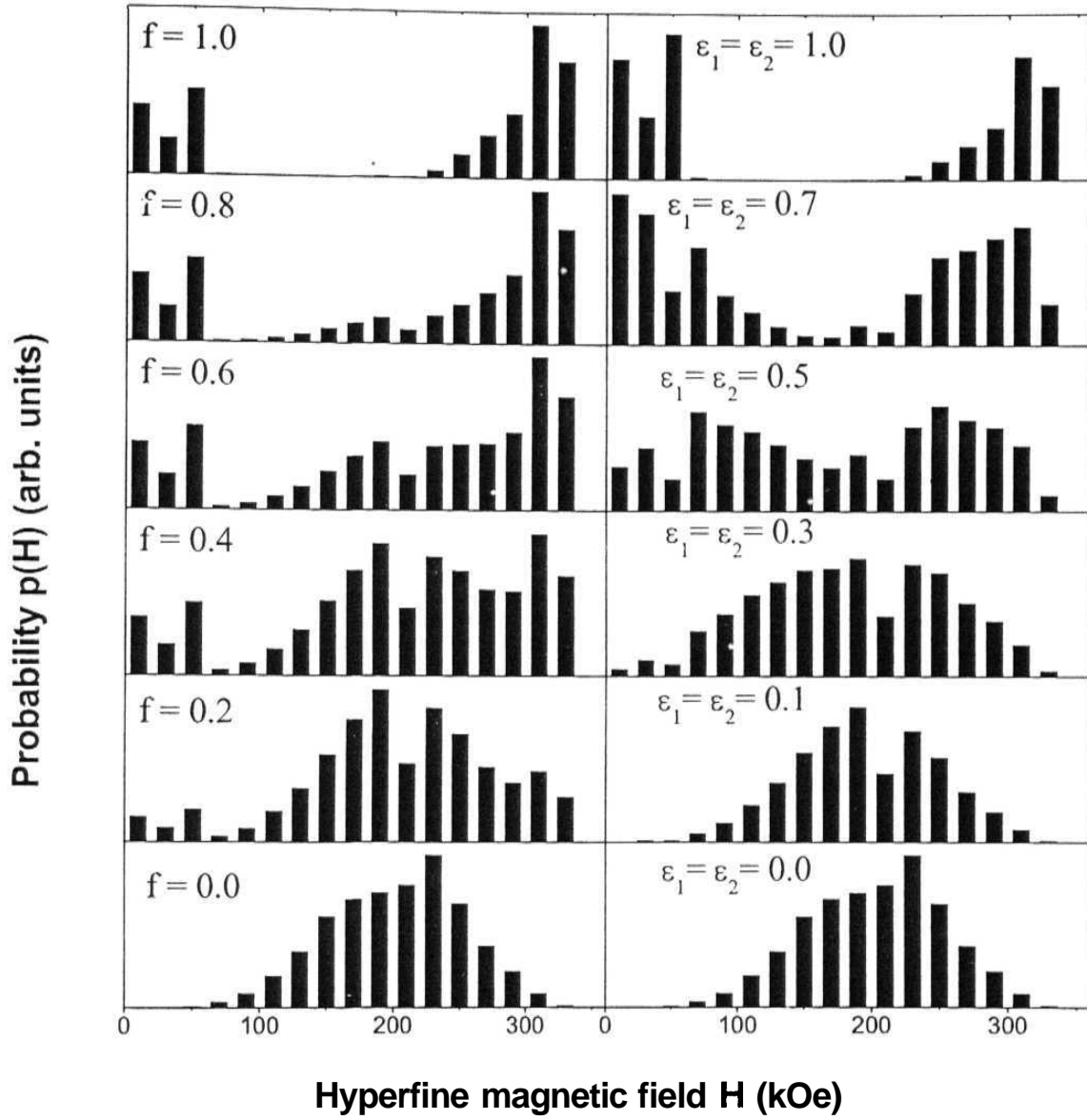


Figure 4.16: (LHS) and (RHS) respectively show the calculated probabilities at different stages of the NG and SD processes at 400 C for the $x = 0.35$ alloy. The detail procedures of the calculations are discussed in the text.

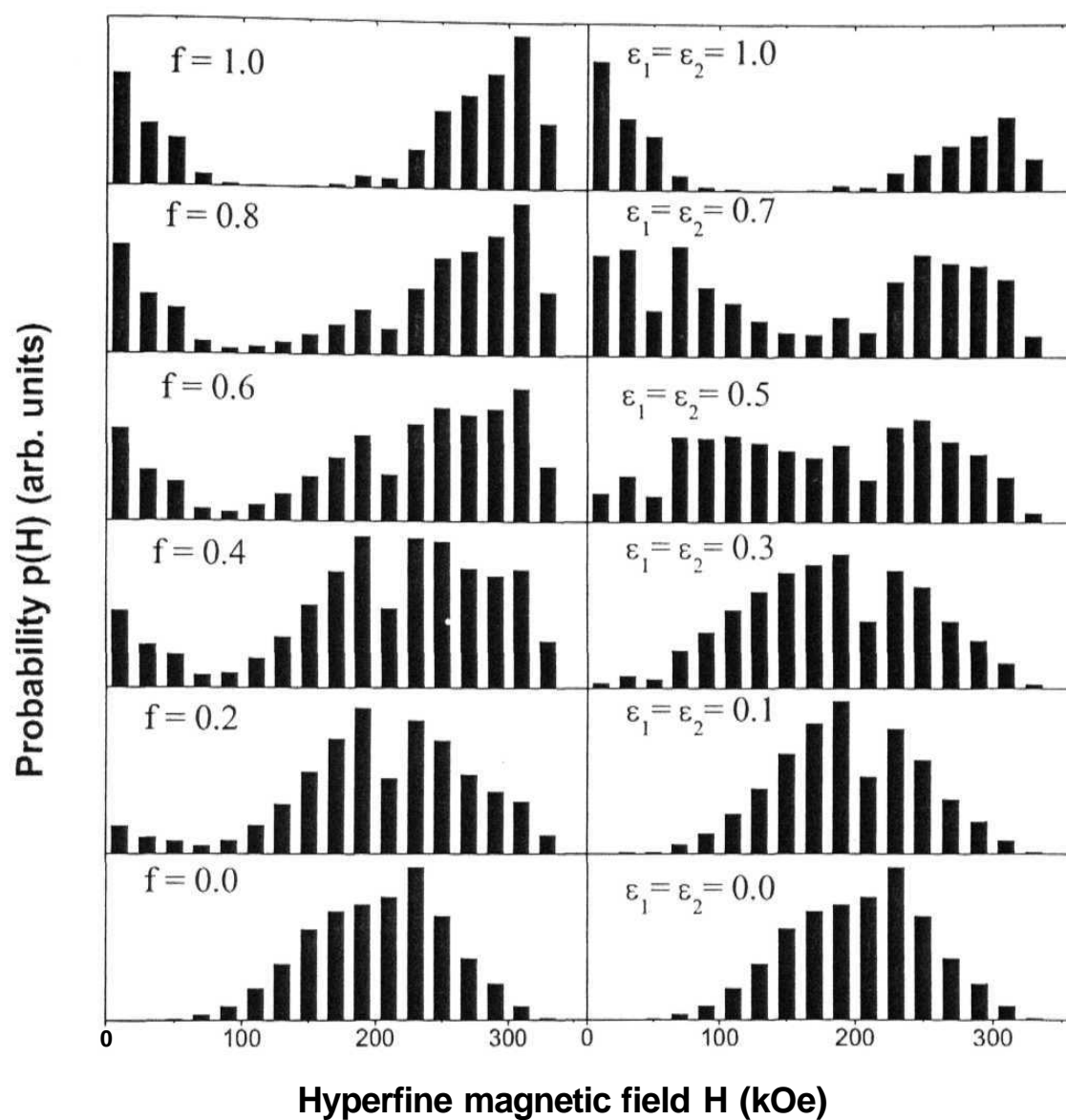


Figure 4.17: (LHS) and (RHS) respectively show the calculated probabilities at different stages of the NG and SD processes at 475 C for the $x = 0.35$ alloy. The detail procedures of the calculations are discussed in the text.

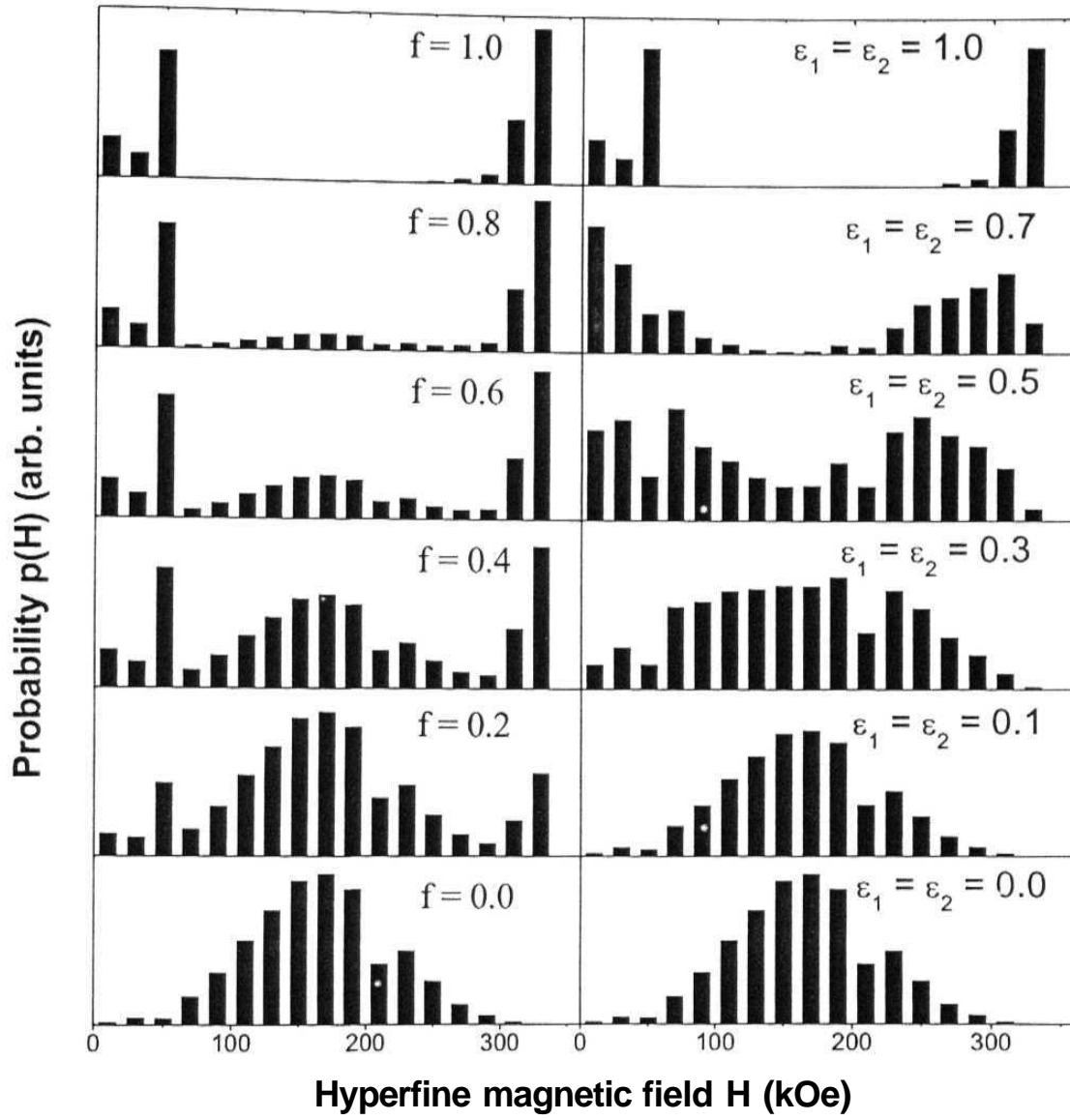


Figure 4.18: (LHS) and (RHS) respectively show the calculated probabilities at different stages of the NG and SD processes at 300 C for the $x = 0.45$ alloy.

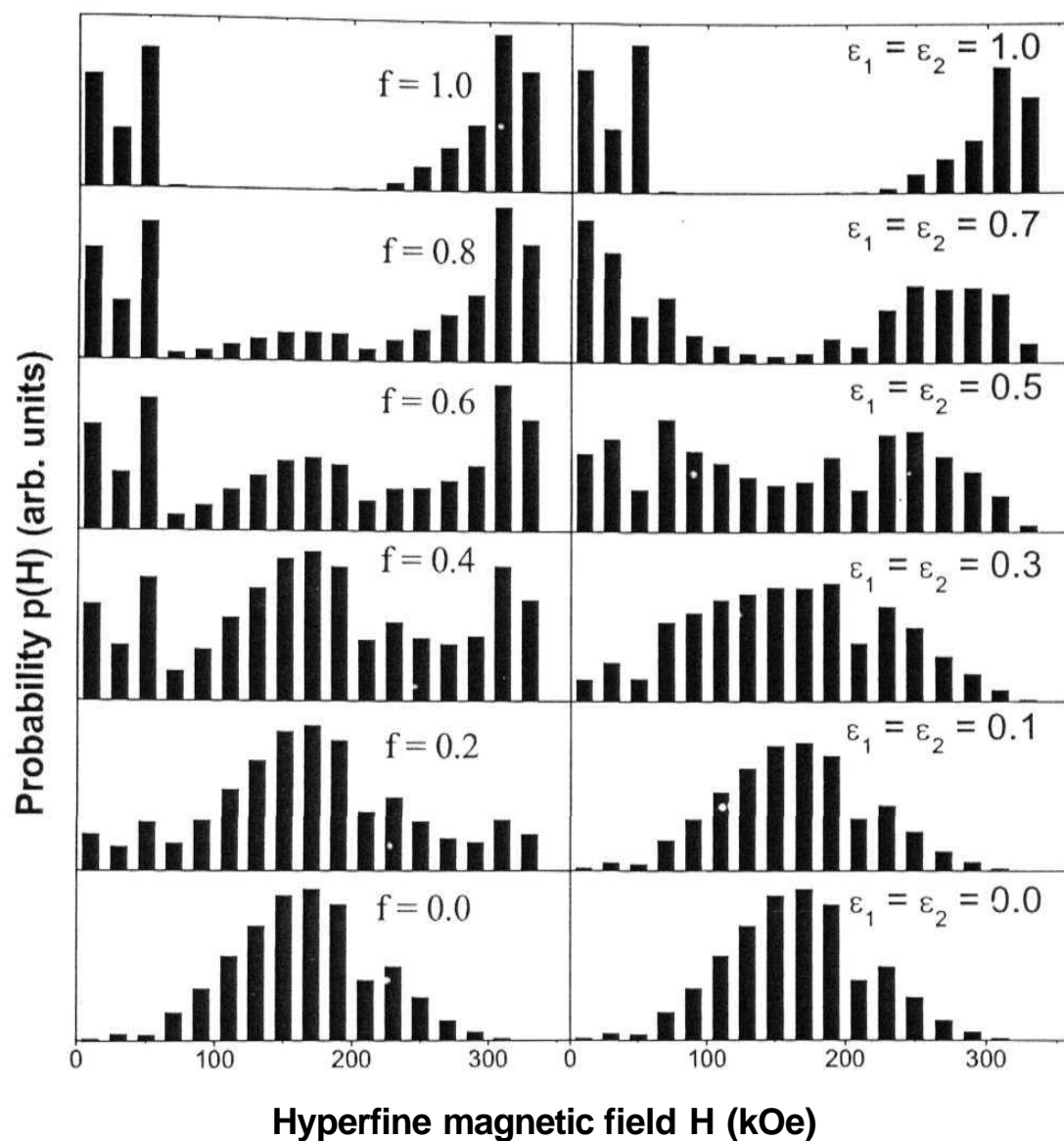


Figure 4.19: (LHS) and (RHS) respectively show the calculated probabilities at different stages of the NG and SD processes at 400 C for the $x = 0.45$ alloy.

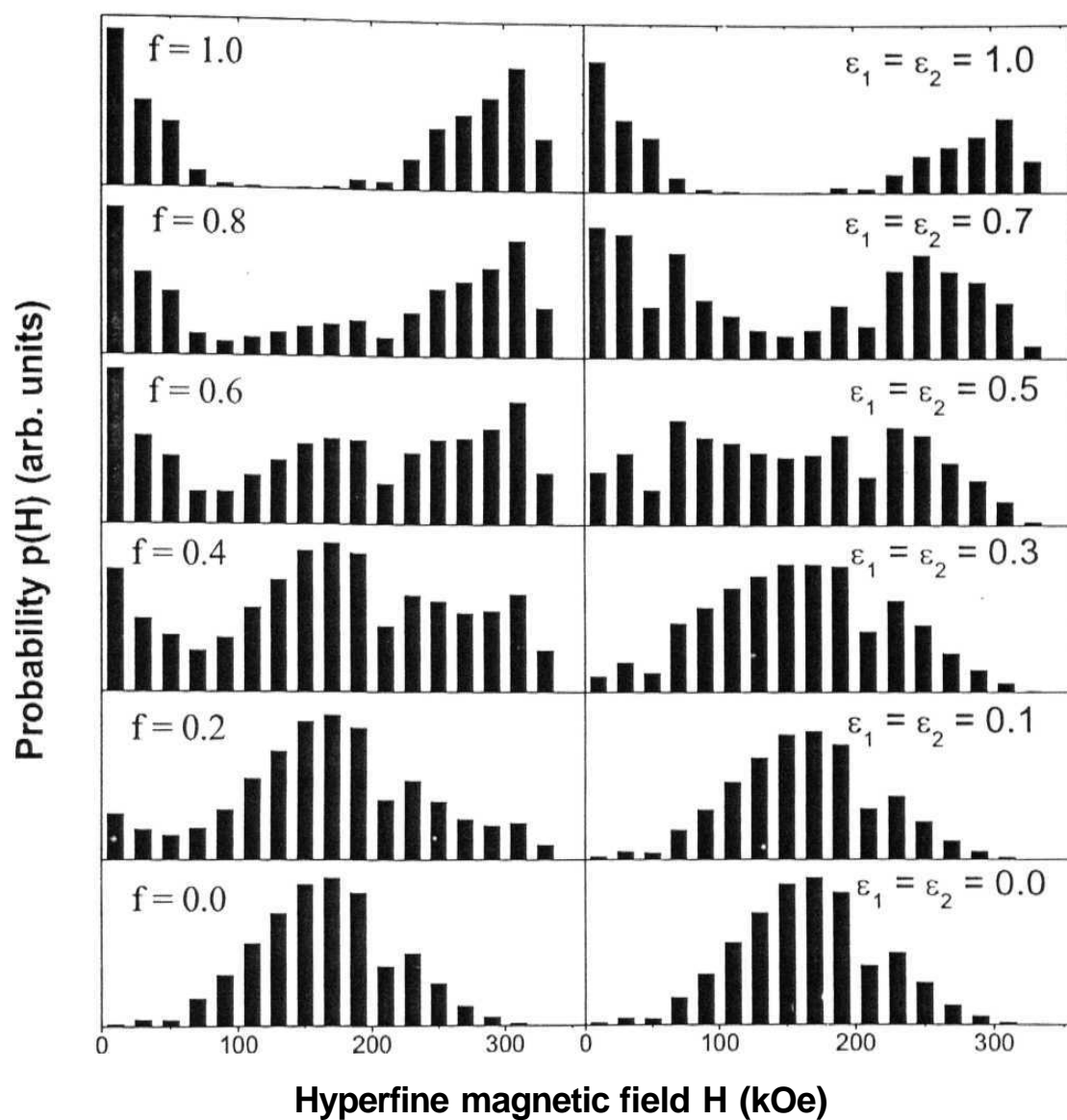


Figure 4.20: (LHS) and (RHS) respectively show the calculated probabilities at different stages of the NG and SD processes at 475°C for the $x = 0.45$ alloy.

It is to be noted from the above figures (4.16-4.20) that though the final distributions are almost the same for both SD and NG (as expected) but during the initial stages (let's say up to $f=0.6$ for NG and $\varepsilon_1=\varepsilon_2=0.5$ for SD) they are quite different. The SD distributions are broadened without the appearance of the extreme end peaks (denoting Fe-rich and Cr-rich phases) whereas NG distributions show the extreme peaks from the beginning itself without initial broadening. This difference in distributions from these two processes is in accordance with the earlier comments [9].

Let us now compare the distributions obtained in figures 4.16 to 4.20 with our experimental distributions of figures 4.14 and 4.15. The initial broadening of the experimental distributions without the extreme fields peaks, in agreement with the calculated distributions obtained for the SD model, is the clear indication of the SD process occurring in these systems with 35 and 45 at % Cr concentration at temperatures 300, 400 and 475°C. The final degree of decomposition obtained using the method of Dubiel [9] was 0.54 at 475°C for the $x=0.45$ alloy system, which was of the same order of magnitude as obtained for the polycrystalline alloy [9]. In case of 10 and 20 at % alloys the calculated distributions obtained at 300°C (for $x = 0.1$) and 400°C (for $x = 0.2$) by assuming SD and NG processes using the above prescriptions are shown in figures 4.21 and 4.22 respectively (LHS-NG and RHS-SD). If we compare these distributions with the experimental distributions of figures 4.10 and 4.11 respectively, then it is evident that the decomposition is proceeding through NG process in case of 20 at % Cr sample and no decomposition for the 10 at % Cr sample.

The second method is to look at the average HMF, $\langle H \rangle$, derived from the Mossbauer spectra. This was suggested as a very good method of finding whether the phase decomposition reaction proceeds through (NG) or (SD) [9]. Figures 4.23a and 4.24a show the temporal evolution of $\langle H \rangle$ at 400 and 475°C for the 35 at % Cr alloy and at 475°C for the 45 at % Cr alloy. The absolute

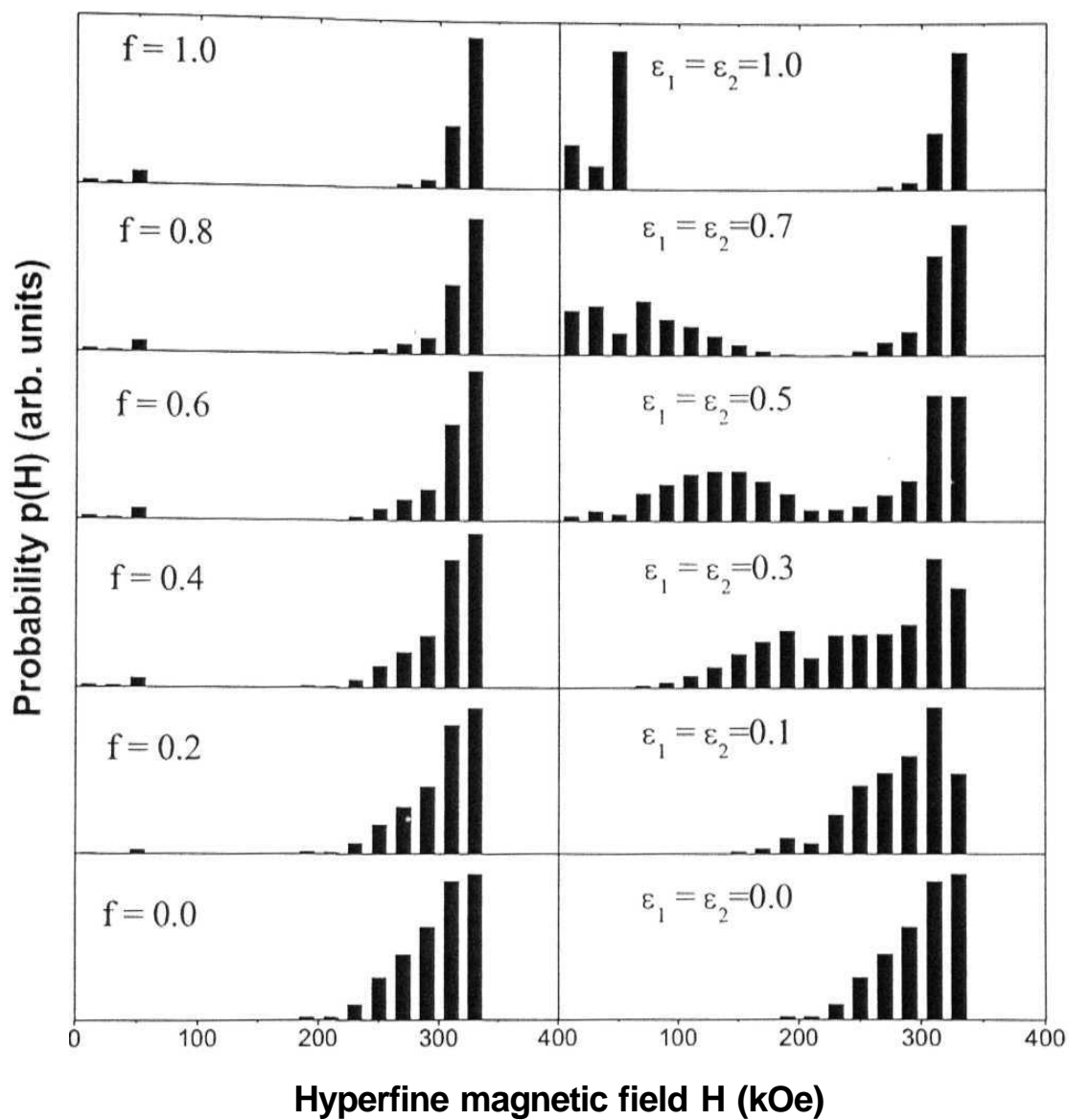


Figure 4.21: (LHS) and (RHS) respectively show the calculated probabilities at different stages of the NG and SD processes at 300 C for the $x = 0.1$ alloy.

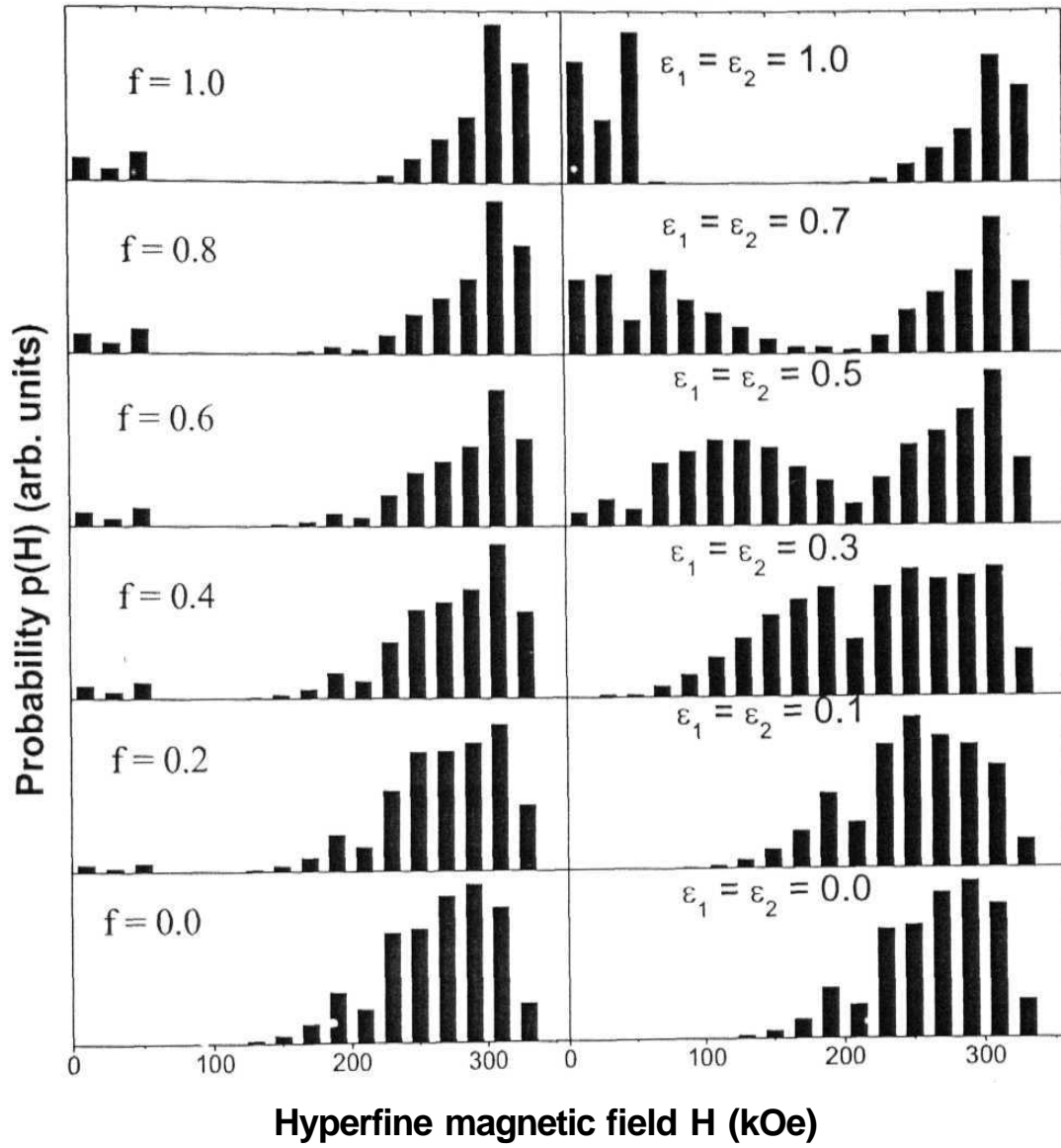


Figure 4.22: (LHS) and (RHS) respectively show the calculated probabilities at different stages of the NG and SD processes at 400°C for the $x = 0.20$ alloy.

rates of changes of grain size and $\langle H \rangle$ are different at these two temperatures (as expected) but the immediate rise in $\langle H \rangle$ with time is a clear indication that the reaction is proceeding through Spinodal decomposition [9]. However for the 10 at % Cr alloy there was hardly any decomposition to change the $\langle H \rangle$, and for the 20 at % Cr sample, the $\langle H \rangle$ at 400° C was nearly constant (changed from 286 kOe for the as-milled state to 295 kOe after ½ hour and 298 kOe after 265 hours of heat treatment) with time. This is in contrast to the sharp changes that occurred in case of 35 and 45 at. % Cr alloys, showing clearly that the NG process is taking place in the 10 and 20 atomic percent Cr alloys.

One interesting result that emerges from our study is that the grain growth is linearly co-related to $\langle H \rangle$ independent of temperatures as shown in figures 4.23b and 4.24b for $x = 0.35$ and $x = 0.45$ alloy compositions. The absolute kinetics of grain growth and SD is also similar as shown in figures 4.23a and 4.24a. This implies that the phase formation through the SD process takes place over a spatial region of the order of the nanocrystalline grain size and the underlying mechanism and driving force for both the processes is same, viz. to minimize the contribution of the interface concentration gradient energy to the total Gibbs free energy.

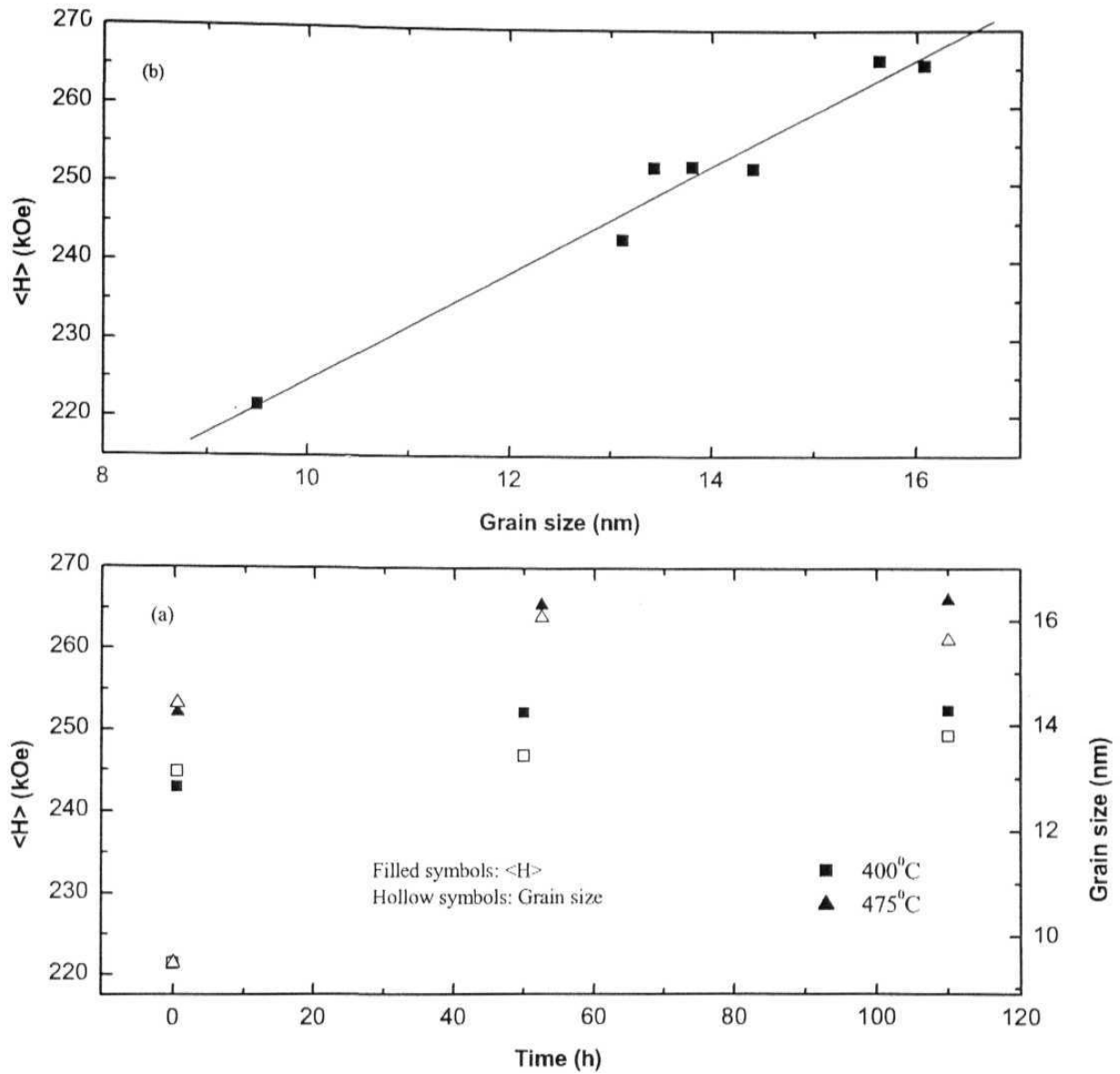


Figure 4.23: (a) Shows the similar kinetics at different temperatures of grain growth and $\langle H \rangle$; (b) Parametric plot shows the temperature independent linear relationship between grain growth and $\langle H \rangle$ for the $x = 0.35$ alloy.

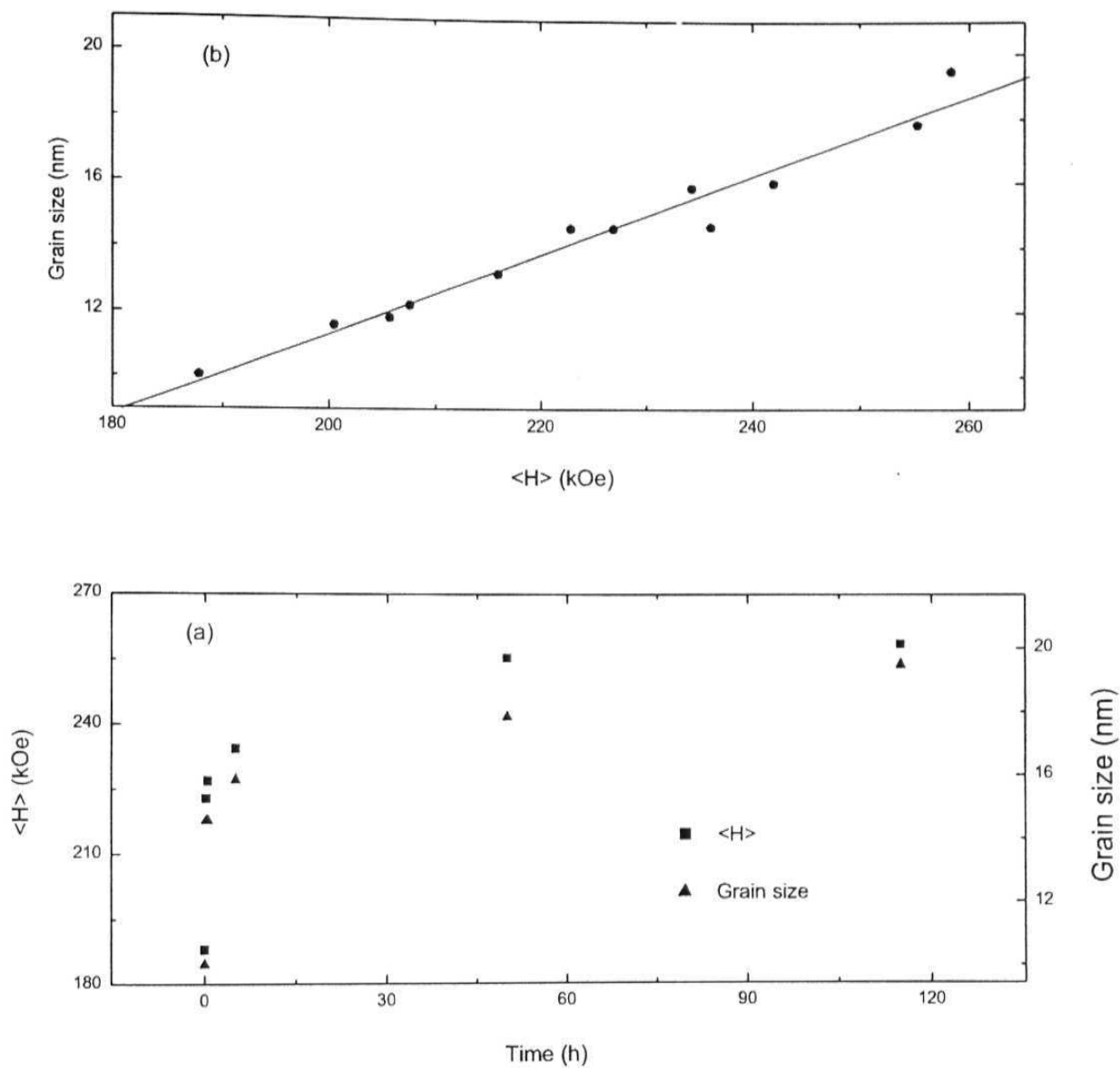


Figure 4.24: (a) Shows the similar kinetics at 475°C of grain growth and $\langle H \rangle$, the behaviour was analogous at 400 and 300°C also. (b) Parametric plot shows the temperature independent linear relationship between grain growth and $\langle H \rangle$ for the $x = 0.45$ alloy.

References

- [1] J. W. Cahn, *Acta Metallurgica* 9, 795 (1961).
- [2] S. Katano and M. Iizumi, *Phys. Rev. Lett.* 52, 835 (1984).
- [3] G. F. Mazenko, O. T. Valls, and F. C. Zhang, *Phys. Rev. B* 32, 5807 (1985).
- [4] S. M. Dubiel, J. Cieslak, and B. Sepiol, in: *Mossbauer Spectroscopy in Materials Science*, edited by M. Miglierini and D. Petridis (Kluwer Academic Publishers, Netherlands, 1999), p. 107.
- [5] T. Ujihara and K. Osamura, *Acta Mater.* 48, 1629 (2000).
- [6] S.M. Dubiel and G. Inden, *Z. Metallk.* 87, (1987) p. 544.
- [7] J. Cieslak and S. M. Dubiel, *J. Alloys and Compounds*, 269, (1998) p. 208.
- [8] J. M. Hyde, M. K. Miller, A. Cerezo, and G. D. W. Smith, *Applied Surface Science* **87/88**, 311 (1995).
- [9] J. Cieslak, S. M. Dubiel, and B. Sepiol, *J. Phys.: Condens. Matter* 12, (2000) p. 6709.

Chapter 5
Precipitation Phase Transformation in Nanocrystalline Fe-Mo
Alloys

5.1 Introduction

The Fe-Mo phase diagram, figure 5.1 (ref 43 chapter 3), shows that Fe rich Fe-Mo alloys form a bcc solid solution (α phase) having a maximum solubility of 24.4 at. % Mo in Fe at a temperature of 1449° C, which decreases rapidly to a low value of 1.14 at. % Mo at 550° C. Below about 900° C there exists an intermetallic compound of stoichiometry Fe_2Mo (λ phase). Earlier measurements on a phase microcrystalline Fe-Mo alloys were done after retaining the high temperature α phase by quenching into cold helium gas. Mossbauer spectroscopy was used to study the phase separation in the two-phase region ($\alpha+\lambda$) at lower temperatures and the solvus compositions were determined at these temperatures [1,2]. In another recent study, the phase decomposition in splat-quenched Fe-20 at. % Mo alloy was studied by atom probe field ion microscopy and high-resolution electron microscopy [3, 4].

In this study we look at the precipitation phase transformation in the nanocrystalline Fe-rich Fe-Mo alloy system and compare the behaviour with the microcrystalline system. Nanocrystalline Fe-Mo alloys were synthesized in the high temperature α phase by means of mechanical alloying and the nanostructure evolution and phase decomposition behaviour was studied using X-ray diffraction and Mossbauer spectroscopic measurements. We find that the transformation proceeds on an accelerated time scale relative to the microcrystalline system and Mo precipitation started only after a critical grain size was attained.

5.2 Experimental

Nanocrystalline $\text{Fe}_{1-x}\text{Mo}_x$ ($x=0.01, 0.015$, and 0.05) alloys were prepared by mechanical alloying of the elemental Fe (Aldrich Sigma 4N) and Mo (M3N \pm , -200 mesh, from Alfa Products) powders for various times ranging from 24 to 250 hours. The $x=0.05$ alloy was heat treated at 520° C and 400° C

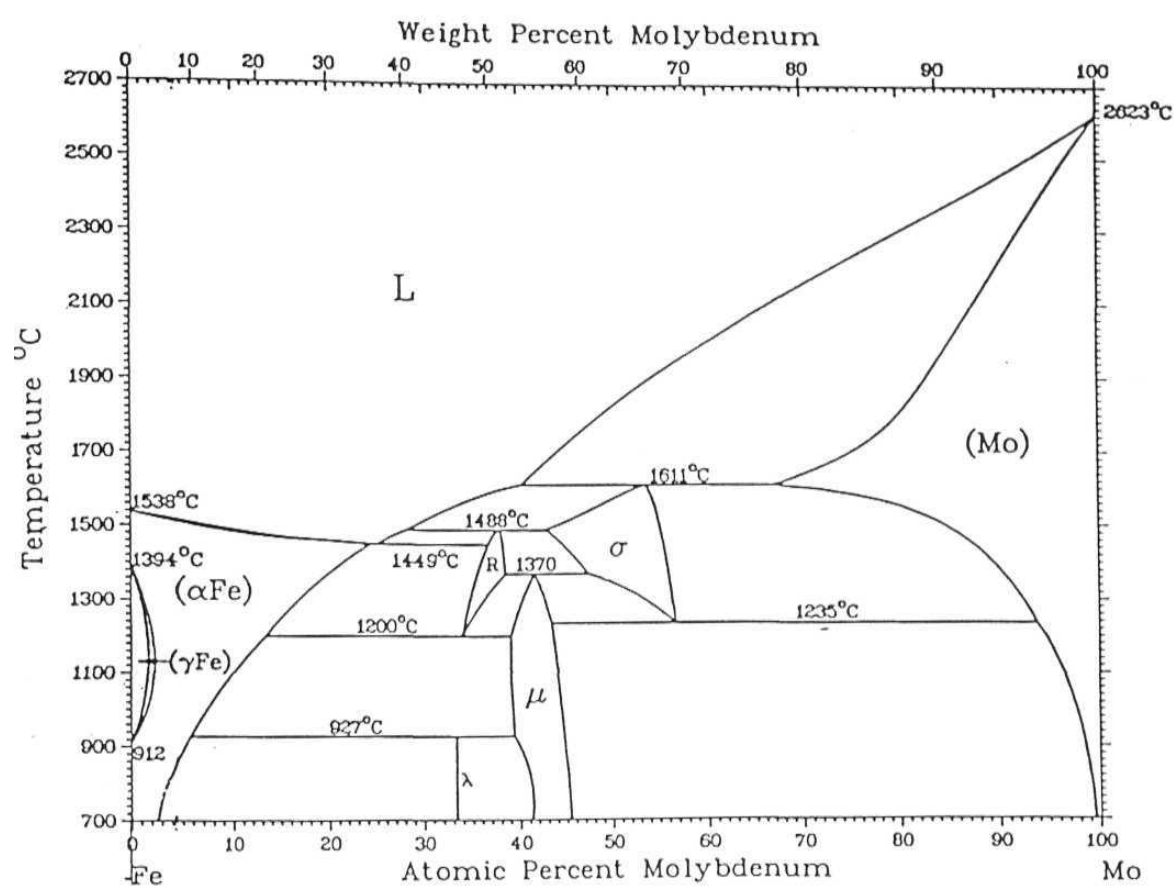


Figure 5.1 Thermodynamic equilibrium phase diagram
For Fe-Mo alloy

Phase	Composition (at. % Mo)	Structure	Prototype
αFe	0 to 24.4	A2	W
γ	0 to 1.7	A1	Cu
λ	33.3	C14	MgZn_2

for various periods of times ranging from 0.5 hour to 275 hours, the $x=0.015$ alloy was heat treated at 520°C for 24 hours and this heat treated sample was subsequently heat treated at 1100°C for 15 minutes. The field distributions obtained from the Mossbauer spectra were fitted to Gaussian functions peaked at the field positions corresponding to HMF seen by Fe atoms with 0, 1, and 2 total number of Mo atoms in the 1st or 2nd nearest neighbor shell; the intensity of these Gaussian gave the fraction of Fe atoms with different number of Mo 1st and 2nd nearest neighbor. This corresponds to a 14 nearest neighbor model for the bcc lattice on the assumption that the field perturbations caused by the 1st and 2nd neighbor Mo solute atoms are approximately the same [ref 69 of chapter 3]. The fraction of the X phase was determined by fitting the absorption near zero velocity region of the Mossbauer spectrum to a paramagnetic quadrupole doublet, with an quadrupole splitting of 0.22 mm/sec and isomer shift of -0.214 mm/sec relative to pure Fe [1]. The Fe contamination of the as-milled Fe-5 atomic percent Mo sample was about 1 atomic percent.

5.3 Results and discussion

The X-ray diffraction patterns of the as-milled alloys are shown in figure 5.2. Homogeneous single phase (a) bcc alloys are formed as a result of mechanical alloying for all compositions although the equilibrium solubility is very low at room temperature (less than 1 at. %). This is consistent with many earlier observations that high-energy ball milling gives phases with extended solid solubility. The average grain size obtained after correction for the instrumental broadening was in the range of 10 to 13 nm for different as-milled alloys/There is a small γ phase loop above temperatures of 900°C in the phase diagram and the 1 at. % Mo alloy was milled for extended periods of time up to 250 hours; however the formation of fcc (γ) phase was not detected.

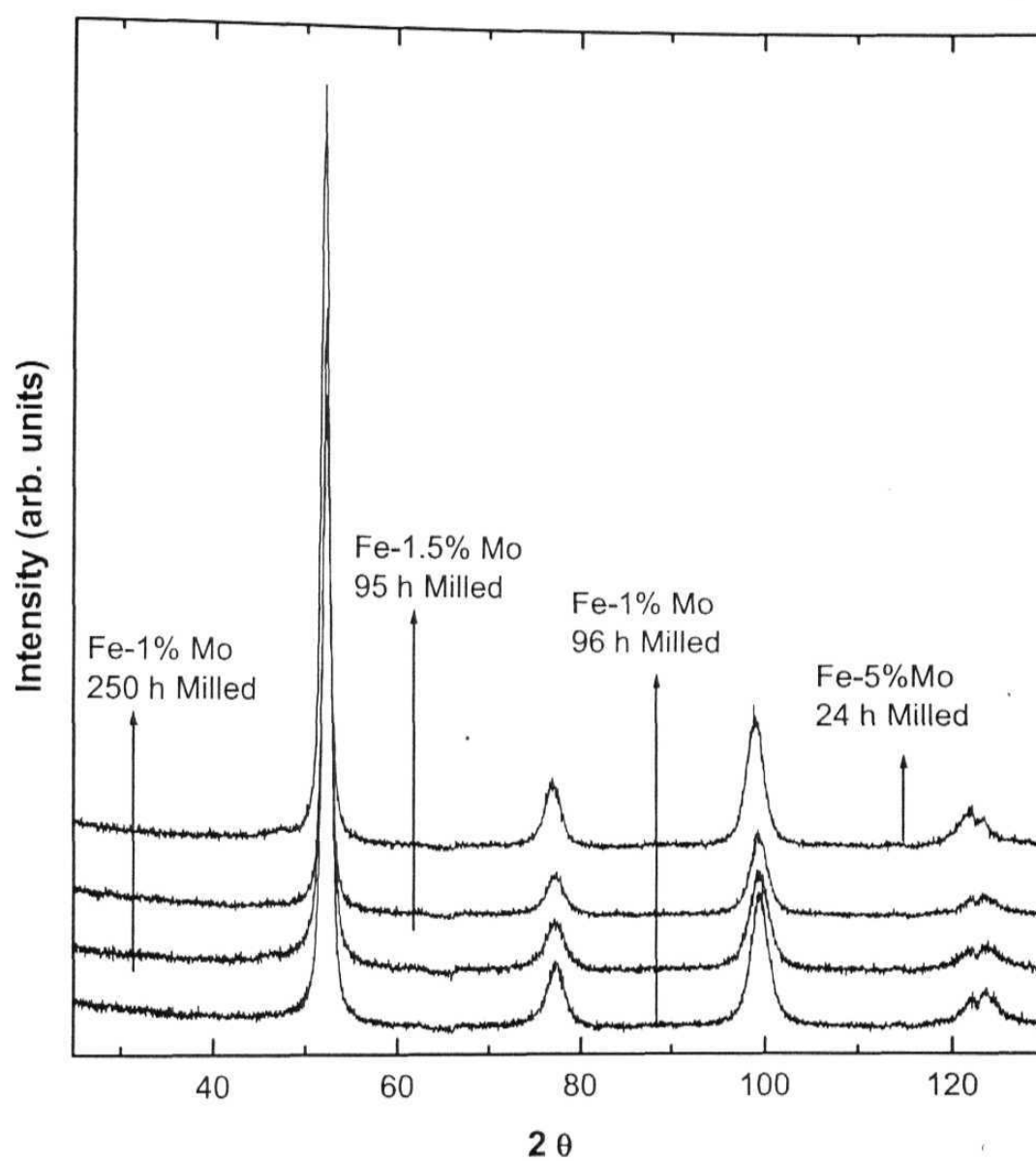


Figure 5.2: X-ray diffraction patterns of as-milled Fe-Mo alloys showing the formation of homogeneous single phase (a) bcc alloys.

The Mössbauer spectra and the corresponding HMF distribution of the as-milled alloys are shown in figure 5.3. These spectra correspond to the formation of homogenous Fe-Mo solid solutions and there is no evidence for a paramagnetic doublet from the λ phase. The Mossbauer spectra are thus consistent with the X-ray data. The satellite lines arising from the presence of one or more Mo neighbours in the near neighbor (nn) environment of Fe are evident in the Mossbauer spectra as well as the hyperfine magnetic field distributions. The main peak in the field distributions at about 333 KOe is attributed to Fe atoms with no Mo near neighbours. The satellite peaks at around 297 and 249 KOe are attributed to Fe atoms with one and two Mo neighbours respectively. These are in good agreement with previously reported values for coarse-grained samples [1,2, Ref. 32 of chapter 2]. The areas under these peaks also correspond very well with the probabilities of different number of near neighbor configurations in the binomial distribution. In using the binomial distribution to estimate the probabilities of the configurations we assumed 14 near neighbours to a given site (8 first neighbours and 6 second neighbours in the bcc lattice) that have approximately the same distance and the hyperfine perturbations from these neighbours are similar [Ref. 32 from chapter 2 and ref. 69 of chapter 3].

The as-milled nanocrystalline alloys were heat treated to see the nano structure evolution and equilibrium phase decomposition behaviour. Figure 5.4 shows the representative Mossbauer spectra and the corresponding HMF distribution for the 5 at. % Mo sample heat treated at 520° C. The intensities of the satellite lines were found to diminish up to 50 hours of heat treatment whereas that of the zero Mo peak was found to increase. Correspondingly there was no evidence for growth of Mo rich X phase in the spectrum. From the phase diagram it was expected that the λ phase should have developed giving rise to a quadrupole split spectrum [1] with no HMF. The absence of the X

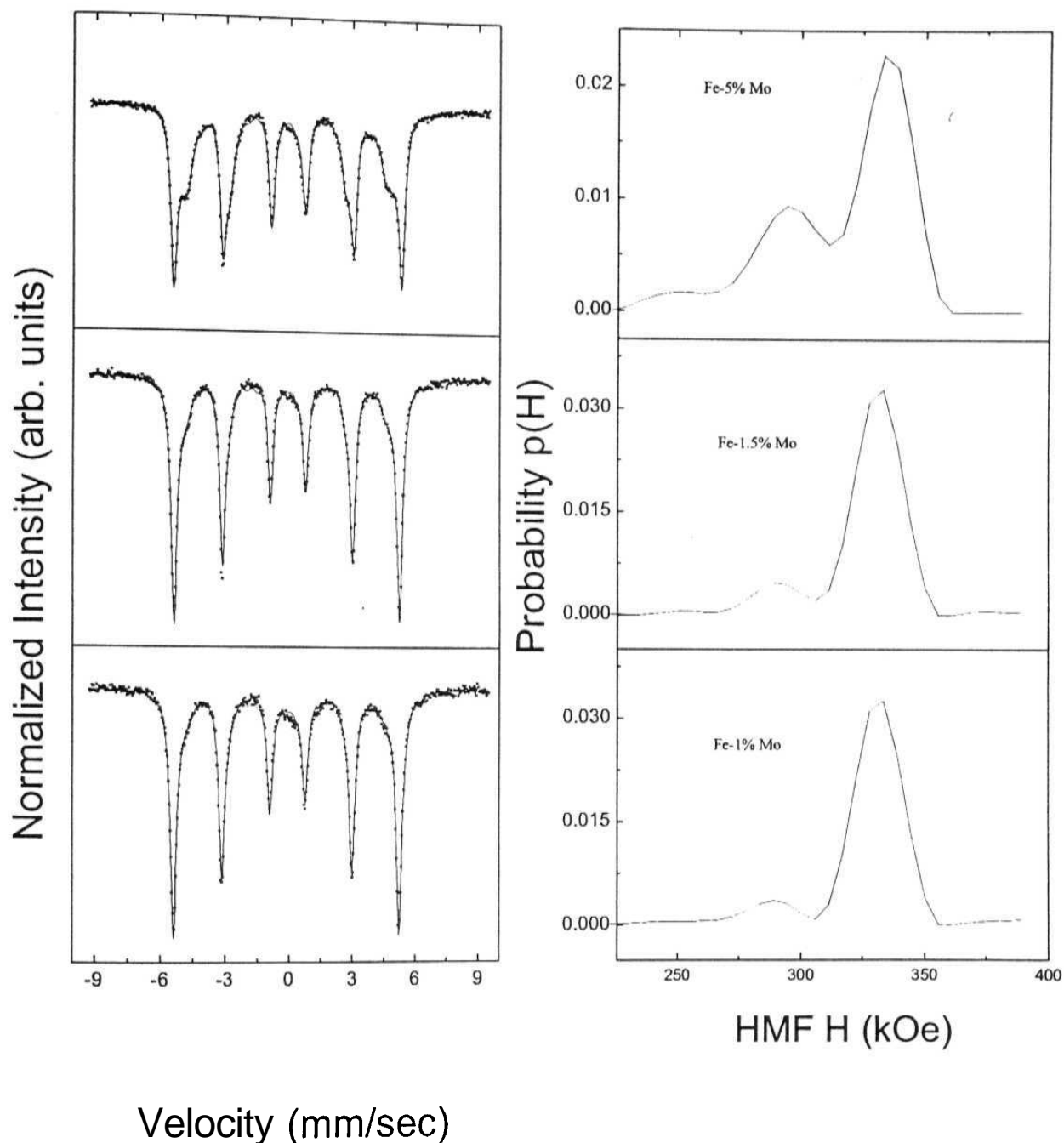


Figure 5.3: Mossbauer Spectra and the corresponding model independent hyperfine magnetic field distributions of as-milled Fe-Mo alloys, showing satellite lines due to different number of Mo neighbours of Fe. In the Mossbauer spectra the experimental data are represented by solid symbols whereas solid lines show the fit to data.

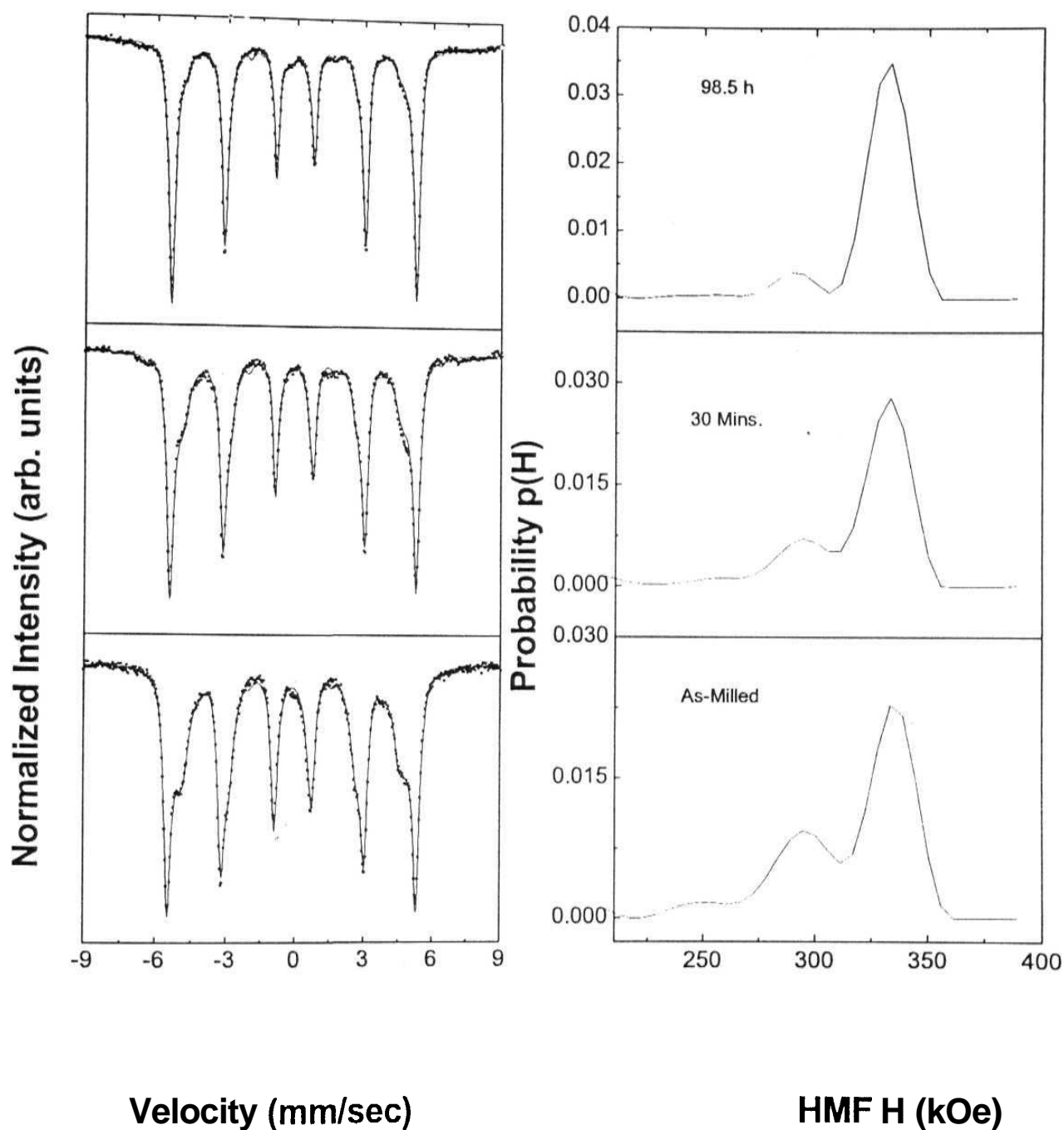


Figure 5.4: The evolution of Mossbauer spectra and hmf distributions for 5 at.% Mo alloy as a function of time. A decrease in satellite peak intensity is seen at earlier times and the formation of λ phase in the 98.5 h heat-treated sample is seen as a small absorption near zero velocity.

phase but the depletion of Mo from the Fe environment shows that Mo clustering is taking place from the α phase. This is in qualitative agreement with earlier observations of coherent Mo clustering observed using electron microscopic [3,4] and diffuse X-ray scattering measurements [5] on microcrystalline alloys. However a comparison of the time dependence of the satellite peak intensities for the microcrystalline (figure 7 of reference 1) and nanocrystalline alloys (presented in figure. 5.5) shows them to be different. For the microcrystalline alloys there is no significant decrease in the satellite peak areas up to 2 hours of heat treatment after which it starts showing a decrease between 2 and 5 hours. For the nanocrystalline system the decrease in satellite peak area is observed to be faster and a significant decrease in intensity takes place even for half an hour of heat treatment. The reason for this accelerated clustering of Mo atoms lies in the larger volume fraction of the grain boundary regions in the nanocrystalline systems, which provide faster diffusion paths.

It may be possible that the behavior observed in microcrystalline Fe-Mo alloys at 550 °C may occur in the nanophase system at a lower temperature due to faster diffusion through grain boundaries. Therefore we heat-treated the as-milled 5 at. % Mo alloy at 400°C for various periods of times up to 100 hours to verify this hypothesis. The results obtained for this heat treatment are presented in figure 5.6. As can be seen from this figure the kinetics of the transformation is indeed slower at this temperature relative to 520°C as expected. However there was no reentrant increase in the satellite peak area as was observed by Marcus et. al. at 550°C in the coarse grained system. There was also no signature of the formation of Fe_2Mo phase up to 100 hours of heat treatment at this temperature, probably due to the slower kinetics of the precipitation reaction at this lower temperature.

The kinetics of grain growth of Fe-5 at % Mo alloy at 520 °C is shown in figure 5.7. Also shown in the figure is the kinetics of Mo precipitation at 520°C. The Mo atoms precipitation is represented by the fraction of Fe atoms

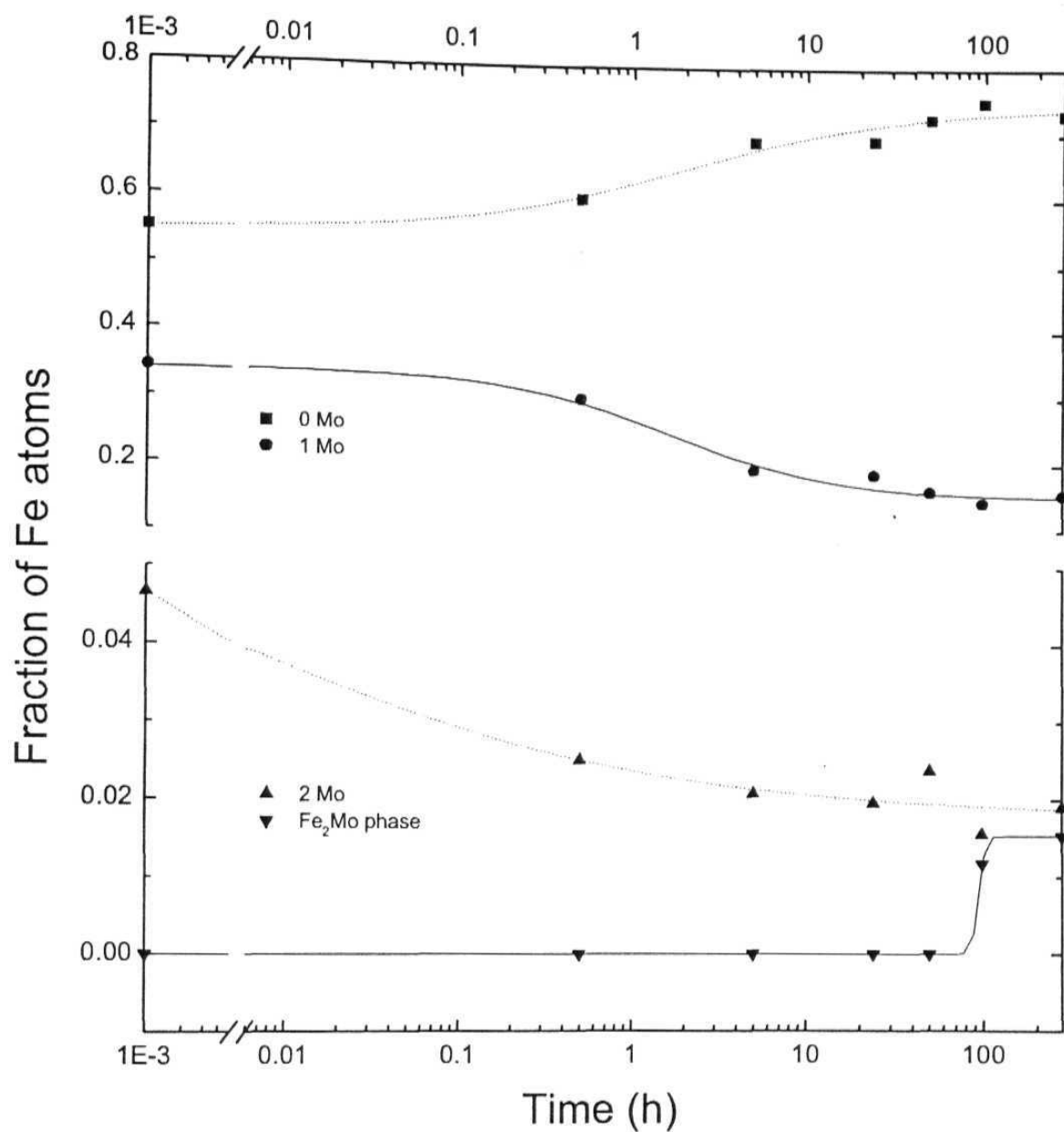


Figure 5.5 Time dependence of the main and satellite peak areas of the α phase as well as the formation of λ phase. The solid lines through the data points show sigmoidal behavior of the areas with time.

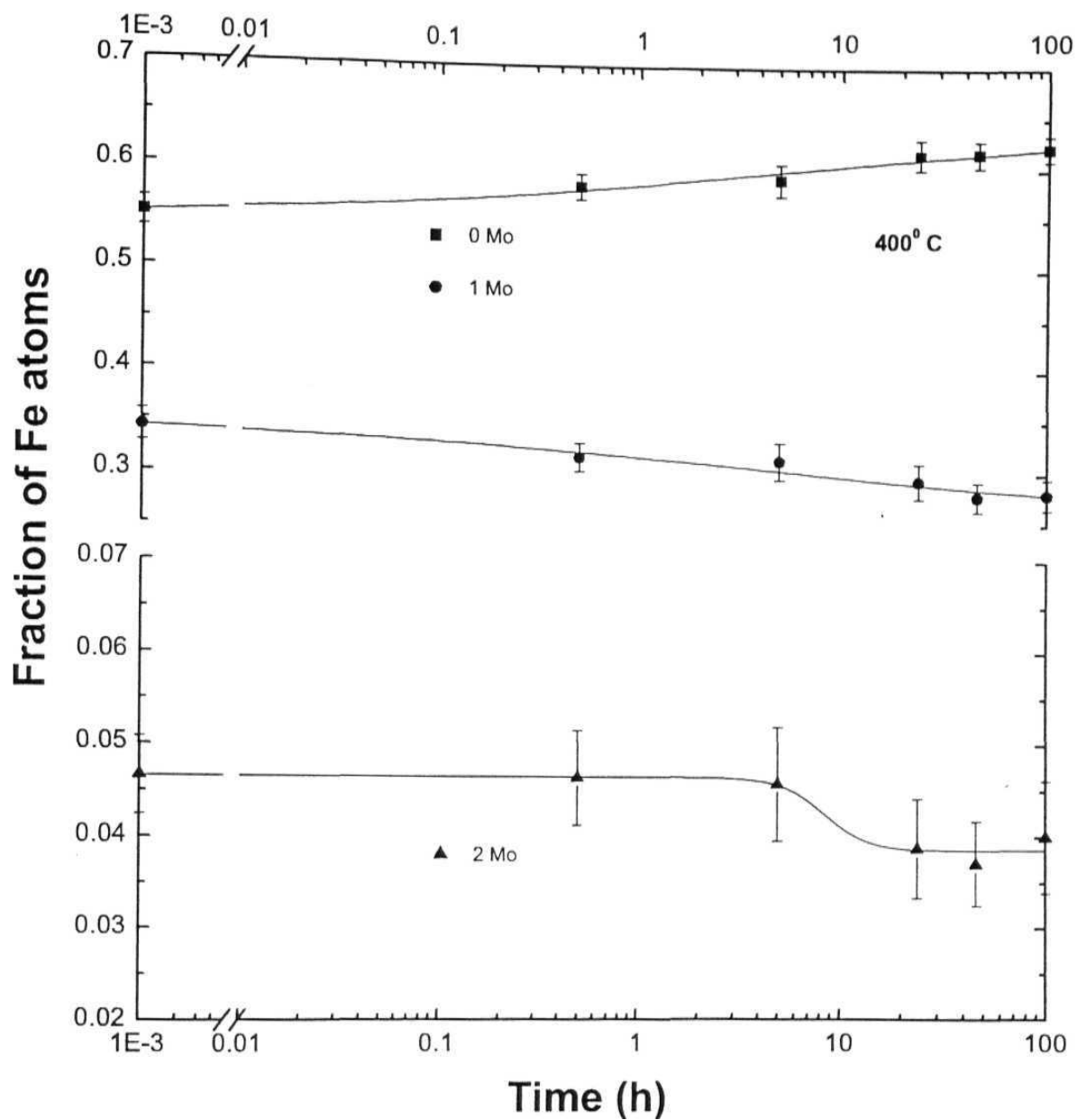


Figure 5.6: Temporal behaviour of the fraction of Fe atoms with 0, 1, and 2 total number of Mo 1st and 2nd nearest neighbours. The solid lines show the sigmoidal fits through the data points.

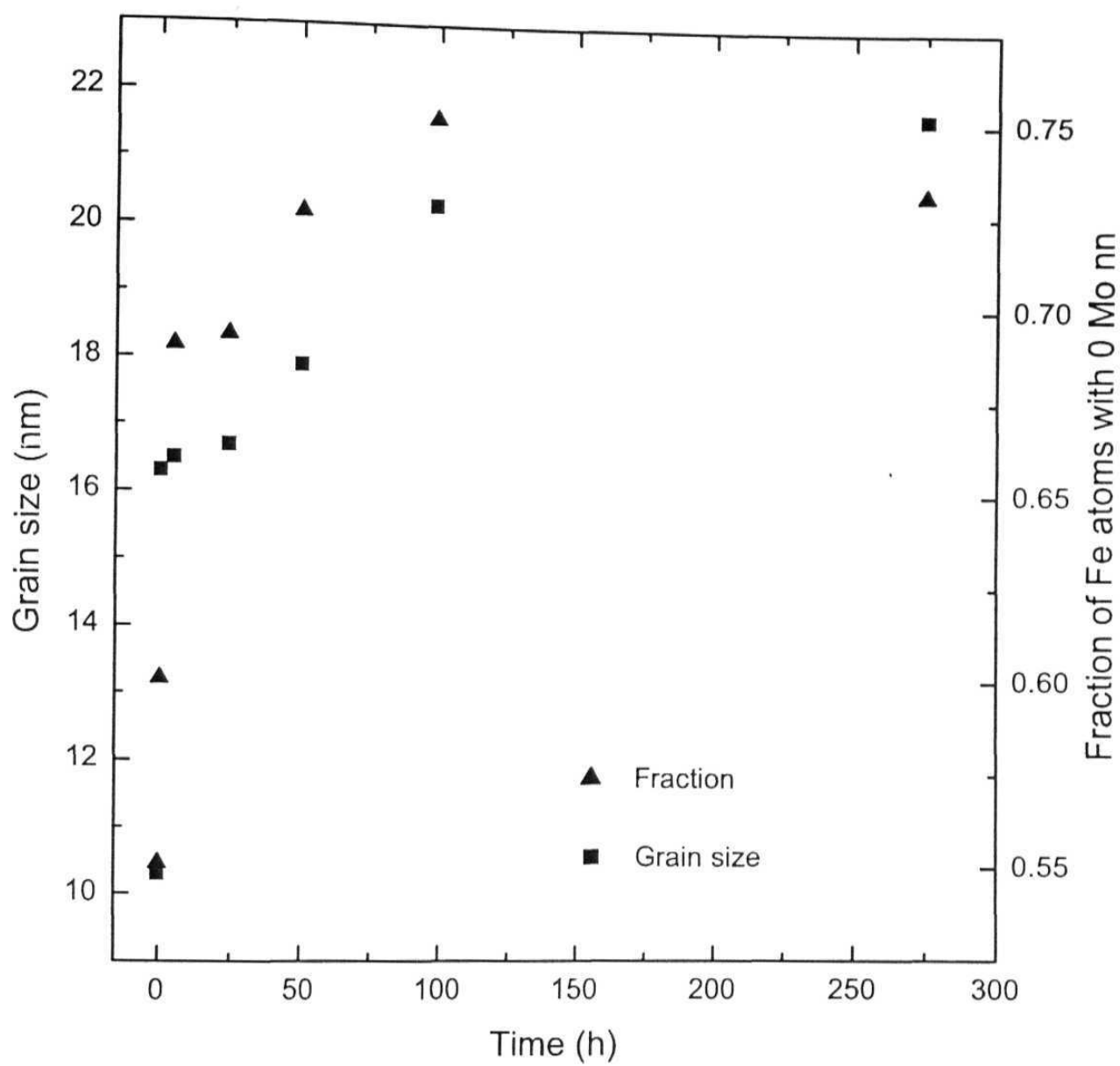


Figure 5.7: Kinetics of grain growth and Mo precipitation at 520°C.

having 0 Mo nm. Though the kinetics of these two processes is similar at later times but during the initial stages (e.g after $\frac{1}{2}$ h of heat treatment) the grain growth takes place faster than the Mo precipitation. We observe that there is an interesting correlation between the grain size and the depletion of Mo atoms from the near neighbor environment of Fe as shown in the parametric plots of figure 5.8. There appears to be a critical size below which the Mo solute atoms remain dissolved in the α phase. The presence of such a critical size also explains the different kinetics of the grain growth and precipitation processes during the initial stages of transformations. Grains grew first to the critical size and then the decomposition process started. This behavior can be explained by considering the additional contribution to the Gibbs free energy from the surface energy (γ) of the nano size grains of radius R in the nanocrystalline phase. This is referred to as a capillary effect or Gibbs Thomson effect [ref 194 of chapter 1] and the surface energy contribution to Gibbs free energy is given by:

$$\Delta G(R) = 2\gamma V_m / R \quad (5.1)$$

where V_m is the molar volume. This surface contribution increases the Gibbs free energy of a nanophase alloy relative to the bulk phase:

$$G(R) = G(\infty) + \Delta G(R) \quad (5.2)$$

The Gibbs free energy of mixing for an alloy system comprising of crystallites of finite size R will contain an additional term $\Delta G(R)$ from the surface energy contribution (equation 5.1)

$$\Delta G_{\text{mix}} = \Delta U_{\text{mix}} - T\Delta S_{\text{mix}} + \Delta G(R) \quad (5.3)$$

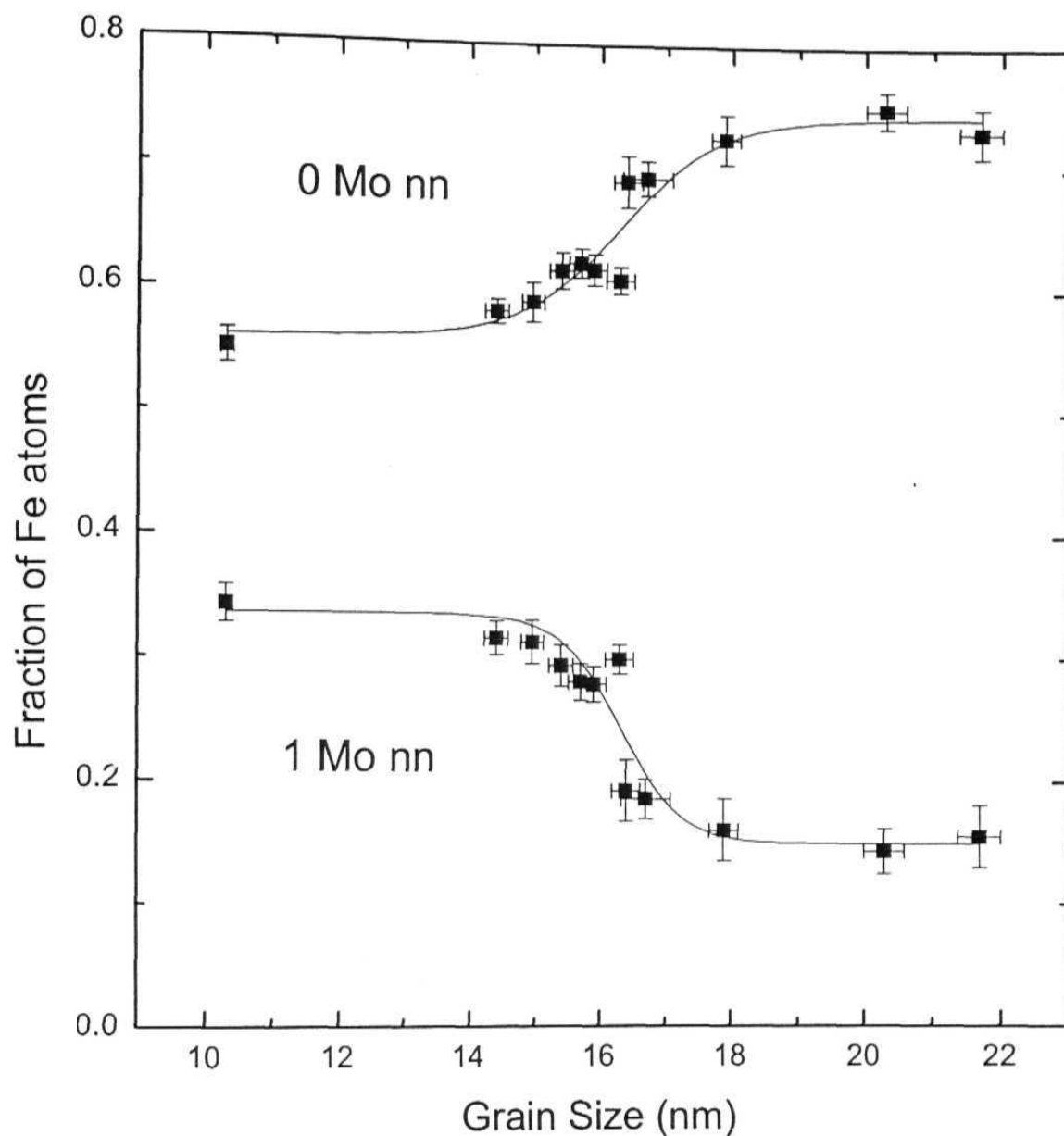


Figure 5.8: Change in the near neighbor environment of Fe due to Mo precipitation plotted as a function of grain size.

where ΔU_{mix} and ΔS_{mix} are internal energy and entropy of mixing and T is the temperature. In a system such as Fe-Mo with positive internal energy of mixing (ΔU_{mix}) the bond energies satisfy $E_{\text{AA}} + E_{\text{BB}} < 2 E_{\text{AB}}$. A solid solution of Fe and Mo at a temperature below the solvus temperature would therefore be possible for nanosize grains if the surface energy term is negative (implying negative γ) and compensates the positive internal energy of mixing to give $\Delta G_{\text{mix}} < 0$. In nanocrystalline alloys prepared by mechanical alloying the grain boundaries are predominantly high angle grain boundaries, which have a relatively open structure and large free volume. The bonds between the atoms in these high angle grain boundaries are broken (ref 194 of chapter 1, page 118). Mo or Fe atoms residing in the grain boundary regions will therefore have lower energy as compared to that of Mo or Fe atoms within the grain because of less number of repulsive Fe-Mo bonds. The surface energy (γ) can therefore be negative. This situation is in contrast to systems with a negative internal energy of mixing where the broken bonds in high angle grain boundary regions have a positive surface energy because of a decrease in the number of attractive AB bonds.

Because of the inverse R dependence of $\Delta G(R)$ there exists a radius R_0 up to which ΔG_{mix} remains negative and beyond which the free energy of mixing ΔG_{mix} becomes positive and the solute stalls to separate from the solid solution. R_0 is obtained by equating ΔG_{mix} in equation (5.3) to zero. This gives

$$R_0 = 2\gamma V_m / \Delta S_{\text{mix}} (T - T_0) \quad (5.4)$$

where T_0 is the solvus temperature, T is the temperature at which the precipitation transformation is experimentally observed, and we have taken $\Delta U_{\text{mix}} = \Delta H_{\text{mix}} = T_0 \Delta S_{\text{mix}}$. An estimate of the grain size at which the solute atoms start separating from the solution is possible if the value of γ is known. However if we assume a typical value for γ of about 200 mJ/m² [ref 194 of

chapter 1], this grain size comes out to be about 16 nm at 520°C for Fe-5 at. % Mo alloy. This estimate appears to be in agreement with our experimental observations.

The location of the Mo clusters seems to be different in the nano system as compared to the microcrystalline system. In the microcrystalline system there was once again an increase in the satellite peak area between 10 hours and 53 hours, after which the Mo rich *X* phase started forming and there was a continuous decrease in the satellite peak area. The initial decrease followed by an increase in satellite peak intensity after 20 hours of heat treatment implies that Mo clusters that may have been precipitated within the grains are once again dissolved in the Fe matrix before the Fe₂Mo phase is formed. In contrast our nanocrystalline alloys show no reentrant increase of satellite peak areas. This implies that the formation of the *X* phase is taking place in the already precipitated Mo clusters. As discussed above, the Mo solute atoms move out of the α phase once the grains grow in size and the most likely place where they can migrate is to the grain boundary regions. The typical size of the coherent Mo precipitates as determined by Isheim [4] from HREM studies was about 2 nm and such clusters could be accommodated in the grain boundary regions. Although we do not have microscopic measurements to find the locations of the precipitates in the nano phase alloy but based on the above arguments it is reasonable to assume that the Mo precipitation as well as the *X* phase formation takes place in the grain boundary regions. This is further corroborated by carrying out a heat treatment at a high temperature of 1100°C for the $x=0.015$ alloy (earlier heat treated at 520°C for 24 hours) in which the satellite intensity has decreased due to Mo clustering (figure 5.9a). The Mossbauer spectra and the hmf distributions for this heat treated sample (figure 5.9b) are similar to the disordered as-milled alloy showing that the precipitated Mo clusters once again dissolve into the matrix above the solvus temperature

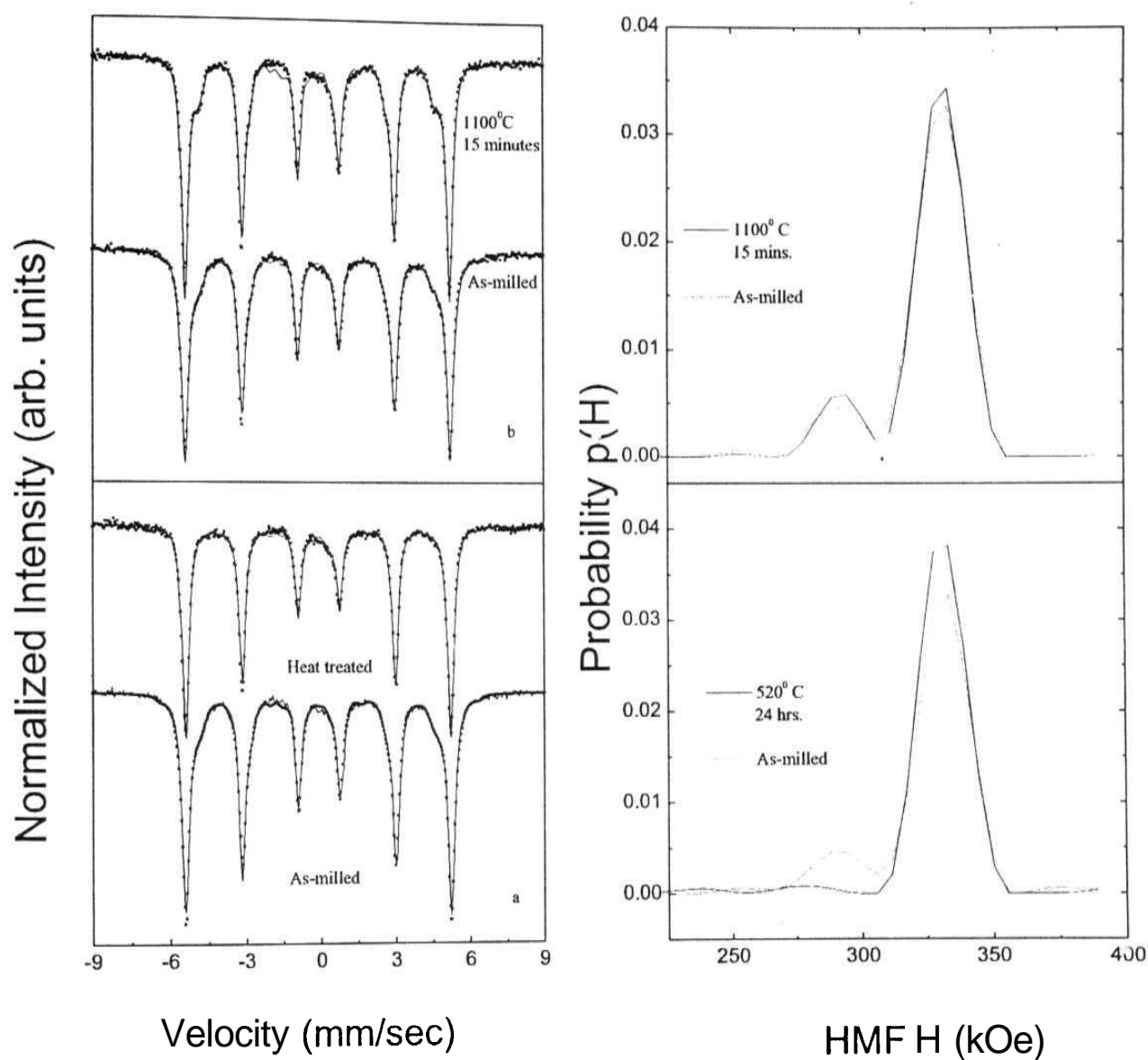


Figure 5.9: Mossbauer spectra and HMF distributions for the 1.5 at. % Mo alloy showing: (a) the decrease in the satellite peak intensity due to Mo segregation to grain boundaries. (b) Similar satellite peak intensities in the as-milled sample and the sample heat-treated at 1100 C.

and the high temperature a phase is retained at room temperature. The grain size is microcrystalline as revealed by the line width of the X-ray diffraction pattern recorded for this sample (figure 5.10).

In conclusion, alloys up to 5 at. % Mo in Fe were synthesized by mechanical alloying and formed in a phase bcc solid solutions with average grain sizes in the range of 10-13 nm. The precipitation transformation ($\alpha \rightarrow \alpha + \lambda$) was found to proceed via a Mo clustering that was correlated with the size of the nano grains. We observed that the precipitation phase transformation in nanocrystalline Fe-Mo alloys was influenced by the surface energy contributions of the nano-sized grains. The increased solubility of Mo in Fe for small size grains as well as the precipitation of Mo beyond a critical size was understood in terms of the capillary effect or Gibbs Thompson effect with a concept of negative surface energy contribution to the Gibbs free energy of mixing arising from atoms residing in the grain boundaiy regions of nanocrystallites for an alloy with positive internal energy of mixing. This contribution increased the stability of the solid solution for nano sized grains and the Mo precipitation started once the grains grew beyond a critical size. We argue that the Mo precipitation takes place in the grain boundaiy regions and the Mo-rich X phase also precipitates directly in the grain boundaiy regions in contrast to the microcrystalline alloys where the Mo clusters formed within the grains and were first dissolved into the Fe-matrix before the X phase was formed.

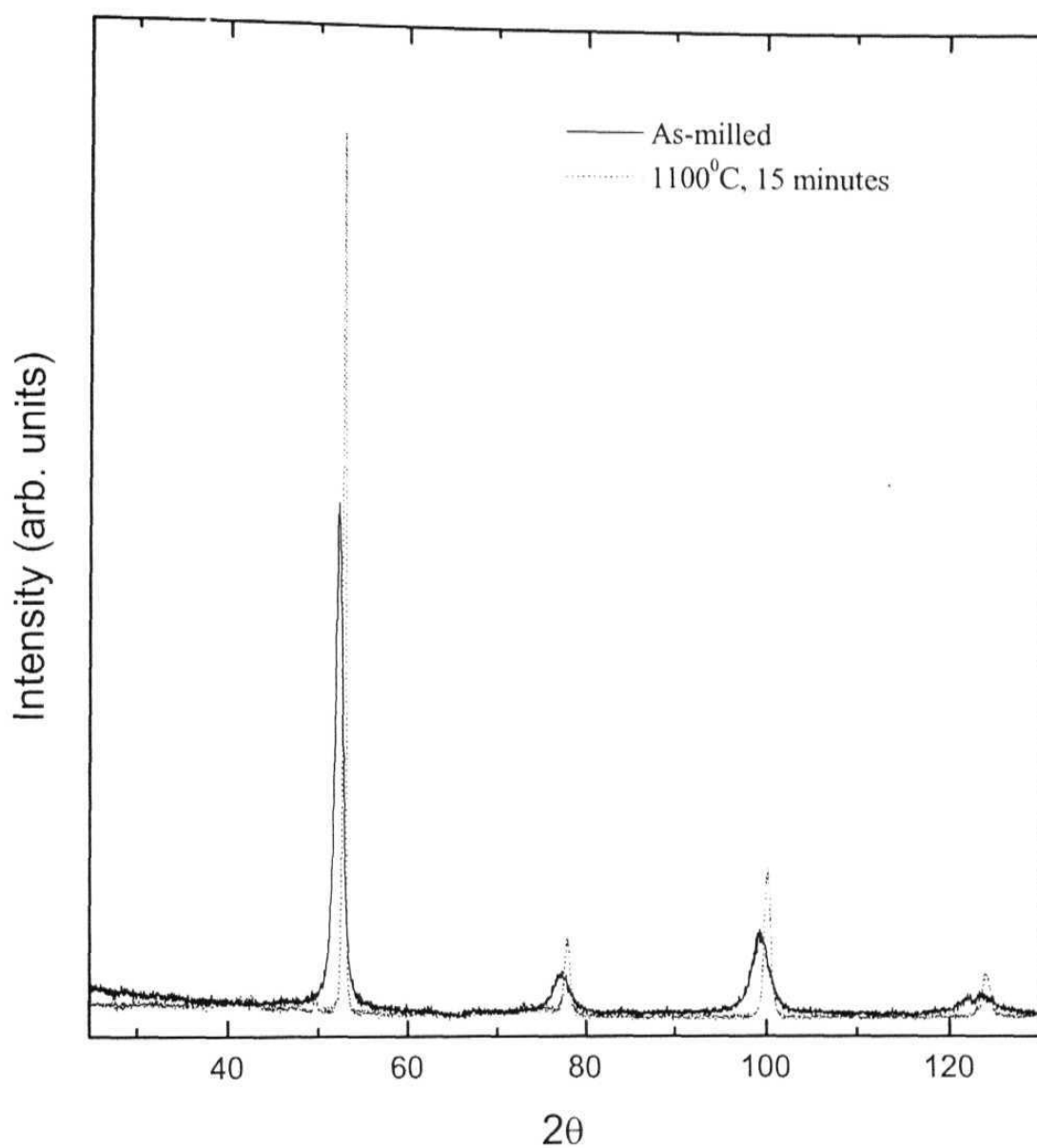


Figure 5.10: X-ray diffraction patterns of the as-milled and re-crystallized (heat treated at 1100°C, 15 minutes) 1.5 at. % Mo alloy. The heat treated sample shows a decrease in the line width due to the formation of coarse grained a phase.

References

- [1] H. L. Marcus, M. E. Fine, and L. H. Schwarz, J. Appl. Phys. 38, 4750 (1967).
- [2] H. L. Marcus and L. H. Schwarz, Phys. Rev. 62, 259 (1967).
- [3] D. Isheim, O. C. Hellman, D. N. Seidman, F. Danoix, and D. Blavette, Scripta Mater. 42, 645 (2000).
- [4] D. Isheim, Acta Mater. 48, 2873 (2000).
- [5] E. Hornbogen, Z. Metallk. 52, 47 (1961).

Chapter 6

Structural Phase Transformations in Fe-Ge and Fe-Mn-Ge alloys: Manifestation of Gibbs-Thompson Effect

The Fe-Ge equilibrium phase diagram (figure 3.22) shows a $L1_2$ ordered ϵ' phase in the temperature range of 400°-700° C near Fe_3Ge stoichiometry. Recently an interesting phase transformation behaviour was observed by Zhou and Bakker [1] during mechanical milling of $L1_2$ ordered Fe_3Ge alloy. The fcc based $L1_2$ structure was first atomically disordered for short periods of milling (about 2 hours) as seen by the disappearance of super-lattice reflections, but later transformed to a disordered bcc structure on further milling. Thus there was not only chemical disorder induced as a result of milling as is usually the case with other ordered alloys but also a structural change driven by mechanical milling.

In this work we studied the phase transformation behavior of Fe_3Ge alloys synthesized in the disordered state by direct milling of the constituent elements and found several new and interesting effects. The as-milled material forms in a disordered bcc α phase (A2 structure) (as discussed earlier in chapter 3), orders initially into the α_1 phase (DO_3 structure) on isothermal heating above 400°C and later transforms to the equilibrium ϵ phase ($L1_2$ structure). This interesting phase transformation behavior is attributed to a grain size effect. We show here that the metastable ordered α_1 phase exists up to a critical grain size after which the Gibbs free energy of the equilibrium ϵ phase is lowered relative to the α_1 phase and the transformation is driven by a capillary effect or the Gibbs-Thomson effect [ref 194 of chapter 1].

We also studied the effect of Mn addition to the $A2 \rightarrow L1_2$ phase transformation in the Fe-Ge system. Earlier it was found (chapter 3) that Mn atoms were segregated to the GB regions on the development of DO_3 order in the nanocrystalline $Fe_{3-x}Mn_xGe$ (with $x = 0.3, 0.45, 0.6$, and 0.75) alloys. Our idea was to see the effect of this boundary segregation on the equilibrium phase transformation. We found that in the case of Mn substituted alloys the $A2 \rightarrow L1_2$ phase transformation was taking place through the formation of a intermediate

DO₃ phase and this transformation was not only governed by the Gibbs-Thompson effect but also by the kinetics of transformation.

6.1 Fe-Ge

a Experimental

The as-milled alloys with Fe₃Ge and Fe_{0.73}Ge_{0.27} stoichiometry were subjected to heat treatments at 480°C, 500°C, 520°C and 540°C for periods of time ranging from few hours to few hundreds of hours to see the evolution of this ordered L1₂ phase from the disordered bcc (A2) phase.

b Results and discussion

Figure 6.1 shows the representative XRD patterns recorded for samples heat treated at the temperatures indicated for periods of times mentioned in the figure. There is no signature of the fcc (L1₂) phase for the samples heat treated at 480, 500, and 520°C for 96, 57 and 26 hours respectively. The presence of only bcc peaks is evident. The narrowing of lines is indicating grain coarsening. Although in the X-Ray patterns the superlattice lines ($\frac{1}{2} \frac{1}{2} \frac{1}{2}$) and (100) corresponding to the DO₃ phase could not be observed because of their very small intensity, but the presence of DO₃ order was confirmed through Mossbauer spectroscopic measurements. The evolution of the fcc peaks with lattice constant of 3.665 Å [2] starts only after 168, 95, and 39 hours of heat treatments at 480, 500, and 520°C. However at 540°C fcc peaks were evolved even after 5 hours of heat treatment. The fcc and bcc line intensities of the patterns show the growth of fcc phase at the expense of bcc phase. Thus the disordered bcc as-milled phase transforms initially to a metastable but DO₃ ordered bcc phase before it transforms finally to L1₂ ordered fcc with an admixture of fcc+bcc phases in the intermediate stages.

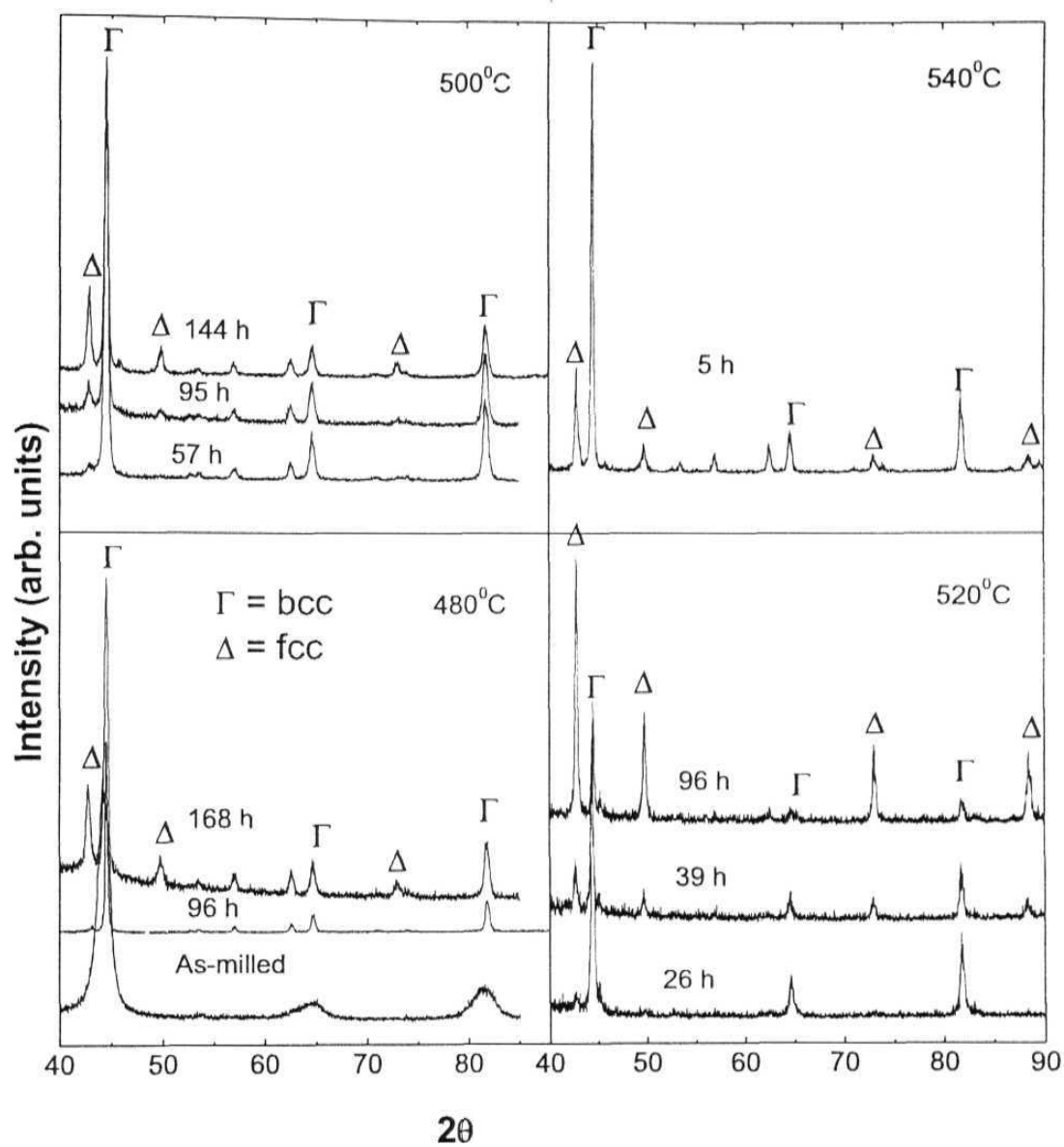


Figure 6.1: Representative XRD patterns of $\text{Fe}_{0.73}\text{Ge}_{0.27}$ alloy samples in as milled state and after different heat treatments as indicated.

Figures 6.2 and 6.3 show the evolution of the Mossbauer spectra and HMF distributions at the above temperatures for the same time of heat treatment. In the initial stages of the transformation there is formation of α_1 phase as can be seen unambiguously by the presence of 330 and 205 KOe peaks in the HMF distribution, characteristic of DO_3 phase. The development of the ϵ phase is seen from the presence of peaks in HMF distributions at 245 kOe. This peak should not be confused with the peak at around 257 kOe arising from 3 Ge 1nn of Fe due to incomplete DO_3 order [ref 27 of chapter 2, ref 24 of chapter 1]. Simultaneously with the increase of the 245 kOe fcc peak there is a decrease in the intensity of the peaks corresponding to the α_1 phase. Mossbauer and X-ray diffraction studies therefore confirm the formation of the ϵ (L1_2) phase via the formation of the α_1 phase from the A2 phase. The Mossbauer spectrum and HMF distribution corresponded to the fully formed ϵ phase after 14 days of heat treatment at 520°C.

There were earlier reports of Mossbauer spectroscopic studies on polycrystalline Fe_3Ge prepared by induction melting [3] or powder metallurgy [2] and atomically ordered by long time heat treatments in the ϵ' phase region to get L1_2 ordered phase. These show two superimposed hyperfine spectra with average fields, isomer shifts (relative to $\alpha\text{-Fe}$), and quadrupole splits values of (243+3) kOe, (0.25+0.03) mm/sec, (0.18 \pm 0.02) mm/sec for one site and (218+3) kOe, (0.25 \pm 0.03) mm/sec, and (-0.35 \pm 0.02) mm/sec respectively at 295 K for the other [2]. The evolution of the 245 kOe field in our heat-treated samples thus confirms the presence of L1_2 order. The other expected field for ϵ phase at 218 kOe overlaps with the 205 kOe DO_3 field and is not resolved in our field distributions. As such the fitting of the spectrum consisting of the 245 kOe L1_2 field is not very good with just a distribution having correlation (1 = $aH + b$), so a fixed field component with above hyperfine parameters was introduced (as allowed by the Le Caer and Dubois fitting program (discussed in

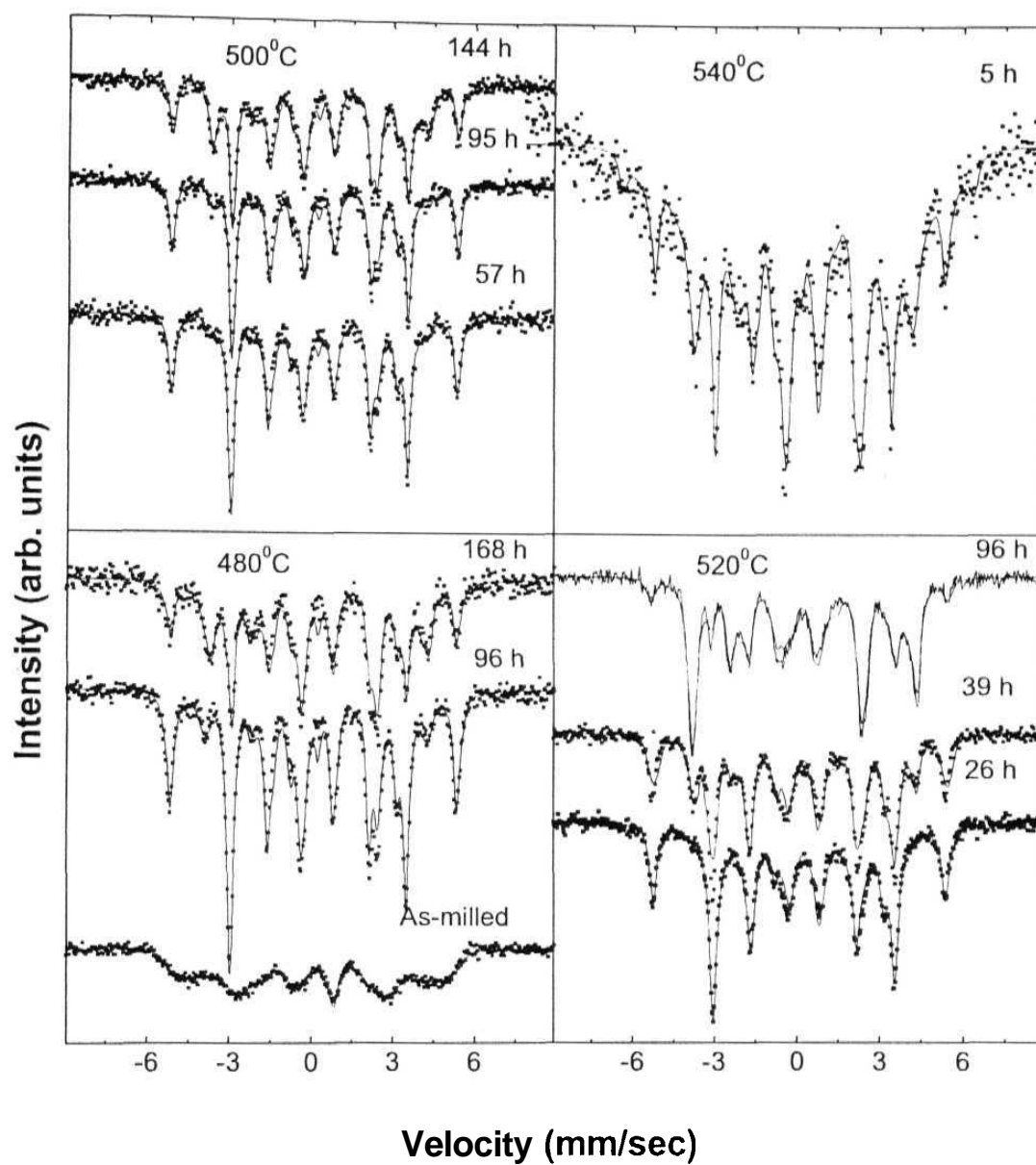


Figure 6.2: Mössbauer spectra of as-milled and various heat treated samples with $\sim\text{Fe Ge}$ compositions showing the $\text{A2-DO}_3\text{-L1}_2$ phase transformation (symbols: exp; sold lines:fit).

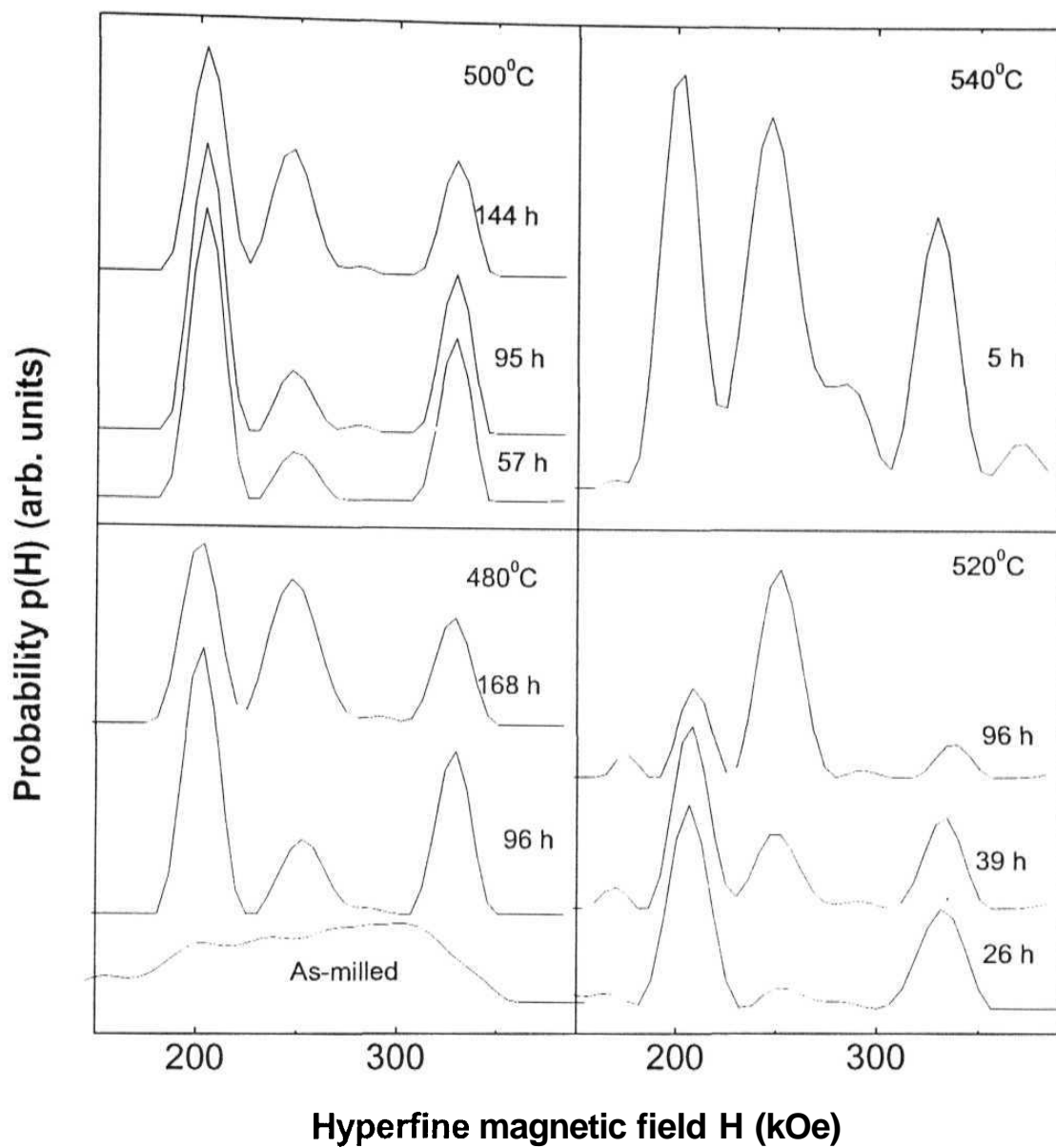


Figure 6.3: HMF distributions evaluated from the spectra of Figure 6.2, showing evolution of distinct peaks due to α_1 phase and ϵ phase at different temperatures and times.

chapter 2)) to improve the fitting. The values of the fixed field h-parameters were varied to some extent to get a better χ^2 . The optimized values of the parameters obtained giving minimum χ^2 was in the range of (245-250) kOe, (0.23-0.27) mm/sec, and (0.15-0.19) mm/sec for the HMF, IS, and QS respectively. The improvement of fitting by introducing such fixed field component also indicates undoubtedly that it is the $L1_2$ field component and not the component arising due to incomplete DO_3 order. The temporal evolution at 520°C of the ε and α_1 phases as evaluated from the total areas of the characteristics peaks of these phases in the HMF distributions is shown in Figure 6.4.

We propose that this phase transformation behavior from the disordered bcc α phase to the equilibrium E ($L1_2$) phase through a metastable ordered α_1 (DO_3) phase is a consequence of the Gibbs Thomson effect (or capillary effect). Manifestation of this effect was also seen in the Mo-clustering of the Fe-Mo homogeneous alloys beyond a critical grain size. Let us recall (from chapter 5) that the Gibbs free energy of an alloy phase increases by an amount $\Delta G = 2\gamma V_m / R$ for a finite size grain of radius R (assuming spherical grains) relative to a very large size system due to the surface energy γ residing in the grain boundary:

$$G(R) \cong G(\infty) + 2\gamma V_m / R \quad (6.1)$$

where V_m is the molar volume.

For finite size grains the Gibbs free energy for the DO_3 grains as well as the $L1_2$ grains will be increased relative to their bulk Gibbs free energy. However due the close packing of the fcc grains the grain boundary energy for the $L1_2$ grains is larger as compared to the DO_3 grains and the increase in Gibbs free energy of $L1_2$ grains will be more as compared to the DO_3 grains. The lower Gibbs free energy DO_3 ordered phase is therefore stabilized for smaller grain size in the initial stages of transformation. However as the grains grow in size

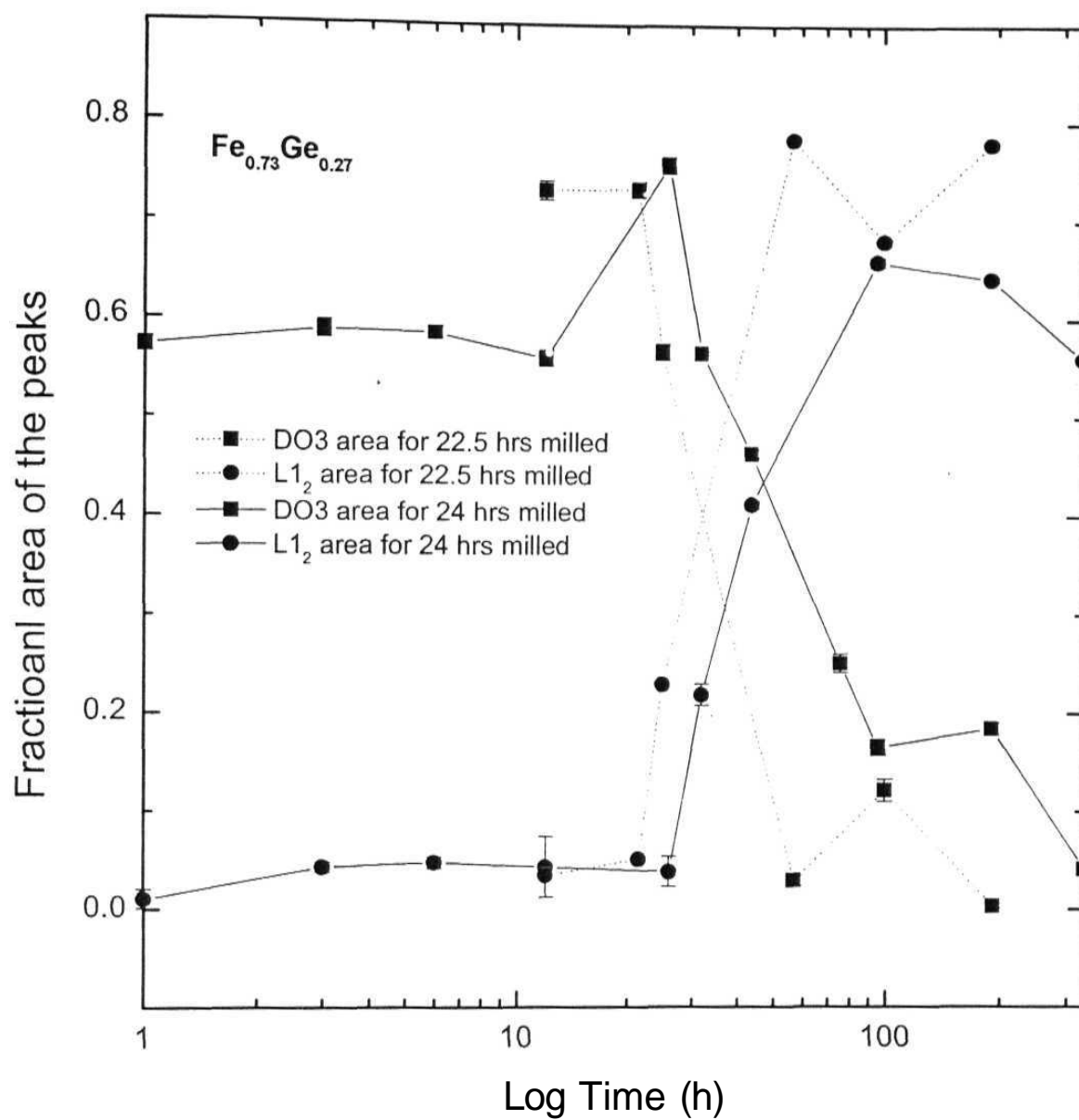
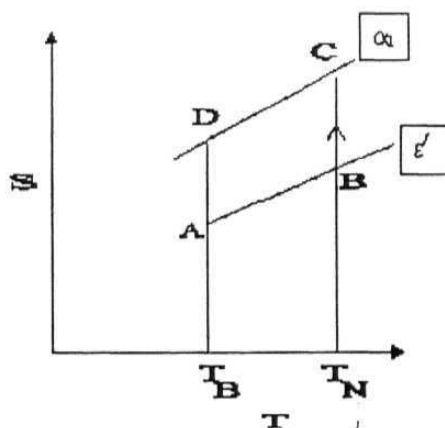


Figure 6.4: Temporal evolution at 520 C of the ϵ and α_1 phases for 24h and 22.5 h milled $\text{Fe}_{0.73}\text{Ge}_{0.27}$ alloys.

the Gibbs free energy of the $L1_2$ ordered phase decreases faster than the Gibbs free energy of the DO_3 ordered phase and they both become equal at a certain grain size R_0 . Beyond R_0 Gibbs free energy of the $L1_2$ ordered phase is lower than that of the DO_3 ordered phase and there is a rapid phase transformation to the $L1_2$ phase. To obtain an estimate of the grain size R_0 at which the $\alpha_1 (DO_3) \rightarrow \epsilon' (L1_2)$ phase transformation takes place at $T=T_N$ (the temperature at which the $\alpha_1(DO_3) \rightarrow \epsilon'(L1_2)$ phase transformation behavior was studied) we equate the Gibbs free energies of the two phases at R_0 $\{G_{\alpha_1}(R_0, T_N) = G_{\epsilon'}(R_0, T_N)\}$. This immediately yields an expression for the Gibbs free energy difference between the two phases for the bulk system at T_N which is given by

$$\Delta G^{\alpha_1 - \epsilon'}(T_N) = G_{\alpha_1}(\infty, T_N) - G_{\epsilon'}(\infty, T_N) = (2/R_0)(\gamma_{\epsilon'} V_{\epsilon'} - \gamma_{\alpha_1} V_{\alpha_1}) \quad (6.2)$$

where γ and V refer respectively to grain boundary energy and molar volume of the phases. The Gibbs free energy difference ($\Delta G^{\alpha_1 - \epsilon'}$) can also be estimated thermodynamically as follows, using the property that both entropy and enthalpy are state functions. Let us consider the S-T diagram below.



In the diagram T_B is the transition temperature at which the $DO_3 \rightarrow L1_2$ transformation takes place in the bulk system, T_N is the temperature at which the heat treatment was carried out, and α_1 and ϵ are the equilibrium phases. The change in entropy at temperature T_N between α_1 and ϵ phase is given by

$$\Delta S = \int_B^C dS = \int_B^A dS + \int_A^D dS + \int_D^C dS$$

Using 2nd law of thermodynamics, i.e. $dS = dQ/T = (C_P dT)/T$, at constant pressure we get the above expression as

$$\begin{aligned} &= \int_B^A (C_P dT)/T + \Delta S(T_B) + \int_D^C (C_P dT)/T \\ &= \Delta S(T_B) + \int_{T_B}^{T_N} ((\Delta C_P^{\alpha_1 - \epsilon'})/T) dT \\ &= (L_B / T_B) + \int_{T_B}^{T_N} ((\Delta C_P^{\alpha_1 - \epsilon'})/T) dT \end{aligned} \quad (6.3a)$$

where L_B is the latent heat involved in the bulk transition.

Similarly the change in enthalpy at temperature T_N between α_1 and ϵ' phase is given by

$$\Delta H = L_B + \int_{T_B}^{T_N} (\Delta C_P^{\alpha_1 - \epsilon'}) dT \quad (6.3b)$$

If we assume that the specific heat difference between the α_1 and the ϵ' phases (ΔC_P) is independent of temperature and employ Thompson and Spaepen [4, 5] approximation then we get

$$\Delta C_P = \Delta S(T_B) = L_B / T_B \quad (6.4)$$

Using equations (6.3a), (6.3b) and (6.4) we can show that Gibbs free energy difference between α_1 and ϵ' phase at T_N

$$\Delta G^{\alpha_1 - \epsilon'}(T_N) = \Delta H - T_N \Delta S = L_B (T_N / T_B) \ln (T_N / T_B) \quad (6.5)$$

A compilation of measured grain boundary energy by Murr [6] lists the values for γ for the δ -Fe (bcc) and γ -Fe (fcc) phases equal to 468 mJ/m² and

756 mJ/m respectively. We used these values of γ for DO₃ (based on bcc structure) and L1₂ (based on fcc structure) phases of Fe₃Ge as a first approximation since no data on Fe₃Ge are available. The enthalpy change across the DO₃→L1₂ transformation for the bulk system is not available but the total enthalpy change which includes annealing out of lattice strain, crystal growth and phase restoration from disordered bcc to L1₂ phase has been measured to be 8.1 kJ/mole by Zhou and Bakker from the DSC data. We use this value for L_B and $T_B = 400$ C according to equilibrium phase diagram to estimate ΔG at T_N values of 480, 500, 520, and 540⁰C using equation (6.4). The molar volumes of 28.73 cm³ (DO₃ phase) and 29.65 cm³ (L1₂ phase) were obtained from the measured lattice constants of the two phases. The critical radius R_0 was calculated using equation (6.2).

The grain growth behavior at different temperatures (T_N) is shown in figure 6.5. The rate at which grains grows is similar at these temperatures. The solid line is the fitting through the experimental points using equation 3.11. The good quality of fit shows grain growth of first order similar to that obtained in case of Fe-Al. Figure 6.6 shows at 520⁰C the temporal evolution of grain size as well as α_1 and ϵ' phases. It is evident that at a particular grain size of around 45 nm only the DO₃→L1₂ phase transformation starts and then the grain growth becomes sluggish whereas amount of L1₂ phase increases and DO₃ phase decreases rapidly. One more important point to be noted from the figure is that in contrast to 350⁰C heat treatment (chapter 3) at this temperature the kinetics of grain growth and DO₃ ordering is not the same. The attainment of maximum possible DO₃ order is over within 1 hour of heat treatment whereas grain growth continues further until the L1₂ phase starts forming. This is interesting and could be explained from the fact that unlike at 350⁰C, the DO₃ phase at this temperature is not the equilibrium phase, and hence though the system is initially quickly going to a metastable phase but the grains grows

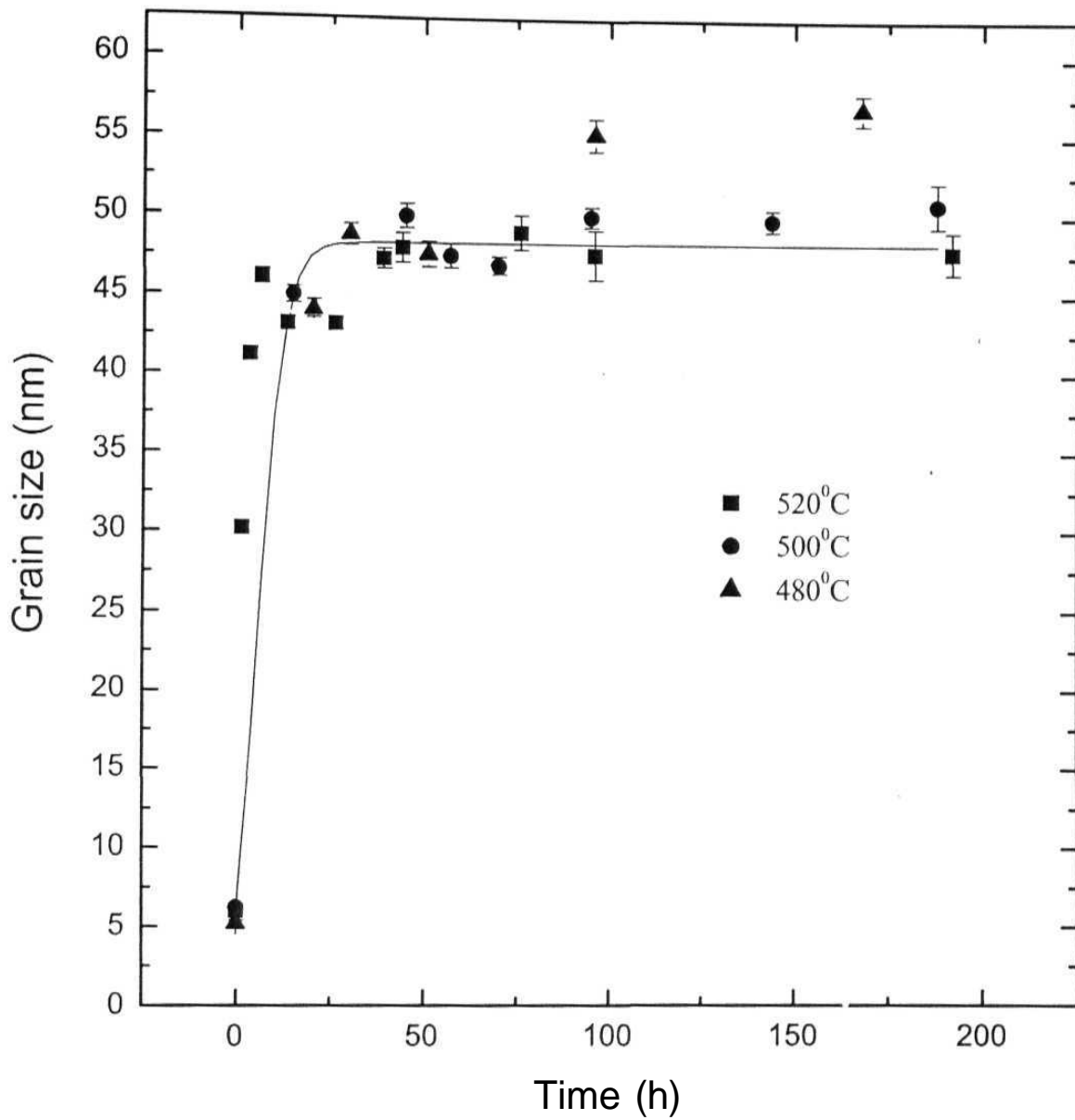


Figure 6.5: Grain growth at different temperatures. It is seen that the rate of grain growth is temperature independent within this range of temperatures.

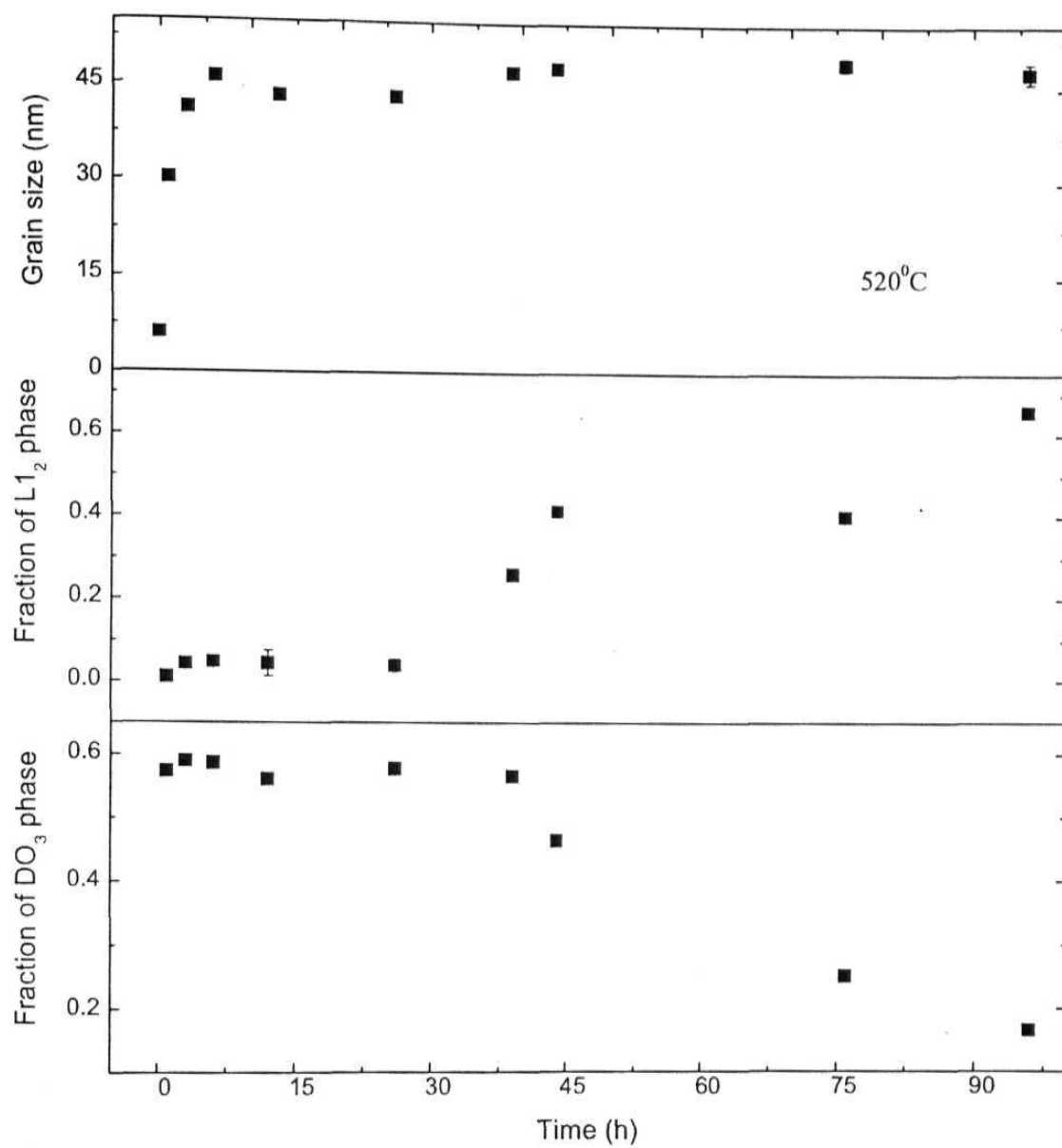


Figure 6.6: Shows the temporal evolutions of grain size and the α_1 and ϵ phases at 520°C. It is seen that at a critical grain size of ~45 nm the $L1_2$ phase starts forming replacing DO_3 phase.

further to reduce the surface energy contribution to Gibbs free energy and to form the equilibrium phase. In figure 6.7 the critical grain sizes at which the $L1_2$ phase starts forming at different temperatures are shown. Figure 6.8 shows the variation of experimentally measured and theoretically calculated values (using equation 6.4) of critical radius R_0 (average grain size at a stage when the $L1_2$ phase just starts showing up) with T_N . In view of the fact that the value used for the $\alpha_1 \rightarrow \epsilon'$ enthalpy change at T_B is an overestimate (since it includes other contributions) and the values for the surface energies (γ) are also approximated, the agreement between the experimental and the calculated values of R_0 can be considered reasonably good, which imparts a fair amount of confidence in our model.

To further confirm that the phase transformation from α_1 (DO_3) to ϵ ($L1_2$) phase is indeed a grain size effect, we prepared another ball milled $Fe_{0.73}Ge_{0.27}$ sample by milling the powders for 22.5 hours. The initial size of the grain was 7.3 nm as compared to the grain size of 6.5 nm for the 24 hours milled sample. The $\alpha_1 \rightarrow \epsilon$ phase transformation for the 22.5 hours milled sample started earlier i.e. only after 25 hours of heat treatment at 520 °C as compared to 32 hours at 520 °C required for the 24 hours milled sample (figure 6.4). The average initial size of the grains here was larger and their growth to the required size for the $\alpha_1(DO_3) \rightarrow \epsilon'(L1_2)$ transformation at 520 °C occurred at an earlier time. This gives an additional support to our hypothesis that the phase transformation observed is a consequence of the Gibbs Thomson effect.

6.2 Fe-Mn-Ge

a Experimental Results and Discussions

$Fe_{3-x}Mn_xGe$ (with $x = 0.3, 0.45, 0.6, \text{ and } 0.75$) as-milled disordered alloys were heat treated at 520 °C for times ranging from 24 to 100 hrs. Figure

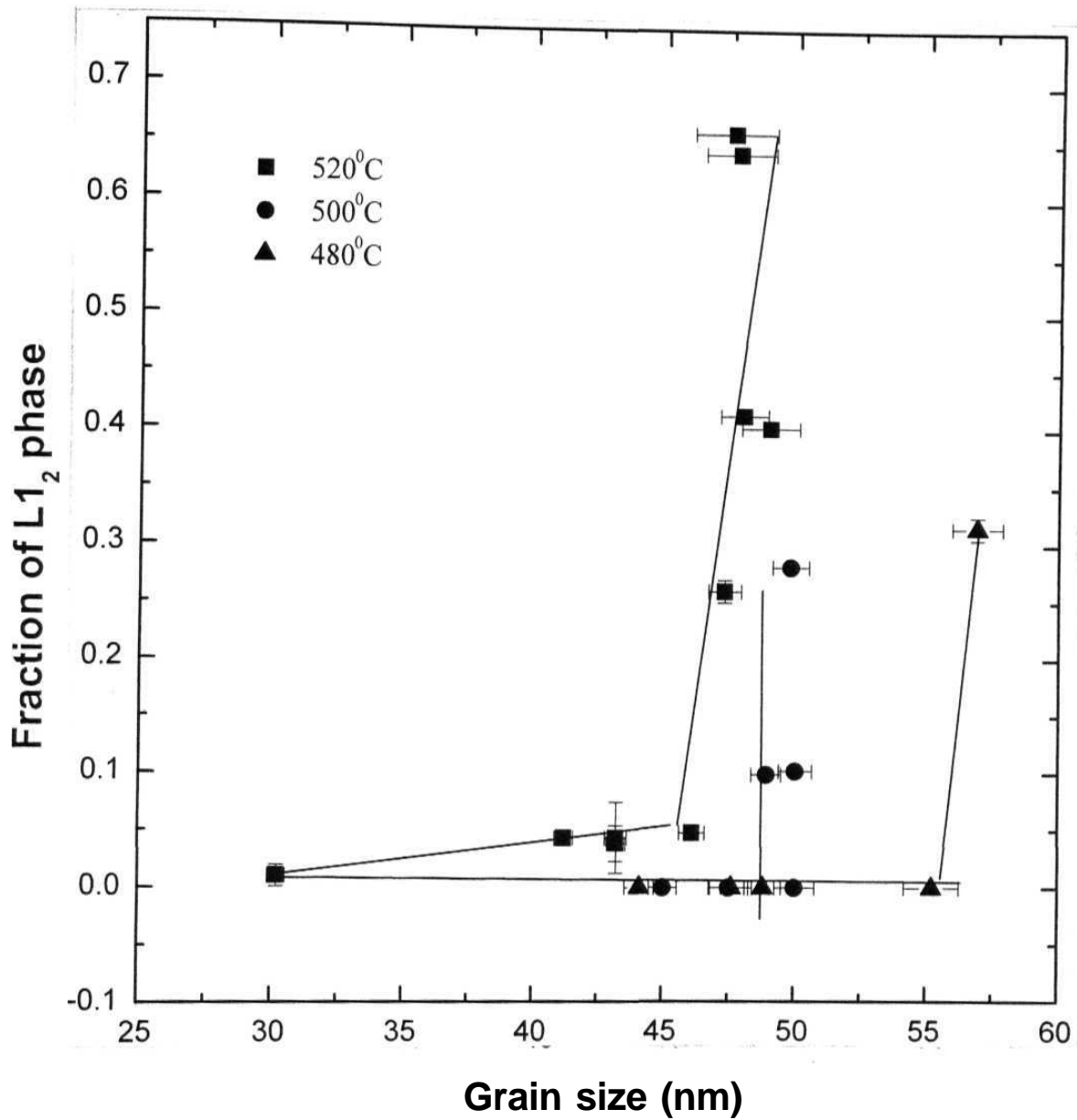


Figure 6.7: The critical grain sizes at which the $L1_2$ phase starts forming at different temperatures are shown. The fact that once the $L1_2$ phase starts forming the grain growth virtually ceases is also seen (solid lines are just guides to eye).

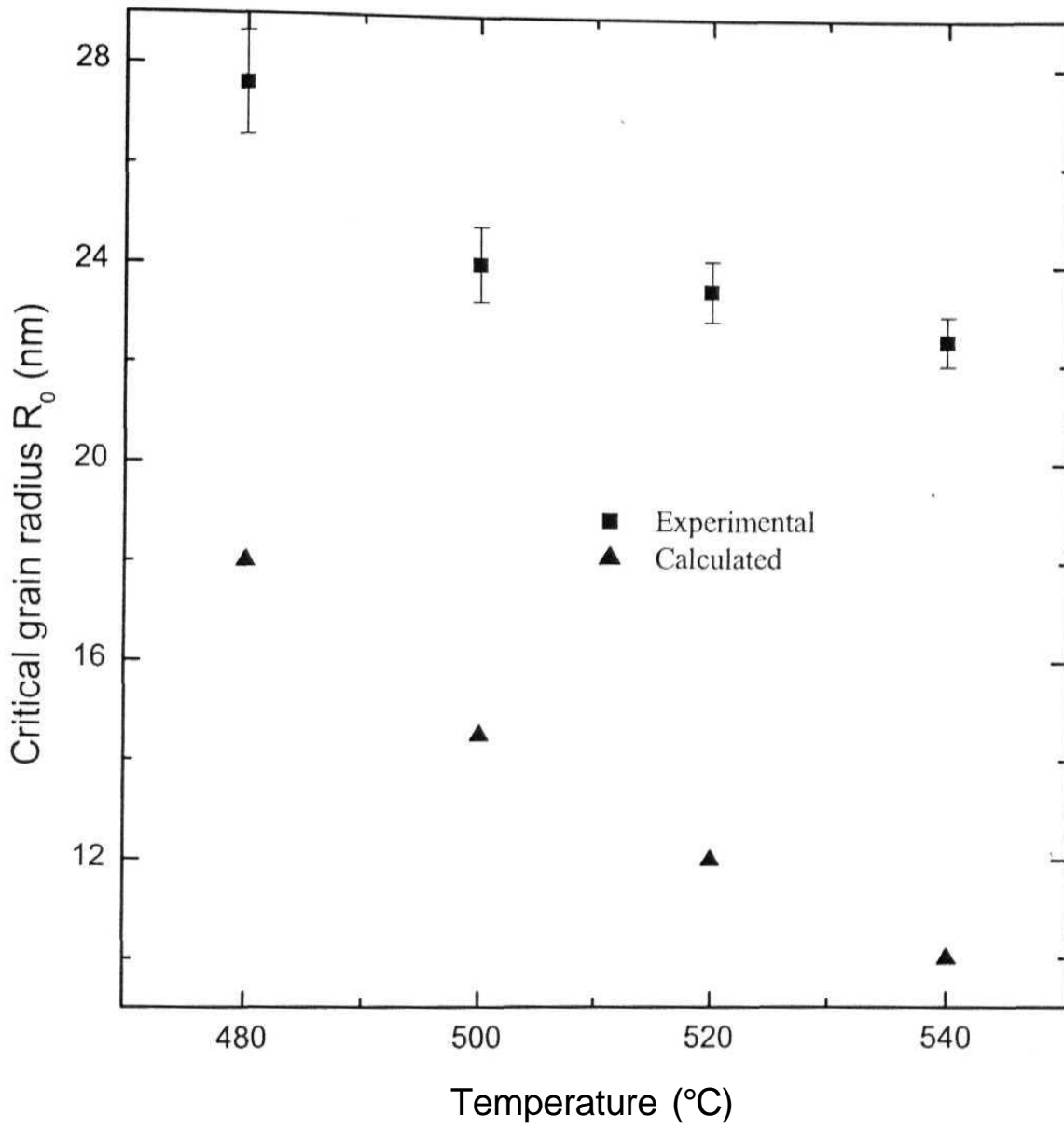


Figure 6.8: Comparison of calculated (using Eq. 6.4) and experimentally obtained critical grain radius (R_0) at different temperatures.

6.9 shows the X-Ray patterns obtained after heat treatment of 24 and 100 hours for the alloy compositions of $x=0.0$ and $x= 0.75$. No Bragg reflection lines arising from the ϵ phase were visible for 24 hours heat treatment, only bcc (DO3 structured) reflection lines were present. The behavior was the same even after 50 hours of heat treatment. The formation of ϵ phase could be seen after 100 hours of heat treatment.

The Mossbauer spectra and the corresponding HMF distributions of different Mn concentration heat-treated alloys are shown in figures 6.10 and 6.11. The evolution after 24 hours of the hyperfine magnetic field peaks arising only from the 4(b) and 8(c) sites Fe atoms of the DO3 ordered structure was similar to that obtained for the samples heat treated at 350°C . No signature of $L1_2$ phase peaks was there. Similar behavior was obtained after 50 hours of heat treatment also. Mn segregation to the GB regions as the DO3 order develops is evident from no resemblance of the distributions of figure 6.11 with that of figure 3.39. The emergence of the ~ 245 kOe field peak, corresponding to ϵ phase, is clearly seen in figures 6.10 and 6.11 after 100 hours of heat treatment. The other field (~ 218 kOe) of the ϵ phase is getting merged with the 200 kOe DO3 site (8(c)) field. We have introduced fixed field component similar to $x = 0.0$ alloy to fit better the $L1_2$ phase line in the Mossbauer spectra of Mn substituted alloys. From the formation of the $L1_2$ phase, which is highly composition sensitive (phase diagram of figure 3.22) it may be postulated that along with Mn, in this case Ge atoms are also segregating to the grain boundaries to maintain the correct composition required to form the ϵ phase. But there is no signature of any other lines except the bcc peaks in the XRD patterns of figure 6.9, which immediately indicates the absence of any Mn rich, Ge rich, or Mn-Ge phase. The Mn and Ge atoms therefore constitute the boundary atoms keeping the underlying lattice as the

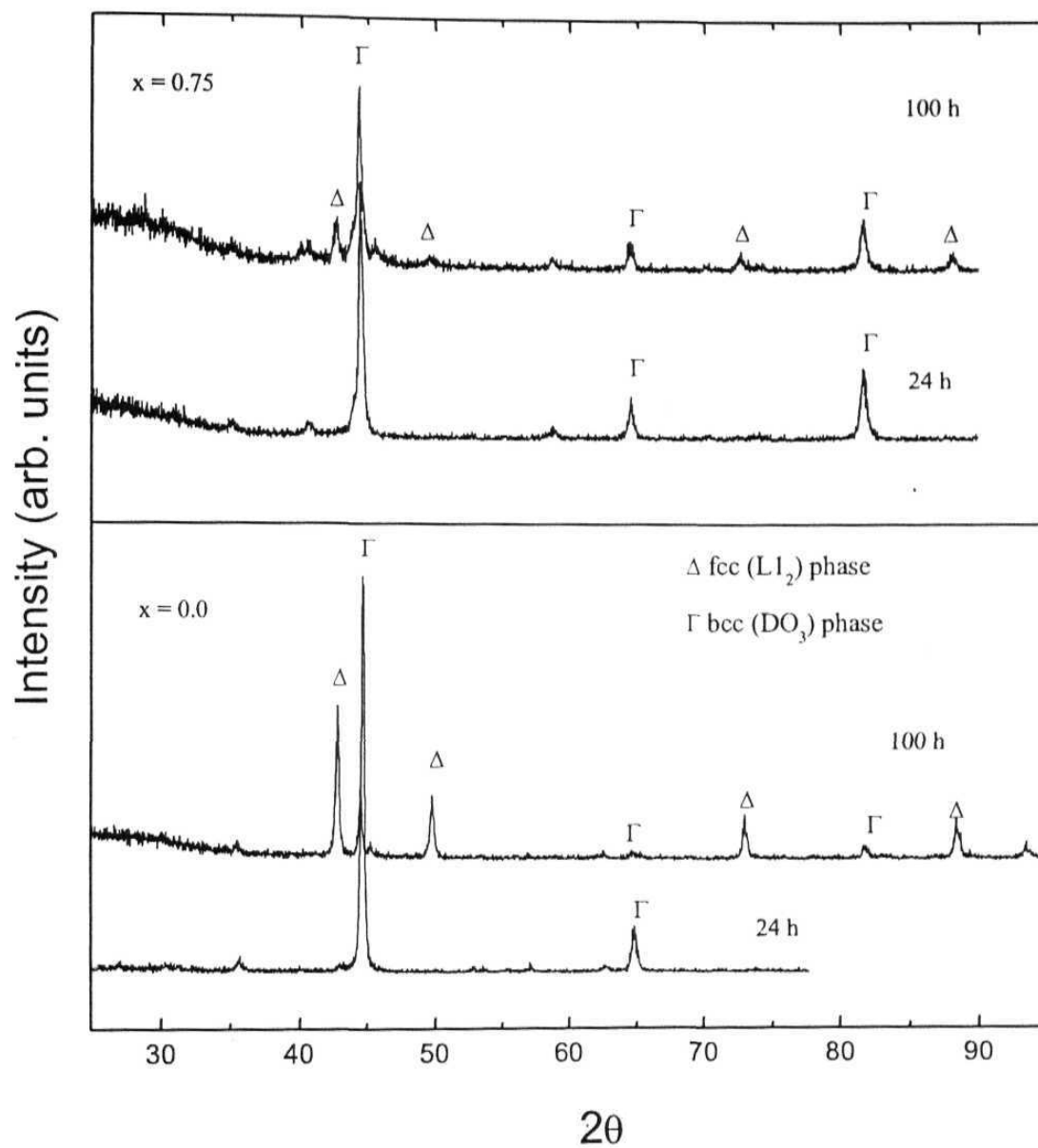


Figure 6.9: Representative X-Ray diffraction patterns of the $\text{Fe}_{3-x}\text{Mn}_x\text{Ge}$ (with $x = 0.0$ and 0.75) alloy samples heat-treated at 520°C for 24 and 100 hours, respectively.

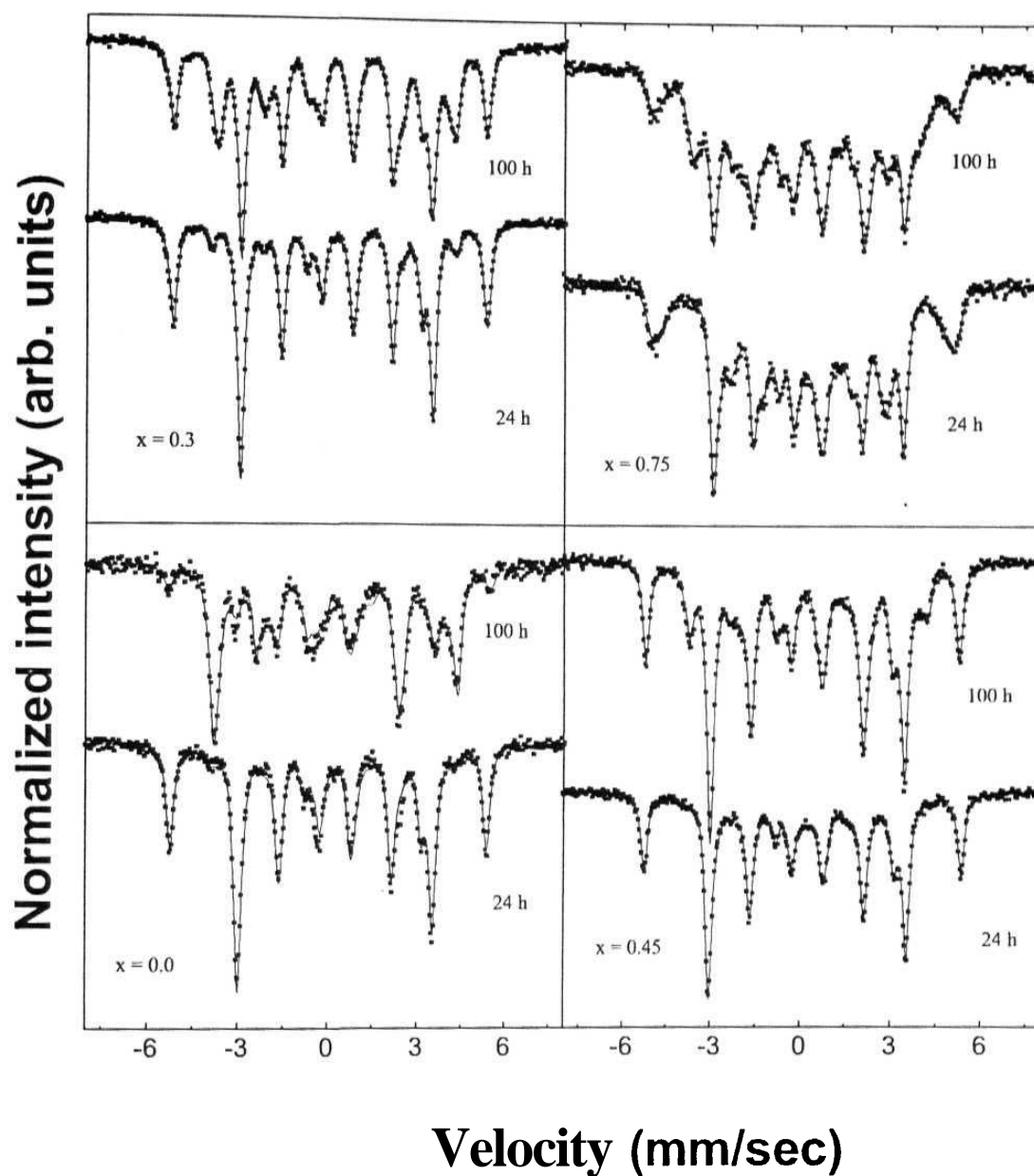


Figure 6.10: Mossbauer spectra of different Mn concentration alloy samples heat-treated at 520°C for 24 and 100 h (symbols: exp; lines: fit).

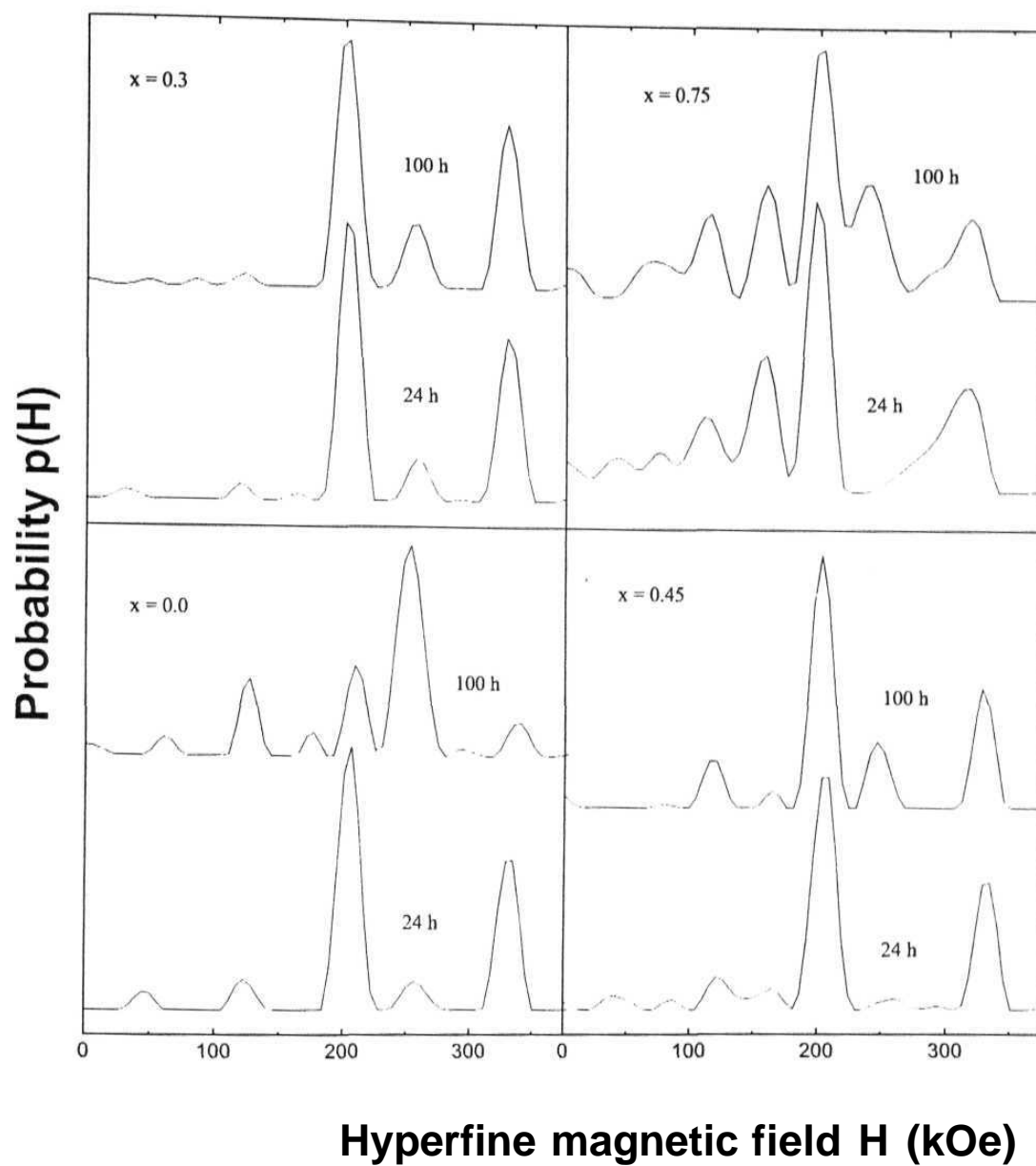


Figure 6.11: HMF distributions of the 520°C, 24 and 100 h heat-treated samples with different Mn concentrations.

DO_3 or $L1_2$ ordered Fe-Ge lattice. This picture of the atomic arrangement will be useful while discussing the kinetics of the $L1_2$ phase formation.

The grain growth behavior at 520°C is shown in figure 6.12. Similar grain growth behavior is observed for the $x=0.0$ and lower Mn concentration (up to $x=0.45$) alloys but the grain growth is decreased by a factor of nearly half for the higher Mn concentration sample. This was in contrast to the behavior observed at 350° C (figure 3.36) where grain growth was similar for all Mn concentrations. Saturation in grain growth is observed for different heat treatment times at 520°C with different Mn concentrations. The difference in grain growth and ϵ phase formation behavior between the $x = 0.0$ and Mn substituted alloys is the saturation of grain growth before $L1_2$ phase started forming. In case of pure Fe_3Ge alloy bcc grains grew continuously to a size of ~ 45 nm (the critical size R_0) when the fcc phase started forming (after about 32 hours of heat treatment). Then the grain growth was retarded and virtually saturated although the fraction of ϵ phase kept on growing. Therefore the formation of the ϵ phase in pure Fe_3Ge was purely a grain size effect (the Gibbs Thomson Effect as alluded to earlier) and not a kinetic effect. In the Mn substituted alloys though the critical grain size for $DO_3 \rightarrow L1_2$ transformation was reached after 24 hours of heat treatment but the formation of the ϵ phase started after about 100 hours. The ϵ phase transformation for pure Fe-Ge was almost complete after 100 hours whereas for Mn substituted alloys it just started after 100 hours. This shows that the $DO_3 \rightarrow L1_2$ transformation in this case is not only a grain size effect (like in Fe_3Ge) but also a kinetic effect. The delayed $DO_3 \rightarrow L1_2$ transformation could be attributed to a slower diffusion rate of Fe and Ge atoms due to GB segregated Mn/Ge atoms. This behavior is also consistent with earlier experimentally observed [7] and theoretically calculated [8] results, which showed slower diffusion rate of atomic species due to grain boundary segregation. Figure 6.13 shows the variation of critical

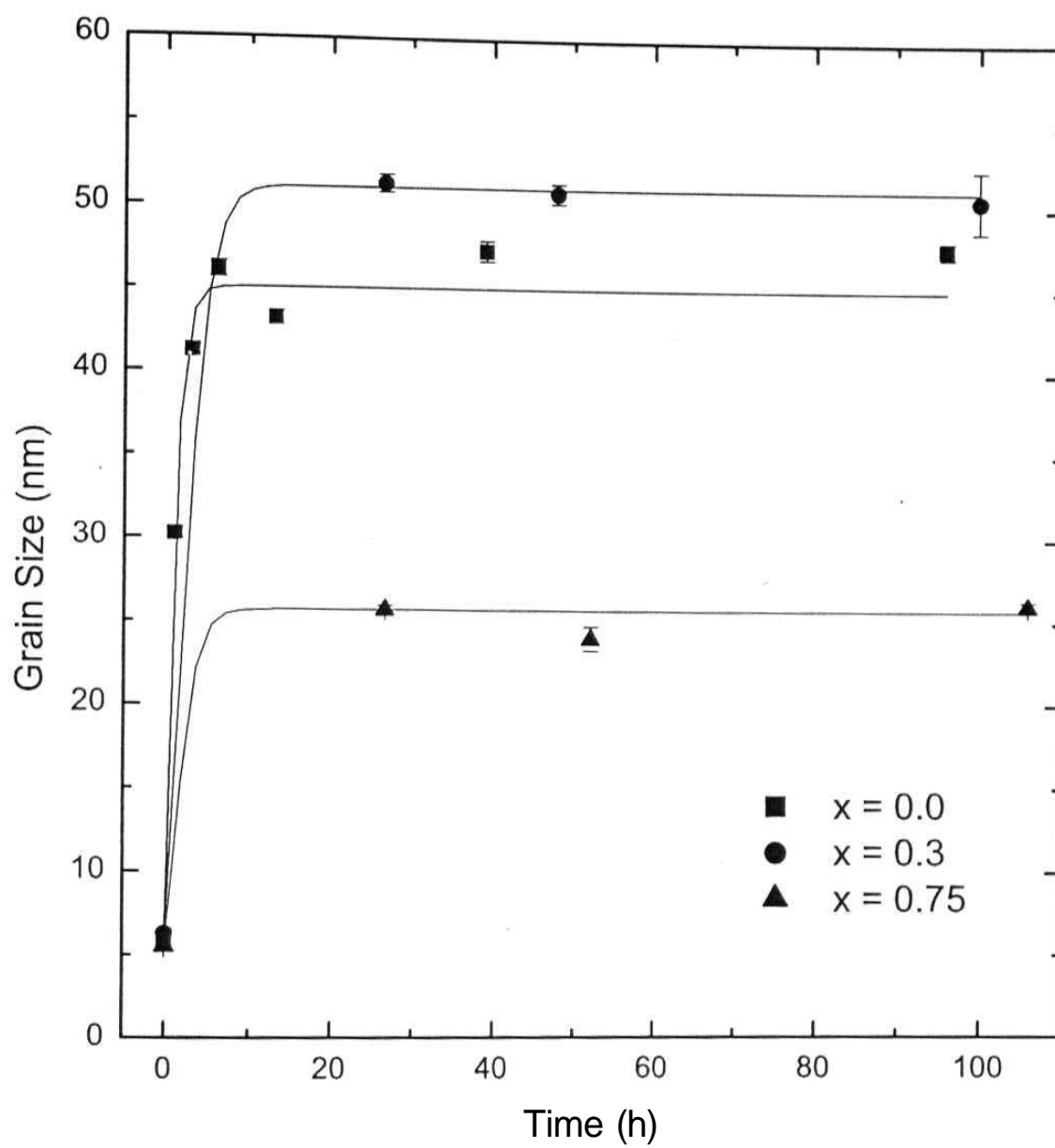


Figure 6.12: Grain growth behavior of the representative alloy samples at 520°C.

grain size (R_0) with Mn concentration. From the fact that R_0 decreases as Mn concentration (x) increases it is clear that grain boundary segregated Mn and also perhaps Ge atoms have a critical role to play on the atomic diffusion to take place for the $\alpha_1 \rightarrow \epsilon'$ phase transformation even when the critical grain size for the transformation is reached.

In conclusion, we studied the phase transformation behavior of chemically disordered bcc (a) phase $\text{Fe}_{1-x}\text{Ge}_x$ alloys near the Fe_3Ge stoichiometry synthesized in the nanocrystalline state by mechanical alloying of the elemental constituents. The evolution of the equilibrium Ll_2 ordered (ϵ) phase was seen to occur via a metastable DO_3 ordered (α_1) phase and the $\alpha_1 \rightarrow \epsilon$ phase transformation took place only after the growth of the grains. This behavior is understood with the help of a capillary effect or the Gibbs Thomson effect wherein the grain boundary energy of the nanosize grains raises the Gibbs free energy of the ϵ' phase relative to the α_1 phase for small sizes and the ϵ phase grows only after a certain grain size is reached. We therefore have observed a significant effect of the surface Gibbs free energy on the phase stability of alloys with grain sizes in the nanometer range, which is precisely the Gibbs Thomson effect. The equilibrium Ll_2 phase formation at 520°C in Mn substituted alloys was influenced not only by the contribution of the surface energy to the total Gibbs free energy in a nanocrystalline alloy but also by the kinetics of the diffusion process.

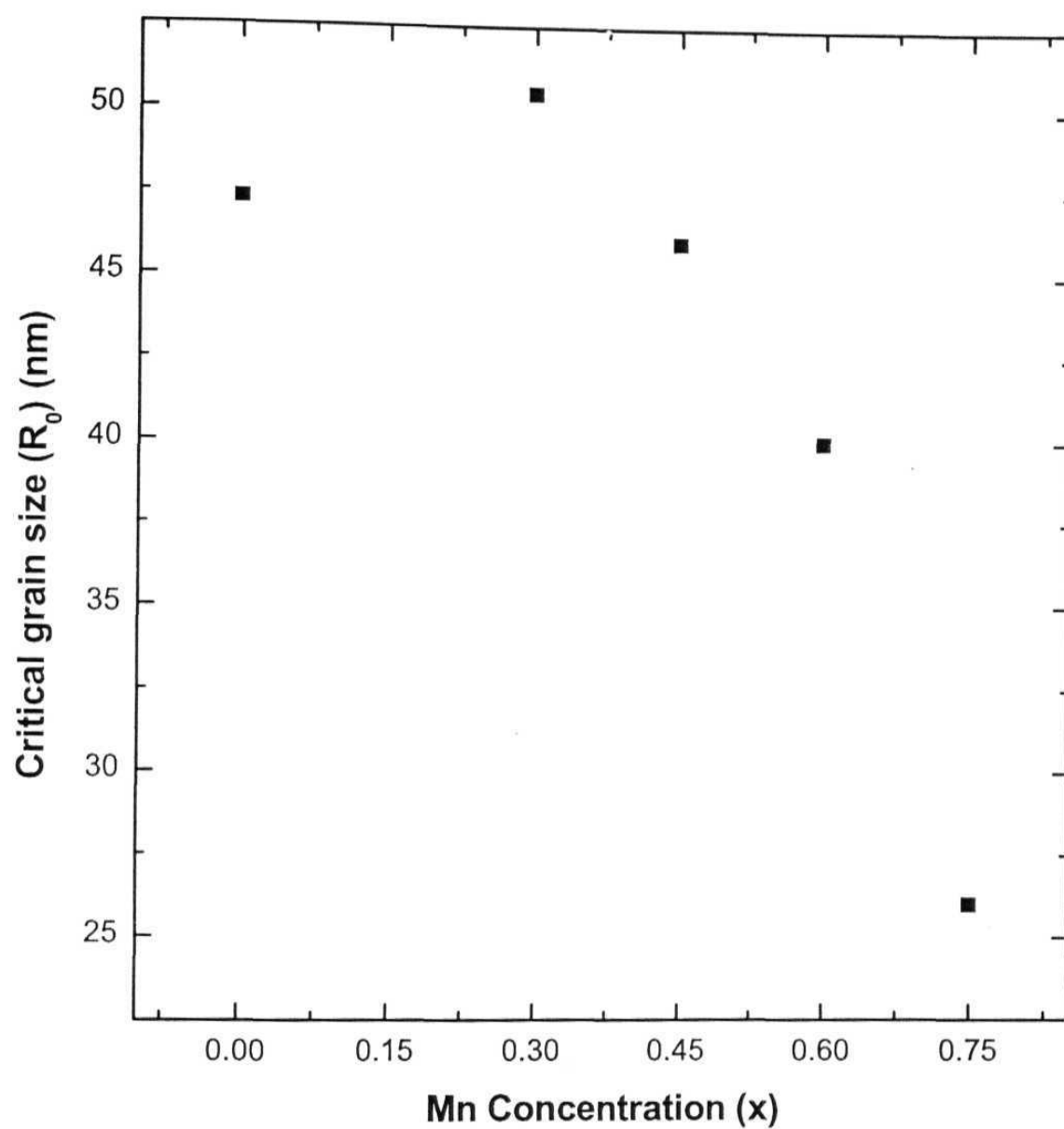


Figure 6.13: Variation of R_0 with Mn concentration.

References

- [1] G. F. Zhou and H. Bakker, *Europhys. Lett.* 30(7), 433 (1995).
- [2] Y. Nakamura and R. Tahara, *J. Phys. Soc. Jap.* **41**, 459 (1976).
- [3] J. W. Drijver, S. O. Sinnema and I. Van der Woude, *J. Phys. F: Metal Phys.* 6, 2165(1976).
- [4] C. V. Thompson and F. Spaepen, *Acta. Metall.* 27, 1855 (1979).
- [5] G. D. Mukherjee, C. Bansal and Ashok Chatterjee, *Solid State Comm.* **104**, pp. 657- 661, 1997.
- [6] L. E. Murr, *Interfacial Phenomenon in metals and Alloys* (Addison Wesley, London, 1975).
- [7] Y. Mishin, C. H. R. Herzig, J. Bernardini, and W. Gust, *Int. Mater. Rev.* **42**, 155(1997).
- [8] X. Y. Liu, W. Xu, S. M. Foiles, and J. B. Adams, *Appl. Phys. Letters* 72, 1578(1998).

Summary of work and future perspectives

In this thesis work I presented the studies on phase transformation behaviour of alloys in the nanocrystalline state. Chemical order-disorder, spinodal decomposition, precipitation, and massive phase transformations were investigated in a wide variety of Fe-based binary, pseudo-binary, and quasi-binary nanocrystalline alloy systems. The small grain size, large volume fraction of surface atoms, and the presence of high diffusivity paths through grain boundaries in these nanocrystalline materials were observed to significantly influence the phase transformation processes.

The following is a brief summary of the significant results obtained in different alloy systems:

Chemical order-disorder

Fe-Al

A rapid growth of DO3 order from the as-milled disordered matrix was seen in the early stages of ordering at 300 and 450⁰C for the alloys with Fe₃Al and Fe_{0.72}Al_{0.28} compositions. But at a later stage it was observed that a substantial amount of B32 ordered phase was present along with the DO3 ordered phase even after long time of heat treatment. This B32 ordered phase was developed in the anti-phase domain boundaries (APDB) of the DO3 ordered domains. The size of the DO3 ordered domains was limited by the grain size. This behavior could be compared with that for microcrystalline alloys where transient B32 ordered phase was observed during the evolution of final DO3 order. First order grain growth and ordering kinetics was observed in contrast to a third order reaction kinetics observed for the microcrystalline alloys.

Fe-Ge

The evolution of DO₃ order from the disordered bcc phase was observed at 350° and 550°C for the Fe_{0.83}Ge_{0.17} alloy composition and at 350°C in Fe₃Ge alloys. The DO₃ order is expected according to equilibrium phase diagram for the 17 at. % Ge alloy but for the 25 at. % Ge alloy equilibrium phase is DO₃+B8₁. Grain growth and ordering kinetics was similar and of first order. First order ordering kinetics was also observed in the evolution of disordered B8₁→ordered B8₁ structure of the Fe_{0.62}Ge_{0.38} alloy at 350°C.

Fe-Mn-Ge

Segregation of Mn atoms to the grain boundaries was observed on the DO₃ order evolution in these systems from a homogeneous disordered initial state. This was in contrast to preferential Mn site substitution in the DO₃ structure observed for the microcrystalline alloys. Similar grain growth and ordering kinetics was observed. Grain growth and DO₃ ordering kinetics was unaffected by the Mn substitution.

FeCo-X(X= Mo, Ge, and W)

Short range $\langle \text{Fe/Co} \rangle$ and $\langle \text{Fe/X} \rangle$ correlations were measured during the kinetic evolution of B2 order from the disorder bcc phase. The kinetic paths in the space spanned by these two short-range order parameters were found to be independent of temperature, in contrast to different kinetic paths observed at different temperature in microcrystalline alloys. This result shows that the diffusion of the different species of atoms took place through the grain boundaries, which acted as short-circuited diffusion paths in these nanocrystalline alloys. Because of these short-circuited diffusion paths, the mobility of the different kinds of atoms were similar. The grain growth and ordering kinetics were similar and there was a linear correlation between the two.

Spinodal decomposition in *Fe-Cr*.

The phase decomposition to Fe-rich α phase and Cr rich α phase from an initial homogeneous disordered bcc phase of the $\text{Fe}_{1-x}\text{Cr}_x$ alloys was observed to be through spinodal decomposition for the $x = 0.35$ and 0.45 alloys and through nucleation and growth process for the $x = 0.2$ alloy. No decomposition was observed for the $x = 0.1$ alloy system. The interesting observation in these alloys was the linear correlation between the grain growth and phase decomposition process indicating that the underlying mechanism for this two processes is the same.

Precipitation transformation in *Fe-Mo*:

The precipitation phase transformation ($\alpha \rightarrow \alpha + \lambda$) in $\text{Fe}_{1-x}\text{Mo}_x$ ($x = 0.01, 0.015, \text{ and } 0.05$) alloys was found to proceed via a coherent Mo clustering similar to large grained microcrystalline alloys but the clustering in the nanocrystalline alloy system took place in the grain boundary regions. The correlation between the grain growth and Mo clustering shows that up to a certain critical grain size Mo atoms remained dissolved in the Fe matrix and then starts segregating to boundaries. This process was explained using the concept of negative surface energy contribution from the nano-grains to the Gibbs' free energy for this phase separating alloy.

The Fe_2Mo (X) phase also precipitated directly in the grain boundary regions in contrast to the microcrystalline system where the Mo clusters within the grains were first dissolved into the Fe-matrix before the X phase was formed.

Massive structural transformations in *Fe-Ge* and *Fe-Mn-Ge*:

The evolution of the equilibrium L_{12} ordered (fcc) phase in Fe_3Ge alloys was seen to occur via a metastable DO_3 ordered (bcc) phase from the

disordered bcc phase. The massive phase transformation from the DO_3 to L_{12} phase occurred only when the bcc grains attained a critical size and this was understood as a manifestation of the Gibbs-Thompson (G-T) effect or capillary effect. In case of Mn substituted alloys this massive transformation was not only governed by G-T effect but also by the kinetics of atomic diffusion.

The work presented in this thesis was based on a study of alloys with nano-grain structure, which have both size dependent and grain boundary effects on phase transformations. In order to establish further the size dependent phase stability effects it may be interesting to study these effects in isolated nano-clusters of these alloys. Nano-clusters of different sizes can be synthesized by gas condensation methods and their phase stability could be studied directly.

The estimate of Gibbs free energy of the nanocrystalline alloys in this work was carried out taking only surface energy contributions into account and this was able to provide reasonable order of magnitude agreements with experimental observations. However it may be required to incorporate strain energy contributions also to get better estimates.

It may also be desirable to study the microstructure evolution of the alloy phases by direct microscopic observations to confirm some of the results presented in this work.